

School of Earth and Planetary Sciences,  
The Institute for Geoscience Research (TIGeR)

Isotopic dating and geochemical characterization of  
petroleum system events: case studies from the McArthur,  
Tarim and Sichuan Basins

Shaojie Li

This thesis is presented for the Degree of  
Doctor of Philosophy  
Of Curtin University

April 2019

## **Declaration**

To the best of my knowledge and belief this thesis contains no material previously published by any other person except where due acknowledgement has been made.

This thesis contains no material which has been accepted for the award of any other degree or diploma in any university.

Shaojie Li

Perth, April, 2019

*“The journey is long, I shall search up and down.”*

*--Qu yuan*

## **Abstract**

The petroleum system is defined as a system consisting of source rock and its generated hydrocarbon, and geological entities (reservoir, caprock and overburden rocks) and events (hydrocarbon generation, charge and alteration) that are necessary for entrapment of hydrocarbons. Petroleum system isotope geochronology is an emerging area of geochemical studies of petroleum systems. Organic-rich naturally occurring substances and authigenic minerals precipitated during petroleum system events are repositories of long-lived radioactive-radiogenic metal isotope pairs (e.g. rhenium-osmium and rubidium-strontium). These isotope geochronometers have robust potential for dating petroleum system events and hydrocarbon-source correlation. However, the application of isotope geochronology to petroleum systems is primarily hindered by the limited fundamental knowledge of the behaviour of radiometric isotopic systems in hydrocarbon generation, charge and alteration. The objectives of this PhD project were to unravel the behaviour of two robust radiometric isotopic systems, rhenium-osmium and rubidium-strontium, in petroleum system events and test their

applicability for dating and characterizing petroleum system events.

The timing of hydrocarbon generation can be documented by the rhenium-osmium (Re-Os) isotope system (**Chapter 2**). The Re-Os isotopic systematics of hydrocarbon source rocks in the Barney Creek Formation (BCF) are investigated by using core samples intersected by two drillholes, GRNT-79-5 and Lamont Pass 3 in the McArthur Basin, northern Australia. A positive isochronous trend is defined by nine samples (Group 1) in the plot of  $^{187}\text{Re}/^{188}\text{Os}$ - $^{187}\text{Os}/^{188}\text{Os}$  ratios, and six samples deviate from the trend in the plot (Group 2). Regression of the isochronous trend yields an isotopic age of  $1624 \pm 62$  Ma (Model 3,  $2\sigma$ , MSWD = 23) with an initial  $^{187}\text{Os}/^{188}\text{Os}$  ratio of  $0.34 \pm 0.20$  ( $2\sigma$ ). The age may not represent the timing of deposition because samples come from a vertical interval spanning over a large distance (96.6 – 511.7 meters in GRNT-79-5 and 781.1 – 803.4 meters in Lamont Pass 3) which may have resulted in heterogeneous initial Os isotopic composition. Instead, the Re-Os isotope system in these samples may have been reset by a post-depositional event, which homogenized the Os isotopic composition. Hydrothermally facilitated lamalginite-to-hydrocarbon conversion (i.e. hydrocarbon generation) is a factor resetting the Re-Os isotope system in Group 1 samples. Organic petrographic observation identified two types of organic matter in the studied samples including lamalginite (kerogen) and solid bitumen (hydrocarbon product), and lamalginite-enriched samples have lower Re-Os contents and  $^{187}\text{Re}/^{188}\text{Os}$  ratios compared to lamalginite-depleted

samples. These features suggest that lamalginite-to-hydrocarbon conversion may have remobilised the elements and fractionated  $^{187}\text{Re}/^{188}\text{Os}$  ratios in these samples.  $T_{\text{max}}$  values of the samples also support that hydrocarbon generation resulted in Re-Os redistribution and Re/Os fractionation as there are positive trends in the plots of  $T_{\text{max}}$ -Re contents,  $T_{\text{max}}$ -Os contents and  $T_{\text{max}}-^{187}\text{Re}/^{188}\text{Os}$  ratios. Hydrocarbon generation may have been facilitated by contemporaneous hydrothermal activity which was responsible for the formation of the BCF-hosted McArthur River Pb-Zn-Ag deposit because it increased the temperature of the BCF to above the oil window temperature. Hydrothermal fluids may have also brought additional Re-Os metal budget to the samples. Re and Os can be extracted from hydrothermal fluids and fixed in organic matter during hydrocarbon generation because of their organophilic properties. Therefore, the Re-Os isochronous trend obtained in this study may have resulted from the hydrothermally facilitated hydrocarbon generation event. In contrast to the closed-system  $^{187}\text{Os}$  isotopic behaviour retained in the Group 1 samples, decoupling of  $^{187}\text{Re}$  and  $^{187}\text{Os}$  in the Group 2 samples indicates open-system behaviour (i.e.  $^{187}\text{Os}$  loss). An increased degree of  $^{187}\text{Os}$  loss occurred in samples with greater deviation from the isochronous trend and the loss event ceased earlier in these samples compared to samples with less deviation from the trend.

The timing of hydrocarbon charge can be constrained by rubidium-strontium (Rb-Sr) illitic clay subsample geochronology (**Chapter 3**).

The Rb-Sr isotopic composition was analyzed for small aliquots (3 – 4 mg) of five individual illitic clay samples from a Silurian bituminous sandstone in the Tarim Basin, northwest China, yielding three discrete isochron ages,  $141 \pm 61$  Ma,  $332 \pm 32$  Ma and  $235 \pm 8$  Ma ( $2\sigma$ ). The studied samples are mainly composed of mixed-layer illite/smectite (I/S). The positive correlation between illitization degree (the percentage of illite in I/S) and  $^{87}\text{Rb}/^{86}\text{Sr}$  ratio suggests illitization of I/S fractionated Rb/Sr. Hydrocarbon charge can inhibit the incorporation of Rb and Sr to I/S particles because hydrocarbons are more depleted in metals compared to the formation water, resulting in closed-system behaviour of the Rb-Sr isotope system. Thus, the Rb-Sr ages represent the timing of hydrocarbon charge. The Rb-Sr ages are also consistent with previously-determined K-Ar ages of the samples (125 Ma, 389 Ma and 234 Ma) and petroleum system analysis. However, Rb-Sr analyses of two samples did not yield isochron ages, suggesting that the conditions for producing isochrons were not satisfied, which may be caused by disturbance of the isotope system by post-charge hydrothermal events. Outcomes of this study show the robust potential of Rb-Sr clay subsample geochronology for cross-checking isotopic ages yielded by other systems (e.g. K-Ar system) and constraining the timing of hydrocarbon charge.

Timing of hydrocarbon alteration can be constrained by Rb-Sr pyrite subsample geochronology (**Chapter 4**). The Rb-Sr data for pyrite subsamples in two Ordovician carbonate reservoir specimens from

the Tarim Basin, northwest China, yielded identical isochron ages within analytical uncertainties:  $206 \pm 13$  ( $2\sigma$ ) and  $224 \pm 28$  Ma ( $2\sigma$ ). Pyrite coexists with solid bitumen in the reservoir, suggesting the potential link between precipitation of pyrite and hydrocarbons. The heavy sulphur isotopic composition of the pyrite (31.032 – 31.799‰) suggests that it formed by thermochemical sulphate reduction (TSR) alteration in paleo-oil pools. Lead isotopes of pyrite indicate that fluids in which the crystals precipitated mainly originated from crustal depositories. Burial history shows that reservoir temperature at 206 – 224 Ma was lower than the temperature necessary for TSR (100 – 180° C), thus the precipitation of TSR-pyrite was likely triggered by regional hydrothermal activity which resulted in a high temperature environment. This study demonstrates that Rb-Sr pyrite subsample geochronology, combined with radiogenic and stable isotope analyses, can be used to determine the timing of hydrocarbon alteration.

Re-Os systematics can be utilized for differentiating and characterizing hydrocarbon sources in a petroleum system containing multiple source rocks (**Chapter 5**). Molecular composition of organic extracts and Re-Os isotopic systematics were investigated for the Neoproterozoic-Cambrian bituminous dolomitic natural gas reservoir in the Sichuan Basin, southwest China. Biodegradation-sensitive organic parameters allowed classification of samples into two groups: group 1 is characterized by an insignificant hump in saturated total ion chromatograms (TICs) and

low C<sub>28</sub> norhopane/C<sub>29</sub> hopane (NH<sub>28</sub>/H<sub>29</sub>) values (0.38 – 0.52); whereas group 2 is characterized by an obvious hump in saturated TICs and higher NH<sub>28</sub>/H<sub>29</sub> values (0.85 – 1.05). This indicates that there are two components, biodegraded and fresh, in these samples, and that samples of group 2 have higher proportions of the biodegraded component. Both components are over-mature (MPI-1 equivalent vitrinite reflectance values are 2.34% – 2.74%), and marine shale is their dominant source rock, as suggested by diagnostic scatter plots (Ph/nC<sub>18</sub>-Pr/nC<sub>17</sub> vs Pr/Ph, Ph/nC<sub>18</sub> vs Pr/nC<sub>17</sub>, C<sub>24</sub>/C<sub>23</sub> vs C<sub>22</sub>/C<sub>21</sub> tricyclic terpanes and C<sub>26</sub>/C<sub>25</sub> tricyclic terpane vs C<sub>31</sub>R/C<sub>30</sub> hopane ratios). Compared to the fresh component, the biodegraded component is characterized by: (1) a higher proportion of carbonate-derived hydrocarbons (higher C<sub>31</sub>R/C<sub>30</sub> hopane ratios) and (2) a higher content of bacterial-derived organic matter (higher C<sub>27</sub>/C<sub>29</sub> ααα 20R sterane ratios). The coexistence of biodegraded and fresh components suggests that two episodes of paleo-oil charge likely occurred in the reservoir and that the earlier-charged hydrocarbons were biodegraded before the charge of the fresh component. Organic source and biodegradation influenced the Re-Os distribution in bituminous dolomite. Samples with higher Re-Os contents are characterized by higher C<sub>31</sub> R/C<sub>30</sub> hopane and NH<sub>28</sub>/H<sub>29</sub> ratios, indicating that carbonate-derived hydrocarbons contain higher Re-Os contents and biodegradation can also result in higher contents of both elements. The positive trend between <sup>187</sup>Re/<sup>188</sup>Os and C<sub>31</sub>R/C<sub>30</sub> hopane ratios further indicates that mixing of carbonate-/shale-derived hydrocarbons may influence

Re/Os fractionation. Duplicate analysis of a single bituminous dolomite revealed significant subsample-scale variation in Re-Os isotopic composition, and the Re-Os isotopic heterogeneity resulted in apparent isochron ages that are older than the depositional age of the host rock. A ternary mixing scenario is presented in the  $1/^{192}\text{Os}$  vs  $^{187}\text{Os}/^{188}\text{Os}$  plot of the samples, including I (high Os concentration and  $^{187}\text{Os}/^{188}\text{Os}$  ratio), II (high Os concentration and low  $^{187}\text{Os}/^{188}\text{Os}$  ratio) and III (low Os concentration and  $^{187}\text{Os}/^{188}\text{Os}$  ratio). According to the correlations between biomarkers and Re-Os systematics, higher Os concentration of components I and II resulted from biodegradation and higher proportions of carbonate source contributions, thus, they likely represent the signatures of the earlier-charged/biodegraded hydrocarbons, whereas component III corresponds to the later-charged fresh hydrocarbons. The mixing of carbonate- and shale-derived hydrocarbons in the earlier-charged components may have fractionated their Re/Os ratios, which further resulted in the variable  $^{187}\text{Os}/^{188}\text{Os}$  ratios between components I and II. Therefore, Os isotopic composition may be a potential indicator for characterizing hydrocarbon source in complex petroleum systems and provide additional evidence for cross-checking results obtained by other methods (e.g. biomarker geochemistry).

Radiometric isotope geochronology provides quantitative constraints on the temporal evolution of petroleum systems. This project has examined the behavior and potential of Re-Os and Rb-Sr isotope systems for dating and characterizing petroleum system events.

Through case studies of ancient petroleum systems in the McArthur, Tarim and Sichuan Basins, outcomes of the project demonstrate that Re-Os isotope geochemistry, Rb-Sr illitic clay and pyrite subsample geochronology can be used for dating hydrocarbon generation, charge and alteration, respectively, and that Re-Os systematics are capable of differentiating and characterizing multiple hydrocarbon sources.

## **Acknowledgements**

This PhD project has been a lengthy and debilitating journey, and I have learnt so much from it not only about isotope geochronology and geochemistry but also about myself. I would like to express my sincere appreciation to people who have helped me during this process.

First of all, I would like to thank my principal supervisor, Associate Professor Xuan-Ce Wang, for his guidance and support in every aspect of this PhD project. I knew little about isotope geochronology and geochemistry at the beginning, and he was always willing to deliver expertise in both research and laboratory work with great patience. Besides pushing me out of my comfort zone, his great help in academic and mental aspects has pulled me through the gloom all the way. He gave me excellent opportunities to improve my technical skills at different geochemistry and geochronology laboratories. He encouraged me to present my research outcomes in academic conferences both in Australia and across the world. He gave me sufficient freedom and support for me to realize my own ideas. With his great effort, I think I have accomplished some good work and

enjoyed this journey.

I would also like to thank Professor Simon Wilde for agreeing to supervise me during my last months of study, when circumstances at Curtin changed. He was especially helpful with explaining some of the intricacies of the English language.

I would like to express my appreciation to Associate Professor Svetlana Tesselina for her help and guidance in laboratory work. She trained me how to use the thermal ionization mass spectrometer and working in an ultra clean environment. I could have not finished the data for the PhD project without her valuable training. Professor Keyu Liu provided great support in collecting samples from oil companies, and I am grateful that he invited me to the *Petroleum System Geochronology workshop* held at the China University of Petroleum. Professor Chris Elders is thanked for his scientific advice.

Academic, technical and administrative staff, PhD and visiting students in The Institute for Geoscience Research (TIGeR) and John de Laeter Centre (JdLC) also gave me a lot of help. Drs Zhen Li (now at JdLC) and Jian-Wei Zi (now at China University of Geosciences, Wuhan) are acknowledged for their scientific advice and help in sample preparation and petrographic study. I appreciate great administrative and technical support from Mr Hao Gao, Ms Annette Labrooy, Mr Glen Lawson, Mr Bradley McDonald, Mr Andrew Wiczorek and Mr Mark Winstanley, who have made my PhD study more efficient. Thanks also go to former and current PhD students

and visiting researchers with whom I spent a wonderful time at TIGeR: Dr Lingan Bai, Mr Daniel Brennan, Dr Mingjian Cao, Dr Peng Chen, Dr Xiang Cui, Mr Hamed Gamal EI Dien, Ms Nanan He, Dr Siyu Hu, Dr Chuan Huang, Dr Zongying Huang, Mr Qiang Jiang, Mr Jiangyu Li, Mr Yebo Liu, Ms Erin Martin, Ms Josephine Moore, Mr Adam Nordsvan, Dr Chunhua Shi, Dr Camilla Stark, Mr Zhikun Su, Ms Silvia Volante, Mr Chong Wang, Ms Danlei Wang, Mr Kai Wang, Mr Yanyang Wang, Mr Zhongwei Wang, Dr Bryant Ware, Ms Luya Wu, Mr Yafei Wu, Mr Yangming Wu, Dr Rong Xu, Dr Nan Zhang and Mr Tianyu Zhao.

Sincere gratitude is also extended to researchers at the Western Australia Organic & Isotope Geochemistry Centre (WA-OIGC), the Institute of Geology and Geophysics Chinese Academy of Sciences (IGGCAS), The University of Queensland, PetroChina and China University of Geosciences. Professor Kliti Grice at WA-OIGC is thanked for the opportunity to work at her laboratory. Dr Alex Holman and Mr Peter Hopper at WA-OIGC are thanked for their training and help in organic geochemical experiments (organic matter extraction, liquid chromatography and gas chromatography-mass spectrometry). Professors Chao-Feng Li and Zhu-yin Chu, who are experts in isotope geochemistry and geochronology, are thanked for their great support when I did Re-Os and Rb-Sr isotope analysis at IGGCAS and wrote scientific papers. Thanks also go to Professor Yueheng Yang (MC-ICP-MS laboratory), Ms Hongyan Li (TIMS laboratory) and higher degree research students, including Ms Chen

Chen, Ms Xue Mi, Ms Qian Ma, Mr Jiejun Jing, Mr Rui Li, Ms Zi Liang and Mr Junjie Xu, with whom I shared great moments when I did geochemistry experiments at IGGCAS. Professor Sue Golding and Dr Sandra Rodrigues at UQ are thanked for providing drillcore samples from the McArthur Basin, northern Australia, and their scientific advice and language improvement for my papers. Drs Lili Gui, Xingzhi Ma and Youyu Zhang at the Research Institute of Petroleum Exploration and Development, PetroChina, are thanked for providing drillcore samples from the Tarim and Sichuan Basins. Professor Sheng He at China University of Geosciences is thanked for his scientific advice and mental support during my PhD study.

In addition, I appreciate the continuous support from my parents who live in my hometown, *Yangquan*, a small city built on the North China Craton. Chatting with them every weekend has always relieved my homesickness. Previous and current room mates in Perth are thanked for the great time that we enjoyed together. This includes Ms Luwan Chen, Dr Huating Chen, Mr Ziwei Chen, Dr Huihui Dong, Ms Qiuyang Geng, Mr Xixian He, Mr Wei Hu, Ms Xinli Huang, Mr Minghong Li, Ms Yurong Liu, Ms Mingzhi Jiang, Dr Guoliang Wang, Dr Qinzeng Yan and Dr Jin Zhang.

Last but not the least, I would like to acknowledge a Curtin International Postgraduate Research Scholarship (CIPRS) for supporting me in finishing the PhD project.

## **List of Publications included as part of thesis**

This thesis is assembled from four research papers under review or to be submitted to international peer-reviewed journals at the time of writing this thesis. The details of four research papers are listed below.

### **Chapter 2**

Li S., Wang, X.-C., Chu, Z.-Y., Wilde, S. A., Rodrigues, S., Golding, D. S., Zhang, Y. A Proterozoic hydrocarbon generation event in northern Australia: constraints from rhenium-osmium isotope and trace metal geochemistry. *Submitted, Precambrian Research.*

### **Chapter 3**

Li S., Wang, X.-C., Li, C.-F., Wilde, S. A., Zhang, Y., Golding, D. S., Liu, K., Zhang, Y. Direct Rubidium-Strontium Dating of Hydrocarbon Charge Using Small Authigenic Illitic Clay Aliquots from the Silurian Bituminous Sandstone in the Tarim Basin, NW

China. *Under review, Scientific Report.*

#### **Chapter 4**

Li S., Wang, X.-C., Li, C.-F., Liu, K., Wilde, S. A., Hu, S.-Y. Direct Dating of Alteration of Paleo-Oil Pools Using Rubidium-Strontium Pyrite Geochronology. *To be submitted. Marine and Petroleum Geology.*

#### **Chapter 5**

Li S., Wang, X.-C., Chu, Z.-Y., Wilde, S. A., Holman, I. A., Grice, K., Liu, K. Organic and Re-Os isotope geochemistry of bituminous dolomite in Anyue gasfield, Sichuan Basin, southwest China. *To be submitted, Organic Geochemistry.*

## **Statement of Contributions of others**

The work presented in this thesis was primarily designed, conducted, interpreted and written by the first author (Shaojie Li). Contributions of other co-authors are stated below.

### **Chapter 2**

Xuan-Ce Wang assisted in interpreting the isotope data and evaluated the conclusions. Zhu-Yin Chu maintained TIMS and purified chemical substances used in the Re-Os chemistry, and evaluated the isotope data and conclusions. Simon Wilde evaluated the conclusions and improved the language quality. Sandra Rodrigues characterised the organic matter types and measured their reflectance values. Sue Golding provided samples and evaluated the conclusions. Yuxiang Zhang helped improve the quality of the figures, tables and language. All authors contributed to the proofreading.

### **Chapter 3**

Xuan-Ce Wang helped perform the chemical and isotopic analyses and evaluated the conclusions. Chao-Feng Li helped with Rb-Sr-Pb isotopic analysis and evaluate the data and conclusions. Simon Wilde evaluated the conclusions and improved the language quality. Youyu Zhang and Keyu Liu provided samples. Sue Golding evaluated the isotope data and conclusions and improved the language quality. Yuxiang Zhang helped improve the quality of the figures, tables and language. All authors contributed to the proofreading.

## **Chapter 4**

Xuan-Ce Wang and Chao-Feng Li helped with Rb-Sr-Pb isotopic analysis and evaluate the data and conclusions. Simon Wilde evaluated the conclusions and improved the language quality. Si-Yu Hu assisted with SEM work. Keyu Liu provided samples and geological information and prepared the pyrite crystals. All authors contributed to the proofreading.

## **Chapter 5**

Xuan-Ce Wang assisted with interpreting isotope data and evaluated the conclusions. Zhu-Yin Chu maintained TIMS and purified chemicals used in Re-Os chemistry, and evaluated the isotope data and conclusions. Simon Wilde evaluated the conclusions and improved the language quality. Alex Holman helped with organic matter extraction and GC-MS analysis. Kliti Grice evaluated the data and conclusions. Keyu Liu provided samples. All authors

contributed to the proofreading.

I, as a one of the co-authors, endorse that the statement of contributions of others by the candidate indicated above is appropriate.

Name	Signature
Xuan-Ce Wang	
Zhu-Yin Chu	
Simon A. Wilde	
Sandra Rodrigues	
Suzanne D. Golding	
Yuxiang Zhang	
Chao-Feng Li	
Youyu Zhang	
Keyu Liu	
Si-Yu Hu	
Alex I. Holman	
Kliti Grice	

# List of Figures

## Chapter 1

**Figure 1.1:** Schematic diagram showing geological elements and events in a petroleum system. Modified after Tissot and Welte (1984).....7

**Figure 1.2:** A: Simplified geological map of the Batten Fault Zone, showing the location of the McArthur River hydrothermal mineral deposit; B: Location of Batten Fault Zone in the McArthur Basin, northern Australia; C: Stratigraphy of the McArthur Group and adjacent units, showing the hydrocarbon source rock and reservoir for the Paleoproterozoic Barney Creek Formation petroleum system..23

**Figure 1.3:** A: Simplified geological map of the Tarim Basin; B: Location of the Tarim Basin in northwest China; C: Stratigraphy of Palaeozoic sediments, showing the hydrocarbon source rock and reservoir for the Cambrian-Ordovician petroleum system. ....25

**Figure 1.4:** A: Simplified geological map of the Sichuan Basin; B: Location of the Sichuan Basin in southwest China; C: Stratigraphy of Precambrian-Mesozoic sediments, showing the hydrocarbon source rock and reservoir for the Ediacaran-Cambrian petroleum system.....26

## Chapter 2

**Figure 2.1:** A: Simplified geological map of the Batten Fault Zone, McArthur Basin, showing the location of drillholes GRNT-79-5 and Lamont Pass 3; B: Location of the study area in the McArthur Basin; C: Stratigraphy of the McArthur Group and adjacent unites, showing available U-Pb detrital zircon ages. The age data are from Page et al. (2000); D: BCF core logs of drillholes GRNT-79-5 and Lamont Pass3. ....63

**Figure 2.2:** Representative photomicrographs of organic components in the Barney Creek Formation source rocks. Both lamalginite (GR1, A: white light; B: fluorescent light.) and solid bitumen were found. Solid bitumen is mainly

disseminated in the matrix (GR4, C: white light; D: fluorescent light; LP1, E: white light; F: fluorescent light.) or as nodules (GR4, G: white light; H: fluorescent light)..... 71

**Figure 2.3:** Scatter plots of the Re-Os data. A: Re vs Os contents. Re-Os contents of the upper crust are from Rudnick and Gao (2003); B:  $^{187}\text{Os}/^{188}\text{Os}$  vs  $^{187}\text{Re}/^{188}\text{Os}$  ratios; C:  $^{187}\text{Os}/^{188}\text{Os}$  vs  $1/^{192}\text{Os}$  ratios of the Group 1 samples; D:  $^{187}\text{Os}/^{188}\text{Os}$  vs  $1/^{192}\text{Os}$  ratios of the Group 2 samples. MSWD denotes mean square weighted deviates.  $\text{Os}_i$  denotes initial  $^{187}\text{Os}/^{188}\text{Os}$  ratio. .... 74

**Figure 2.4:** Relationships between Re-Os systematics and organic composition and  $T_{\text{max}}$  of Group 1 samples. A: Re content vs lamalginite content/TOC; B: Os content vs lamalginite content/TOC; C: Re content vs  $T_{\text{max}}$ ; D: Os content vs  $T_{\text{max}}$ ; E:  $^{187}\text{Re}/^{188}\text{Os}$  ratio vs lamalginite content/TOC; F:  $^{187}\text{Re}/^{188}\text{Os}$  ratio vs  $T_{\text{max}}$ . ... 82

**Figure 2.5:** A:  $^{187}\text{Os}/^{188}\text{Os}$  vs  $^{187}\text{Re}/^{188}\text{Os}$  ratios showing how the Group 2 samples vary through time; B: a model neglecting the radiogenic reduction in  $^{187}\text{Re}/^{188}\text{Os}$  ratio of the Group 2 samples because it is much smaller compared to the variation in  $^{187}\text{Os}/^{188}\text{Os}$  (Table 2.3). .... 86

### Chapter 3

**Figure 3.1:** A: Location of the Tarim Basin in China. B: Map showing the locations of sampling drillholes. Maps are modified after Li et al. (2015c) and Xu et al. (2014). .... 105

**Figure 3.2:** Phanerozoic lithostratigraphic column of the Tarim Basin. Modified after Jia and Wei (2002) and Kang and Kang (1996). .... 106

**Figure 3.3:** Strata histograms showing the sampling depth in each drillhole. A: YM35-1; B: H6; C: KQ1; D: Q1; and E: TZ67..... 110

**Figure 3.4:** Scatter plots of Rb vs Sr contents. A: YM35-1; B: H6; C: KQ1; D: Q1; and E: TZ67..... 116

**Figure 3.5:** Scatter plots of  $^{87}\text{Rb}/^{86}\text{Sr}$  vs  $^{87}\text{Sr}/^{86}\text{Sr}$  ratios. The black line in each diagram is the isochron regressed from data of all subsamples. The red dash line is the isochron regressed through selected data. A: YM35-1. The red dashed line is regressed without subsample A-3; B: H6. The red dashed line is regressed without subsample B-4; C: KQ1. The red dashed line is regressed without subsample C-5; D: Q1. The red dashed line is regressed without subsamples D-2 and D-3; E: TZ67. .... 117

**Figure 3.6:** Scatter plots of  $^{87}\text{Sr}/^{86}\text{Sr}$  vs  $1/\text{Sr}$  ratios. A: YM35-1; B: H6; C: KQ1; D: Q1. The black dashed line is the regression of subsamples D-1, D-4 and D-5; E: TZ67. .... 118

**Figure 3.7:** The average Rb-Sr contents and  $^{87}\text{Rb}/^{86}\text{Sr}$  ratios of each sample are compared with the XRD data. A:  $^{87}\text{Rb}/^{86}\text{Sr}$  vs interstratified ratio (IR) of I/S. IR is the percentage of smectite layers in I/S; B: potassium (K) content vs IR of I/S; C: Rb content vs K content; D: Rb content vs IR of I/S; E: Sr content vs IR of I/S. .... 121

**Figure 3.8:** Based on the Rb-Sr and K-Ar age data and basin modelling results, the timing of hydrocarbon charge in the SBS of is constrained: A: H6, Yanshanian period; B: KQ1, Late Caledonian to Hercynian period and C: TZ67, Indosinian period. D: Generalized map showing the timing of hydrocarbon charge. The burial history diagrams are modified after Zhu et al. (2012b) for H6 and Zhang et al. (2011) for KQ1 and TZ67. .... 124

**Figure 3.9:** Schematic diagram showing the temporal and spatial relation between the hydrocarbon charge and early Permian Tarim LIP in the Tarim Basin. .... 127

## Chapter 4

**Figure 4.1:** Major structural units within the Kuqa Depression of the Tarim Basin, NW China, showing the location of drillhole YD-2 within the Southern Slope Belt. The inset shows the locations of the Kuqa Depression and Tarim Basin in China (modified after Liu et al. (2016)). .... 145

**Figure 4.2:** A: Main features of drillhole YD-2. Limited amounts of heavy oil have been obtained from Ordovician strata (4945 m and 4983.5 m). B: A cross-section shows the structure and strata nearby drillhole YD2. The location of the cross-section is shown in Figure 4.1. C–Cambrian; O–Ordovician; S–Silurian; P–Permian; T–Triassic; J–Jurassic; K–Cretaceous. .... 147

**Figure 4.3:** Stereo binocular microscope photomicrographs (reflective light) showing that (A) pyrites are disseminated in the samples and coexist with calcite in specimen A, and (B) that bitumen coexists with pyrite and calcite in specimen B. .... 150

**Figure 4.4:** A: typical SEM image of thin section showing embayment structures between pyrite, calcite and quartz, suggesting coeval precipitation from hydrothermal fluid. B-I: high resolution SEM images showing pyrites are clean and lack mineral or fluid inclusions. The red rectangles show the sites of selected

images, identified by the appropriate letters..... 152

**Figure 4.5:** SEM-EDS elemental mapping of potassium (K) in pyrite shown in Figures 4.4B (A), 4.4C (B), 4.4D (C), 4.4E (D), 4.4F (E), 4.4G (F), 4.4H(G) and 4.4I (H). The results show that the K content of the pyrites is below the detection limit for of the instrument, supporting the absence of K-rich inclusion..... 152

**Figure 4.6:** A-B: Rubidium-Strontium isochrons of pyrite separates from carbonate rock specimens A and B, respectively. ( $Sr_i$  represents the initial  $^{87}Sr/^{86}Sr$  ratio. MSWD is the mean square of weighted deviates.) ..... 155

**Figure 4.7:** Comparison of Rb-Sr concentration data for pyrite in this study (specimens A and B) and pyrite samples obtained from high-temperature ore systems (log-log scale). Ore-related pyrite samples in the red rectangle have Rb and Sr concentration lower than pyrite in this study, and these samples occupy ~12.9% of the entire dataset. Rb-Sr data sources: Cao et al., 2015; Dong et al., 2016; Han et al., 2007; Hu et al., 2015; Li et al., 2008; Ni et al., 2012; Ravikant and Golani, 2011; Sun et al., 2014; Wang et al., 2015; Wang et al., 2014; Yang and Zhou, 2001; Yao et al., 2006; Zhang et al., 2003; Zhao et al., 2013; Zhou et al., 2013..... 156

**Figure 4.8:** A: Location of the Tarim Basin in China; B: Map showing sample sites for Pb and Sr isotope data from published studies. a-n–Sample sites of felsic material (e.g. granite); 1-12–Sample sites of mafic (e.g. basalt) and ultramafic material (e.g. ultramafic intrusion); A-C–Sample sites of metamorphic material (e.g. schist). ..... 159

**Figure 4.9:** A:  $Sr_i-^{206}Pb/^{204}Pb$ , B:  $Sr_i-^{207}Pb/^{204}Pb$ , C:  $Sr_i-^{208}Pb/^{204}Pb$  and D: S isotope ratios of the pyrites in this study compared with spatially and temporally associated materials from the literature. Whole-rock Pb isotope ratios were corrected to their initial ratios. C–Cambrian; O–Ordovician; TSR–thermochemical sulfate reduction; BSR–bacterial sulfate reduction;  $Sr_i$ –initial  $^{87}Sr/^{86}Sr$  value; VCDT–Vienna Canyon Diablo Troilite. Lead and strontium isotope data sources: (1) felsic rocks: Chiaradia et al. (2006) and Yu et al., (2011); (2) mafic and ultramafic rocks: Zhou et al. (2009), Zhang et al. (2010), Zhang et al. (2012), Zou et al. (2015), Sun et al. (2013); (3) metamorphic rocks: Chiaradia et al. (2006) and Liao et al. (2014). Sulfur isotope data sources: (1) Ordovician BSR-derived pyrites: Cai et al. (2002), Jia et al. (2015), Lü et al. (2007) and Zhu and Meng (2010); (2) Ordovician TSR-derived pyrites: Cai et al. (2001), Cai et al. (2009a), Jia et al. (2015), and Zhu and Meng (2010); (3) Middle-Upper Ordovician sulfates: Lü et al. (2007); (4) Ordovician TSR-derived  $H_2S$ : Zhu et al. (2014); (5) Lower Ordovician sulfates: Cai et al. (2002); (6) Lower Ordovician

kerogen: Cai et al. (2009b); (7) Middle-Upper Ordovician kerogen: Cai et al. (2009b); (8) Middle-Upper Ordovician non-degraded oil: Cai et al. (2009b); (9) Cambrian BSR-derived pyrites: Jia et al. (2015) and Li et al. (2012); (10) Cambrian sulfates: Cai et al. (2001), Cai et al. (2002), Jia et al. (2015) and Li et al. (2012); (11) Cambrian formation water: Jia et al. (2015); (12) Cambrian TSR-derived H<sub>2</sub>S: Jia et al. (2015); (13) Cambrian kerogen: Cai et al. (2009b)..... 160

**Figure 4.10:** Lead isotope ratios of pyrite sub-samples compared with spatially and temporally associated materials. A: <sup>207</sup>Pb/<sup>204</sup>Pb-<sup>206</sup>Pb/<sup>204</sup>Pb; B: <sup>208</sup>Pb/<sup>204</sup>Pb-<sup>206</sup>Pb/<sup>204</sup>Pb. Lead isotope ratios in (A) and (B) are corrected to their initial ratios. The fields of metamorphic, felsic and mafic-ultramafic rocks are drawn according to lead isotope data of material from the literature. Lead isotope data sources: (1) felsic rocks: Chiaradia et al. (2006) and Yu et al., (2011); (2) mafic and ultramafic rocks: Zhou et al. (2009), Zhang et al. (2010), Zhang et al. (2012), Zou et al. (2015), Sun et al. (2013); (3) metamorphic rocks: Chiaradia et al. (2006) and Liao et al. (2014)..... 161

## Chapter 5

**Figure 5.1:** A: Simplified geological map of the Sichuan Basin, showing the location of the Anyue gasfield and studied petroleum drillholes. B: Location of Sichuan Basin in southwest China. .... 183

**Figure 5.2:** Burial history, petroleum system elements (source rock, reservoir and cap rocks) and petroleum accumulation events diagrams for the Neoproterozoic-Cambrian Anyue gas system in central Sichuan Basin. Modified after Zou et al.(2015). .... 185

**Figure 5.3:** Representative total ion chromatograms (TICs) of saturated fractions of the studied samples. .... 192

**Figure 5.4:** The ratio of C<sub>28</sub> norhopane/C<sub>29</sub> hopane (NH<sub>28</sub>/H<sub>29</sub>) is correlated positively with organic indicators including pregnane/regular sterane (A), tricyclic terpane (TT)/hopane (H) (B), Pr/nC<sub>17</sub> (C) and Ph/nC<sub>18</sub> (D)..... 202

**Figure 5.5:** Scatter plots for characterizing the source of organic matter and depositional environment of the hydrocarbon source rocks. A: Pr/Ph vs Ph/nC<sub>18</sub>-Pr/nC<sub>17</sub>; B: Pr/nC<sub>17</sub> vs Ph/nC<sub>18</sub>; and C: ternary plot of C<sub>27</sub>-C<sub>28</sub>-C<sub>29</sub> regular steranes. .... 204

<b>Figure 5.6:</b> Scatter plots for characterizing lithological types and depositional environment of hydrocarbon source rock. A: C <sub>24</sub> /C <sub>23</sub> tricyclic terpane (TT) vs C <sub>22</sub> /C <sub>21</sub> TT; B: C <sub>31</sub> R/C <sub>30</sub> hopane (H) vs C <sub>26</sub> /C <sub>25</sub> TT; C: Pr/Ph vs gammacerane index. ....	206
<b>Figure 5.7:</b> Re-Os data of the studied samples. A: Re vs Os contents. Data of the Upper Crust average are from Rudnick and Gao (2003); B: <sup>187</sup> Os/ <sup>188</sup> Os vs <sup>187</sup> Re/ <sup>188</sup> Os ratios; and C: <sup>187</sup> Os/ <sup>188</sup> Os vs 1/ <sup>192</sup> Os ratios. ....	210
<b>Figure 5.8:</b> Correlations between Re-Os data and organic indicators. A: Re content vs C <sub>28</sub> norhopane/C <sub>29</sub> hopane (NH <sub>28</sub> /H <sub>29</sub> ); B: Os content vs NH <sub>28</sub> /H <sub>29</sub> ; C: Re content vs C <sub>31</sub> R/C <sub>30</sub> hopane; D: Os content vs C <sub>31</sub> R/C <sub>30</sub> hopane; and E: <sup>187</sup> Re/ <sup>188</sup> Os vs C <sub>31</sub> R/C <sub>30</sub> hopane.....	211
<b>Figure 5.9:</b> A: <sup>187</sup> Os/ <sup>188</sup> Os vs <sup>187</sup> Re/ <sup>188</sup> Os ratios of group 1 samples; B: <sup>187</sup> Os/ <sup>188</sup> Os vs 1/ <sup>192</sup> Os ratios of group 1 samples; C: <sup>187</sup> Os/ <sup>188</sup> Os vs <sup>187</sup> Re/ <sup>188</sup> Os ratios of group 2 samples; and D: <sup>187</sup> Os/ <sup>188</sup> Os vs 1/ <sup>192</sup> Os ratios of group 2 samples. ....	213
<b>Figure 5.10:</b> The <sup>187</sup> Os/ <sup>188</sup> Os vs <sup>187</sup> Re/ <sup>188</sup> Os plot shows that three Os isotopic components are identified in the bituminous dolomite reservoir of the Anyue gasfield. Components I, II and III represents the earlier-charged/carbonate-dominated, earlier-charged/shale-dominated and later-charged/shale-dominated hydrocarbons. ....	215
<b>Figure A5.1:</b> Total ion chromatograms (TICs) of saturated fractions of the studied samples.....	228
<b>Figure A5.2:</b> M/Z 85 mass chromatograms showing distribution patterns of <i>n</i> -alkanes of the studied samples. ....	229
<b>Figure A5.3:</b> M/Z 191 mass chromatograms showing distribution patterns of terpanes of the studied samples. Hydrocarbon compounds are identified as labelled: 1: C <sub>19</sub> tricyclic terpane (TT); 2: C <sub>20</sub> TT; 3: C <sub>21</sub> TT; 4: C <sub>22</sub> TT; 5: C <sub>23</sub> TT; 6: C <sub>24</sub> TT; 7: C <sub>25</sub> TT; 8: C <sub>24</sub> tetracyclic terpane; 9: C <sub>26</sub> TT; 10: C <sub>28</sub> TT; 11: C <sub>29</sub> TT; 12: C <sub>27</sub> 18α hopane (Ts); 13: C <sub>27</sub> 17α hopane (Tm); 14: C <sub>29</sub> hopane; 15: C <sub>29</sub> Ts; 16: C <sub>30</sub> hopane; 17: C <sub>29</sub> moretane; 18: C <sub>31</sub> hopanes; 19: Gammacerane; 20: C <sub>32</sub> hopanes; 21: C <sub>33</sub> hopanes; 22: C <sub>34</sub> hopanes; 23: C <sub>35</sub> hopanes.....	230
<b>Figure A5.4:</b> M/Z 177 mass chromatograms showing distribution patterns of demethylated hopanes of the studied samples. ....	231
<b>Figure A5.5:</b> M/Z 217 mass chromatograms showing distribution patters of steranes of the studied samples. Hydrocarbon compounds are identified as labelled:	

1: C<sub>21</sub> pregnane; 2: C<sub>22</sub> pregnane; 3: C<sub>27</sub> βα 20S diasterane; 4: C<sub>27</sub> βα 20R diasterane; 5: C<sub>27</sub> αβ 20S diasterane; 6: C<sub>27</sub> αβ 20R diasterane; 7: C<sub>27</sub> ααα 20S regular sterane; 8: C<sub>27</sub> αββ 20R regular sterane; 9: C<sub>27</sub> regular αββ 20S sterane; 10: C<sub>27</sub> regular ααα 20R sterane; 11: C<sub>28</sub> ααα 20S regular sterane; 12: C<sub>28</sub> αββ 20R regular sterane; 13 C<sub>28</sub> αββ 20S regular sterane; 14: C<sub>28</sub> ααα 20R regular sterane; 15: C<sub>29</sub> ααα 20S regular sterane; 16: C<sub>29</sub> αββ 20R regular sterane; 17: C<sub>29</sub> αββ 20S regular sterane; 18: C<sub>29</sub> ααα 20R regular sterane. ....232

**Figure A5.6:** Mass chromatograms showing distribution patterns of aromatic hydrocarbons. Hydrocarbon compounds are identified as labelled. 1: Phenanthrene; 2: 3-methylphenanthrene (MP); 3: 2-MP; 4: 9-MP; 5: 1-MP; 6: 3,5-dimethylphenanthrene (DMP) + 2,6-DMP; 7:2,7-DMP; 8: 1,3-DMP + 2,10-DMP + 3,9-DMP + 3,10-DMP; 9: 1,6-DMP + 2,9-DMP + 2,5-DMP; 10: 1,7-DMP; 11: Dibenzothiophene (DBT); 12: 4- methyl dibenzothiophene (MDBT); 13: 2-MDBT + 3-MDBT; 14: 1-MDBT; 15: 1,3,6- trimethylphenanthrene (TMP) + 1,3,10-TMP + 2,6,10-TMP + 2-ethyl, 5-MP; 16: 1,3,7-TMP + 2,6,9-TMP + 2,7,9-TMP + 7-ethyl, 1-MP; 17: 1,3,9-TMP + 2,3,6-TMP; 18: 1,6,9-TMP + 1,7,9-TMP + 2,3,7-TMP; 19: 1,3,8-TMP; 20: 2,3,10-TMP; 21: 1,6,7-TMP; 22: 1,2,6-TMP. ....234

**Figure A5.7:** The ratio of C<sub>28</sub> norhopane/C<sub>29</sub> hopane (NH<sub>28</sub>/H<sub>29</sub>) is plotted against different organic indicators, including C<sub>27</sub>/C<sub>29</sub> ααα 20R regular sterane (A), C<sub>29</sub>Ts/(C<sub>29</sub>Ts+C<sub>29</sub> hopane) (B), Pr/Ph (C), Ts/Ts+Tm (D), C<sub>29</sub> ααα20S/20S+20R sterane (E), C<sub>29</sub> αββ/(αββ + ααα) (F), C<sub>31</sub>R/C<sub>30</sub> hopane (G), C<sub>22</sub>/C<sub>21</sub>TT (H), gammacerane index (I), C<sub>26</sub>/C<sub>25</sub>TT(J) and C<sub>24</sub>/C<sub>23</sub>TT (K).....235

# List of Tables

## Chapter 2

<b>Table 2.1:</b> TOC, $T_{max}$ , organic material composition and Re-Os isotope data of Barney Creek source rock samples intersected by drillholes GRNT-79-5 and Lamont Pass 3 in the McArthur Basin, northern Australia.....	72
<b>Table 2.2:</b> Regression statistics of $^{187}\text{Re}/^{188}\text{Os}$ - $^{187}\text{Os}/^{188}\text{Os}$ isotope data of samples .....	78
<b>Table 2.3:</b> Termination and amount of $^{187}\text{Os}$ loss in the BCF Group 2 samples .	86

## Chapter 3

<b>Table 3.1:</b> Basic information concerning illitic samples in this study of the Tarim Basin .....	110
<b>Table 3.2:</b> Rubidium-Strontium isotope data for illitic clays in this study of the Tarim Basin .....	115

## Chapter 4

<b>Table 4.1:</b> Rubidium-strontium-lead-sulfur isotope data for pyrite sub-samples from specimens A and B in this study .....	154
---	-----

## Chapter 5

<b>Table 5.1:</b> Basic information for bituminous dolomite samples from the Anyue gasfield used in this study .....	193
<b>Table 5.2:</b> Molecular ratios of n-alkanes and isoprenoid paraffin extracted from bituminous dolomite samples from the Anyue gasfield .....	194
<b>Table 5.3:</b> Molecular ratios of terpane extracted from bituminous dolomite	

samples from the Anyue gasfield .....	196
<b>Table 5.4:</b> Molecular ratios of sterane and aromatic hydrocarbons extracted from bituminous dolomite samples from the Anyue gasfield .....	197
<b>Table 5.5:</b> Re-Os elemental and isotopic data for bituminous dolomite samples from the Anyue gasfield .....	199

## Table of Contents

<b>DECLARATION</b> .....	I
<b>ABSTRACT</b> .....	III
<b>ACKNOWLEDGEMENTS</b> .....	XI
<b>LIST OF PUBLICATIONS INCLUDED AS PART OF THESIS</b> .....	XV
<b>STATEMENT OF CONTRIBUTIONS OF OTHERS</b> .....	XVII
<b>LIST OF FIGURES</b> .....	XX
<b>LIST OF TABLES</b> .....	XXVII
<b>CHAPTER 1</b> .....	5
<b>INTRODUCTION</b> .....	5
1.1 PETROLEUM SYSTEM .....	5
1.2 PETROLEUM SYSTEM GEOCHRONOLOGY .....	7
1.2.1 Rhenium-osmium isotopic system.....	9
1.2.2 Rubidium-Strontium Isotopic System.....	14
1.3 PETROLEUM GEOCHEMISTRY .....	15
1.3.1 Inorganic Geochemical Parameters.....	16
1.3.2 Organic Geochemical Parameters .....	18
1.4 ANCIENT PETROLEUM SYSTEMS IN THE McARTHUR, TARIM AND SICHUAN BASINS.....	20
1.4.1 McArthur Basin .....	21
1.4.2 Tarim Basin .....	23
1.4.3 Sichuan Basin .....	25
1.5 AIMS OF THIS THESIS .....	27
<b>REFERENCES</b> .....	32
<b>CHAPTER 2</b> .....	58
<b>A PROTEROZOIC HYDROCARBON GENERATION EVENT IN NORTHERN AUSTRALIA: CONSTRAINTS FROM RHENIUM-OSMIUM ISOTOPE GEOCHEMISTRY</b> .....	58
<b>ABSTRACT</b> .....	59
<b>2.1 INTRODUCTION</b> .....	61

2.2 GEOLOGICAL BACKGROUND .....	63
2.3 SAMPLES AND METHODS .....	66
2.3.1 Petrographic and Organic geochemical analysis .....	66
2.3.2 Inorganic geochemical analysis .....	68
2.4 RESULTS .....	69
2.4.1 Composition and maturity level of organic matter .....	69
2.4.2 Re-Os elemental and isotopic systematics .....	73
2.5 DISCUSSION .....	75
2.5.1 Classification of the studied samples .....	75
2.5.2 A post-depositional reset event for the Re-Os isotope system .....	76
2.5.3 Re-Os redistribution induced by hydrothermal-facilitated organic matter conversion .....	79
2.5.4 Open-system Os isotopic behaviour in Group 2 samples .....	83
2.5.5 Implications for prospecting of hydrocarbon generation .....	87
2.6 CONCLUSIONS .....	87
ACKNOWLEDGMENTS .....	89
REFERENCES .....	89
<b>CHAPTER 3 .....</b>	<b>99</b>
<b>DIRECT RUBIDIUM-STRONTIUM DATING OF HYDROCARBON CHARGE USING SMALL AUTHIGENIC ILLITIC CLAY ALIQUOTS FROM THE SILURIAN BITUMINOUS SANDSTONE IN THE TARIM BASIN, NW CHINA .....</b>	<b>99</b>
ABSTRACT .....	100
3.1 INTRODUCTION .....	102
3.2 GEOLOGICAL BACKGROUND .....	104
3.3 SAMPLE INFORMATION AND ANALYTICAL METHOD .....	107
3.4 RESULTS .....	112
3.5 DISCUSSION .....	118
3.5.1 Rb-Sr systematics of SBS illitic clays .....	118
3.5.2 Geological significance of the Rb-Sr isochron ages .....	122
3.5.3 Implications for Rb-Sr clay hydrocarbon charge geochronology .....	124
3.6 CONCLUSIONS .....	127
ACKNOWLEDGMENTS .....	129
REFERENCES .....	130
<b>CHAPTER 4 .....</b>	<b>140</b>
<b>DIRECT DATING OF ALTERATION OF PALEO-OIL POOLS USING</b>	

<b>RUBIDIUM-STRONTIUM PYRITE GEOCHRONOLOGY .....</b>	<b>140</b>
<b>ABSTRACT .....</b>	<b>141</b>
<b>4.1 INTRODUCTION.....</b>	<b>143</b>
<b>4.2 GEOLOGICAL BACKGROUND .....</b>	<b>144</b>
<b>4.3 SAMPLES AND ANALYTICAL METHOD .....</b>	<b>147</b>
<b>4.4 RESULTS.....</b>	<b>150</b>
<b>4.4.1 Petrographic observations.....</b>	<b>150</b>
<b>4.4.2 Rb-Sr-Pb-S isotope data and isochron ages .....</b>	<b>153</b>
<b>4.5 DISCUSSION.....</b>	<b>155</b>
<b>4.5.1 Pyrite Rb-Sr geochronology: a robust dating technique for petroleum systems.....</b>	<b>155</b>
<b>4.5.2 Source of metals in hydrothermal fluid.....</b>	<b>157</b>
<b>4.5.3 Source of sulfur .....</b>	<b>161</b>
<b>4.5.4 Timing of alteration of the paleo-oil pool.....</b>	<b>163</b>
<b>4.6 CONCLUSIONS.....</b>	<b>165</b>
<b>ACKNOWLEDGMENTS .....</b>	<b>166</b>
<b>REFERENCES .....</b>	<b>167</b>
<b>CHAPTER 5 .....</b>	<b>178</b>
<b>ORGANIC AND RE-OS ISOTOPE GEOCHEMISTRY OF BITUMINOUS DOLOMITE IN ANYUE GASFIELD, SICHUAN BASIN, SOUTHWEST CHINA .....</b>	<b>178</b>
<b>ABSTRACT .....</b>	<b>179</b>
<b>5.1 INTRODUCTION.....</b>	<b>182</b>
<b>5.2 GEOLOGICAL BACKGROUND .....</b>	<b>184</b>
<b>5.3 SAMPLES AND METHODS.....</b>	<b>187</b>
<b>5.3.1 Microwave-assisted extraction and silica gel chromatography of organic matter .....</b>	<b>187</b>
<b>5.3.2 Gas chromatography-mass spectrometry .....</b>	<b>188</b>
<b>5.3.3 Re-Os chemistry, negative thermal ionization mass spectrometry (N-TIMS) and multicollector-inductively coupled plasma mass spectrometry (MC-ICP-MS) .....</b>	<b>189</b>
<b>5.4 RESULTS.....</b>	<b>191</b>
<b>5.4.1 Molecular composition of extractable organic matter .....</b>	<b>191</b>
<b>5.4.2 Re-Os systematics.....</b>	<b>198</b>
<b>5.5 DISCUSSION.....</b>	<b>200</b>
<b>5.5.1 Binary mixing of biodegraded and fresh hydrocarbon components .....</b>	<b>200</b>

<b>5.5.2 Source of organic matter</b> .....	202
<b>5.5.3 Lithology and formation environment of source rocks</b> .....	204
<b>5.5.4 Thermal maturity assessment</b> .....	206
<b>5.5.5 Re-Os geochemistry of bituminous dolomite</b> .....	208
<b>5.6 CONCLUSIONS</b> .....	216
<b>ACKNOWLEDGMENTS</b> .....	218
<b>REFERENCES</b> .....	219
<b>APPENDIX 5</b> .....	228
<b>CHAPTER 6</b> .....	237
<b>CONCLUSIONS</b> .....	237
<b>DATING HYDROTHERMALLY FACILITATED HYDROCARBON GENERATION BY     RE-OS ISOTOPE GEOCHEMISTRY</b> .....	238
<b>DATING HYDROCARBON CHARGE BY RB-SR ILLITIC CLAY SUBSAMPLE     GEOCHRONOLOGY</b> .....	240
<b>DATING HYDROCARBON ALTERATION BY RB-SR PYRITE SUBSAMPLE     GEOCHRONOLOGY</b> .....	240
<b>CHARACTERIZING HYDROCARBON SOURCE BY ORGANIC AND RE-OS     ISOTOPIC GEOCHEMISTRY</b> .....	241
<b>LIMITATIONS AND FUTURE WORK</b> .....	244
<b>BIBLIOGRAPHY</b> .....	248

# **Chapter 1**

## **Introduction**

### **1.1 Petroleum System**

Petroleum system investigation is a prospecting tool which aims to detect the presence of oil and gas in a sedimentary basin (Magoon and Dow, 1994). The term “petroleum system” was introduced by Dow (1974) and it originated from “oil system”, which was defined as containing source rock and oils derived from this source rock. This concept initially was used to predict the distribution of oils of the same origin (Dow, 1974). Afterwards, Perrodon and Masse (1984) defined “petroleum system” as an organized set of geological processes affecting the reserve potential in a petroleum province. There were also several terms related to hydrocarbon investigation at the level comparable to petroleum system, such as “generative basin” (Demaison, 1984), “hydrocarbon machine” (Meissner et al., 1984) and “independent petroliferous system” (Ulmishek, 1986). In 1994, Magoon and Dow defined the current most widely-used concept “petroleum system” as a unifying concept comprising three aspects: (1) geological elements (source rock, reservoir, seal and overburden rock), (2) oil and gas generated by source rock and (3)

geological events (hydrocarbon generation/expulsion, migration, charge and oil cracking).

Figure 1.1 is a schematic diagram showing the destiny of hydrocarbon in the geological context. Source rock of a petroleum system is defined as a rock capable of generating or has generated movable quantities of hydrocarbons (Tissot and Welte, 1984). Kerogen, which is neither soluble in aqueous alkaline nor organic solvents, is the major organic constituent in source rock (Tissot and Welte, 1984; Vandenbroucke and Largeau, 2007). In addition to a small proportion directly inherited from living organisms, the majority of hydrocarbons is derived from the thermal degradation of kerogen (Tissot and Welte, 1984). These authors defined three consecutive stages of hydrocarbon generation: (1) diagenesis: Organic matter is immature and hydrocarbons are scarce; (2) catagenesis: Oil is the principal product and gas is also generated by thermal cracking of kerogen; and (3) metagenesis: Gas is the principal product and is generated through thermal cracking of either kerogen or pre-existing oil. Hydrocarbons could be either retained in a source rock (Jarvie et al., 2007), or migrate away from a source rock (i.e. “expulsion” or “primary migration”) during the main stages of hydrocarbon generation (Tissot and Welte, 1984). After travelling along migration conduits, such as porous rock beds, unconformities or faults (i.e. “secondary migration”), hydrocarbons could be entrapped in porous reservoir rocks on condition that the migration front was blocked by impermeable rocks (i.e. “caprock”;

Schowalter, 1979; Tissot and Welte, 1984). The reservoired hydrocarbons are thermodynamically metastable and susceptible to alteration, e.g. thermal degradation and biodegradation, resulting in compositional fractionation and formation of solid bitumen and natural gas (Tissot and Welte, 1984).

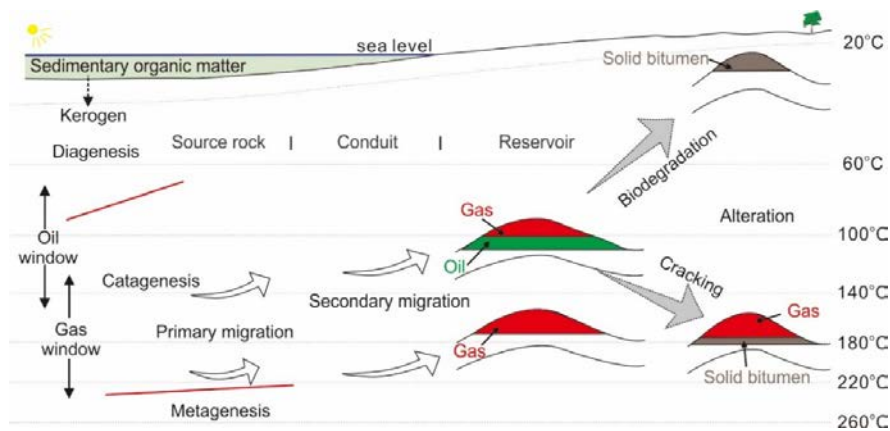


**Figure 1.1:** Schematic diagram showing geological elements and events in a petroleum system. Modified after Tissot and Welte (1984).

## 1.2 Petroleum system geochronology

A petroleum system encompasses a set of geological events such as hydrocarbon generation, migration/charge and alteration, and knowing the timing of these processes is significant for understanding the evolution of a petroleum system (Magoon and Dow, 1994). Besides determining the “critical moment” by basin modelling investigation (a time point designated by investigators as when most hydrocarbons generated/migrated/accumulated; Magoon and Dow, 1994), or constraining the timing of hydrocarbon charge

by fluid inclusion studies (Mclimans, 1987), applying radiometric isotope pairs to directly dating petroleum systems has gained increasing attention. Radiometric dating is a technique based on the decay of an unstable radionuclide to a stable nonradioactive isotope of another chemical element (i.e. radiogenic daughter product). The decay is a function of time and can be expressed as:

$$N(t) = N_0 e^{-\lambda t} \quad (1)$$

Where  $N(t)$  and  $N_0$  represent the radionuclide quantity at time  $t$  and initial state ( $t=0$ ), respectively, and  $\lambda$  is the exponential decay constant of the radionuclide.

Isochron dating techniques are commonly-used geochronology methods based on the decay equation to determine the closure time of isotopic systems (e.g. Re-Os and Rb-Sr) in a suite of cogenetic geological samples (Faure and Mensing, 2005):

$$D_m = D_i + (P/D)_m (e^{\lambda t} - 1) \quad (2)$$

Where  $D_m$  and  $D_i$  denote measured and initial isotopic ratios of radiogenic daughters (e.g.  $^{187}\text{Os}/^{188}\text{Os}$ ), respectively,  $(P/D)_m$  denotes the radiometric parent/daughter ratio (e.g.  $^{187}\text{Re}/^{188}\text{Os}$ ),  $\lambda$  is the decay constant of the radionuclide and  $t$  denotes the timing of isotopic closure. To yield an isochron, three criteria should be met: (1) a sufficient spread in parent-to-daughter ratios; (2) homogeneous initial radiogenic daughter isotopic ratios and (3) closed-system behavior.

Radioactive/radiogenic metallic element pairs can be accommodated by naturally occurring organic materials and authigenic minerals that are precipitated during petroleum system events. Therefore, timing of petroleum system events may be determined by isochron dating of isotopic closure in these geological entities using appropriate sampling protocols.

### **1.2.1 Rhenium-osmium isotopic system**

Rhenium and osmium are chalcophilic, siderophilic and organophilic metals, with average concentrations of ~0.198 and ~0.031 part per billion (ppb) in the upper continental crust, respectively (Rudnick and Gao, 2003). In 1948, Naldrett and Libby reported their discovery of  $^{187}\text{Re}$ -to- $^{187}\text{Os}$  by  $\beta^-$  decay, establishing the theoretic basis for Re-Os geochronology (Naldrett and Libby, 1948). The wide application of this dating method was facilitated by precise determination of the  $^{187}\text{Re}$  decay constant (Smoliar et al., 1996; Selby et al., 2007b). Technical development has also improved the precision of the method, such as isotope dilution negative thermal ionization mass spectrometry (Creaser et al., 1991) and carius tube digestion (Shirey and Walker, 1995).

The decay constant remains unchanged for dating targets formed in different environments and geological stages because radioactive decay is unaffected either by intrinsic properties (e.g. electron density around the radioactive nuclei) or external conditions (e.g. temperature or pressure; Faure and Mensing, 2005). The decay

constant can be measured via direct counting experiments or indirect geochronology methods.

Direct counting experiment: The  $^{187}\text{Re}$  decay constant was first estimated by counting beta-particles of rhenium metal and heptasulfide, which yielded a value of  $\sim 2.31 \times 10^{-13} \text{ yr}^{-1}$  (Naldrett and Libby, 1948). The experiment was improved by applying microbolomete (Alessandrello et al., 1999; Galeazzi et al., 2000; Arnaboldi et al., 2003), yet the results were not consistent and ranged between  $\sim 1.39 \times 10^{-13} \text{ yr}^{-1}$  and  $\sim 2.31 \times 10^{-11} \text{ yr}^{-1}$  (Ashktorab et al., 1993). Measuring  $^{187}\text{Os}$  radiogenic growth in solutions with known Re content is also be able to estimate decay constant, whereas it yielded  $^{187}\text{Re}$  decay constants with large uncertainties ( $1.59 \pm 0.05 \times 10^{-11} \text{ yr}^{-1}$  and  $1.64 \pm 0.05 \times 10^{-11} \text{ yr}^{-1}$  (Lindner et al., 1986, 1989). Indirect geochronological method: Rhenium-enriched minerals or rocks, e.g. molybdenite and meteorites, were chosen as samples, and the decay constant was calculated based on age data yielded by other radiometric isotopic systems with known decay constants, such as uranium-lead (U-Pb),  $^{40}\text{Ar}$ - $^{39}\text{Ar}$  ( $^{40}\text{Ar}$ - $^{39}\text{Ar}$ ), rubidium-strontium (Rb-Sr) and samarium-neodymium (Sm-Nd) (Luck et al., 1980, Smoliar et al., 1996, Shirey and Walker, 1998, Luck and Allègre, 1983, Shen et al., 1996, Selby et al., 2007b). Smoliar et al (1996) reported a  $\lambda^{187}\text{Re}$  value of  $1.666 \times 10^{-11} \text{ yr}^{-1}$  as calculated based on group III iron meteorites crystallization ages which were constrained by the  $^{53}\text{Mn}$ - $^{53}\text{Cr}$  isotope system (Smoliar et al., 1996). This value was reproduced by Selby et al (2007b), obtaining a

similar value of  $1.6668 \pm 0.0034 \times 10^{-11} \text{ yr}^{-1}$  by Re-Os dating of hydrothermal molybdenite and U-Pb dating of zircon in the associated magmatic rock. Therefore,  $1.666 \times 10^{-11} \text{ yr}^{-1}$  was adopted in most Re-Os geochronology studies (Georgiev et al., 2016; Cumming et al., 2014; Lillis and Selby, 2013; Mao et al., 2008; Lawley et al., 2013).

Isotope dilution analysis is a method used to determine concentration of an element in a sample solution by adding known amounts of an isotopic tracer (also known as the “spike”). To yield accurate and precise isotopic data, sample-spike equilibrium is required during sample digestion (Reisberg and Meisel, 2002). Several sample digestion techniques have been developed for Re-Os geochronology, such as the nickel sulphide fire assay technique (Hoffman et al., 1978), alkaline fusion (Morgan and Walker, 1989), leaching technique (Pegram et al., 1992), carius tube digestion (Shirey and Walker, 1995) and high pressure asher (HPA) digestion (Meisel et al., 2001). Carius tube digestion is the conventional method used today, which allows nearly complete dissolution of samples with a low blank contribution (Shirey and Walker, 1995; Reisberg and Meisel, 2002). HPA is an emerging digestion technique for organic-rich sedimentary rocks and crude oils (Sen and Peucker-Ehrenbrink, 2014; Mahdaoui et al., 2015; Georgiev et al., 2016). Although HPA apparatus is expensive, it prevents explosion during digesting organic-rich samples, which may occur using carius tubes (Reisberg and Meisel, 2002). In terms of digestion solvents, inverse aqua regia

and chromium oxide sulfuric acid are two commonly-used mediums for organic-rich samples. Selby and Creaser (2003) proposed that chromium oxide sulfuric acid is a better choice for Re-Os source rock geochronology because this solvent may preferentially liberate hydrogenous Re-Os from source rock samples and improve the precision of isochron ages.

Negative thermal ionization mass spectrometry (N-TIMS) is the most commonly used technique for determining Re-Os isotopic ratios. Thermal ionization is achieved by providing a current through a high-melting-point/high-work-function metal filament on which the sample is deposited. Re-Os isotope ratios are measured by TIMS in negative ion mode because Re and Os have high first ionization energy ( $\sim 7.8$  eV and  $\sim 8.7$  eV, respectively) whilst negatively charged oxides  $\text{ReO}_4^-$  and  $\text{OsO}_3^-$  are easier to produce than Re-Os cations (Campbell-Miller and Simard, 1996; Creaser et al., 1991; Reisberg and Meisel, 2002). Multi-collector inductively coupled plasma-mass spectrometry (MC-ICP-MS) is an alternative analytical method for Re-Os measurement (Nozaki et al., 2012; Suzuki et al., 2004; Rosman and Taylor, 1998; Li et al., 2010, Makishima and Nakamura, 2006; Schoenberg et al., 2000; Norman et al., 2002; Sen and Peucker-Ehrenbrink, 2014). Similar to TIMS, MC-ICP-MS also has the ability to produce high-precision isotopic data, and one of its advantages over TIMS is the time-saving measurement procedure (Reisberg and Meisel, 2002). However, Os has significant memory effect for MC-ICP-MS during sample introduction, which may

further result in biased isotope data, thus TIMS is still the optimal choice for Os measurement (Hirata, 2000, Reisberg and Meisel, 2002; Li et al., 2010; Makishima and Nakamura, 2006).

Organic-rich rock (e.g. source rock), crude oil, and solid bitumen are datable targets for Re-Os geochronology. A Re-Os isochron age for a source rock provides an estimate of the depositional age based on the hypothesis that the Re-Os budget in the source rock is mainly sequestered from the water column during deposition. To guarantee a homogeneous initial Os isotopic composition, samples for Re-Os source rock geochronology are usually collected from a narrow stratigraphic section (<10 meters) (Kendall et al., 2009). Re-Os hydrocarbon geochronology can be traced back to 2005 when Selby and Creaser (2005a) reported a Re-Os age of  $111.6 \pm 5.3$  Ma for heavy oils from an oil sand deposit in Canada. Experimental investigations determined that Re and Os may be bonded by heteroatomic ligands (e.g. O-, S- and N-), present as metal-organic complex (e.g. Re porphyrin) or reside in aromatic fractions in crude oil and inherited from the source rock during hydrocarbon generation (Selby et al., 2007a, Cumming et al., 2014, Rooney et al., 2012). Re-Os oil geochronology case studies across the world show that the Re-Os age of oil approximates the timing of hydrocarbon generation (Finlay et al., 2011; Lillis and Selby, 2013; Cumming et al., 2014; Georgiev et al., 2016). Solid bitumen also contains high concentrations of Re and Os, yet Re-Os ages for solid bitumen samples generally have large uncertainties, which may be due to the

insignificant Re/Os fractionation during the formation of solid bitumen (Ge et al., 2016; Cumming et al., 2014).

### **1.2.2 Rubidium-Strontium Isotopic System**

Rubidium (Rb) and strontium (Sr) are large-ion lithophile elements (LILE), with average concentrations of ~84 and ~320 part per million (ppm) in the upper continental crust, respectively (Rudnick and Gao, 2003). Rubidium has two isotopes,  $^{85}\text{Rb}$  and  $^{87}\text{Rb}$ , and strontium has four isotopes,  $^{84}\text{Sr}$ ,  $^{86}\text{Sr}$ ,  $^{87}\text{Sr}$  and  $^{88}\text{Sr}$  (Meija et al., 2016).  $^{87}\text{Rb}$  is a radionuclide which produces  $^{87}\text{Sr}$  through beta decay, and the  $^{87}\text{Rb}$ -to- $^{87}\text{Sr}$  decay was first discovered in 1937 by Hemmendinger and Smythe (1937) and Mattauch (1937). The  $^{87}\text{Rb}$ - $^{87}\text{Sr}$  isotope system is a long-lived decay system and the decay constant of  $^{87}\text{Rb}$  is  $1.396 \times 10^{-11} \text{ yr}^{-1}$  as estimated by measuring radiogenic  $^{87}\text{Sr}$  atoms in purified  $\text{RbClO}_4$  salt over 30 years (Rotenberg et al., 2012) and calibrating Rb-Sr ages with U-Pb ages for the same magmatic intrusions (Nebel et al., 2011). Application of Rb-Sr geochronology in earth sciences is facilitated by the precise determination of Rb-Sr concentrations and isotopic compositions using isotope dilution TIMS and MC-ICP-MS (Nebel et al., 2011) and optimized chemistry workflows (e.g. Li et al., 2015a, b).

Authigenic minerals precipitated during petroleum system events can be hosts for Rb-Sr. Authigenic pyrite is ubiquitous in petroliferous basins and is commonly associated with source rock deposition (Berner, 1984), hydrocarbon generation/expulsion

(Rasmussen, 2005), secondary migration/ charge (Ellis, 2007), and post-accumulation alteration (Machel et al., 1995). Pyrite usually contains Rb and Sr at ppm levels, and Rb-Sr isochron ages can be obtained through bulk analysis of a suite of cogenetic pyrite samples (e.g. Li et al., 2008; Yang and Zhou, 2001). Closure temperature for the Rb-Sr isotope system in pyrite is higher than 200°C (Yang and Zhou, 2001), indicating that post-precipitation events in petroleum systems, which generally occur below 200 °C, would not be able to alter the Rb-Sr isotopic system in pyrite (Ellis, 2007, Machel et al., 1995). Mixed layer illite/smectite (I/S) is another datable target for the Rb-Sr isotope system in hydrocarbon reservoirs. The I/S particles are metastable and the smectite-to-illite inversion (i.e. illitization) can occur if there is sufficient potassium, which is the dominant interlayer cation in illite. Hydrocarbon fluid is more depleted in potassium compared to formation water, thus hydrocarbon charge may inhibit illitization and maintain closure for the Rb-Sr isotope system in I/S particles (Hamilton et al., 1989, Zhang et al., 2011). Therefore, the Rb-Sr isochron age of I/S may approximate the timing of hydrocarbon charge. The Rb-Sr isochron age can be either obtained through bulk analysis of a suite of samples or acid-leaching analysis of a single sample (Bofinger et al., 1968, Middleton et al., 2014, Morton, 1985, Zwingmann et al., 1999).

### **1.3 Petroleum Geochemistry**

Petroliferous basins may contain more than one set of potential

source rocks, and the distribution of hydrocarbons generated by different source rocks can be variable (Dow, 1974). Hydrocarbon-source correlation is a significant aspect of petroleum system investigation as it may identify hydrocarbon migration pathways and exploration targets in a basin (Dow, 1974). Migrated hydrocarbon is capable of preserving signatures that are similar to parental kerogen or hydrocarbons retained in the source rock with respect to their inorganic and organic geochemistry.

### **1.3.1 Inorganic Geochemical Parameters**

Source rock and hydrocarbons are important repositories for trace metals. Trace metals could reflect the redox condition, sediment source, lithofacies, and depositional environment of the source rock and its signature may be transferred to the hydrocarbon products. For example, vanadium and nickel are two elements highly concentrated in source rock and hydrocarbons, with contents in the range of 0.2 – 4760 part per million (ppm) and 7 –1240 ppm, respectively (Lewan and Maynard, 1982). These two metal species in the source rock may be sequestered from interstitial water before lithification of the sediment, and complexed with organic matter as tetrapyrrole compounds (Lewan and Maynard, 1982). The metallic tetrapyrroles can be transferred to hydrocarbons during hydrocarbon generation, and their refractory nature enables these organometallic complex to survive through post-generation geological processes (Lewan and Maynard, 1982). Transition metals, such as

molybdenum and chromium, are also found closely associated with organic compounds (Odermatt and Curiale, 1991). In addition, hydrocarbons may also inherit the provenance characteristics of the source rock as documented in various metal ratios (Zr/Cr, Ni/Y, La/Sc and La/Co; e.g. Shi et al., 2015).

Recent studies show that osmium isotopic composition ( $^{187}\text{Os}/^{188}\text{Os}$ ) may also be used for hydrocarbon-source correlation. Osmium has seven naturally occurring isotopes including  $^{184}\text{Os}$ ,  $^{186}\text{Os}$ ,  $^{187}\text{Os}$ ,  $^{188}\text{Os}$ ,  $^{189}\text{Os}$ ,  $^{190}\text{Os}$  and  $^{192}\text{Os}$  (Meija et al., 2016).  $^{187}\text{Os}$  is the radiogenic product of  $^{187}\text{Re}$  ( $^{187}\text{Re}$ ) and  $^{188}\text{Os}$  is a stable isotope (Naldrett and Libby, 1948). Applying Os isotopic composition for oil-source correlations was first proposed by Selby et al. (2007a) as they found that oils generated by older source rocks tend to have more radiogenic Os isotopic compositions. Their further studies indicated that the Re and Os in hydrocarbons may be directly inherited from the source rock, and hydrocarbons may have similar  $^{187}\text{Os}/^{188}\text{Os}$  ratios to the source rock at the time of hydrocarbon generation (Finlay et al., 2011, 2012; Lillis and Selby, 2013; Cumming et al., 2014). Platinum-group elements (PGEs), which have similar geochemical behaviour to Re and Os, were also found useful in fingerprinting hydrocarbons as the elemental ratios (e.g. Pt/Pd) may preserve the signature of the source rock and not be fractionated by post-depositional processes (Finlay et al., 2012).

### 1.3.2 Organic Geochemical Parameters

Molecular and stable isotopic composition of hydrocarbons are conventional parameters for hydrocarbon-source correlation (Peters et al., 2005), and the source information indicated by organic parameters is also useful for investigating the behaviour of radiometric isotopic systems in petroleum system events.

Biomarkers (also known as “biological markers”, “molecular fossils” or “geochemical fossils”) are a series of organic compounds directly inherited from depositional organic matter and preserve the carbon skeleton of their precursors (Peters et al., 2005). Therefore, biomarkers, such as terpane and sterane, can reflect features of the organic source and formation environment of the source rocks (Peters et al., 2005). Some biomarkers are also sensitive to thermal and micro-organism alteration, which result in conversion of different isomers or compounds. For example, C<sub>29</sub>  $\alpha\alpha\alpha$  20R regular sterane is transformed to C<sub>29</sub>  $\alpha\beta\beta$  20S regular sterane with an increase in temperature, and demethylation of hopanes occurs when subjected to micro-organism degradation (Peters et al., 2005).

Polycyclic aromatic hydrocarbons (PAHs) are aromatic compounds comprising more than one benzene ring, such as naphthalene, phenanthrene and their methylated homologues. PAHs are common in sediments and may be formed by either low-temperature processes, such as diagenetic aromatization of triterpenoids (Wakeham et al., 1980; Chaffee and Johns, 1983; Stout, 1992), or

high-temperature processes, such as alkyl-cracking and resynthesis of pre-existing aromatic compounds by combustion (Hites et al., 1977; Laflamme and Hites, 1978) or hydrothermal alteration (Kawka and Simoneit, 1990; Chen et al., 2003). PAHs can also be used for thermal maturation evaluation as the increase of maturation level would result in the conversion of different isomers (e.g. the shift of  $\alpha$ -type to  $\beta$ -type isomers of naphthalenes and methylphenanthrenes; Radke et al., 1986). Compared to biomarker maturity indicators, which often reach their endpoint at oil maturity, aromatic indicators may still be valid at the over-mature stage (Radke et al., 1986; Radke, 1988; Boreham et al., 1988).

Stable isotopic study is also an important organic geochemical tool for hydrocarbon-source correlation. Carbon consists of two stable isotopes,  $^{12}\text{C}$  and  $^{13}\text{C}$  (Meija et al., 2016), and the carbon isotope ratio of oil is mainly determined by the organic source, as post-depositional maturation only results in insignificant isotopic fractionation (less than 4 per mill; Fuex, 1977; Clayton, 1991). Therefore, the carbon isotopic ratio of oil and source rock is an effective indicator for evaluating the origin of organic matter (terrigenous vs marine). This includes the Sofer plot (carbon isotope ratios of saturated vs aromatic hydrocarbons; Sofer, 1984), the carbon isotopic profile of n-alkanes (Murray et al., 1994), and the carbon isotopic ratio of individual aromatic compounds (e.g. dimethylnaphthalene; Maslen et al., 2011). The carbon isotope ratio of natural gas is not only determined by source but also fractionated

by gas generation processes. Natural gas can be produced by bacterial activity (Rosenfeld and Silverman, 1959) or thermal cracking of organic matter (Chung and Sackett, 1979), with bacterial gas having a more depleted carbon isotope ratio compared to thermal gas (Fuex, 1977).

Sulphur has three stable isotopes,  $^{32}\text{S}$ ,  $^{33}\text{S}$  and  $^{34}\text{S}$  (Meija et al., 2016), and can be complexed with hydrocarbons into organosulphur compounds in kerogen and oil (Hughes, 1984). Sulphur isotopic fractionation is fundamentally influenced by bacterial or thermal sulphate reduction (Machel et al., 1995, Machel, 2001). The coexistence of dissolved sulphate and hydrocarbons is thermodynamically unstable, and sulphate can be reduced by hydrocarbons through bacterial metabolism (bacterial sulphate reduction, BSR) or thermochemical pathways (thermochemical sulphate reduction, TSR). BSR is common in diagenetic settings (Machel et al., 1995), and may result in depletion in  $\delta^{34}\text{S}$  by up to 70 ‰ (Wortmann et al., 2001). The occurrence of TSR requires high temperatures (100–180°C; Machel et al., 1995; Machel, 2001). TSR-influenced hydrocarbons have more enriched  $\delta^{34}\text{S}$  values compared to non-TSR influenced hydrocarbons (up to 24‰; Machel, 2001).

## **1.4 Ancient Petroleum Systems in the McArthur, Tarim and Sichuan Basins**

Increasing demand for oil and gas resources has extended the

exploration frontier to ancient geological environments, such as Precambrian and Paleozoic petroleum systems (Zhu et al., 2013a; Jarrett et al., 2018; Crick, 1992; Zou et al., 2015). Recent discoveries in ancient petroleum systems demonstrated the pervasive occurrence of hydrocarbons in Precambrian-Paleozoic strata, such as the Paleoproterozoic McArthur Group in the McArthur Basin, northern Australia (Jarrett et al., 2018; Crick et al., 1988), Ordovician-Silurian oil/gas pools in the Tarim Basin, northwest China (Zhang et al., 2000; Huang et al., 2016; Tian et al., 2008) and Neoproterozoic-Cambrian gas pools in the Sichuan Basin, southwest China (Wei et al., 2008; Cheng et al., 2018).

### **1.4.1 McArthur Basin**

**The McArthur Basin** is an intracratonic basin located in northern Australia (Figures 1.2A and 1.2B) and it contains the oldest economically accessible hydrocarbons in the world in the Paleoproterozoic Barney Creek Formation petroleum system (Figure 1.2C; Crick, 1992; Flannery and George, 2014). The Barney Creek Formation (BCF) is a set of marine carbonate-siliciclastic- volcanic sedimentary rocks that was deposited during the rifting stage of the basin (Bull, 1998). It contains thick, fine-grained, organic-rich sedimentary beds with total organic carbon (TOC) between 0.2 and 2%, and they are recognized as the source rocks for hydrocarbons reservoired in the McArthur Group (e.g. Teena dolomite, Coxco dolomite and Reward dolomite; Crick, 1992). Pervasive oil and gas

shows in the McArthur Group indicate that hydrocarbon generation occurred in the Barney Creek Formation (Jackson et al., 1986, 1988). In addition, the Barney Creek Formation is also the host of the world-class McArthur River lead-zinc-silver hydrothermal mineral deposit (Figure 1.2A. Chen et al., 2003, Large et al., 2005). Geochemical studies of the Barney Creek Formation petroleum system have mainly focused on source rock evaluation (organic matter abundance, type and thermal maturity level; Jarrett et al., 2018; Rodrigues et al., 2015), petrographic observation of hydrocarbons and their organic precursors (bitumen and kerogen; Rodrigues et al., 2015) and evaluating the trapping conditions for shale gas/shale oil (Baruch et al., 2015). Outcomes of these studies indicate that the Barney Creek Formation has great hydrocarbon potential. Geochronological data for the Barney Creek Formation were mainly determined by uranium-lead isotopic dating of detrital zircons in tuff interbeds and the ages provide a reference for the depositional ages of the strata (Page et al., 2000). Burial and thermal history analysis suggested that hydrocarbon generation in the Barney Creek Formation occurred soon after deposition and lasted until the deposition of the overlying Mesoproterozoic Roper Group (Crick et al., 1988).

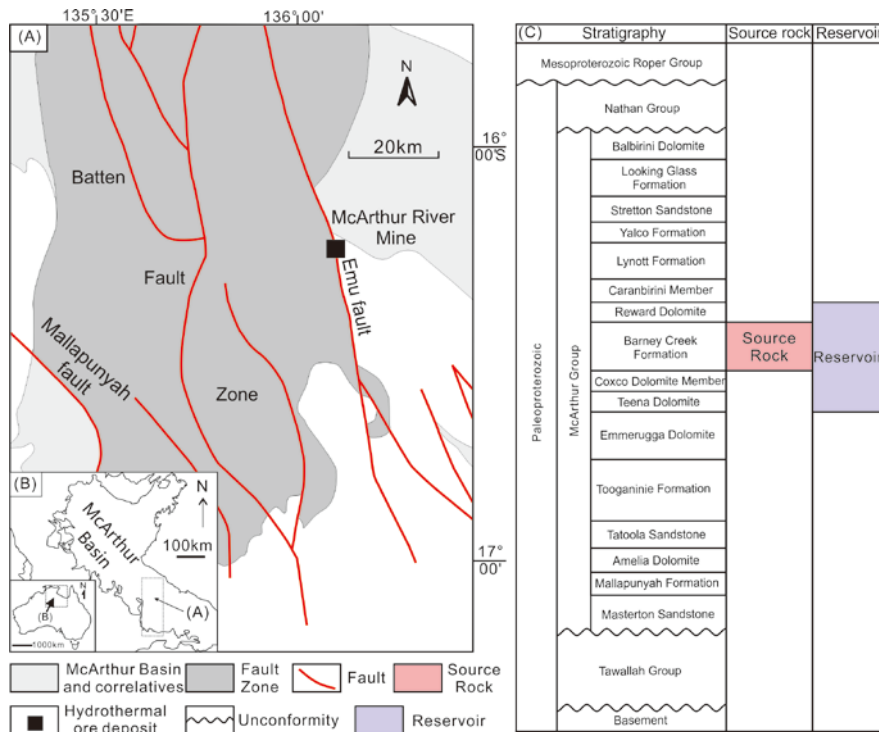


**Figure 1.2:** A: Simplified geological map of the Batten Fault Zone, showing the location of the McArthur River hydrothermal mineral deposit; B: Location of Batten Fault Zone in the McArthur Basin, northern Australia; C: Stratigraphy of the McArthur Group and adjacent units, showing the hydrocarbon source rock and reservoir for the Paleoproterozoic Barney Creek Formation petroleum system.

## 1.4.2 Tarim Basin

**The Tarim Basin** is a large petroliferous basin in northwest China (Figures 1.3A and 1.3B; Hanson et al., 2000; Xiao et al., 1996). The Paleozoic petroleum system (Figure 1.3C) contributes the majority of oil reserves in the basin (Huang et al., 2016). Organic-rich beds in the Cambrian-Ordovician rocks are recognized as hydrocarbon

source rocks for the Paleozoic petroleum system (Huang et al., 2016). The Cambrian-Ordovician strata are a marine sedimentary succession comprising shales, mudstones and marlstones, and they contain organic-rich beds with TOC values of 0.7–7.6% (Huang et al., 2016). Hydrocarbons were accumulated in Ordovician carbonate rock and Silurian sandstone reservoirs through multiple hydrocarbon charge events (Huang et al., 2016; Zhang et al., 2000; Tian et al., 2008). Ordovician-hosted hydrocarbons are mainly distributed in the central Tarim Basin (Tazhong and Tabei uplifts), and Silurian-hosted hydrocarbons are distributed in the central and eastern Tarim Basin (Bachu, Tazhong and Tabei uplifts; Figure 1.3A). The potassium-argon (K-Ar) dating of authigenic illitic clays in the Silurian sandstone showed that the timing of hydrocarbon charge was variable across the basin, ranging from 125 Ma to 416 Ma (Zhang et al., 2011, 2016; Zhu et al., 2013a). Multi-stage tectonic movements have affected the Paleozoic petroleum system, resulting in a range of hydrocarbons in the reservoir, e.g. gas, condensate, light oil, heavy oil and solid bitumen (Zhu et al., 2012a, b, 2013b, 2014; Tian et al., 2008). In addition to analyses of the molecular and stable isotopic composition of hydrocarbons and conduct oil-source correlations (Huang et al., 2016; Li et al., 2015c; Zhang et al., 2002; Cai et al., 2009; Jia et al., 2008, 2010; Tian et al., 2008), researchers have also identified that magmatic and hydrothermal events associated with an early Permian Tarim Large Igneous Province (Figure 1.3A) have affected reservoir qualities, e.g. karstification of the carbonate reservoir and altered the properties of hydrocarbons, e.g. increase in

sulphur content and presence of combustion biomarkers in oils (Cai et al., 2008, 2016, Huang et al., 2016).

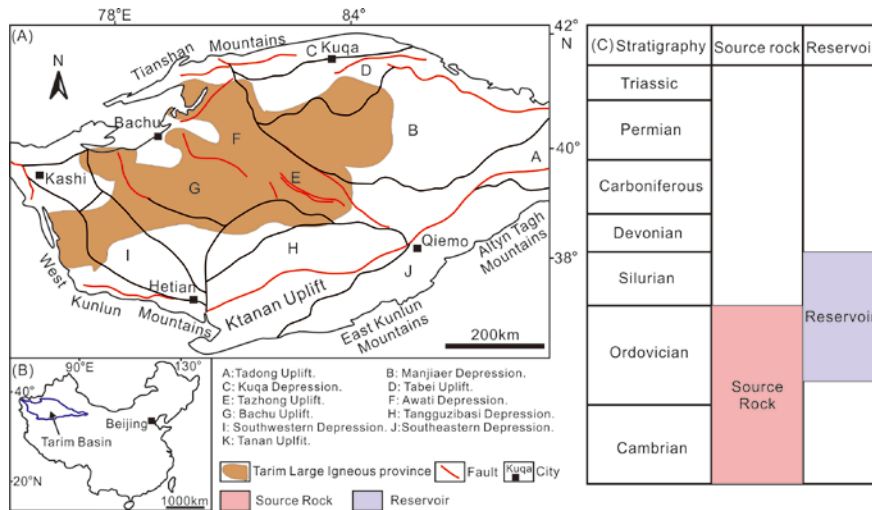


**Figure 1.3:** A: Simplified geological map of the Tarim Basin; B: Location of the Tarim Basin in northwest China; C: Stratigraphy of Palaeozoic sediments, showing the hydrocarbon source rock and reservoir for the Cambrian-Ordovician petroleum system.

### 1.4.3 Sichuan Basin

**The Sichuan Basin** is an important gas province situated in southwest China (Figures 1.4A and 1.4B; Korsch et al., 1991; Ma et al., 2007, 2008; Guo and Zhang, 2014; Dai et al., 2014; Wei et al., 2015). The Neoproterozoic-Cambrian dolomitic rock is one of the oldest giant gas reservoirs in China and contains ~100 trillion cubic meters of natural gas in the central Sichuan Basin (Figure 1.4C; Zou et al., 2015; Du et al., 2014). Organic-rich rocks in the Neoproterozoic-Cambrian marine successions have TOC values of

0.50% – 8.49%, and are recognized as hydrocarbon source rock for natural gas in the dolomitic reservoir (Wei et al., 2008; Shi et al., 2017; Cheng et al., 2018). Natural gas is dominated by methane and generated through thermal cracking of pre-existing oils as suggested by the carbon isotope ratios (Zou et al., 2015; Wei et al., 2015). Oil cracking also has left abundant solid bitumen in the reservoir (Zou et al., 2015). Molecular and trace element geochemistry of the reservoir bitumen indicated that hydrocarbons were derived from a shale-dominated source rock with partial contributions from carbonate rocks, with the source rocks deposited under anoxic conditions (Shi et al., 2017; Cheng et al., 2018). Petroleum system modelling and fluid inclusion analysis indicate there were three critical moments for the gas accumulation in the Neoproterozoic-Cambrian reservoir, including two episodes of paleo-oil accumulation during the Ordovician-Silurian and Triassic-Middle Jurassic periods, respectively, and one oil cracking/gas generation event after the second episode of oil accumulation (Zou et al., 2015).

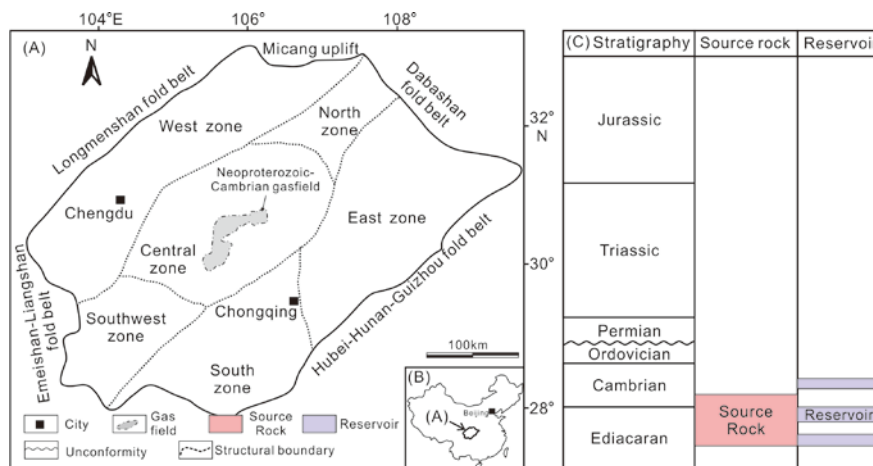


**Figure 1.4:** A: Simplified geological map of the Sichuan Basin; B:

Location of the Sichuan Basin in southwest China; C: Stratigraphy of Precambrian-Mesozoic sediments, showing the hydrocarbon source rock and reservoir for the Ediacaran-Cambrian petroleum system.

## **1.5 Aims of This Thesis**

Absolute timing of petroleum system events is a significant constraint on petroleum system investigation and in reducing the risks associated with hydrocarbon exploration, because such knowledge assists in predicting hydrocarbon distribution in petroliferous basins. Besides conventional methods, such as basin modelling (Magoon and Dow, 1994) and fluid inclusion analysis (Liu and Eadington, 2005), radiometric isotopic geochronology is an emerging technique for dating petroleum system events, such as Re-Os and Rb-Sr isotopic geochronology. Radiometric isotopic systems in authigenic minerals or organic-rich materials record the timing of the latest closure of the isotopic chronometers. Therefore, the isotopic age data can be used for constraining petroleum system events if the closure of the isotopic chronometers is genetically associated with the events.

Regardless of the great potential of Re-Os and Rb-Sr geochronology for petroleum system analysis, there are still a few pending questions about the behaviour of these isotopic systems in petroleum system events. For example, the origin of Re and Os in crude oil, whether it is derived from source rock or formation water (Hurtig et al., 2019; Wu et al., 2016; Mahdaoui et al., 2015), the mechanism of Re/Os

fractionation during source rock deposition (Cumming et al., 2012; Yamashita et al., 2007; Cohen et al., 1999), hydrocarbon generation (Rooney et al., 2012; Cumming et al., 2014), charge (Hurtig et al., 2019; Wu et al., 2016; Mahdaoui et al., 2015) and alteration (Mahdaoui et al., 2013; Lillis and Selby, 2013). The lack of knowledge about the behaviour of the Re-Os isotopic system in petroleum system events has challenged the application of Re-Os geochronology in constraining hydrocarbon generation and the utility of Os isotopic composition for hydrocarbon-source correlation (Wu et al., 2016; Mahdaoui et al., 2015). Rubidium-strontium is another robust isotope geochronometer hosted by minerals commonly present in petroliferous basins, e.g. pyrite and clay minerals. Although Rb-Sr isotope geochronology has been applied to constraining geological processes such as ore formation (Yang and Zhou, 2001), thermal history reconstruction (Uysal et al., 2001), hydrothermal fluid circulation (Middleton et al., 2014), the behaviour and potential applicability of this geochronometer for petroleum system events (e.g. hydrocarbon generation, charge and alteration) have not been fully understood.

Resolving these puzzles related to the behaviour of Re-Os and Rb-Sr isotopic systems will facilitate the application of these robust geochronometers for direct dating of geological processes in petroleum systems, oil-source correlation and characterizing the chemical/physical condition of petroleum system events, especially for ancient (e.g. Precambrian) and highly-altered petroleum systems

in which organic indicators are insufficient. By incorporating organic geochemistry, stable isotope geochemistry and organic petrography with Re-Os and Rb-Sr isotope geochronology, the primary aim of this PhD thesis is to investigate the behaviour of these robust radiogenic isotopic systems (Re-Os and Rb-Sr) in petroleum system events and demonstrate the applicability of these isotopic systems for dating and characterizing these events.

## **Chapter 2**

In **Chapter 2**, the Re-Os isotopic systematics of hydrocarbon source rock within the Barney Creek Formation (BCF) in the McArthur Basin, northern Australia are determined. Previous studies suggested that hydrothermal activities, which were responsible for the formation of the BCF-hosted McArthur River ore deposit, have influenced hydrocarbon generation in the BCF, for example, the molecular and stable isotopic composition of saturated and aromatic hydrocarbons in the BCF show characteristics similar to hydrothermally generated petroleum (Logan et al., 2001, Williford et al., 2011, Chen et al., 2003). Rhenium and osmium are two organophilic metallic elements, commonly enriched in organic-rich geological materials, such as hydrocarbon source rocks, crude oil and solid bitumen (e.g. Creaser et al., 2002, Ge et al., 2016, Selby and Creaser, 2005). Therefore, the Re-Os isotopic systematics in the BCF source rock may also be influenced by the hydrothermally facilitated hydrocarbon generation process.

### **Chapter 3**

In **Chapter 3**, the applicability of Rb-Sr authigenic illitic clay subsamples for geochronology in order to constrain the timing of hydrocarbon charge will be determined by analysing samples from the Silurian bituminous sandstone in the Tarim Basin. Authigenic illitic clay in the Silurian bituminous sandstone is dominated by mixed layer illite/smectite (I/S. Zhang et al., 2016). K-Ar isotopic, mineralogical and basin modelling studies have suggested that hydrocarbon charge in the Silurian bituminous sandstone inhibited the inversion of smectite to illite (Zhang et al., 2016). Thus, hydrocarbon charge may also result in isotopic closure of the Rb-Sr system. To minimize the possibility of generating mixing lines, the Rb-Sr isotopic composition of multiple extractions of the same sample (i.e. “subsamples”) will be analyzed by working on small aliquots (3 – 4 mg) with a low-blank Rb/Sr chemical procedure and high-sensitivity ID-TIMS (Li et al., 2015a, b). This dating method has the potential to yield an isochron age for a single sample, and the age can be cross-checked with the K-Ar age of the same sample.

### **Chapter 4**

In **Chapter 4**, the applicability of Rb-Sr authigenic pyrite subsamples for geochronology in order to constrain the timing of hydrocarbon alteration will be investigated by using samples from the Ordovician carbonate reservoir in the Tarim Basin. Authigenic

pyrite is ubiquitous and coexists with hydrocarbons in the Ordovician carbonate reservoir in the Tarim Basin. This indicates a close relationship between precipitation of pyrite and petroleum system events. Similar to the chemical method applied in **Chapter 3**, the isochron age will be established by analysing the Rb-Sr isotopic composition of subsamples (2–6 mg) of a single pyrite sample. Sulphur and lead isotopic compositions of the pyrite samples will also be analysed to determine the genesis of pyrite.

## **Chapter 5**

In **Chapter 5**, the applicability of Re-Os systematics for hydrocarbon fingerprinting in highly-altered petroleum systems will be investigated by sampling the Neoproterozoic-Cambrian bituminous dolomite in the Sichuan Basin. The Neoproterozoic-Cambrian petroleum system in the Sichuan Basin has a complex history, e.g. multi-stage paleo-oil accumulation, oil cracking and biodegradation. Therefore, evidence from different aspects of geochemistry (both organic and inorganic) should result in a comprehensive understanding of the source of the hydrocarbons. Both molecular composition of organic extracts and Re-Os isotopic systematics of bituminous dolomite samples will be analysed in order to (1) investigate the influence of organic matter characteristics on Re-Os distribution in the bituminous dolomite and (2) differentiate hydrocarbons derived from different source rocks using their organic and Re-Os isotopic signatures.

## References

ALESSANDRELLO, A., BEEMAN, J., BROFFERIO, C., CREMONESI, O., FIORINI, E., GIULIANI, A., HALLER, E., MARGESIN, B., MONFARDINI, A. & NUCCIOTTI, A. 1999. Bolometric measurements of beta decay spectra of  $^{187}\text{Re}$  with crystals of silver perrhenate. *Physics Letters B*, 457, 253-260.

ARNABOLDI, C., BROFFERIO, C., CREMONESI, O., FIORINI, E., BIANCO, C. L., MARTENSSON, L., NUCCIOTTI, A., PAVAN, M., PESSINA, G. & PIRRO, S. 2003. Bolometric bounds on the antineutrino mass. *Physical Review Letters*, 91, 161802.

ASHKTORAB, K., JÄNECKE, J. & BECCHETTI, F. 1993. Beta decay of  $\text{Re }^{187}$  and cosmochronology. *Physical Review C*, 47, 2954.

BARUCH, E. T., KENNEDY, M. J., LÖHR, S. C. & DEWHURST, D. N. 2015. Feldspar dissolution-enhanced porosity in Paleoproterozoic shale reservoir facies from the Barney Creek Formation (McArthur Basin, Australia). *AAPG Bulletin*, 99, 1745-1770.

BERNER, R. A. 1984. Sedimentary pyrite formation: an update.

Geochimica et cosmochimica Acta, 48, 605-615.

BOFINGER, V., COMPSTON, W. & VERNON, M. 1968. The application of acid leaching to the Rb-Sr dating of a Middle Ordovician shale. *Geochimica et Cosmochimica Acta*, 32, 823-833.

BOREHAM, C., CRICK, I. & POWELL, T. 1988. Alternative calibration of the Methylphenanthrene Index against vitrinite reflectance: Application to maturity measurements on oils and sediments. *Organic Geochemistry*, 12, 289-294.

BULL, S. 1998. Sedimentology of the Palaeoproterozoic Barney Creek formation in DDH BMR McArthur 2, southern McArthur basin, northern territory. *Australian Journal of Earth Sciences*, 45, 21-31.

CAI, C., AMRANI, A., WORDEN, R. H., XIAO, Q., WANG, T., GVIRTZMAN, Z., LI, H., SAID-AHMAD, W. & JIA, L. 2016. Sulfur isotopic compositions of individual organosulfur compounds and their genetic links in the Lower Paleozoic petroleum pools of the Tarim Basin, NW China. *Geochimica et Cosmochimica Acta*, 182, 88-108.

CAI, C., LI, K., LI, H. & ZHANG, B. 2008. Evidence for cross formational hot brine flow from integrated  $^{87}\text{Sr}/^{86}\text{Sr}$ , REE and fluid inclusions of the Ordovician veins in Central Tarim, China. *Applied Geochemistry*, 23, 2226-2235.

CAI, C., ZHANG, C., CAI, L., WU, G., JIANG, L., XU, Z., LI, K., MA, A. & CHEN, L. 2009. Origins of Palaeozoic oils in the Tarim Basin: evidence from sulfur isotopes and biomarkers. *Chemical Geology*, 268, 197-210.

CAMPBELL-MILLER, M. D. & SIMARD, B. 1996. First ionization potentials of tungsten and rhenium by mass-selected double-resonance ionization spectroscopy. *JOSA B*, 13, 2115-2120.

CHAFFEE, A. L. & JOHNS, R. 1983. Polycyclic aromatic hydrocarbons in Australian coals. I. Angularly fused pentacyclic tri- and tetraaromatic components of Victorian brown coal. *Geochimica et Cosmochimica Acta*, 47, 2141-2155.

CHEN, J., WALTER, M. R., LOGAN, G. A., HINMAN, M. C. & SUMMONS, R. E. 2003. The Paleoproterozoic McArthur River (HYC) Pb/Zn/Ag deposit of northern Australia: organic geochemistry and ore genesis. *Earth and Planetary Science Letters*, 210, 467-479.

CHENG, B., CHEN, Z., CHEN, T., YANG, C. & WANG, T.-G. 2018. Biomarker signatures of the Ediacaran–Early Cambrian origin petroleum from the central Sichuan Basin, South China: Implications for source rock characteristics. *Marine and Petroleum Geology*, 96, 577-590.

CHUNG, H. M. & SACKETT, W. M. 1979. Use of stable carbon isotope compositions of pyrolytically derived methane as maturity

indices for carbonaceous materials. *Geochimica et Cosmochimica Acta*, 43, 1979-1988.

CLAYTON, C. 1991. Carbon isotope fractionation during natural gas generation from kerogen. *Marine and Petroleum Geology*, 8, 232-240.

COHEN, A. S., COE, A. L., BARTLETT, J. M. & HAWKESWORTH, C. J. 1999. Precise Re–Os ages of organic-rich mudrocks and the Os isotope composition of Jurassic seawater. *Earth and Planetary Science Letters*, 167, 159-173.

CREASER, R., PAPANASTASSIOU, D. & WASSERBURG, G. 1991. Negative thermal ion mass spectrometry of osmium, rhenium and iridium. *Geochimica et Cosmochimica Acta*, 55, 397-401.

CRICK, I. H. 1992. Petrological and maturation characteristics of organic matter from the Middle Proterozoic McArthur Basin, Australia. *Australian Journal of Earth Sciences*, 39, 501-519.

CRICK, I. H., BOREHAM, C. J., COOK, A. C. & POWELL, T. G. 1988. Petroleum geology and geochemistry of Middle Proterozoic McArthur Basin, northern Australia II: assessment of source rock potential. *AAPG Bulletin*, 72, 1495-1514.

CUMMING, V. M., SELBY, D. & LILLIS, P. G. 2012. Re–Os geochronology of the lacustrine Green River Formation: insights into direct depositional dating of lacustrine successions, Re–Os

systematics and paleocontinental weathering. *Earth and Planetary Science Letters*, 359, 194-205.

CUMMING, V. M., SELBY, D., LILLIS, P. G. & LEWAN, M. D. 2014. Re–Os geochronology and Os isotope fingerprinting of petroleum sourced from a Type I lacustrine kerogen: Insights from the natural Green River petroleum system in the Uinta Basin and hydrous pyrolysis experiments. *Geochimica et Cosmochimica Acta*, 138, 32-56.

DAI, J., ZOU, C., LIAO, S., DONG, D., NI, Y., HUANG, J., WU, W., GONG, D., HUANG, S. & HU, G. 2014. Geochemistry of the extremely high thermal maturity Longmaxi shale gas, southern Sichuan Basin. *Organic Geochemistry*, 74, 3-12.

DEMAISON, G. 1984. The generative basin concept. *AAPG Memoir, Petroleum Geochemistry and Basin Evaluation*, 1-14.

DOW, W. G. 1974. Application of oil-correlation and source-rock data to exploration in Williston Basin. *AAPG bulletin*, 58, 1253-1262.

DU, J., ZOU, C., XU, C., HE, H., SHEN, P., YANG, Y., LI, Y., WEI, G., WANG, Z. & YANG, Y. 2014. Theoretical and technical innovations in strategic discovery of a giant gas field in Cambrian Longwangmiao Formation of central Sichuan paleo-uplift, Sichuan Basin. *Petroleum Exploration and Development*, 41, 294-305.

ELLIS, G. 2007. Hydrocarbon entrapment in Triassic to late Jurassic reservoirs in the Timor Sea, Australia-new insights. *APPEA Journal*, 47, 39-53.

FAURE, G. & MENSING, T. M. 2005. *Isotopes: principles and applications*, John Wiley & Sons Inc. 928p.

FINLAY, A. J., SELBY, D. & OSBORNE, M. J. 2011. Re-Os geochronology and fingerprinting of United Kingdom Atlantic margin oil: Temporal implications for regional petroleum systems. *Geology*, 39, 475-478.

FINLAY, A. J., SELBY, D. & OSBORNE, M. J. 2012. Petroleum source rock identification of United Kingdom Atlantic Margin oil fields and the Western Canadian Oil Sands using Platinum, Palladium, Osmium and Rhenium: Implications for global petroleum systems. *Earth and Planetary Science Letters*, 313, 95-104.

FLANNERY, E. N. & GEORGE, S. C. 2014. Assessing the syngeneity and indigeneity of hydrocarbons in the ~ 1.4 Ga Velkerri Formation, McArthur Basin, using slice experiments. *Organic Geochemistry*, 77, 115-125.

FUEX, A. 1977. The use of stable carbon isotopes in hydrocarbon exploration. *Journal of Geochemical Exploration*, 7, 155-188.

GALEAZZI, M., FONTANELLI, F., GATTI, F. & VITALE, S. 2000. End-point energy and half-life of the  $^{187}\text{Re}$   $\beta$  decay. *Physical Review*

C, 63, 014302.

GE, X., SHEN, C., SELBY, D., DENG, D. & MEI, L. 2016. Apatite fission-track and Re-Os geochronology of the Xuefeng uplift, China: Temporal implications for dry gas associated hydrocarbon systems. *Geology*, 44, 491-494.

GEORGIEV, S. V., STEIN, H. J., HANNAH, J. L., GALIMBERTI, R., NALI, M., YANG, G. & ZIMMERMAN, A. 2016. Re-Os dating of maltenes and asphaltenes within single samples of crude oil. *Geochimica et Cosmochimica Acta*, 179, 53-75.

GUO, T. & ZHANG, H. 2014. Formation and enrichment mode of Jiaoshiba shale gas field, Sichuan Basin. *Petroleum Exploration and Development*, 41, 31-40.

HAMILTON, P., KELLEY, S. & FALLICK, A. E. 1989. K-Ar dating of illite in hydrocarbon reservoirs. *Clay Minerals*, 24, 215-231.

HANSON, A., ZHANG, S., MOLDOWAN, J., LIANG, D. & ZHANG, B. 2000. Molecular organic geochemistry of the Tarim Basin, northwest China. *AAPG Bulletin*, 84, 1109-1128.

HEMMENDINGER, A. & SMYTHE, W. 1937. The radioactive isotope of rubidium. *Physical Review*, 51, 1052.

HIRATA, T. 2000. Development of a flushing spray chamber for inductively coupled plasma-mass spectrometry. *Journal of Analytical Atomic Spectrometry*, 15, 1447-1450.

HITES, R. A., LAFLAMME, R. E. & FARRINGTON, J. W. 1977. Sedimentary polycyclic aromatic hydrocarbons: the historical record. *Science*, 198, 829-831.

HOFFMAN, E., NALDRETT, A., VAN LOON, J., HANCOCK, R. & MANSON, A. 1978. The determination of all the platinum group elements and gold in rocks and ore by neutron activation analysis after preconcentration by a nickel sulphide fire-assay technique on large samples. *Analytica Chimica Acta*, 102, 157-166.

HUANG, H., ZHANG, S. & SU, J. 2016. Palaeozoic oil–source correlation in the Tarim Basin, NW China: A review. *Organic Geochemistry*, 94, 32-46.

HUGHES, W. B. 1984. Use of thiophenic organosulfur compounds in characterizing crude oils derived from carbonate versus siliciclastic sources. *AAPG Studies in Geology*, 181-196.

HURTIG, N., GEORGIEV, S., STEIN, H. & HANNAH, J. 2019. Re-Os systematics in petroleum during water-oil interaction: The effects of oil chemistry. *Geochimica et Cosmochimica Acta*, 247, 142-161.

JACKSON, M., SWEET, I. & POWELL, T. 1988. Studies on petroleum geology and geochemistry, Middle Proterozoic, McArthur Basin Northern Australia I: petroleum potential. *APEA Journal*, 28, 283-302.

JACKSON, M. J., POWELL, T. G., SUMMONS, R. E. & SWEET,

I. P. 1986. Hydrocarbon shows and petroleum source rocks in sediments as old as  $1.7 \times 10^9$  years. *Nature*, 322, 727-729.

JARRETT, A. J. M., COX, G. M., SOUTHBY, C., HONG, Z., PALATY, P., CARR, L. & HENSON, P. 2018. Source rock geochemistry of the McArthur Basin, northern Australia: Rock-Eval pyrolysis data release. *Record* 2018/24. *Geoscience Australia, Canberra*, 24, 1-25.

JARVIE, D. M., HILL, R. J., RUBLE, T. E. & POLLASTRO, R. M. 2007. Unconventional shale-gas systems: The Mississippian Barnett Shale of north-central Texas as one model for thermogenic shale-gas assessment. *AAPG bulletin*, 91, 475-499.

JIA, W., PENG, P. & XIAO, Z. 2008. Carbon isotopic compositions of 1, 2, 3, 4-tetramethylbenzene in marine oil asphaltenes from the Tarim Basin: Evidence for the source formed in a strongly reducing environment. *Science in China Series D: Earth Sciences*, 51, 509-514.

JIA, W., XIAO, Z., YU, C. & PENG, P. A. 2010. Molecular and isotopic compositions of bitumens in Silurian tar sands from the Tarim Basin, NW China: Characterizing biodegradation and hydrocarbon charging in an old composite basin. *Marine and Petroleum Geology*, 27, 13-25.

KAWKA, O. E. & SIMONEIT, B. R. 1990. Polycyclic aromatic hydrocarbons in hydrothermal petroleum from the Guaymas Basin

spreading center. *Applied Geochemistry*, 5, 17-27.

KENDALL, B., CREASER, R. A. & SELBY, D. 2009. 187Re-187Os geochronology of Precambrian organic-rich sedimentary rocks. Geological Society, London, Special Publications, 326, 85-107.

KORSCH, R., HUAZHAO, M., ZHAOCAI, S. & GORTER, J. 1991. The Sichuan basin, southwest China: a late Proterozoic (Sinian) petroleum province. *Precambrian Research*, 54, 45-63.

LAFLAMME, R. E. & HITES, R. A. 1978. The global distribution of polycyclic aromatic hydrocarbons in recent sediments. *Geochimica et Cosmochimica Acta*, 42, 289-303.

LARGE, R. R., BULL, S. W., MCGOLDRICK, P. J. & WALTERS, S. 2005. Stratiform and strata-bound Zn-Pb-Ag deposits in Proterozoic sedimentary basins, northern Australia. *Economic Geology*, 100, 931-963.

LAWLEY, C., SELBY, D. & IMBER, J. 2013. Re-Os molybdenite, pyrite, and chalcopyrite geochronology, lupa goldfield, southwestern Tanzania: tracing metallogenic time scales at midcrustal shear zones hosting orogenic Au deposits. *Economic Geology*, 108, 1591-1613.

LEWAN, M. & MAYNARD, J. 1982. Factors controlling enrichment of vanadium and nickel in the bitumen of organic sedimentary rocks. *Geochimica et Cosmochimica Acta*, 46, 2547-

2560.

LI, C.-F., CHU, Z.-Y., GUO, J.-H., LI, Y.-L., YANG, Y.-H. & LI, X.-H. 2015a. A rapid single column separation scheme for high-precision Sr–Nd–Pb isotopic analysis in geological samples using thermal ionization mass spectrometry. *Analytical Methods*, 7, 4793-4802.

LI, C.-F., GUO, J.-H., CHU, Z.-Y., FENG, L.-J. & WANG, X.-C. 2015b. Direct High-Precision Measurements of the  $^{87}\text{Sr}/^{86}\text{Sr}$  Isotope Ratio in Natural Water without Chemical Separation Using Thermal Ionization Mass Spectrometry Equipped with 1012  $\Omega$  Resistors. *Analytical Chemistry*, 87, 7426-7432.

LI, J., LIANG, X.-R., XU, J.-F., SUZUKI, K. & DONG, Y.-H. 2010. Simplified technique for the measurements of Re-Os isotope by multicollector inductively coupled plasma mass spectrometry (MC-ICP-MS). *Geochemical Journal*, 44, 73-80.

LI, Q.-L., CHEN, F., YANG, J.-H. & FAN, H.-R. 2008. Single grain pyrite Rb–Sr dating of the Linglong gold deposit, eastern China. *Ore Geology Reviews*, 34, 263-270.

LI, S., AMRANI, A., PANG, X., YANG, H., SAID-AHMAD, W., ZHANG, B. & PANG, Q. 2015c. Origin and quantitative source assessment of deep oils in the Tazhong Uplift, Tarim Basin. *Organic Geochemistry*, 78, 1-22.

LILLIS, P. G. & SELBY, D. 2013. Evaluation of the rhenium–osmium geochronometer in the Phosphoria petroleum system, Bighorn Basin of Wyoming and Montana, USA. *Geochimica et Cosmochimica Acta*, 118, 312-330.

LINDNER, M., LEICH, D., BORG, R., RUSS, G., BAZAN, J., SIMONS, D. & DATE, A. 1986. Direct laboratory determination of the  $^{187}\text{Re}$  half-life. *Nature*, 320, 246-248.

LINDNER, M., LEICH, D. A., RUSS, G. P., BAZAN, J. M. & BORG, R. J. 1989. Direct determination of the half-life of  $^{187}\text{Re}$ . *Geochimica et Cosmochimica Acta*, 53, 1597-1606.

LIU, K. & EADINGTON, P. 2005. Quantitative fluorescence techniques for detecting residual oils and reconstructing hydrocarbon charge history. *Organic Geochemistry*, 36, 1023-1036.

LOGAN, G. A., HINMAN, M. C., WALTER, M. R. & SUMMONS, R. E. 2001. Biogeochemistry of the 1640 Ma McArthur River (HYC) lead-zinc ore and host sediments, Northern Territory, Australia. *Geochimica et Cosmochimica Acta*, 65, 2317-2336.

LUCK, J.-M. & ALLÈGRE, C. J. 1983.  $^{187}\text{Re}$ – $^{187}\text{Os}$  systematics in meteorites and cosmochemical consequences. *Nature*, 302, 130-132.

LUCK, J.-M., BIRCK, J.-L. & ALLEGRE, C.-J. 1980.  $^{187}\text{Re}$ – $^{187}\text{Os}$  systematics in meteorites: early chronology of the Solar

System and age of the Galaxy. *Nature*, 283, 256-259.

MA, Y., GUO, X., GUO, T., HUANG, R., CAI, X. & LI, G. 2007. The Puguang gas field: New giant discovery in the mature Sichuan Basin, southwest China. *AAPG Bulletin*, 91, 627-643.

MA, Y., ZHANG, S., GUO, T., ZHU, G., CAI, X. & LI, M. 2008. Petroleum geology of the Puguang sour gas field in the Sichuan Basin, SW China. *Marine and Petroleum Geology*, 25, 357-370.

MACHEL, H. 2001. Bacterial and thermochemical sulfate reduction in diagenetic settings—old and new insights. *Sedimentary Geology*, 140, 143-175.

MACHEL, H. G., KROUSE, H. R. & SASSEN, R. 1995. Products and distinguishing criteria of bacterial and thermochemical sulfate reduction. *Applied Geochemistry*, 10, 373-389.

MAGOON, L. B. & DOW, W. G. 1994. The petroleum system, in L. B. Magoon and W. G. Dow, eds., *The petroleum system—from source to trap*. *AAPG Memoir* 60, 3–24.

MAHDAOUI, F., MICHELS, R., REISBERG, L., PUJOL, M. & POIRIER, Y. 2015. Behavior of Re and Os during contact between an aqueous solution and oil: Consequences for the application of the Re–Os geochronometer to petroleum. *Geochimica et Cosmochimica Acta*, 158, 1-21.

MAHDAOUI, F., REISBERG, L., MICHELS, R., HAUTEVELLE,

Y., POIRIER, Y. & GIRARD, J.-P. 2013. Effect of the progressive precipitation of petroleum asphaltenes on the Re–Os radioisotope system. *Chemical Geology*, 358, 90-100.

MAKISHIMA, A. & NAKAMURA, E. 2006. Determination of Os and Re isotope ratios at subpicogram levels using MC-ICPMS with solution nebulization and multiple ion counting. *Analytical Chemistry*, 78, 3794-3799.

MAO, J., XIE, G., BIERLEIN, F., QÜ, W., DU, A., YE, H., PIRAJNO, F., LI, H. M., GUO, B. & LI, Y. 2008. Tectonic implications from Re–Os dating of Mesozoic molybdenum deposits in the East Qinling–Dabie orogenic belt. *Geochimica et Cosmochimica Acta*, 72, 4607-4626.

MASLEN, E., GRICE, K., MÉTAYER, P. L., DAWSON, D. & EDWARDS, D. 2011. Stable carbon isotopic compositions of individual aromatic hydrocarbons as source and age indicators in oils from western Australian basins. *Organic Geochemistry*, 42, 387-398.

MATTAUCH, J. 1937. Das Paar  $^{87}\text{Rb}$ — $^{87}\text{Sr}$  und die Isobarenregel. *Naturwissenschaften*, 25, 189-191.

MCLIMANS, R. K. 1987. The application of fluid inclusions to migration of oil and diagenesis in petroleum reservoirs. *Applied Geochemistry*, 2, 585-603.

MEIJA, J., COPLEN, T. B., BERGLUND, M., BRAND, W. A., DE

BIÈVRE, P., GRÖNING, M., HOLDEN, N. E., IRRGEHER, J., LOSS, R. D. & WALCZYK, T. 2016. Isotopic compositions of the elements 2013 (IUPAC technical Report). Pure and Applied Chemistry, 88, 293-306.

MEISEL, T., MOSER, J., FELLNER, N., WEGSCHEIDER, W. & SCHOENBERG, R. 2001. Simplified method for the determination of Ru, Pd, Re, Os, Ir and Pt in chromitites and other geological materials by isotope dilution ICP-MS and acid digestion. Analyst, 126, 322-328.

MEISSNER, F. F., WOODWARD, J. & CLAYTON, J. L. 1984. Stratigraphic relationships and distribution of source rocks in the greater Rocky Mountain region. In *Hydrocarbon Source Rocks of the Greater Rocky Mountain Region* (eds. J. WOODWARD, F. F. MEISSNER & J. L. CLAYTON). Rocky Mountain Association of Geologists. 1-34p.

MIDDLETON, A. W., UYSAL, I. T., BRYAN, S. E., HALL, C. M. & GOLDING, S. D. 2014. Integrating  $^{40}\text{Ar}$ – $^{39}\text{Ar}$ ,  $^{87}\text{Rb}$ – $^{87}\text{Sr}$  and  $^{147}\text{Sm}$ – $^{143}\text{Nd}$  geochronology of authigenic illite to evaluate tectonic reactivation in an intraplate setting, central Australia. *Geochimica et Cosmochimica Acta*, 134, 155-174.

MORGAN, J. W. & WALKER, R. J. 1989. Isotopic determinations of rhenium and osmium in meteorites by using fusion, distillation and ion-exchange separations. *Analytica Chimica Acta*, 222, 291-300.

MORTON, J. P. 1985. Rb-Sr evidence for punctuated illite/smectite diagenesis in the Oligocene Frio Formation, Texas Gulf Coast. *Geological Society of America Bulletin*, 96, 114-122.

MURRAY, A. P., SUMMONS, R. E., BOREHAM, C. J. & DOWLING, L. M. 1994. Biomarker and n-alkane isotope profiles for Tertiary oils: relationship to source rock depositional setting. *Organic Geochemistry*, 22, 521IN5-542IN6.

NALDRETT, S. & LIBBY, W. 1948. Natural radioactivity of rhenium. *Physical Review*, 73, 487.

NEBEL, O., SCHERER, E. E. & MEZGER, K. 2011. Evaluation of the  $^{87}\text{Rb}$  decay constant by age comparison against the U–Pb system. *Earth and Planetary Science Letters*, 301, 1-8.

NORMAN, M., BENNETT, V., MCCULLOCH, M. & KINSLEY, L. 2002. Osmium isotopic compositions by vapor phase sample introduction using a multi-collector ICP-MS. *Journal of Analytical Atomic Spectrometry*, 17, 1394-1397.

NOZAKI, T., SUZUKI, K., RAVIZZA, G., KIMURA, J. I. & CHANG, Q. 2012. A Method for Rapid Determination of Re and Os Isotope Compositions Using ID-MC-ICP-MS Combined with the Sparging Method. *Geostandards and Geoanalytical Research*, 36, 131-148.

ODERMATT, J. R. & CURIALE, J. A. 1991. Organically bound

metals and biomarkers in the Monterey Formation of the Santa Maria Basin, California. *Chemical Geology*, 91, 99-113.

PAGE, R., JACKSON, M. & KRASSAY, A. 2000. Constraining sequence stratigraphy in north Australian basins: SHRIMP U–Pb zircon geochronology between Mt Isa and McArthur River. *Australian Journal of Earth Sciences*, 47, 431-459.

PEGRAM, W., KRISHNASWAMI, S., RAVIZZA, G. & TUREKIAN, K. 1992. The record of sea water 187Os/186Os variation through the Cenozoic. *Earth and Planetary Science Letters*, 113, 569-576.

PERRODON, A. & MASSE, P. 1984. Subsidence, sedimentation and petroleum systems. *Journal of Petroleum Geology*, 7, 5-25.

PETERS, K., WALTERS, C. & MOLDOWAN, J. 2005. The Biomarker Guide, vol. 2. Biomarkers in petroleum systems and Earth history, 483-705p.

RADKE, M. 1988. Application of aromatic compounds as maturity indicators in source rocks and crude oils. *Marine and Petroleum Geology*, 5, 224-236.

RADKE, M., WELTE, D. & WILLSCH, H. 1986. Maturity parameters based on aromatic hydrocarbons: Influence of the organic matter type. *Organic geochemistry*, 10, 51-63.

RASMUSSEN, B. 2005. Evidence for pervasive petroleum

generation and migration in 3.2 and 2.63 Ga shales. *Geology*, 33, 497-500.

REISBERG, L. & MEISEL, T. 2002. The Re-Os Isotopic System: A Review of Analytical Techniques. *Geostandards Newsletter*, 26, 249-267.

RODRIGUES, S., BLUETT, J., FERGUSON, B. R., GOLDING, S. D. & TITUS, L. 2015. Maturation profile at the Glyde Gas Discovery in the Southern McArthur Basin, Australia. *Search and Discovery Article #10799*, AAPG Datapages.

ROONEY, A. D., SELBY, D., LEWAN, M. D., LILLIS, P. G. & HOUZAY, J.-P. 2012. Evaluating Re–Os systematics in organic-rich sedimentary rocks in response to petroleum generation using hydrous pyrolysis experiments. *Geochimica et Cosmochimica Acta*, 77, 275-291.

ROSENFELD, W. D. & SILVERMAN, S. R. 1959. Carbon isotope fractionation in bacterial production of methane. *Science*, 130, 1658-1659.

ROSMAN, K. & TAYLOR, P. 1998. Isotopic compositions of the elements 1997 (Technical Report). *Pure and Applied Chemistry*, 70, 217-235.

ROTENBERG, E., DAVIS, D. W., AMELIN, Y., GHOSH, S. & BERGQUIST, B. A. 2012. Determination of the decay-constant of

$^{87}\text{Rb}$  by laboratory accumulation of  $^{87}\text{Sr}$ . *Geochimica et Cosmochimica Acta*, 85, 41-57.

RUDNICK, R. L. & GAO, S. 2003. Composition of the continental crust. *Treatise on geochemistry*, 3, 1-64p.

SCHOENBERG, R., NÄGLER, T. F. & KRAMERS, J. D. 2000. Precise Os isotope ratio and Re–Os isotope dilution measurements down to the picogram level using multicollector inductively coupled plasma mass spectrometry. *International Journal of Mass Spectrometry*, 197, 85-94.

SCHOWALTER, T. T. 1979. Mechanics of secondary hydrocarbon migration and entrapment. *AAPG bulletin*, 63, 723-760.

SELBY, D. & CREASER, R. A. 2003. Re–Os geochronology of organic rich sediments: an evaluation of organic matter analysis methods. *Chemical Geology*, 200, 225-240.

SELBY, D. & CREASER, R. A. 2005. Direct Radiometric Dating of Hydrocarbon Deposits Using Rhenium-Osmium Isotopes. *Science*, 308, 1293-1295.

SELBY, D., CREASER, R. A. & FOWLER, M. G. 2007a. Re–Os elemental and isotopic systematics in crude oils. *Geochimica et Cosmochimica Acta*, 71, 378-386.

SELBY, D., CREASER, R. A., STEIN, H. J., MARKEY, R. J. & HANNAH, J. L. 2007b. Assessment of the  $^{187}\text{Re}$  decay constant by

cross calibration of Re–Os molybdenite and U–Pb zircon chronometers in magmatic ore systems. *Geochimica et Cosmochimica Acta*, 71, 1999-2013.

SEN, I. S. & PEUCKER-EHRENBRINK, B. 2014. Determination of Osmium Concentrations and  $^{187}\text{Os}/^{188}\text{Os}$  of Crude Oils and Source Rocks by Coupling High-Pressure, High-Temperature Digestion with Sparging  $\text{OsO}_4$  into a Multicollector Inductively Coupled Plasma Mass Spectrometer. *Analytical Chemistry*, 86, 2982-2988.

SHEN, J., PAPANASTASSIOU, D. & WASSERBURG, G. 1996. Precise Re–Os determinations and systematics of iron meteorites. *Geochimica et Cosmochimica Acta*, 60, 2887-2900.

SHI, C., CAO, J., BAO, J., ZHU, C., JIANG, X. & WU, M. 2015. Source characterization of highly mature pyrobitumens using trace and rare earth element geochemistry: Sinian–Paleozoic paleo-oil reservoirs in South China. *Organic Geochemistry*, 83, 77-93.

SHI, C., CAO, J., TAN, X., LUO, B., ZENG, W. & HU, W. 2017. Discovery of oil bitumen co-existing with solid bitumen in the Lower Cambrian Longwangmiao giant gas reservoir, Sichuan Basin, southwestern China: Implications for hydrocarbon accumulation process. *Organic Geochemistry*, 108, 61-81.

SHIREY, S. B. & WALKER, R. J. 1995. Carius tube digestion for low-blank rhenium-osmium analysis. *Analytical Chemistry*, 67,

2136-2141.

SHIREY, S. B. & WALKER, R. J. 1998. The Re-Os isotope system in cosmochemistry and high-temperature geochemistry. *Annual Review of Earth and Planetary Sciences*, 26, 423-500.

SMOLIAR, M. I., WALKER, R. J. & MORGAN, J. W. 1996. Re-Os ages of group IIA, IIIA, IVA, and IVB iron meteorites. *Science*, 271, 1099.

SOFER, Z. 1984. Stable carbon isotope compositions of crude oils: application to source depositional environments and petroleum alteration. *AAPG Bulletin*, 68, 31-49.

STOUT, S. A. 1992. Aliphatic and aromatic triterpenoid hydrocarbons in a Tertiary angiospermous lignite. *Organic Geochemistry*, 18, 51-66.

SUZUKI, K., MIYATA, Y. & KANAZAWA, N. 2004. Precise Re isotope ratio measurements by negative thermal ionization mass spectrometry (NTI-MS) using total evaporation technique. *International Journal of Mass Spectrometry*, 235, 97-101.

TIAN, H., XIAO, X., WILKINS, R. W., GAN, H., XIAO, Z., LIU, D. & GUO, L. 2008. Formation and evolution of Silurian paleo-oil pools in the Tarim Basin, NW China. *Organic Geochemistry*, 39, 1281-1293.

TISSOT, B. P. & WELTE, D. H. 1984. Petroleum formation and

occurrence, Springer-Verlag, Heidelberg. 699p.

ULMISHEK, G. 1986. Stratigraphic aspects of petroleum resource assessment. In *Oil and Gas Assessment: Methods and Applications* (eds. D.D. RICE). AAPG Studies in Geology. 21, 59-68.

UYSAL, I. T., GOLDING, S. D. & THIEDE, D. S. 2001. K–Ar and Rb–Sr dating of authigenic illite–smectite in Late Permian coal measures, Queensland, Australia: implication for thermal history. *Chemical Geology*, 171, 195-211.

VANDENBROUCKE, M. & LARGEAU, C. 2007. Kerogen origin, evolution and structure. *Organic Geochemistry*, 38, 719-833.

WAKEHAM, S. G., SCHAFFNER, C. & GIGER, W. 1980. Polycyclic aromatic hydrocarbons in Recent lake sediments—II. Compounds derived from biogenic precursors during early diagenesis. *Geochimica et Cosmochimica Acta*, 44, 415-429.

WEI, G., CHEN, G., DU, S., ZHANG, L. & YANG, W. 2008. Petroleum systems of the oldest gas field in China: Neoproterozoic gas pools in the Weiyuan gas field, Sichuan Basin. *Marine and Petroleum Geology*, 25, 371-386.

WEI, G., XIE, Z., SONG, J., YANG, W., WANG, Z., LI, J., WANG, D., LI, Z. & XIE, W. 2015. Features and origin of natural gas in the Sinian–Cambrian of central Sichuan paleo-uplift, Sichuan Basin, SW China. *Petroleum Exploration and Development*, 42, 768-777.

WILLIFORD, K. H., GRICE, K., LOGAN, G. A., CHEN, J. & HUSTON, D. 2011. The molecular and isotopic effects of hydrothermal alteration of organic matter in the Paleoproterozoic McArthur River Pb/Zn/Ag ore deposit. *Earth and Planetary Science Letters*, 301, 382-392.

WORTMANN, U. G., BERNASCONI, S. M. & BÖTTCHER, M. E. 2001. Hypersulfidic deep biosphere indicates extreme sulfur isotope fractionation during single-step microbial sulfate reduction. *Geology*, 29, 647-650.

WU, J., LI, Z. & WANG, X.-C., 2016. Comment on “Behavior of Re and Os during contact between an aqueous solution and oil: Consequences for the application of the Re–Os geochronometer to petroleum” [*Geochim. Cosmochim. Acta* 158 (2015) 1–21]. *Geochimica et Cosmochimica Acta*, 186, 344-347.

XIAO, X., LIU, D. & FU, J. 1996. Multiple phases of hydrocarbon generation and migration in the Tazhong petroleum system of the Tarim Basin, People's Republic of China. *Organic Geochemistry*, 25, 191-197.

YAMASHITA, Y., TAKAHASHI, Y., HABA, H., ENOMOTO, S. & SHIMIZU, H. 2007. Comparison of reductive accumulation of Re and Os in seawater–sediment systems. *Geochimica et Cosmochimica Acta*, 71, 3458-3475.

YANG, J.-H. & ZHOU, X.-H. 2001. Rb-Sr, Sm-Nd, and Pb isotope

systematics of pyrite: Implications for the age and genesis of lode gold deposits. *Geology*, 29, 711-714.

ZHANG, S., HANSON, A., MOLDOWAN, J., GRAHAM, S., LIANG, D., CHANG, E. & FAGO, F. 2000. Paleozoic oil-source rock correlations in the Tarim basin, NW China. *Organic Geochemistry*, 31, 273-286.

ZHANG, S., LIANG, D., LI, M., XIAO, Z. & HE, Z. 2002. Molecular fossils and oil-source rock correlations in Tarim Basin, NW China. *Chinese Science Bulletin*, 47, 20-27.

ZHANG, Y., LIU, K. & LUO, X. 2016. Evaluation of  $^{40}\text{Ar}/^{39}\text{Ar}$  Geochronology of Authigenic Illites in Determining Hydrocarbon Charge Timing: A Case Study from the Silurian Bituminous Sandstone Reservoirs, Tarim Basin, China. *Acta Geologica Sinica (English Edition)*, 90, 684-703.

ZHANG, Y., ZWINGMANN, H., LIU, K., TODD, A. & LUO, X. 2011. Hydrocarbon charge history of the Silurian bituminous sandstone reservoirs in the Tazhong uplift, Tarim Basin, China. *AAPG Bulletin*, 95, 395-412.

ZHU, G., CUI, J., SU, J., YANG, H., ZHANG, B., HU, J. & ZHU, Y. 2012a. Accumulation and reformation of Silurian reservoir in the northern Tarim Basin. *Acta Geologica Sinica (English edition)*, 86, 209-225.

ZHU, G., ZHANG, B., YANG, H., SU, J. & HAN, J. 2014. Origin of deep strata gas of Tazhong in Tarim Basin, China. *Organic Geochemistry*, 74, 85-97.

ZHU, G., ZHANG, S., LIU, K., YANG, H., ZHANG, B., SU, J. & ZHANG, Y. 2013a. A well-preserved 250 million-year-old oil accumulation in the Tarim Basin, western China: Implications for hydrocarbon exploration in old and deep basins. *Marine and Petroleum Geology*, 43, 478-488.

ZHU, G., ZHANG, S., SU, J., HUANG, H., YANG, H., GU, L., ZHANG, B. & ZHU, Y. 2012b. The occurrence of ultra-deep heavy oils in the Tabei Uplift of the Tarim Basin, NW China. *Organic Geochemistry*, 52, 88-102.

ZHU, G., ZHANG, S., SU, J., ZHANG, B., YANG, H., ZHU, Y. & GU, L. 2013b. Alteration and multi-stage accumulation of oil and gas in the Ordovician of the Tabei Uplift, Tarim Basin, NW China: Implications for genetic origin of the diverse hydrocarbons. *Marine and Petroleum Geology*, 46, 234-250.

ZOU, C., YANG, Z., DAI, J., DONG, D., ZHANG, B., WANG, Y., DENG, S., HUANG, J., LIU, K., YANG, C., WEI, G. & PAN, S. 2015. The characteristics and significance of conventional and unconventional Sinian–Silurian gas systems in the Sichuan Basin, central China. *Marine and Petroleum Geology*, 64, 386-402.

ZWINGMANN, H., CLAUER, N. & GAUPP, R. 1999. Structure-

related geochemical (REE) and isotopic (K-Ar, Rb-Sr,  $\delta^{18}\text{O}$ ) characteristics of clay minerals from Rotliegend sandstone reservoirs (Permian, northern Germany). *Geochimica et Cosmochimica Acta*, 63, 2805-2823.

## **Chapter 2**

# **A Proterozoic hydrocarbon generation event in northern Australia: constraints from rhenium-osmium isotope geochemistry**

**Shaojie Li, Xuan-Ce Wang, Zhu-Yin Chu, Simon A. Wilde, Sandra Rodrigues, Suzanne D. Golding, Yuxiang Zhang**

*Precambrian Research, Submitted*

## Abstract

The Proterozoic Barney Creek hydrocarbon system in the McArthur Basin, northern Australia, contains the oldest economically viable hydrocarbons in the world. This study investigated the Re-Os isotopic systematics of hydrocarbon source rocks in the Barney Creek Formation that was intersected by two drillholes, GRNT-79-5 and Lamont Pass 3. A positive isochronous trend is defined by nine samples (Group 1) in the plot of  $^{187}\text{Re}/^{188}\text{Os}$ - $^{187}\text{Os}/^{188}\text{Os}$  ratios, and six samples deviate from the trend in the plot (Group 2). Regression of the isochronous trend yields an isotopic age of  $1624 \pm 62$  Ma (Model 3,  $2\sigma$ , MSWD = 23) with an initial  $^{187}\text{Os}/^{188}\text{Os}$  ratio of  $0.34 \pm 0.20$  ( $2\sigma$ ). The age may not represent the timing of deposition because samples come from a vertical interval spanning over a large distance (96.6 – 511.7 meters in GRNT-79-5 and 781.1 – 803.4 meters in Lamont Pass 3) which may have resulted in heterogeneous initial Os isotopic composition. Instead, the Re-Os isotope system in these samples may have been reset by a post-depositional event, which homogenized the Os isotopic composition. Hydrothermally facilitated lamalginite-to-hydrocarbon conversion (i.e. hydrocarbon generation) is a factor resetting the Re-Os isotope system in Group 1 samples. Organic petrographic observation identified two types of organic matter in the studied samples including lamalginite (kerogen) and solid bitumen (hydrocarbon product), and lamalginite-enriched samples have lower Re-Os contents and  $^{187}\text{Re}/^{188}\text{Os}$  ratios compared to lamalginite-depleted samples. These features suggest that

lamalginitite-to-hydrocarbon conversion may have remobilised two elements and fractionated  $^{187}\text{Re}/^{188}\text{Os}$  ratios in these samples.  $T_{\text{max}}$  values of the samples also support that hydrocarbon generation resulted in Re-Os re-distribution and Re/Os fractionation as there are positive trends in the plots of  $T_{\text{max}}$ -Re contents,  $T_{\text{max}}$ -Os contents and  $T_{\text{max}}$ - $^{187}\text{Re}/^{188}\text{Os}$  ratios. Hydrocarbon generation may have been facilitated by the contemporaneous hydrothermal activity which was responsible for the formation of the BCF-hosted McArthur River Pb-Zn-Ag deposit because it increased the temperature of BCF to above the oil window temperature. Hydrothermal fluids may have also brought additional Re-Os metal budget to the samples. Re and Os can be extracted from hydrothermal fluids and fixed in organic matter during hydrocarbon generation because of their organophilic properties. Therefore, the Re-Os isochronous trend obtained in this study may be resulted from the hydrothermally facilitated hydrocarbon generation event. In contrast to the closed-system  $^{187}\text{Os}$  isotopic behaviour retained in the Group 1 samples, decoupling of  $^{187}\text{Re}$  and  $^{187}\text{Os}$  in the Group 2 samples indicates an open-system behaviour (i.e.  $^{187}\text{Os}$  loss). Higher degree of  $^{187}\text{Os}$  loss occurred in samples with higher extent of deviation from the isochronous trend and the loss event ceased earlier in these samples compared to samples with lower extent of deviation from the trend.

**Key words:** Re-Os isotope geochemistry, Proterozoic hydrocarbon generation event, Barney Creek Formation source rock, McArthur Basin, northern Australia.

## 2.1 Introduction

Although the majority of global hydrocarbon reserves are mainly discovered in Phanerozoic depositional basins (Klemme and Ulmishek, 1991), Precambrian basins were increasingly recognized as potential targets for exploration of conventional and unconventional hydrocarbon resources (Craig et al., 2013). Recent discoveries have demonstrated pervasive occurrence of hydrocarbons in Precambrian rocks, for example, natural gas reservoirs in the Neoproterozoic Dengying Formation, Sichuan Basin, southwest China (Zou et al., 2015), oil inclusions in the Mesoproterozoic Bessie Creek Sandstones, McArthur Basin, northern Australia (Volk et al., 2003), bitumen nodules in the Mesoarchean Gorge Creek Group and Neoarchean Fortescue Group in the Pilbara Craton, western Australia (Rasmussen, 2005), and Proterozoic oil and gas fields in the Lena-Tunguska petroleum province in western Siberia, Russia (Meyerhoff, 1980).

The Proterozoic McArthur Group in the McArthur Basin, northern Australia, is one of the oldest strata that contain potentially economically viable hydrocarbons in the world (Crick, 1992, Munson, 2014, Summons et al., 1988). Organic-rich, fine-grained sediments of the Barney Creek Formation (BCF) within the McArthur Group are considered as potential hydrocarbon source rocks (Crick, 1992) and unconventional plays (Baruch et al., 2015). Although mounting evidence demonstrates the presence of

hydrocarbon generation in the BCF (Crick, 1992, Baruch et al., 2015), there is still a knowledge gap in understanding the timing of the process. In this study, we tried to address this issue utilizing rhenium-osmium (Re-Os) isotopes geochemistry of source rock samples from the BCF that was intersected by two drillholes, GRNT-79-5 and Lamont Pass 3 in southern McArthur Basin (Figures 2.1A and 2.1B).

Previous studies suggested that hydrothermal activities, which were responsible for the formation of the BCF-hosted McArthur River ore deposit, have influenced hydrocarbon generation in the BCF, for example, the molecular and stable isotopic composition of saturated and aromatic hydrocarbons in the BCF show characteristics similar to hydrothermally generated petroleum (Logan et al., 2001, Williford et al., 2011, Chen et al., 2003). Rhenium and osmium are two organophilic metallic elements, commonly enriched in organic-rich geological materials, such as hydrocarbon source rocks, crude oil and solid bitumen (Creaser et al., 2002, Ge et al., 2016, Selby and Creaser, 2005). Therefore, the Re-Os isotopic systematics in the BCF source rock may also be influenced by the hydrothermally facilitated hydrocarbon generation process.

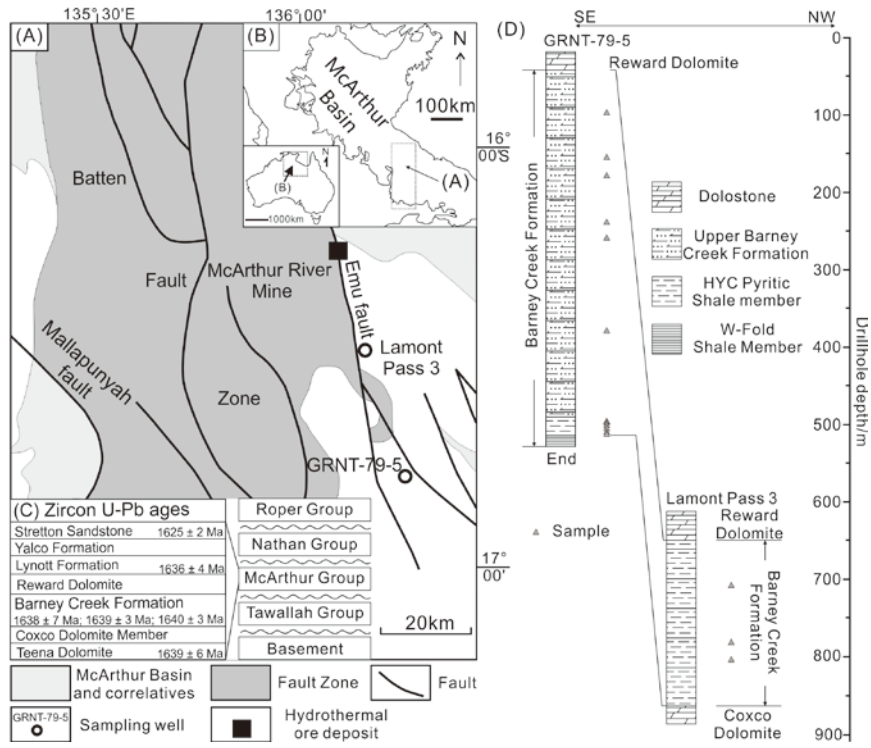


**Figure 2.1:** A: Simplified geological map of the Batten Fault Zone, McArthur Basin, showing the location of drillholes GRNT-79-5 and Lamont Pass 3; B: Location of the study area in the McArthur Basin; C: Stratigraphy of the McArthur Group and adjacent unites, showing available U-Pb detrital zircon ages. The age data are from Page et al. (2000); D: BCF core logs of drillholes GRNT-79-5 and Lamont Pass3.

## 2.2 Geological background

The McArthur Basin is an ancient depositional basin located in northern Australia (Figure 2.1B) and mainly consists of Proterozoic sediments, including the Tawallah, McArthur, Nathan and Roper groups (Figure 2.1C. Lindsay, 2001, Rawlings, 1999). The BCF is an unmetamorphosed, fine-grained rock sequence within the

McArthur Group and it is sandwiched between two dolomite sequences, the overlying Reward Dolomite and the underlying Coxco Dolomite (Figure 2.1C, Lindsay, 2001, Rawlings, 1999). The BCF can be divided into three members, the W-Fold Shale Member (green and dolomitic siltstone and shale, tuff interbed), the HYC (Here's Your Chance) Pyritic Shale member (carbonaceous, dolomitic and pyritic siltstone and mudstone) and the Upper Barney Creek Formation (thinly bedded or planar laminated, dolomitic, carbonaceous and pyritic siltstone and shale) (Davidson and Dashlooty, 1993, Bull, 1998).

Barney Creek sediments were deposited in a north-south trending intracratonic rift basin (Bull, 1998). The depositional environment of the BCF was originally thought to be a lacustrine setting, but it was reinterpreted as a marine setting based on new sedimentological and organic geochemical observations (Bull, 1998, Chen et al., 2003). The economic significance of the BCF is highlighted by its enrichment in base metals and organic matter. The giant stratified sedimentary exhalative (SEDEX) McArthur River lead-zinc-silver (Pb-Zn-Ag) deposit is hosted by the BCF (Large et al., 2005). The McArthur River ore deposit is one of the largest hydrothermal mineral deposits in the world and contains ~227 Mt of Pb+Zn+Ag metal (9.25% Zn, 4.1% Pb and 41 ppm Ag, Large et al., 2005). Organic-rich fine-grained sediments also occur in the BCF, with total organic carbon values (TOC in %) generally distributed between 0.2% and 2% (Holman et al., 2014). The maturation level of organic matter

in the BCF varies from immature to over-mature and is affected by contemporaneous hydrothermal alteration (Crick, 1992, Glikson et al., 1992, Glikson, 2001). The common presence of hydrocarbon shows in the BCF (e.g. bitumen, oil seepages and gas flows) indicates the occurrence of pervasive hydrocarbon generation/migration (Crick et al., 1988, Dunster, 2007, Rodrigues et al., 2015). Based on burial history and source rock geochemical analysis, Crick et al (1988) inferred that hydrocarbon generation in the BCF probably occurred soon after its deposition and lasted until the deposition of the overlying Roper Group (~1589 Ma, Page et al., 2000).

Geochronological studies of sediments in the McArthur Basin mainly utilized uranium-lead (U-Pb) dating of detrital zircons in interbedded tuffs (Page et al., 2000, Page and Sweet, 1998), with some age data obtained by rubidium-strontium (Rb-Sr) dating of clay (Kralik, 1982) and Re-Os dating of black shale (Kendall et al., 2009a, Abbassi et al., 2017). U-Pb age data of zircons from tuff beds in the lower part of the BCF suggests the depositional age of the BCF was ~1640 Ma ( $1638 \pm 7$  Ma,  $1639 \pm 3$  Ma,  $1640 \pm 3$  Ma, Figure 2.1C, Page et al., 2000). Rb-Sr dating of illite and carbonate leachate of a homogeneous dolomitic siltstone in the upper BCF yielded an isochron age of  $1537 \pm 52$  Ma, yet the regression might be biased due to initial Sr isotopic heterogeneity (Kralik, 1982).

There has been recent progress in Re-Os organic-rich sediment geochronology in the McArthur Basin, although only a few Re-Os

isotope studies on the BCF are reported (Abbassi et al., 2017; Kendall et al., 2009a). Kendall et al. (2009a) reported two Re-Os isochron ages ( $1361 \pm 21$  and  $1417 \pm 29$  Ma) for the upper and lower intervals of the Velkerri Formation of the Roper Group intersected by the drillhole Urapunga-4 in the central McArthur Basin. A similar Re-Os age of  $1427 \pm 52$  Ma was reported for the same strata by Abbassi et al. (2017). In addition, their study also generated a younger age of  $382 \pm 81$  Ma for bitumen in the Velkerri Formation and the age was interpreted as the timing of hydrocarbon migration (Abbassi et al., 2017).

## **2.3 Samples and methods**

Samples for this study came from BCF mudstones intersected by two drillholes, GRNT-79-5 and Lamont Pass 3, which are located near the Emu Fault, southern McArthur Basin (Figure 2.1A). Twelve samples were collected from the depths of 96.6 – 511.7 meters in GRNT-79-5 and three samples were collected from the depths of 708.4 – 803.4 meters in Lamont Pass 3 (Figure 2.1D). Petrographic, organic and inorganic geochemical analyses were undertaken on each drillcore sample. Organic geochemical analysis includes pyrolysis analysis. Inorganic geochemical analysis includes Re-Os chemistry, negative thermal ionization mass spectrometry (N-TIMS) and multi-collector inductive coupled plasma mass spectrometry (MC-ICP-MS).

### **2.3.1 Petrographic and Organic geochemical analysis**

Core samples were slabbed and small blocks were cut to fit 5×3 cm moulds. Petrographic blocks were prepared with a cold-setting epoxy-resin mixture and polished using standard techniques for coal petrography. For the identification of different organic components, the ASTM D7708 (2015) standard was adopted, as well as the recommendations in Taylor et al. (1998) and Glikson et al. (2006). Petrographic studies were conducted with a Leica MD6000 M microscope equipped with a Diskus-Fossil system at The University of Queensland. The microscope was calibrated using two standards, a YAG standard (0.908 %) and a black standard (0.0 %). Fluorescent light excitation was used to assist in the identification of the properties of the organic components.

A HAWK instrument was used to determine the organic geochemical parameters from dry, finely ground (250 µm) samples weighing 50 – 200 mg at the Energy Resources Consulting Pty Ltd in Brisbane. The pyrolysis stage of the HAWK was conducted under inert conditions, at an initial iso-temperature of 300°C for 3 min to release free hydrocarbons in the samples (S1, mg HC/g Rock). Thermal cracking of the potential hydrocarbon generating kerogen (S2, mg HC/g Rock) and the oxygen containing pyrolysable kerogen (S3, mg CO<sub>2</sub>/g Rock) were carried out by automatic heating at 25°C/ min rate to reach the maximum temperature of 750°C. The oxidation stage was performed over a temperature range of 300°C to 750 °C (heating rate of 25°C per minute) to measure the residual inert organic carbon (S4, mg CO and CO<sub>2</sub>/g Rock and RC, wt.%) and a

portion of the mineral carbon (pyroMinC, wt.%). The bulk total organic carbon (TOC, wt.%) is the sum of the total pyrolysable carbon and the residual carbon. Tmax is the temperature at which the maximum generation of hydrocarbons from cracking of kerogen.

## **2.3.2 Inorganic geochemical analysis**

Portions of fresh rock samples were cleaned with distilled water and dried completely prior to be broken into chips by a clean cloth-wrapped hammer. Rock chips were ground into powders (~200 mesh) using an agate mill before inorganic geochemistry analytical work.

### **2.3.2.1 Re-Os chemistry and N-TIMS and MC-ICP-MS**

Re-Os chemistry/mass spectrometry work was undertaken at the State Key Laboratory of Lithospheric Evolution, Institute of Geology and Geophysics, Chinese Academy of Sciences (IGGCAS), Beijing. Rock chips were ground into powders (~200 mesh) using an agate mill. Approximately 500 milligram powders of each sample were mixed with  $^{185}\text{Re}$ - $^{190}\text{Os}$  isotopic tracers and digested in 8 ml CrVI-H<sub>2</sub>SO<sub>4</sub> solution in a Carius tube at 220 °C for 48 hours (Selby and Creaser, 2003). Rhenium and osmium fractions were separated by solvent extraction (tetrachloromethane, CCl<sub>4</sub>). The rhenium fraction was purified through anion exchange chromatography, and the osmium fraction was purified using micro-distillation.

The purified rhenium fraction was dissolved in dilute nitric acid and measured by MC-ICP-MS (Thermo Fisher Scientific Neptune) in

static mode using Faraday Cups. The purified osmium fraction was loaded on a high-purity platinum filament using Ba(OH)<sub>2</sub> as an ion emitter and measured by N-TIMS (GV, Isoprobe-T) in single ion counter peak-jumping mode using secondary electron multipliers. Acids used during the Re-Os chemistry were all analytical reagent (AR) grade and were purified utilizing a Savillex<sup>TM</sup> DST-1000 sub-boiling distillation system. Ultrapure water with a resistivity of 18.2 MΩ.cm<sup>-1</sup> obtained from a Milli-Q Element system was used throughout this work.

Total procedural blanks were less than 1.0 pg for Os with <sup>187</sup>Os/<sup>188</sup>Os ratio of 0.170, and less than 13 pg for Re. Throughout the period of this study, the UMCP Os standard yielded <sup>187</sup>Os/<sup>188</sup>Os ratio of 0.11384 ± 0.00068 (n = 4, 2σ). The in-house Re standard solution gave <sup>187</sup>Re/<sup>185</sup>Re = 1.69831 ± 0.00050 (n = 4, 2σ). The Re and Os contents, and <sup>187</sup>Os/<sup>188</sup>Os ratios were blank-corrected. <sup>187</sup>Os/<sup>188</sup>Os ratios were normalized to <sup>192</sup>Os/<sup>188</sup>Os = 3.08271. Re-Os isochron ages were calculated using the ISOPLOT3.0 software (Ludwig, 2003), applying a decay constant (λ<sup>187</sup>Re) of 1.666×10<sup>-11</sup> yr<sup>-1</sup> (Selby et al., 2007, Smoliar et al., 1996).

## **2.4 Results**

### **2.4.1 Composition and maturity level of organic matter**

Organic petrographic and geochemical data for the twelve samples from GRNT-79-5 and three samples from Lamont Pass 3 are listed

in Table 2.1. In terms of petrographic components (Figure 2.2), the samples from GRNT-79-5 are essentially composed of lamalginite (non-degraded filamentous algal bodies. Samples GR1 to GR5) or a mix of lamalginite and solid bitumen (samples GR6 to GR12), while the samples from Lamont Pass 3 are essentially composed of solid bitumen (Table 2.1). Solid bitumen is formless or present as a nodule. The presence of solid bitumen is an indicator that hydrocarbons were produced (Figures. 2.2C-2.2H, Landis and Castaño, 1995). BCF mudstone samples have high content of organic matter. TOC values for samples from GRNT-79-5 are distributed between 0.86% and 5.04% (Table 2.1). Whereas, samples from Lamont Pass 3 have TOC values of 2.04 – 4.02% (Table 2.1). Therefore, samples in this study can be regarded as hydrocarbon source rocks because of their abundant content of organic matter. Most of the samples in this study can be classified as good (TOC = 2.0 – 4.0%) and fair source rocks (TOC = 0.5 – 2%), with one sample (GR7) belonging to the excellent source rock class (TOC > 4%) (Hunt, 1996).

$T_{max}$  values for samples from GRNT-79-5 are 436 – 444 °C (Table 2.1). Samples from Lamont Pass 3 have  $T_{max}$  values in the range of 438–454 °C (Table 2.1).  $T_{max}$ , a conventional maturity parameter used in petroleum systems, suggests that these samples have entered the oil window, and most of the samples are at the early oil maturity stage (435 – 445 °C) with one sample (LP3) reaching peak oil maturity stage (Tissot and Welte, 1984). Therefore, hydrocarbon generation has occurred in these source rock samples.

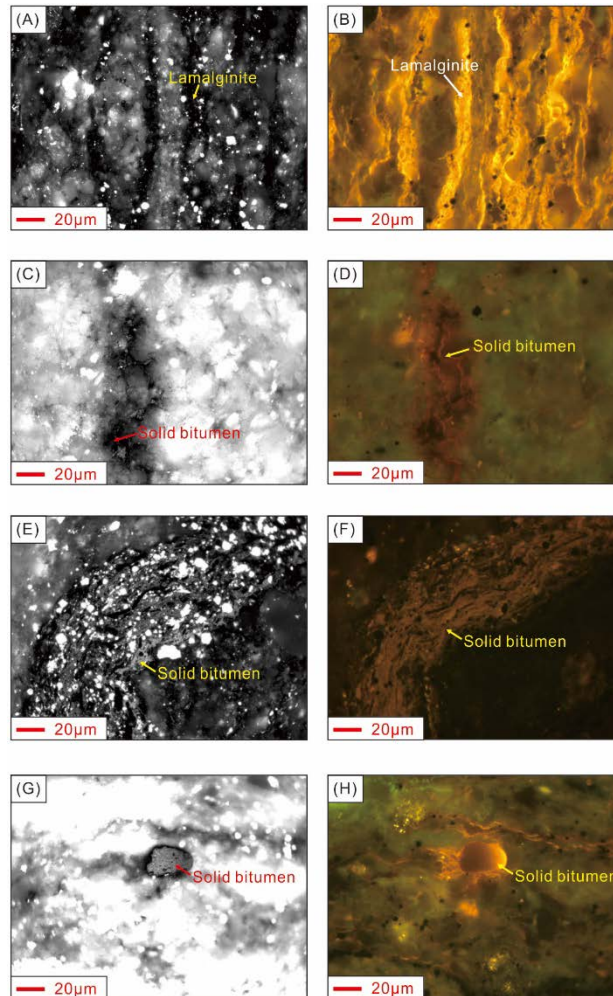


**Figure 2.2:** Representative photomicrographs of organic components in the Barney Creek Formation source rocks. Both lamalginites (GR1, A: white light; B: fluorescent light.) and solid bitumen were found. Solid bitumen is mainly disseminated in the matrix (GR4, C: white light; D: fluorescent light; LP1, E: white light; F: fluorescent light.) or as nodules (GR4, G: white light; H: fluorescent light).

**Table 2.1:** TOC,  $T_{\max}$ , organic material composition and Re-Os isotope data of Barney Creek source rock samples intersected by drillholes GRNT-79-5 and Lamont Pass 3 in the McArthur Basin, northern Australia

Sample ID	Depth (m)	TOC (%)	$T_{\max}$ (°C)	Organic material composition		Re (ppb)	Os (ppb)	$^{187}\text{Re}/^{188}\text{Os}$	2s	$^{187}\text{Os}/^{188}\text{Os}$	2s	$1/^{192}\text{Os}$ (ppb <sup>-1</sup> )	
				Lamalginitite (%)	Solid bitumen (%)								
GRNT-79-5	GR1	96.6	3.15	436	91	9	0.580	0.0387	100.48	0.11	3.2994	0.0040	89.65
	GR2	154.2	2.43	438	88	12	0.834	0.1321	34.954	0.035	1.2847	0.0015	21.35
	GR3	177.8	2.68	440	91	9	1.550	0.0556	176.20	0.10	2.5159	0.0277	57.88
	GR4	237.8	3.32	438	55	45	1.451	0.0861	99.242	0.254	1.8666	0.0055	34.93
	GR5	258.0	1.99	437	94	6	2.907	0.0700	243.88	0.46	1.7831	0.0057	42.59
	GR6	377.9	0.99	439	32	68	0.847	0.0584	95.756	0.315	3.0621	0.0195	58.14
	GR7	495.1	5.04	443	8	92	7.955	0.3527	172.01	1.75	4.6094	0.0447	11.05
	GR8	495.9	1.4	437	25	75	2.478	0.1054	189.68	0.36	5.3710	0.0193	39.31
	GR9	499.9	0.86	436	22	78	1.984	0.1008	144.88	0.16	4.2559	0.0077	37.55
Lamont Pass3	GR1	503.9	1.1	438	25	75	3.912	0.0498	422.72	0.66	1.0447	0.0019	55.10
	GR1	508.8	1.01	443	38	62	7.074	0.0884	432.95	0.27	1.0894	0.0011	31.17
	GR1	511.7	1.07	444	0	100	7.656	0.2297	383.52	1.40	10.897	0.033	25.85
	LP1	708.4	2.04	438	0	100	0.833	0.0304	196.69	0.10	3.9856	0.1650	121.5
	LP2	781.1	2.17	443	0	100	1.284	0.1068	73.618	0.062	2.2404	0.0027	29.30
	LP3	803.4	4.02	454	0	100	11.44	0.3672	329.92	0.59	9.4179	0.1620	14.86

\* Re and Os contents, and  $^{187}\text{Os}/^{188}\text{Os}$  ratios were blank-corrected.  $^{187}\text{Os}/^{188}\text{Os}$  ratios were normalized to  $^{192}\text{Os}/^{188}\text{Os} = 3.08271$ .

## 2.4.2 Re-Os elemental and isotopic systematics

The studied samples have Re and Os contents generally higher than the average Upper Crust (Table 2.1 and Figure 2.3A, Rudnick and Gao, 2003). Re and Os contents of samples from GRNT-79-5 are 0.5801 – 7.955 part per billion (ppb) and 0.0387 – 0.3527 ppb, respectively (Table 2.1). Samples from Lamont Pass 3 have 0.8331 – 11.44 ppb of Re and 0.0304 – 0.3672 ppb of Os (Table 2.1). Os contents positively correlate with Re contents ( $R^2=0.71$ , Figure 2.3A).

$^{187}\text{Re}/^{188}\text{Os}$  and  $^{187}\text{Os}/^{188}\text{Os}$  ratios of samples from GRNT-79-5 are distributed in the range of 34.954 – 432.95 and 1.0447 – 10.897, respectively (Table 2.1). Samples from Lamont Pass 3 have  $^{187}\text{Re}/^{188}\text{Os}$  and  $^{187}\text{Os}/^{188}\text{Os}$  ratios of 73.618 – 329.92 and 2.2404 – 9.4179, respectively (Table 2.1).

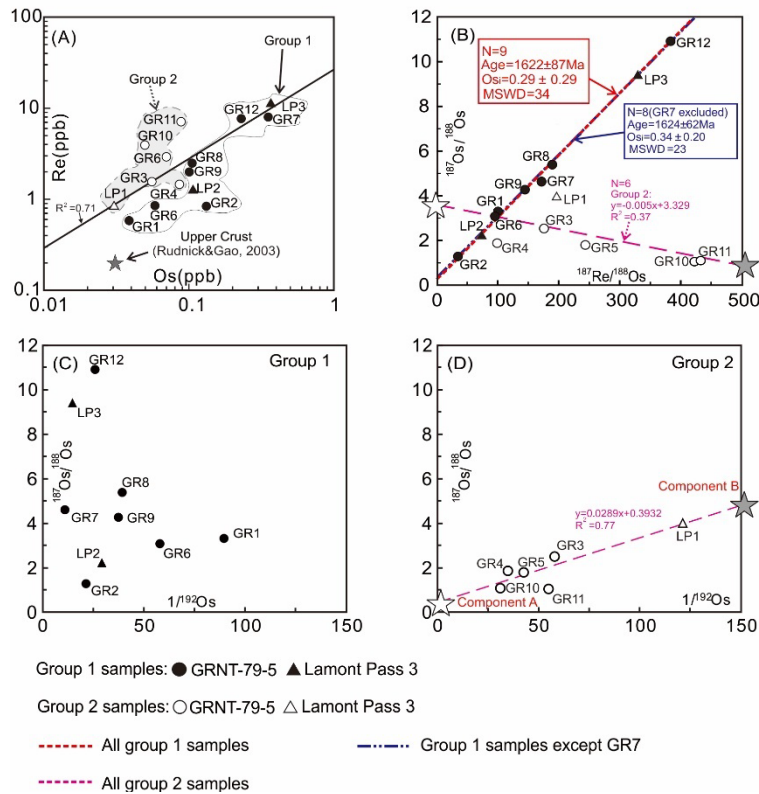


**Figure 2.3:** Scatter plots of the Re-Os data. A: Re vs Os contents. Re-Os contents of the upper crust are from Rudnick and Gao (2003); B:  $^{187}\text{Os}/^{188}\text{Os}$  vs  $^{187}\text{Re}/^{188}\text{Os}$  ratios; C:  $^{187}\text{Os}/^{188}\text{Os}$  vs  $1/^{192}\text{Os}$  ratios of the Group 1 samples; D:  $^{187}\text{Os}/^{188}\text{Os}$  vs  $1/^{192}\text{Os}$  ratios of the Group 2 samples. MSWD denotes mean square weighted deviates.  $\text{Os}_i$  denotes initial  $^{187}\text{Os}/^{188}\text{Os}$  ratio.

## 2.5 Discussion

### 2.5.1 Classification of the studied samples

A positive isochronous trend is present in the  $^{187}\text{Re}/^{188}\text{Os}$ - $^{187}\text{Os}/^{188}\text{Os}$  plot (Figure 2.3B), and samples are classified into two groups according to their affinity to the trend (Table 2.2). The  $^{187}\text{Re}/^{188}\text{Os}$  and  $^{187}\text{Os}/^{188}\text{Os}$  data of samples GR1, GR2, GR6, GR8, GR9, GR12, LP2, LP3 and GR7 define a good linear correlation with a coefficient of determination ( $R^2$ ) of 0.9966 (Table 2.2). Among these samples, GR7 deviates slightly from the trend and  $R^2$  value of the regression without GR7 increases to 0.9988 (Table 2.2). Although there is a minor difference in  $R^2$  values of these two regressions, both regressions yield similar isotopic ages ( $1622 \pm 87$  Ma ( $2\sigma$ ), Model 3, MSWD = 34 and  $1624 \pm 62$  Ma ( $2\sigma$ ), Model 3, MSWD = 23, respectively) and initial  $^{187}\text{Os}/^{188}\text{Os}$  ratios ( $\text{Osi}$ ) overlapping within uncertainties ( $0.29 \pm 0.29$  and  $0.34 \pm 0.2$ ,  $2\sigma$ , respectively. Figure 2.3B and Table 2.2). The isochronous trend is unlikely a mixing isochron because there is no correlation between the  $1/^{192}\text{Os}$  and  $^{187}\text{Os}/^{188}\text{Os}$  ratios (Figure 2.3C). Therefore, these nine samples are classified as Group 1. The rest of the samples, GR3, GR4, GR5, GR10, GR11 and LP1 which deviate from the isochronous trend in the  $^{187}\text{Re}/^{188}\text{Os}$ - $^{187}\text{Os}/^{188}\text{Os}$  plot, are classified as Group 2. Compared to the regression of  $^{187}\text{Re}/^{188}\text{Os}$  and  $^{187}\text{Os}/^{188}\text{Os}$  data of the Group 1 samples, regressions including both Group 1 and Group 2 samples have smaller  $R^2$  values, and isotopic ages and  $\text{Osi}$  values yielded

from these regressions have higher uncertainties (Table 2.2). Instead, Group 2 samples display a negative trend in the plot of  $^{187}\text{Re}/^{188}\text{Os}$ - $^{187}\text{Os}/^{188}\text{Os}$  ratios (Figure 2.3B) and a positive trend in the plot of  $1/^{192}\text{Os}$ - $^{187}\text{Os}/^{188}\text{Os}$  ratios (Figure 2.3D).

## **2.5.2 A post-depositional reset event for the Re-Os isotope system**

Three criteria should be met to build a Re-Os isochron: (1) a sufficient spread in  $^{187}\text{Re}/^{188}\text{Os}$  ratios, (2) homogeneous  $\text{Os}_i$  and (3) closed-system behaviour (Creaser et al., 2002, Cumming et al., 2012, Finlay et al., 2011, Georgiev et al., 2016). A Re-Os isochron date of organic-rich marine source rock could approximate the depositional age (Kendall et al., 2009b). This hypothesis is mainly based on the assumption that the majority of the Os budget in the source rock was inherited from seawater where Os isotopes could be sufficiently equilibrated as the Os residence time in seawater is longer than the seawater mixing time (8 – 10 kyrs *vs* ~1.5 kyrs, Oxburgh, 2001). In addition, the Os isotopic composition of seawater varies rapidly through time (8 – 10 kyrs, Cohen et al., 1999, Oxburgh, 2001, Peucker - Ehrenbrink and Ravizza, 2000), whereas the sedimentation rate of marine source rock is commonly low (e.g. 2m/Ma, Creaser et al., 2002). Therefore, to guarantee a homogeneous initial  $^{187}\text{Os}/^{188}\text{Os}$  ratio and further yield a Re-Os isochron age for constraining the timing of deposition, source rock samples were commonly collected from a narrow stratigraphic

section (<10 meters; Kendall et al., 2009b).

In this study, the Re-Os isotope data of samples from Group 1 define an isochronous trend and regression of the trend yields an isotopic age of  $1624 \pm 62$  Ma with an  $Os_i$  of  $0.34 \pm 0.20$  (Figure 2.3B). These samples are distributed in a vertical interval spanning over a large distance (96.6 – 511.7 meters in GRNT-79-5 and 781.1 – 803.4 meters in Lamont Pass 3. Figure 2.1D and Table 2.1), thus it is likely that the samples inherited the heterogeneous Os isotopic composition from seawater when they were deposited. This implies that the Re-Os isochron age may not represent the timing of deposition, instead, the Re-Os isotope system in these samples may have been reset by post-depositional processes. The BCF is the host for the giant hydrothermal ore deposit (McArthur River Ore deposit), and the hydrothermal event occurred soon after the deposition of the host rock (Symons, 2007). Therefore, the post-depositional hydrothermal event may have homogenised the Os isotopic composition and reset the Re-Os isotope system in these samples.

**Table 2.2:** Regression statistics of  $^{187}\text{Re}/^{188}\text{Os}$ - $^{187}\text{Os}/^{188}\text{Os}$  isotope data of samples

Samples	GR1, GR2, GR6, GR8, GR9, GR12, LP2, LP3	GR1, GR2, GR6, GR8, GR9, GR12, LP2, LP3, GR7	GR1, GR2, GR6, GR8, GR9, GR12, LP2, LP3, GR3	GR1, GR2, GR6, GR8, GR9, GR12, LP2, LP3, GR4	GR1, GR2, GR6, GR8, GR9, GR12, LP2, LP3, GR5	GR1, GR2, GR6, GR8, GR9, GR12, LP2, LP3, GR10	GR1, GR2, GR6, GR8, GR9, GR12, LP2, LP3, GR11	GR1, GR2, GR6, GR8, GR9, GR12, LP2, LP3, LP1
<sup>a</sup> R <sup>2</sup>	0.9988	0.9966	0.9277	0.9846	0.7445	0.2801	0.2668	0.9659
<sup>b</sup> Age/Ma	1624 ± 62	1622 ± 87	1616 ± 360	1661 ± 170	1448 ± 680	759 ± 980	729 ± 980	1602 ± 240
<sup>c</sup> Os <sub>i</sub>	0.34 ± 0.2	0.29 ± 0.29	0.1 ± 1.2	0.07 ± 0.56	0.3 ± 2.4	2.1 ± 3.9	2.2 ± 3.9	0.18 ± 0.84
<sup>d</sup> MSWD	23	34	426	274	818	1140	1135	167

<sup>a</sup>R<sup>2</sup> denotes coefficient of determination of the regression of  $^{187}\text{Re}/^{188}\text{Os}$  and  $^{187}\text{Os}/^{188}\text{Os}$  ratios of the samples.

<sup>b</sup>Age/Ma denotes the isotopic age regressed from the  $^{187}\text{Re}/^{188}\text{Os}$  and  $^{187}\text{Os}/^{188}\text{Os}$  ratios of the samples.

<sup>c</sup>Os<sub>i</sub> denotes the initial  $^{187}\text{Os}/^{188}\text{Os}$  ratio regressed from the  $^{187}\text{Re}/^{188}\text{Os}$  and  $^{187}\text{Os}/^{188}\text{Os}$  ratios of the samples.

<sup>d</sup>MSWD denotes the mean standard weighted deviates.

### **2.5.3 Re-Os redistribution induced by hydrothermal-facilitated organic matter conversion**

Organic petrographic investigation identified two types of organic matter in the studied samples including lamalginite and solid bitumen. Lamalginites are non-degraded algal bodies with filamentous shapes (Hutton, 1987), and they are kerogens in the Barney Creek Formation and can be converted to hydrocarbons (i.e. solid bitumen) with the increase of temperature (Crick et al., 1988). Therefore, the percentage of lamalginite in organic matter can be used to indicate the extent of lamalginite-to-hydrocarbon conversion (i.e. hydrocarbon generation). Contents of lamalginite in the samples are normalized by TOC values (lamalginite/TOC), representing the percentage of lamalginite in the organic matter budget of a sample. Lamalginite-enriched samples have higher Re-Os contents compared to lamalginite-depleted samples (Figures 2.4A and 2.4B), and this indicates that the lamalginite-hosted Re-Os budget may have transported to hydrocarbon products. Osmium may be more preferentially partitioning into hydrocarbons compared to Re during the conversion of organic matter as there is a negative trend in the  $^{187}\text{Re}/^{188}\text{Os}$  lamalginite/TOC plot (Figure 2.4E). Therefore, the lamalginite-to-hydrocarbon conversion may be a factor fractionating Re/Os ratios of the samples from the Group 1.  $T_{\text{max}}$  is a conventional parameter for evaluating the thermal maturity of samples (Tissot and Welte, 1984). The positive trends exhibiting in the plots of  $T_{\text{max}}$ -Re and  $T_{\text{max}}$ -Os contents (Figures 2.4C and 2.4D) indicate that Re and

Os are more concentrated in samples at higher maturity levels where higher proportions of lamalginite have been converted to hydrocarbons.  $T_{\max}$  values also support that hydrocarbon generation fractionated the  $^{187}\text{Re}/^{188}\text{Os}$  ratios of the samples from Group 1, as there is a positive trend between their  $T_{\max}$  and  $^{187}\text{Re}/^{188}\text{Os}$  values (Figure 2.4F).

Temperature is an essential factor controlling hydrocarbon generation as source rocks enter the oil window at 60 – 80 °C (Tissot and Welte, 1984). The increase in temperature could be either due to burial or abnormal heating by hydrothermal events (Tissot and Welte, 1984). Previous studies indicated that the deposition of the BCF occurred around ~1640 Ma according to uranium-lead ages of zircons from the tuff bed within the lower part of the BCF ( $1638 \pm 7$  Ma,  $1639 \pm 3$  Ma,  $1640 \pm 3$  Ma. (Page et al., 2000). The hydrothermal mineralization in the BCF may have occurred 2 – 3 million years after the deposition of the host rock when the BCF was buried to a depth of ~800 meters below the surface ( $1636 \pm 4$  Ma (Symons, 2007). The metal-bearing hydrothermal fluid heated the BCF to a temperature higher than 120°C for ~0.1 million years (Symons, 2007). This temperature reached the peak oil maturity (Tissot and Welte, 1984), thus the hydrothermal activity, which was responsible for the formation of McArthur River ore deposit, most likely facilitated the Proterozoic hydrocarbon generation event in BCF source rocks. Hydrocarbon generation in the BCF source rocks was not an instantaneous event but may have lasted millions of years

(Crick et al., 1988), and this large time span would cause the scatter of the Re-Os isochron age.

Enrichment of Re and Os in samples with lower content of lamalginite and higher  $T_{\max}$  values may be attributed to the hydrothermal metal re-charging. Lower percentages of lamalginite in organic matter and higher  $T_{\max}$  values indicate that higher extent of lamalginite-hydrocarbon conversion have occurred in the samples, and hydrothermal activity may have more intensive thermal impact on these samples compared to samples containing higher percentages of lamalginite. Mukherjee and Large (2017)'s study suggests that hydrothermal fluids may have brought additional transition metals (e.g. Zn, Cu and Ag) into the BCF. Therefore, it is speculated that Re and Os can be extracted from metal-bearing hydrothermal fluids and fixed in organic matter during the hydrothermal-facilitated lamalginite-to-hydrocarbon conversion process because of their organophilic properties.

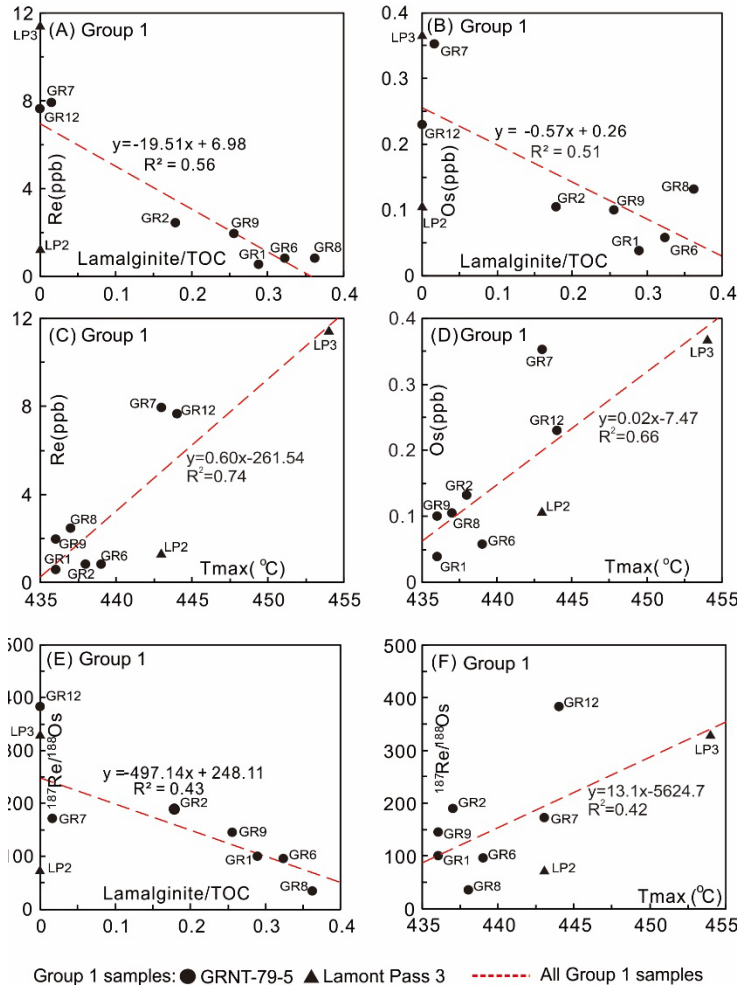


**Figure 2.4:** Relationships between Re-Os systematics and organic composition and  $T_{max}$  of Group 1 samples. A: Re content vs lamalginite content/TOC; B: Os content vs lamalginite content/TOC; C: Re content vs  $T_{max}$ ; D: Os content vs  $T_{max}$ ; E:  $^{187}\text{Re}/^{188}\text{Os}$  ratio vs lamalginite content/TOC; F:  $^{187}\text{Re}/^{188}\text{Os}$  ratio vs  $T_{max}$ .

## 2.5.4 Open-system Os isotopic behaviour in Group 2 samples

Group 2 samples deviate from the isochronous trend but define a negative trend in the  $^{187}\text{Re}/^{188}\text{Os}$ - $^{187}\text{Os}/^{188}\text{Os}$  plot (Figure 2.3B). The positive trend exhibited between  $1/^{192}\text{Os}$  and  $^{187}\text{Os}/^{188}\text{Os}$  ratios indicates the binary mixing of components A (low  $^{187}\text{Os}/^{188}\text{Os}$  and high Os content) and B (high  $^{187}\text{Os}/^{188}\text{Os}$  and low Os content) in these samples (Figure 2.3D). Component A is also characterized by a high  $^{187}\text{Re}/^{188}\text{Os}$  ratio and component B is characterized by a low  $^{187}\text{Re}/^{188}\text{Os}$  ratio, and this is inconsistent with the Os isotopic composition of both components (Figure 2.3B). Therefore, partial  $^{187}\text{Os}$  loss could have occurred in the Group 2 samples as indicated by the decoupled  $^{187}\text{Re}/^{188}\text{Os}$ - $^{187}\text{Os}/^{188}\text{Os}$  relationship.

Mathematical modelling has been conducted in order to estimate the extent of  $^{187}\text{Os}$  loss and its timing (Figures 2.5A and 2.5B). A modelled  $^{187}\text{Os}/^{188}\text{Os}$  ratio,  $O_{sa}$ , can be calculated assuming it had an  $O_{si}$  of 0.34 which is regressed from the isochron (Figure 2.3B), and maintained closed since the 1624 Ma hydrocarbon generation event:

$$O_{sa} = 0.34 + ^{187}\text{Re}/^{188}\text{Os}_m \cdot (e^{\lambda \cdot 1624\text{Ma}} - 1) \quad (1)$$

where  $^{187}\text{Re}/^{188}\text{Os}_m$  denotes  $^{187}\text{Re}/^{188}\text{Os}$  ratio measured by mass spectrometry.

The difference (%) between modelled and measured values

( $\Delta^{187}\text{Os}/^{188}\text{Os}$ ) is established to quantitatively determine the  $^{187}\text{Os}$  loss:

$$\Delta^{187}\text{Os}/^{188}\text{Os} = \frac{O_{Sa} - ^{187}\text{Os}/^{188}\text{Os}_m}{O_{Sa}} \times 100\% \quad (2)$$

where  $^{187}\text{Os}/^{188}\text{Os}_m$  denotes the  $^{187}\text{Os}/^{188}\text{Os}$  ratio measured by mass spectrometry.

Closure time of the  $^{187}\text{Os}$  loss event can also be estimated through a simplified model as show in Figure 2.5B because the Re-Os isotope system would record the timing of the latest  $^{187}\text{Os}$  isotopic closure. The model is based on the consideration that the radiogenic-induced  $^{187}\text{Re}/^{188}\text{Os}$  deduction (<2%) is insignificant compared to the proportion of  $^{187}\text{Os}$  loss (30.5% – 91.2%, Table 2.3).

As shown in Figure 2.5B, set the time of  $^{187}\text{Os}$  closure is  $t$  Ma, where

Point 1: isotopic values of a sample at the initial stage;

Point 2: isotopic values of a sample at  $t$  Ma if no  $^{187}\text{Os}$  was lost;

Point 3: isotopic values of a sample at  $t$  Ma with partial  $^{187}\text{O}$  loss ( $\Delta^{187}\text{Os}/^{188}\text{Os}$ );

Point 4: present-day isotopic values of a sample; and

Point 4': projection of the point 4 on the isochron representing the end time of  $^{187}\text{Os}$  lost (i.e. point 4' has an  $^{187}\text{Os}/^{188}\text{Os}$  value same as the point 4).

As the closure time of  $^{187}\text{Os}$  loss is  $t$  Ma, thus, according to the isochron equation:

$$\tan\beta = e^{\lambda t} \quad (3)$$

Geometrically, angle  $\alpha$  equals angle  $\beta$ , thus:

$$\tan\beta = \tan\alpha = \frac{d_1}{d_2} \quad (4)$$

And:

$d_1$  = difference between  $^{187}\text{Os}/^{188}\text{Os}$  values of points 2 and 4;

$d_2$  = difference between  $^{187}\text{Re}/^{188}\text{Os}$  values of points 4 and 4'.

Substituting Eq. (4) into Eq. (3), the following equation is obtained:

$$e^{\lambda t} = \frac{O_{Si} + {}^{187}\text{Re}/{}^{188}\text{Os}_m (e^{\lambda t} - 1) - {}^{187}\text{Os}/{}^{188}\text{Os}_m}{{}^{187}\text{Re}/{}^{188}\text{Os}_m - \frac{{}^{187}\text{Os}/{}^{188}\text{Os}_m - O_{Si}}{e^{\lambda t} - 1}} \quad (5)$$

Therefore, closure time of the  $^{187}\text{Os}$  loss event can be expressed as follows:

$$t = 1/\lambda \ln(1 + ({}^{187}\text{Re}/{}^{188}\text{Os}_m) / ({}^{187}\text{Os}/{}^{188}\text{Os}_m - O_{Si}) / ({}^{187}\text{Re}/{}^{188}\text{Os}_m)) \quad (6)$$

where  $O_{Si}$  denotes the initial  $^{187}\text{Os}/^{188}\text{Os}$  ratio (given 0.34 here).

Calculation results (Table 2.3) show that higher degree of  $^{187}\text{Os}$  loss occurred in samples with higher extent of deviation from the isochronous trend in the  $^{187}\text{Re}/^{188}\text{Os}$ - $^{187}\text{Os}/^{188}\text{Os}$  plot (e.g. samples

GR10 and GR11) and the loss event ceased earlier in these samples compared to samples with lower extent of deviation from the trend (e.g. samples LP1 and GR3).

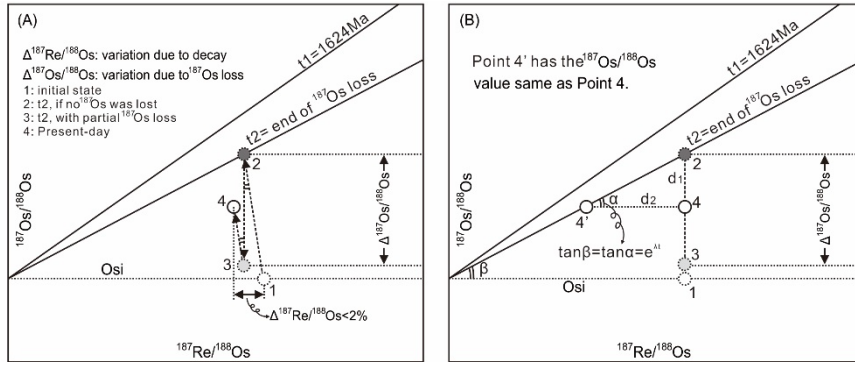


**Figure 2.5:** A:  $^{187}\text{Os}/^{188}\text{Os}$  vs  $^{187}\text{Re}/^{188}\text{Os}$  ratios showing how the Group 2 samples vary through time; B: a model neglecting the radiogenic reduction in  $^{187}\text{Re}/^{188}\text{Os}$  ratio of the Group 2 samples because it is much smaller compared to the variation in  $^{187}\text{Os}/^{188}\text{Os}$  (Table 2.3).

**Table 2.3:** Termination and amount of  $^{187}\text{Os}$  loss in the BCF Group 2 samples

Drillhole	Sample ID	End of $^{187}\text{Os}$ loss in Ma	* $\Delta^{187}\text{Os}/^{188}\text{Os}$	** $\Delta^{187}\text{Re}/^{188}\text{Os}$
Lamont Pass3	LP1	1102	30.5%	1.8%
	GR3	737	51.4%	1.2%
GRNT-79-5	GR4	916	39.0%	1.5%
	GR5	354	74.6%	0.6%
	GR10	100	91.2%	0.2%
	GR11	104	91.1%	0.2%

\* $\Delta^{187}\text{Os}/^{188}\text{Os}$  denotes the difference (%) between modelled and measured  $^{187}\text{Os}/^{188}\text{Os}$  ratio due to  $^{187}\text{Os}$  loss.

\*\* $\Delta^{187}\text{Re}/^{188}\text{Os}$  denotes the decrease (%) of  $^{187}\text{Re}/^{188}\text{Os}$  ratio due to radiogenic decay from 1624 Ma to the termination of  $^{187}\text{Os}$  loss.

### **2.5.5 Implications for prospecting of hydrocarbon generation**

Through applying organic petrology and Re-Os isotope geochemistry on hydrocarbon source rock in the BCF, this study provides isotopic evidence for the occurrence of a Proterozoic hydrocarbon generation event in the McArthur Basin. This demonstrates the prospecting potential of the BCF hydrocarbon system for both conventional and unconventional reserves.

## **2.6 Conclusions**

This study investigated the Re-Os isotopic systematics of the Barney Creek Formation (BCF) hydrocarbon source rock in the McArthur Basin, northern Australia, using samples from drillholes GRNT-79-5 and Lamont Pass 3. A positive isochronous trend is defined by nine samples (Group 1) in the plot of  $^{187}\text{Re}/^{188}\text{Os}$ - $^{187}\text{Os}/^{188}\text{Os}$  ratios, and six samples deviate from the trend in the plot (Group 2). Regression of the isochronous trend yields an isotopic age of  $1624 \pm 62$  Ma (Model 3,  $2\sigma$ , MSWD=23) with an initial  $^{187}\text{Os}/^{188}\text{Os}$  ratio of  $0.34 \pm 0.20$  ( $2\sigma$ ). The age may not represent the timing of deposition because samples come from a vertical interval spanning over a large distance (96.6 – 511.7 meters in GRNT-79-5 and 781.1 – 803.4 meters in Lamont Pass 3) which may have resulted in heterogeneous initial Os isotopic composition. Instead, the Re-Os isotope system in

these samples may have been reset by a post-depositional event, which homogenized the Os isotopic composition. Hydrothermally facilitated lamalginite-to-hydrocarbon conversion (i.e. hydrocarbon generation) is a factor resetting the Re-Os isotope system in Group 1 samples. Organic petrographic observation identified two types of organic matter in the studied samples including lamalginite (kerogen) and solid bitumen (hydrocarbon product), and lamalginite-enriched samples have lower Re-Os contents and  $^{187}\text{Re}/^{188}\text{Os}$  ratios compared to lamalginite-depleted samples. These features suggest that lamalginite-to-hydrocarbon conversion may have remobilised two elements and fractionated  $^{187}\text{Re}/^{188}\text{Os}$  ratios in these samples.  $T_{\text{max}}$  values of the samples also support that hydrocarbon generation resulted in Re-Os re-distribution and Re/Os fractionation as there are positive trends in the plots of  $T_{\text{max}}$ -Re contents,  $T_{\text{max}}$ -Os contents and  $T_{\text{max}}$ - $^{187}\text{Re}/^{188}\text{Os}$  ratios. Hydrocarbon generation may have been facilitated by the contemporaneous hydrothermal activity which was responsible for the formation of the BCF-hosted McArthur River Pb-Zn-Ag deposit because it increased the temperature of BCF to above the oil window temperature. Hydrothermal fluids may have also brought additional Re-Os metal budget to the samples. Re and Os can be extracted from hydrothermal fluids and fixed in organic matter during hydrocarbon generation because of their organophilic properties. Therefore, the Re-Os isochronous trend obtained in this study may be resulted from the hydrothermally facilitated hydrocarbon generation event. In contrast to the closed-system  $^{187}\text{Os}$  isotopic behaviour retained in the Group 1 samples, decoupling of

$^{187}\text{Re}$  and  $^{187}\text{Os}$  in the Group 2 samples indicates an open-system behaviour (i.e.  $^{187}\text{Os}$  loss). Higher degree of  $^{187}\text{Os}$  loss occurred in samples with higher extent of deviation from the isochronous trend in the  $^{187}\text{Re}/^{188}\text{Os}$ - $^{187}\text{Os}/^{188}\text{Os}$  plot and the loss event ceased earlier in these samples compared to samples with lower extent of deviation from the trend.

## **Acknowledgments**

This work was supported by the Strategic Priority Research Program of the Chinese Academy of Sciences (grant No. XDA20070304), “Hundred Talents Program” of Shanxi Province, China, and the Australise Resources and Environment Solutions (ARES). Luke Titus and Armour Energy Ltd are thanked for providing access to cores and funding together with the Australian Government Department of Industry and Science that enabled re-evaluation of the thermal maturity of McArthur Basin source rocks.

## **References**

ABBASSI, S., KENNEDY, M. & SCHAEFER, B. 2017. Dating Deposition and Petroleum Migration from the Same Samples Using the Re/Os Geochronometer. Goldschmidt Abstracts, 2.

ASTM D7708. 2015. Standard Test Method for Microscopical Determination of the Reflectance of Vitrinite Dispersed in Sedimentary Rocks. Annual book of ASTM Standards: Petroleum Products, Lubricants, and Fossil Fuels; Gaseous Fuels; Coal and Coke 5, 5.06: ASTM International, West Conshohocken, PA.

BARUCH, E. T., KENNEDY, M. J., LÖHR, S. C. & DEWHURST, D. N. 2015. Feldspar dissolution-enhanced porosity in Paleoproterozoic shale reservoir facies from the Barney Creek Formation (McArthur Basin, Australia) Feldspar Dissolution-Enhanced Porosity in Paleoproterozoic Shale Reservoir Facies from the Barney Creek Formation. AAPG Bulletin, 99, 1745-1770.

BULL, S. 1998. Sedimentology of the Palaeoproterozoic Barney Creek formation in DDH BMR McArthur 2, southern McArthur basin, northern territory. Australian Journal of Earth Sciences, 45, 21-31.

CHEN, J., WALTER, M. R., LOGAN, G. A., HINMAN, M. C. & SUMMONS, R. E. 2003. The Paleoproterozoic McArthur River (HYC) Pb/Zn/Ag deposit of northern Australia: organic geochemistry and ore genesis. Earth and Planetary Science Letters, 210, 467-479.

COHEN, A. S., COE, A. L., BARTLETT, J. M. & HAWKESWORTH, C. J. 1999. Precise Re–Os ages of organic-rich mudrocks and the Os isotope composition of Jurassic seawater. Earth and Planetary Science Letters, 167, 159-173.

CRAIG, J., BIFFI, U., GALIMBERTI, R., GHORI, K., GORTER, J., HAKHOO, N., LE HERON, D., THUROW, J. & VECOLI, M. 2013. The palaeobiology and geochemistry of Precambrian hydrocarbon source rocks. *Marine and Petroleum Geology*, 40, 1-47.

CREASER, R. A., SANNIGRAHI, P., CHACKO, T. & SELBY, D. 2002. Further evaluation of the Re-Os geochronometer in organic-rich sedimentary rocks: A test of hydrocarbon maturation effects in the Exshaw Formation, Western Canada Sedimentary Basin. *Geochimica et Cosmochimica Acta*, 66, 3441-3452.

CRICK, I. H. 1992. Petrological and maturation characteristics of organic matter from the Middle Proterozoic McArthur Basin, Australia. *Australian Journal of Earth Sciences*, 39, 501-519.

CRICK, I. H., BOREHAM, C. J., COOK, A. C. & POWELL, T. G. 1988. Petroleum geology and geochemistry of Middle Proterozoic McArthur Basin, northern Australia II: assessment of source rock potential. *AAPG Bulletin*, 72, 1495-1514.

CUMMING, V. M., SELBY, D. & LILLIS, P. G. 2012. Re-Os geochronology of the lacustrine Green River Formation: insights into direct depositional dating of lacustrine successions, Re-Os systematics and paleocontinental weathering. *Earth and Planetary Science Letters*, 359, 194-205.

DAVIDSON, G. & DASHLOOTY, S. 1993. The Glyde Sub - basin: A volcanoclastic - bearing pull - apart basin coeval with the

McArthur River base - metal deposit, Northern Territory. *Australian Journal of Earth Sciences*, 40, 527-543.

DUNSTER, J. 2007. Gas shows in Glyde sub-basin, accessed June 9, 2014. Minerals Exploration Reports, Northern Territory Geological Survey. <http://www.geoscience.nt.gov.au/gemis/ntgsjspui/handle/1/74198>.

FINLAY, A. J., SELBY, D. & OSBORNE, M. J. 2011. Re-Os geochronology and fingerprinting of United Kingdom Atlantic margin oil: Temporal implications for regional petroleum systems. *Geology*, 39, 475-478.

GE, X., SHEN, C., SELBY, D., DENG, D. & MEI, L. 2016. Apatite fission-track and Re-Os geochronology of the Xuefeng uplift, China: Temporal implications for dry gas associated hydrocarbon systems. *Geology*, 44, 491-494.

GEORGIEV, S. V., STEIN, H. J., HANNAH, J. L., GALIMBERTI, R., NALI, M., YANG, G. & ZIMMERMAN, A. 2016. Re-Os dating of maltenes and asphaltenes within single samples of crude oil. *Geochimica et Cosmochimica Acta*, 179, 53-75.

GLIKSON, M. 2001. The application of electron microscopy and microanalysis in conjunction with organic petrology to further the understanding of organic-mineral association: examples from Mount Isa and McArthur Basins, Australia. *International Journal of Coal Geology*, 47, 139-159.

GLIKSON, M., GOLDING, S. & SOUTHGATE, P. 2006. Thermal evolution of the ore-hosting Isa superbasin: Central and northern Lawn Hill platform. *Economic Geology*, 101, 1211-1229.

GLIKSON, M., TAYLOR, D. & MORRIS, D. 1992. Lower Palaeozoic and Precambrian petroleum source rocks and the coalification path of alginite. *Organic Geochemistry*, 18, 881-897.

HOLMAN, A. I., GRICE, K., JARAULA, C. M. & SCHIMMELMANN, A. 2014. Bitumen II from the Paleoproterozoic Here's Your Chance Pb/Zn/Ag deposit: Implications for the analysis of depositional environment and thermal maturity of hydrothermally-altered sediments. *Geochimica et Cosmochimica Acta*, 139, 98-109.

HUNT, J.M. 1996. *Petroleum Geochemistry and Geology*. Second Edition. W.H. Freeman and Company, New York, 743p.

KENDALL, B., CREASER, R. A., GORDON, G. W. & ANBAR, A. D. 2009a. Re-Os and Mo isotope systematics of black shales from the Middle Proterozoic Velkerri and Wollogorang Formations, McArthur Basin, northern Australia. *Geochimica et Cosmochimica Acta*, 73, 2534-2558.

KENDALL, B., CREASER, R. A. & SELBY, D. 2009b. <sup>187</sup>Re-<sup>187</sup>Os geochronology of Precambrian organic-rich sedimentary rocks. Geological Society, London, Special Publications, 326, 85-107.

KLEMME, H. & ULMISHEK, G. F. 1991. Effective petroleum source rocks of the world: stratigraphic distribution and controlling depositional factors (1). AAPG Bulletin, 75, 1809-1851.

KRALIK, M. 1982. Rb-Sb age determinations on Precambrian carbonate rocks of the Carpentarian McArthur basin, Northern Territories, Australia. Precambrian Research, 18, 157-170.

LANDIS, C.R. & Castaño, J.R. 1995. Maturation and bulk chemical properties of a suite of solid hydrocarbons. Organic Geochemistry, 22, 137-149.

LARGE, R. R., BULL, S. W., MCGOLDRICK, P. J. & WALTERS, S. 2005. Stratiform and strata-bound Zn-Pb-Ag deposits in Proterozoic sedimentary basins, northern Australia. Economic Geology, 100, 931-963.

LINDSAY, J. 2001. Basin dynamics and mineralisation, McArthur Basin, northern Australia. Australian Journal of Earth Sciences, 48, 703-720.

LUDWIG, K. 2003. User's manual for Isoplot 3.00: a geochronological toolkit for Microsoft Excel. Berkeley Geochronology Center. Special publication, 4, 1-71.

MEYERHOFF, A. A. 1980. Geology and petroleum fields in Proterozoic and Lower Cambrian strata, Lena-Tunguska petroleum province, eastern Siberia, USSR. AAPG Special Volumes: Giant Oil

and Gas Fields of the Decade 1968-1978, 225-252.

MUKHERJEE, I. & LARGE, R. 2017. Application of pyrite trace element chemistry to exploration for SEDEX style Zn-Pb deposits: McArthur Basin, Northern Territory, Australia. *Ore Geology Reviews*, 81, 1249-1270.

MUNSON, T. 2014. Petroleum geology and potential of the onshore Northern Territory, 2014, Northern Territory Geological Survey.

OXBURGH, R. 2001. Residence time of osmium in the oceans. *Geochemistry, Geophysics, Geosystems*, 2.

PAGE, R., JACKSON, M. & KRASSAY, A. 2000. Constraining sequence stratigraphy in north Australian basins: SHRIMP U-Pb zircon geochronology between Mt Isa and McArthur River. *Australian Journal of Earth Sciences*, 47, 431-459.

PAGE, R. & SWEET, I. 1998. Geochronology of basin phases in the western Mt Isa Inlier, and correlation with the McArthur Basin. *Australian Journal of Earth Sciences*, 45, 219-232.

PEUCKER - EHRENBRINK, B. & RAVIZZA, G. 2000. The marine osmium isotope record. *Terra Nova*, 12, 205-219.

RASMUSSEN, B. 2005. Evidence for pervasive petroleum generation and migration in 3.2 and 2.63 Ga shales. *Geology*, 33, 497-500.

RAWLINGS, D. 1999. Stratigraphic resolution of a multiphase intracratonic basin system: the McArthur Basin, northern Australia. *Australian Journal of Earth Sciences*, 46, 703-723.

RODRIGUES, S., BLUETT, J., FERGUSON, B. R., GOLDING, S. D. & TITUS, L. 2015. Maturation profile at the Glyde Gas Discovery in the Southern McArthur Basin, Australia. *Search and Discovery Article #10799*, AAPG Datapages.

RUDNICK, R. L. & GAO, S. 2003. Composition of the continental crust. *Treatise on geochemistry*, 3, 1-64p.

SELBY, D. & CREASER, R. A. 2003. Re–Os geochronology of organic rich sediments: an evaluation of organic matter analysis methods. *Chemical Geology*, 200, 225-240.

SELBY, D. & CREASER, R. A. 2005. Direct Radiometric Dating of Hydrocarbon Deposits Using Rhenium-Osmium Isotopes. *Science*, 308, 1293-1295.

SELBY, D., CREASER, R. A., STEIN, H. J., MARKEY, R. J. & HANNAH, J. L. 2007. Assessment of the  $^{187}\text{Re}$  decay constant by cross calibration of Re–Os molybdenite and U–Pb zircon chronometers in magmatic ore systems. *Geochimica et Cosmochimica Acta*, 71, 1999-2013.

SMOLIAR, M. I., WALKER, R. J. & MORGAN, J. W. 1996. Re-Os ages of group IIA, IIIA, IVA, and IVB iron meteorites. *Science*, 271,

1099.

SUMMONS, R. E., POWELL, T. G. & BOREHAM, C. J. 1988. Petroleum geology and geochemistry of the Middle Proterozoic McArthur Basin, Northern Australia: III. Composition of extractable hydrocarbons. *Geochimica et Cosmochimica Acta*, 52, 1747-1763.

SYMONS, D. 2007. Paleomagnetism of the HYC Zn-Pb SEDEX Deposit, Australia: evidence of an epigenetic origin. *Economic Geology*, 102, 1295-1310.

TAYLOR, G.H., TEICHMULLER, M., DAVIS, A., DIESSEL, C.F.K., LITTKE, R. & ROBERT, P. 1998. *Organic Petrology*. Gebrüder Borntraeger, Berlin. 704p.

TISSOT, B.P. & WELTE, D.H. 1984. *Petroleum formation and occurrence*. Second edition. Springer-Verlag, Heidelberg. 699p.

VOLK, H., DUTKIEWICZ, A., GEORGE, S. & RIDLEY, J. 2003. Oil migration in the Middle Proterozoic Roper Superbasin, Australia: evidence from oil inclusions and their geochemistries. *Journal of Geochemical Exploration*, 78, 437-441.

WILLIFORD, K. H., GRICE, K., LOGAN, G. A., CHEN, J. & HUSTON, D. 2011. The molecular and isotopic effects of hydrothermal alteration of organic matter in the Paleoproterozoic McArthur River Pb/Zn/Ag ore deposit. *Earth and Planetary Science Letters*, 301, 382-392.

ZOU, C., YANG, Z., DAI, J., DONG, D., ZHANG, B., WANG, Y.,  
DENG, S., HUANG, J., LIU, K., YANG, C., WEI, G. & PAN, S.  
2015. The characteristics and significance of conventional and  
unconventional Sinian–Silurian gas systems in the Sichuan Basin,  
central China. *Marine and Petroleum Geology*, 64, 386-402.

## **Chapter 3**

# **Direct Rubidium-Strontium Dating of Hydrocarbon Charge Using Small Authigenic Illitic Clay Aliquots from the Silurian Bituminous Sandstone in the Tarim Basin, NW China**

**Shaojie Li, Xuan-Ce Wang, Chao-Feng Li, Simon A. Wilde, Youyu Zhang, Suzanne D. Golding, Keyu Liu, Yuxiang Zhang**

*Scientific Reports, Under review*

## Abstract

Illitic clay is ubiquitous in clastic hydrocarbon reservoirs, and the host for several radiometric isotopes such as the potassium-argon (K-Ar) and rubidium-strontium (Rb-Sr) systems. This study applied the isotope-dilution thermal ionization mass spectrometry technique for small sample aliquots (3 – 4 mg) to conduct illite Rb-Sr isotope dating of five illitic clay samples from the Silurian bituminous sandstone (SBS) intersected by five drillholes in the Tarim Basin, NW China. The  $^{87}\text{Rb}/^{86}\text{Sr}$  ratio of clays is fractionated mainly by the addition of Rb during the illitization of mixed-layer illite/smectite (I/S), which is the dominant clay species in the Tarim Basin samples. The subsample-scale Rb/Sr isotope values suggest that each subsample may contain I/S particles of slightly variable degrees of illitization. Three of the analyzed samples (H6, KQ1 and TZ67) generated Rb-Sr isochron ages of  $141 \pm 61$  Ma,  $332 \pm 32$  Ma and  $235 \pm 8$  Ma (errors quoted at  $2\sigma$ ), respectively. These results are similar to the corresponding K-Ar ages (125 Ma, 389 Ma and 234 Ma). The isotopic ages are consistent with the timing of hydrocarbon charge which varies in different drillholes as constrained by basin modelling, indicating that a closed-system behavior is attained by the hydrocarbon charge that inhibits the illitization of I/S. The Rb-Sr isotope analyses of the other two samples (YM35-1 and Q1) that did not yield isochron ages suggest the conditions for producing isochrons were not satisfied, which may be caused by disturbance of the isotope system by post-charge hydrothermal event. The

outcomes of this study show the robust potential of Rb-Sr clay subsample geochronology for cross-checking isotopic ages yielded by other systems (e.g. K-Ar system) and constraining the timing of hydrocarbon charge.

**Key words:** Rb-Sr subsample geochronology; illite; isotope-dilution thermal ionization mass spectrometry; hydrocarbon charge; Silurian bituminous sandstone; Tarim Basin.

### 3.1 Introduction

In a hydrocarbon system, knowledge of the timing of the hydrocarbon charge is crucial for understanding its evolution. Emplacement of hydrocarbon in a porous reservoir alters its chemical condition and affects mineral diagenesis (Busch et al., 2018; Ehrenberg and Nadeau, 1989; Hamilton et al., 1989; Pollastro, 1993; Zhang et al., 2011). Authigenic illitic clay commonly occurs in hydrocarbon reservoirs and its diagenesis is sensitive to fluid flow (Busch et al., 2018; Zhang et al., 2011). Several long-lived radiometric isotope systems, including potassium-argon (K-Ar) and rubidium-strontium (Rb-Sr), are hosted in illitic clay, and these isotope systems can document the timing of clay diagenesis and constrain fluid flow history (Clauer et al., 2014; Gorokhov et al., 2001; Hamilton et al., 1989; Morton, 1985a; Uysal et al., 2001; Zwingmann et al., 1999).

Potassium-Ar clay geochronology has been proven a useful tool for investigating fluid flow in depositional basins (Hamilton et al., 1989; Zhang et al., 2011; Zwingmann et al., 1999). The K-Ar method is based on the  $\beta^+$  decay of  $^{40}\text{K}$  to  $^{40}\text{Ar}$  (Wasserburg et al., 1956), and an isotopic age is acquired through separate measurements of K and Ar on two aliquots of a single sample (Clauer, 2013). The  $^{40}\text{Ar}$ - $^{39}\text{Ar}$  method is a variant for the K-Ar method, with an additional irradiation pre-treatment of samples, where  $^{39}\text{K}$  is transformed into  $^{39}\text{Ar}$  by fast neutrons (Clauer, 2013). Although the  $^{40}\text{Ar}$ - $^{39}\text{Ar}$  method

has recognized practical analytical improvement compared to the K-Ar method, e.g. simultaneous analysis of radioactive and radiogenic atoms on the same aliquot, which prevents uncertainties induced by sample heterogeneity (Clauer, 2013), the  $^{39}\text{Ar}$  recoil associated with the irradiation procedure may result in spurious age data for micrometer-size clay minerals (Clauer et al., 2011; Yun et al., 2010; Zhang et al., 2016).

The Rb-Sr isotope system is another applicable geochronometer for illitic clays. The isochron age is yielded through the regression of Rb-Sr isotope data obtained generally by either bulk analysis or the acid-leaching technique (Bofinger et al., 1968; Middleton et al., 2014; Morton, 1985b; Zwingmann et al., 1999). The age yielded by bulk analysis represents an average estimate of a suite of cogenetic samples, instead of a single sample, thus may be unfavorable for precious samples (e.g. petroleum drillcore). Rb-Sr analysis of different acid leaching fractions of a sample may yield an isochron age for the single sample because Sr is more leachable than Rb, thus generating Rb/Sr fractionation between leachate and residue (Clauer et al., 1993; Mutlu et al., 2010; Zwingmann et al., 1999). However, ions at leachable sites may be susceptible to geo-fluid flows and Sr isotopic heterogeneity may occur between different leaching fractions, resulting in spurious ages (Gorokhov et al., 2001).

Owing to the development of the low-blank Rb/Sr chemistry procedure and high-sensitivity isotope-dilution thermal ionization mass spectrometry (ID-TIMS) (Li et al., 2015a, b), it becomes

achievable to determine the Rb-Sr isotopic composition for illitic clays in small quantities (3 – 4 mg). Therefore, an isochron may be established for a single clay sample through Rb-Sr analysis of multiple extractions from the same sample (i.e. “subsamples”) without additional experimental leaching steps. The aim of this study is to illustrate the feasibility of this dating method through cross-checking against K-Ar ages for the samples initially analyzed by Zhang et al. (2016).

Silurian bituminous sandstone (SBS) is a significant hydrocarbon reservoir in the Tarim Basin, northwest (NW) China. In recent years, a series of K-Ar clay geochronology studies of this target have been reported, showing that clay diagenesis in the SBS is related to the hydrocarbon charge (Zhang et al., 2011, 2016; Zhu et al., 2012a, b, 2013a, b). In this paper, subsample Rb-Sr data for five SBS clay samples are presented. These samples have been characterized in terms of mineralogy and K-Ar geochronology by Zhang et al., (2016).

## **3.2 Geological background**

The Tarim Basin is a large petroliferous basin in NW China (Figure 3.1A), covering an area of  $\sim 5.6 \times 10^5$  km<sup>2</sup> (Hanson et al., 2000; Hu et al., 2016; Huang et al., 2016; Jia and Wei, 2002; Kang and Kang, 1996). The basin is divided into eleven units, including six depressions (Manjiaer, Kuqa, Awati, Tangguzibasi, Southwestern and Southeastern depressions) and five uplifts (Tadong, Tabei,

Tazhong, Bachu and Tanan uplifts) (Figure 3.1B; Hu et al., 2016; Li et al., 2015c). Multiple Phanerozoic tectonic events, related to global episodes, including Caledonian (Ordovician–Devonian), Hercynian (Carboniferous–Permian), Indosinian (Triassic), Yanshanian (Jurassic–Cretaceous) and Himalayan movements (Paleogene–Quaternary), have affected the basin (Figure 3.2; Jia and Wei, 2002; Kang and Kang, 1996), that is filled with Paleozoic–Cenozoic sediments (Figure 3.2; Hu et al., 2016; Jia and Wei, 2002). Cambrian–Ordovician carbonate rocks and Silurian–Devonian clastic rocks were deposited in a marine environment (Figure 3.2; Guo et al., 2016; Hanson et al., 2000; Jia and Wei, 2002; Luo et al., 2015; Xiao et al., 2016). A Carboniferous–Permian transitional basin was formed subsequently, after which continental clastic sediments were deposited during the Mesozoic to Cenozoic (Figure 3.2; Guo et al., 2016; Hu et al., 2016; Jia and Wei, 2002).

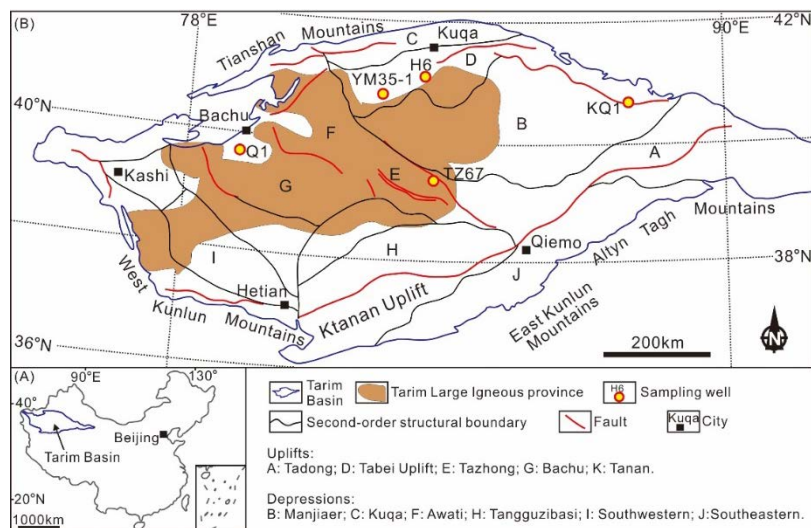


**Figure 3.1:** A: Location of the Tarim Basin in China. B: Map showing the

locations of sampling drillholes. Maps are modified after Li et al. (2015c) and Xu et al. (2014).

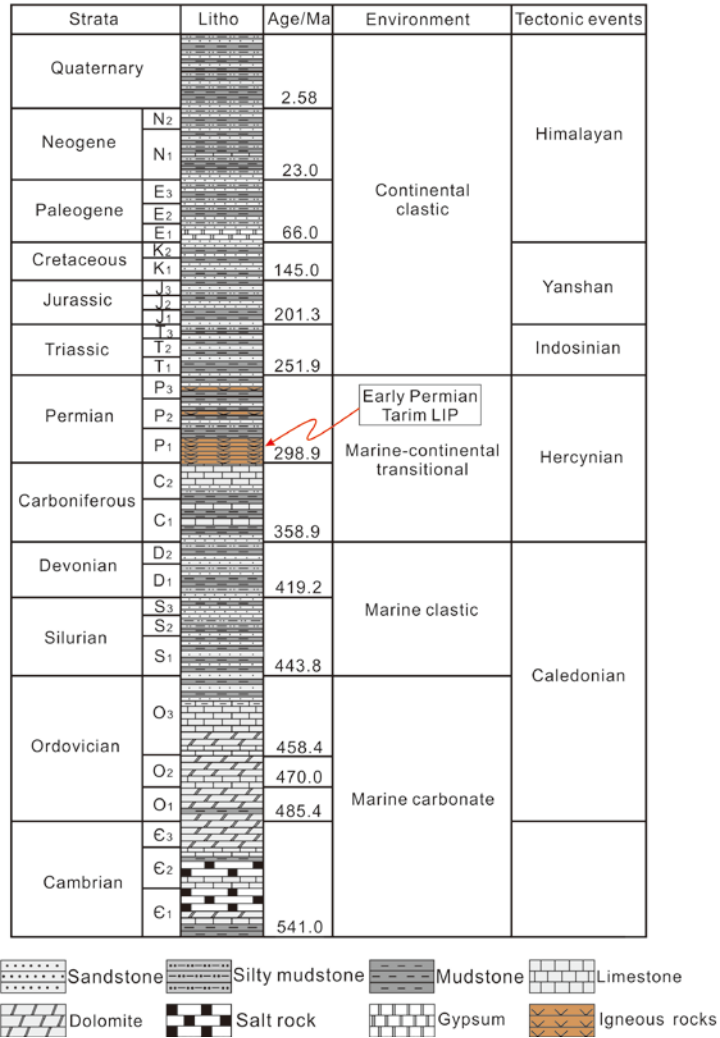


**Figure 3.2:** Phanerozoic lithostratigraphic column of the Tarim Basin. Modified after Jia and Wei (2002) and Kang and Kang (1996).

Lower Silurian sandstone is a significant hydrocarbon reservoir in the Tarim Basin and accommodates abundant solid bitumen, and thus the reservoir is also named the Silurian bituminous sandstone

(SBS; Tian et al., 2008; Zhang et al., 2011). Hydrocarbons in the SBS have marine molecular and stable isotopic compositions and show genetic affinity to the underlying Cambrian-Ordovician source rocks (Tian et al., 2008). The SBS is mainly distributed in the area surrounding the Manjiaer and Awati depressions (Tian et al., 2008). Illite K-Ar geochronology shows that the timing of hydrocarbon charge in the SBS varies locally, owing to variation in the timing of hydrocarbon generation (Zhang et al., 2011, 2016).

### **3.3 Sample information and analytical method**

The samples used in this study were 0.3 – 0.15  $\mu\text{m}$  fractions of five clay samples utilized in the study by Zhang et al. (2016). The five illitic clay samples were separated from sandstone drillcores YM35-1, H6, KQ1, Q1 and TZ67 (Figure 3.1B), using the method described in Zhang et al. (2016). Grain size fractions (<0.15, 0.15 – 0.3, 0.3 – 0.5 and 0.5 – 1.0  $\mu\text{m}$ ) were separated in distilled water using a progressive high-speed ultra-centrifuge (Zhang et al., 2016). The 0.3 – 0.15  $\mu\text{m}$  fraction was selected for the Rb-Sr isotopic study based on the following considerations: (1) detrital minerals are generally coarser in size, whereas they may be mixed in the 0.5 – 0.3 and 1 – 0.5  $\mu\text{m}$  size fractions (Uysal et al., 2001, 2005; Zhang et al., 2011); (2) the finest fraction (<0.15  $\mu\text{m}$ ) may also contain inherited  $^{87}\text{Sr}$  atoms of detrital origin (Clauer et al., 1997, 1984). Thus, the 0.3 – 0.15  $\mu\text{m}$  size fraction is the most appropriate for this study. Scanning electron microscopic (SEM) and X-ray powder diffraction (XRD)

investigations by Zhang et al. (2016) also confirmed the purity and authigenic origin of this size fraction. Ordered mixed layer illite/smectite (I/S) is the dominant species in all these samples with no detrital K-feldspar or illite identified (Zhang et al., 2016).

YM35-1: this sample was collected from a depth of 5574 m in drillhole YM35-1 (Table 3.1 and Figure 3.3A), which is located in the Tabei uplift, northern Tarim Basin (Figure 3.1B). The present-day thickness of Silurian strata in the drillhole is ~124 meters (Figure 3.3A). The sample contains two clay species: I/S (97%) and chlorite (3%) (Table 3.1). The interstratified ratio (IR) of I/S (i.e. the percentage of smectite layers in I/S, which negatively correlates with the degree of illitization of I/S) is 5% (Table 3.1), and K concentration is 6.07% (Table 3.1). The K-Ar dating of the sample yields an age of 287 Ma (Table 3.1; Zhang et al., 2016).

H6: the sample was taken from a depth of 6311.1m in drillhole H6 (Table 3.1 and Figure 3.3B). The drillhole is located in the Tabei uplift, northern Tarim Basin (Figure 3.1B) and intersects ~383 meters of Silurian strata (Figure 3.3B). The sample contains 92% I/S, 4% illite and 4% kaolinite (Table 3.1). The IR of I/S is 20% (Table 3.1), and the K content is 5.1% (Table 3.1). An isotopic age of 125 Ma was obtained from this sample by the K-Ar method (Table 3.1; Zhang et al., 2016).

KQ1: the sample was taken from a depth of 2799.7m in drillhole KQ1 (Table 3.1 and Figure 3.3C) which is located at the eastern

margin of the Manjiaer depression, eastern Tarim Basin (Figure 3.1B). The drillhole reveals ~822 meters of Silurian strata (Figure 3.3C). The sample contains 66% I/S, 11% illite and 23% chlorite (Table 3.1), and the IR of I/S is 25% (Table 3.1). This sample has 4.95% K (Table 3.1), and the K-Ar age is 390 Ma (Table 3.1; Zhang et al., 2016).

Q1: the sample was taken from a depth of 1719.1 m in drillhole Q1 (Table 3.1 and Figure 3.3D), which is situated in the Bach uplift, western Tarim Basin (Figure 3.1B) and intersects ~421 meters of Silurian strata (Figure 3.3D). The sample contains 73% I/S and 27% chlorite (Table 3.1), and the IR of I/S is 5% (Table 3.1). The K content is 5.89% (Table 3.1), and the K-Ar dating of the sample yields an age of 386 Ma (Table 3.1; Zhang et al., 2016).

TZ67: the sample was collected from a depth of 4642.78 m in drillhole TZ67 (Table 3.1 and Figure 3.3E). The drillhole is located in the Tazhong uplift, central Tarim Basin (Figure 3.1B), and intersects ~181 meters of Silurian strata (Figure 3.3E). The sample only contains I/S particles with IR of 30% (Table 3.1). The K content is 4.42% (Table 3.1), and the K-Ar age for this sample is 234 Ma (Table 3.1; Zhang et al., 2016).

**Table 3.1:** Basic information concerning illitic samples in this study of the Tarim Basin

Drillhole	Depth/m	Era	Clay fraction size ( $\mu\text{m}$ )	Clay mineral content (%)				<sup>f</sup> IR /%	<sup>g</sup> K /%	K-Ar age/Ma
				<sup>b</sup> I/S	<sup>c</sup> I	<sup>d</sup> K	<sup>e</sup> C			
YM35-1	5574	<sup>a</sup> S <sub>1</sub>	0.3-0.15	97	0	0	3	5	6.07	287
H6	6311.1	S <sub>1</sub>	0.3-0.15	92	4	4	0	20	5.1	125
KQ1	2799.7	S <sub>1</sub>	0.3-0.15	66	11	0	23	25	4.95	389
Q1	1719.1	S <sub>1</sub>	0.3-0.15	73	0	0	27	5	5.89	386
TZ67	4642.78	S <sub>1</sub>	0.3-0.15	100	0	0	0	30	4.42	234

<sup>a</sup>S denotes Silurian.

<sup>b</sup>I/S denotes mixed layer illite/smectite.

<sup>c</sup>I denotes illite.

<sup>d</sup>K denotes kaolinite.

<sup>e</sup>C denotes chlorite.

<sup>f</sup>IR (%) denotes interstratified ratio, i.e. the percentage of smectite layers in mixed layer illite/smectite.

<sup>g</sup>K (%) denotes K content in the samples.

\*Clay mineral content, IR values, K content and K-Ar age data for the samples in this study were analysed and reported by Zhang et al., 2016.

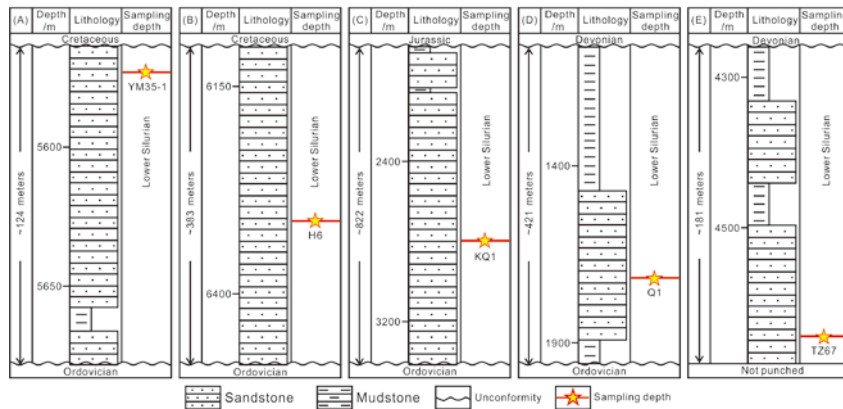


**Figure 3.3:** Strata histograms showing the sampling depth in each drillhole. A: YM35-1; B: H6; C: KQ1; D: Q1; and E: TZ67.

The Rb-Sr chemistry and mass spectrometry analyses were completed at the State Key Laboratory of Lithospheric Evolution, Institute of Geology and Geophysics, Chinese Academy of Sciences (IGGCAS), Beijing. Five portions of each sample were randomly picked and each subsample was weighed so that 3 – 4 mg was obtained using an AG104 Mettler Toledo analytical balance. They were then dissolved with  $^{87}\text{Rb}$ - $^{84}\text{Sr}$  isotopic tracers in 0.1 mL HF (22N) and 0.03 mL  $\text{HNO}_3$  (14N) in screw-top PFA Savillex vials. The Rb and Sr fractions were separated and purified via a mini-column containing  $\sim 30$   $\mu\text{L}$  of Sr Spec resin (Li et al., 2015a). Isotope ratios for Rb and Sr were determined using a multi-collector Triton plus TIMS instrument (Li et al., 2015a, b).  $^{87}\text{Sr}/^{86}\text{Sr}$  ratios were normalized to  $^{88}\text{Sr}/^{86}\text{Sr} = 8.375209$  using the exponential law. Duplicate analyses of Sr standard NBS987 during this study yielded a mean  $^{87}\text{Sr}/^{86}\text{Sr}$  value of  $0.710244 \pm 0.000012$  ( $2\sigma$ ,  $n=4$ ) in good agreement with the reported value of  $0.710251 \pm 0.000016$  (Li et al., 2015a). Analytical uncertainties for  $^{87}\text{Rb}/^{86}\text{Sr}$  ratios were less than 1%. The blank during the analytical session was lower than 3 pg for Rb and 6 pg for Sr. The Rb-Sr isochron ages for samples were calculated using the ISOPLOT3.0 software (Ludwig, 2003), applying a decay constant ( $\lambda^{87}\text{Rb}$ ) of  $1.396 \times 10^{-11} \text{ yr}^{-1}$  (Rotenberg et al., 2012). Acids used during the Rb-Sr chemistry were all analytical reagent (AR) grade and were purified utilizing a Savillex<sup>TM</sup> DST-1000 sub-boiling distillation system. Ultrapure water with resistivity of  $18.2 \text{ M}\Omega\text{cm}^{-1}$  obtained from a Milli-Q Element system was used throughout this work.

### 3.4 Results

The results of Rb-Sr isotope dating of the five illite samples are presented in Table 3.2. The details for each sample are as follows:

YM35-1: the five subsamples have Rb and Sr contents of 249.7–457.6 ppm and 54.01–96.04 ppm, respectively (Table 3.2) and defined a positive linear trend between Rb and Sr contents (Figure 3.4A). The average contents of Rb and Sr are 389.0 and 81.57 ppm, respectively (Table 3.2). The  $^{87}\text{Rb}/^{86}\text{Sr}$  and  $^{87}\text{Sr}/^{86}\text{Sr}$  ratios are 13.35–13.86 and 0.760815–0.762334, respectively (Table 3.2), with an average  $^{87}\text{Rb}/^{86}\text{Sr}$  of 13.54 (Table 3.2). Subsample A-3 has  $^{87}\text{Sr}/^{86}\text{Sr}$  higher than the other subsamples (Table 3.2), and is not included in the calculations. The regression of the remaining four subsamples yields an isochron age of  $111 \pm 36$  Ma ( $2\sigma$ , Figure 3.5A). There is no obvious relation between  $^{87}\text{Sr}/^{86}\text{Sr}$  and  $1/\text{Sr}$  (Figure 3.6A).

H6: the Rb contents range from 173.7 to 201.2 ppm and positively correlate with Sr contents (69.94–79.50 ppm, Table 3.2 and Figure 3.4B). The average contents of Rb and Sr are 184.7 and 73.93 ppm, respectively (Table 3.2). The  $^{87}\text{Rb}/^{86}\text{Sr}$  and  $^{87}\text{Sr}/^{86}\text{Sr}$  ratios are 7.169–7.342 and 0.728541–0.728876, respectively (Table 3.2), with an average  $^{87}\text{Rb}/^{86}\text{Sr}$  value of 7.244 (Table 3.2). Regression of the isotope data yields an isochron age of  $148 \pm 68$  Ma ( $2\sigma$ , Figure 3.5B). One subsample (B-4) slightly deviates from the isochron, and the regression without this point yields an identical age within uncertainty ( $141 \pm 61$  Ma,  $2\sigma$ ; Figure 3.5B). Initial  $^{87}\text{Sr}/^{86}\text{Sr}$  ( $\text{Sr}_i$ )

values of the two regressions also overlap within uncertainty ( $0.7137 \pm 0.0069$  and  $0.7145 \pm 0.0062$ , respectively; Figure 3.5B). There is no relation between  $^{87}\text{Sr}/^{86}\text{Sr}$  and  $1/\text{Sr}$ , indicating that the isochrons are not mixing lines (Figure 3.6B).

KQ1: contains 159.2–265.4 ppm Rb and 96.27–155.0 ppm Sr, with Rb and Sr average contents of 223.0 and 138.5 ppm, respectively (Table 3.2). The Rb contents positively correlate with Sr contents (Figure 3.4C). The  $^{87}\text{Rb}/^{86}\text{Sr}$  and  $^{87}\text{Sr}/^{86}\text{Sr}$  ratios are 4.449–4.971 and 0.733376–0.735775, respectively (Table 3.2), and the average  $^{87}\text{Rb}/^{86}\text{Sr}$  ratio is 4.680 (Table 3.2). Regression of Rb-Sr data for the five subsamples yields an isochron age of  $351 \pm 97$  Ma and  $\text{Sr}_i$  of  $0.7116 \pm 0.0064$  ( $2\sigma$ , Figure 3.5C). One point slightly deviates from the main trend (C-5; Figure 3.5C), and the regression without this point yields a similar isochron age of  $332 \pm 32$  Ma and  $\text{Sr}_i$  of  $0.7127 \pm 0.0021$  ( $2\sigma$ , Figure 3.5C). There is no relation between  $^{87}\text{Sr}/^{86}\text{Sr}$  and  $1/\text{Sr}$ , indicating that the isochrons are not mixing lines (Figure 3.6C).

Q1: contains 173.7–227.7 ppm Rb and 44.26–58.53 ppm Sr, with average Rb and Sr contents of 203.2 and 51.90 ppm, respectively (Table 3.2). The Rb contents positively correlate with Sr contents (Figure 3.4D). The  $^{87}\text{Rb}/^{86}\text{Sr}$  and  $^{87}\text{Sr}/^{86}\text{Sr}$  ratios are 10.71–12.15 and 0.769862–0.779446, respectively (Table 3.2), and the average for  $^{87}\text{Rb}/^{86}\text{Sr}$  is 11.43 (Table 3.2). Regression of all Rb-Sr data yields an age of  $484 \pm 51$  Ma and a  $\text{Sr}_i$  of  $0.6972 \pm 0.0082$  ( $2\sigma$ , Figure 3.5D). A linear trend with a steeper slope is defined by the Rb-Sr isotope

data of three subsamples (D-1, D-4 and D-5; Figure 3.5D). The linear relation between  $1/\text{Sr}$  and  $^{87}\text{Sr}/^{86}\text{Sr}$  for the three subsamples suggests that this three-point “isochron” is a mixing line (Figure 3.6D).

TZ67: the Rb contents range from 93.24 and 120.2 ppm, and Sr contents vary from 59.98 and 81.84 ppm (Table 3.2). The average values for Rb and Sr are 105.4 and 72.16 ppm, respectively (Table 3.2). The  $^{87}\text{Rb}/^{86}\text{Sr}$  and  $^{87}\text{Sr}/^{86}\text{Sr}$  ratios are 3.559–4.629 and 0.721805–0.725351, respectively (Table 3.2), and the average  $^{87}\text{Rb}/^{86}\text{Sr}$  ratio is 4.267 (Table 3.2). Regression of Rb-Sr data yields a precise isochron age of  $235 \pm 8$  Ma ( $2\sigma$ ) with the  $\text{Sr}_i$  of  $0.71011 \pm 0.00048$  (Figure 3.5E). There is no relation between  $^{87}\text{Sr}/^{86}\text{Sr}$  and  $1/\text{Sr}$ , indicating that the isochron is not a mixing line (Figure 3.6E).

**Table 3.2:** Rubidium-Strontium isotope data for illitic clays in this study of the Tarim Basin

ID	No	Rb /ppm	Sr /ppm	<sup>87</sup> Rb / <sup>86</sup> Sr	<sup>87</sup> Sr / <sup>86</sup> Sr	Error (2σ)	Average value		
							Rb /ppm	Sr /ppm	<sup>87</sup> Rb / <sup>86</sup> Sr
Y M 35 -1	A-1	371.6	80.97	13.35	0.760815	0.000009			
	A-2	457.6	96.04	13.86	0.761497	0.000012			
	A-3	249.7	54.01	13.45	0.762334	0.000014	380.0	81.57	13.54
	A-4	422.1	91.06	13.49	0.760862	0.000012			
	A-5	399.1	85.76	13.54	0.761158	0.000013			
H6	B-1	201.2	79.50	7.342	0.728876	0.000012			
	B-2	176.7	70.42	7.280	0.728789	0.000011			
	B-3	191.3	77.41	7.169	0.728541	0.000012	184.7	73.93	7.244
	B-4	180.3	72.41	7.222	0.728740	0.000014			
	B-5	173.7	69.94	7.205	0.728636	0.000010			
K Q1	C-1	265.4	155.0	4.971	0.735775	0.000012			
	C-2	231.9	142.9	4.709	0.734660	0.000013			
	C-3	223.3	145.6	4.449	0.733376	0.000014	223.0	138.5	4.680
	C-4	235.2	152.6	4.473	0.733485	0.000014			
	C-5	159.2	96.27	4.800	0.735392	0.000012			
Q1	D-1	227.7	58.18	11.40	0.774273	0.000014			
	D-2	215.3	58.53	10.71	0.769862	0.000013			
	D-3	215.9	51.81	12.15	0.779446	0.000010	203.2	51.90	11.43
	D-4	183.2	46.73	11.42	0.774809	0.000013			
	D-5	173.7	44.26	11.45	0.775439	0.000014			
TZ 67	E-1	120.2	78.10	4.462	0.724730	0.000012			
	E-2	100.5	81.84	3.559	0.721805	0.000013			
	E-3	103.7	64.98	4.629	0.725351	0.000010	105.4	72.16	4.267
	E-4	93.24	59.98	4.507	0.724920	0.000012			
	E-5	109.4	75.92	4.176	0.723921	0.000013			

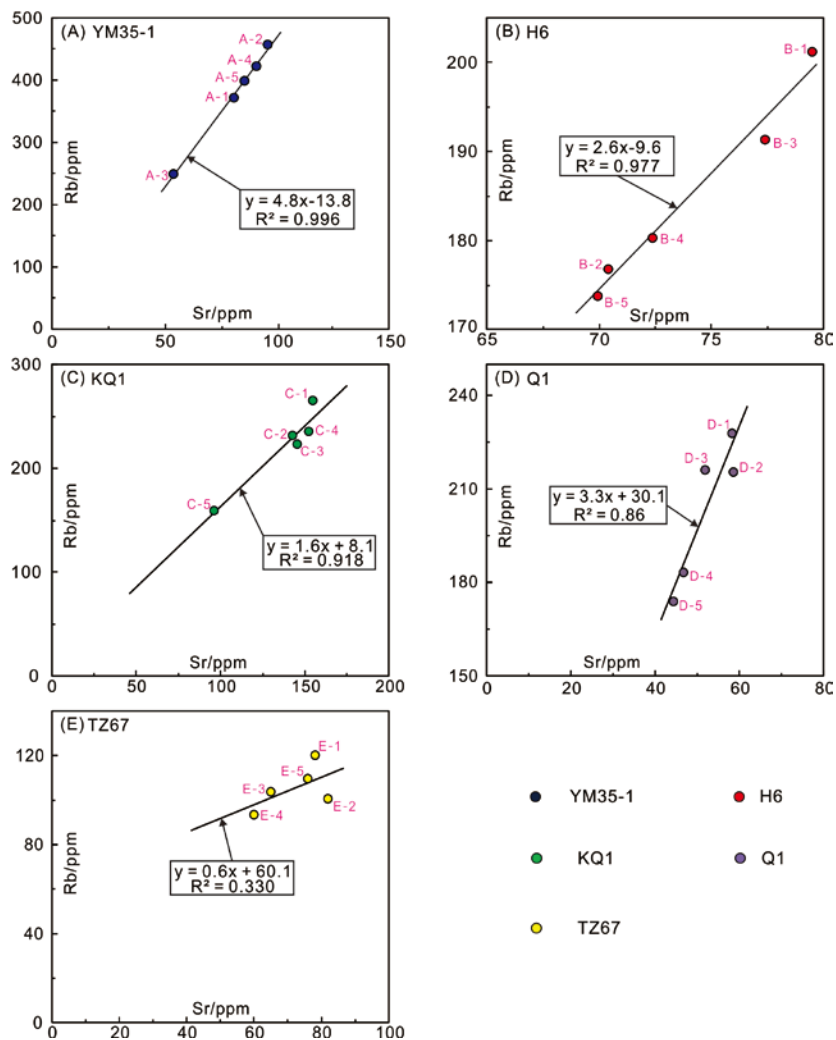


**Figure 3.4:** Scatter plots of Rb vs Sr contents. A: YM35-1; B: H6; C: KQ1; D: Q1; and E: TZ67.

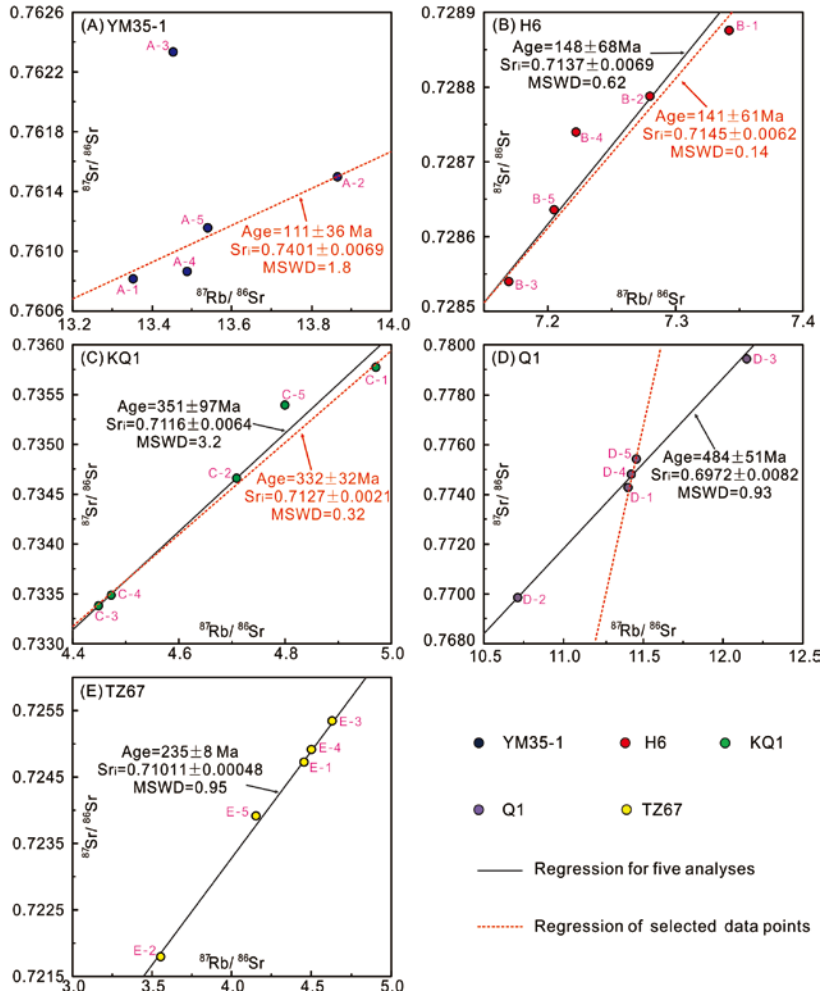


**Figure 3.5:** Scatter plots of  $^{87}\text{Rb}/^{86}\text{Sr}$  vs  $^{87}\text{Sr}/^{86}\text{Sr}$  ratios. The black line in each diagram is the isochron regressed from data of all subsamples. The red dash line is the isochron regressed through selected data. A: YM35-1. The red dashed line is regressed without subsample A-3; B: H6. The red dashed line is regressed without subsample B-4; C: KQ1. The red dashed line is regressed without subsample C-5; D: Q1. The red dashed line is regressed without subsamples D-2 and D-3; E: TZ67.

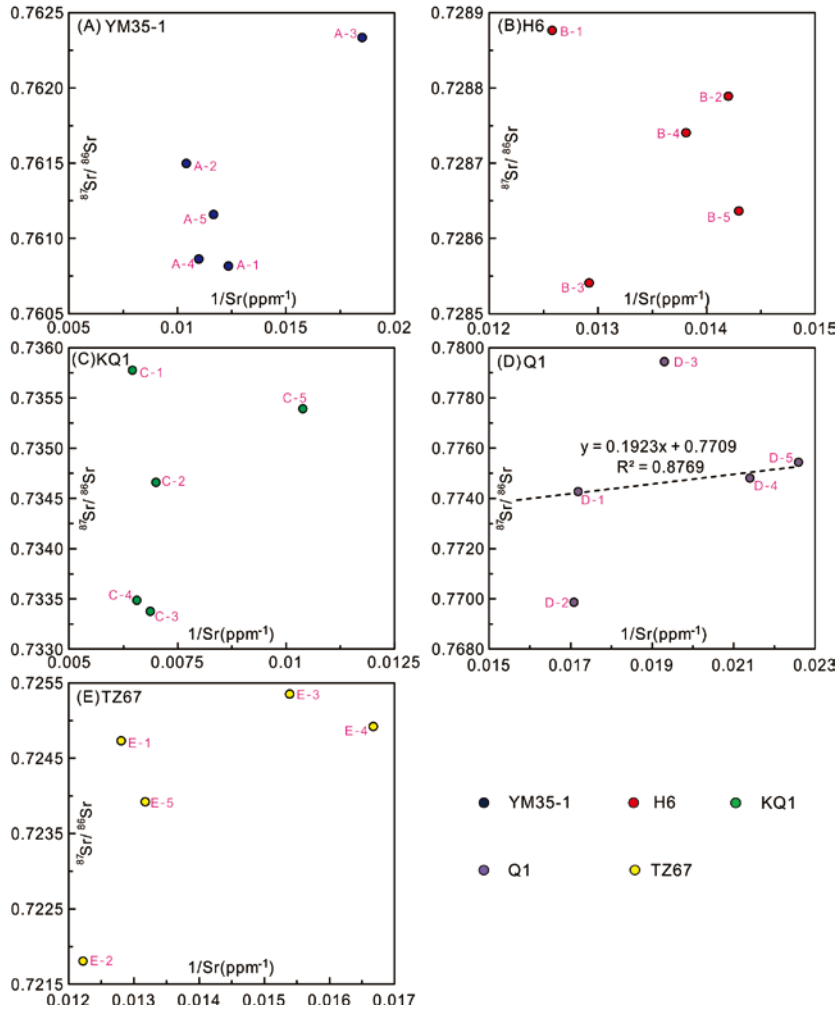


**Figure 3.6:** Scatter plots of  $^{87}\text{Sr}/^{86}\text{Sr}$  vs  $1/\text{Sr}$  ratios. A: YM35-1; B: H6; C: KQ1; D: Q1. The black dashed line is the regression of subsamples D-1, D-4 and D-5; E: TZ67.

## 3.5 Discussion

### 3.5.1 Rb-Sr systematics of SBS illitic clays

To establish a Rb-Sr isochron, three criteria should be met: (1) a

sufficient spread in  $^{87}\text{Rb}/^{86}\text{Sr}$ , (2) homogeneous initial Sr isotopes ( $\text{Sr}_i$ ), and (3) closed-system behavior (Clauer et al., 2014; Gorokhov et al., 2001; Middleton et al., 2014; Uysal et al., 2001).

The mixed layer illite/smectite (I/S) is the dominant clay species in all the analyzed samples, totaling more than 50% of the entire clay composition (Table 3.1). The good negative correlation of  $^{87}\text{Rb}/^{86}\text{Sr}$  with IR of I/S (Figure 3.7A) implies that the  $^{87}\text{Rb}/^{86}\text{Sr}$  ratio of the samples is controlled by the illitization of I/S. Smectite illitization is a ubiquitous process in the depositional environment (Altaner and Ylagan, 1997; Bethke et al., 1986). I/S is composed of smectite and illite layers, and the smectite can be transformed to illite with sufficient K supply (Altaner and Ylagan, 1997; Bethke et al., 1986), as the negative relation between IR values and K contents shows in Figure 3.7B. Because Rb has a geochemical behavior similar to K (Figure 3.7C), Rb is also introduced to I/S during the illitization process (Figure 3.7D). The broad positive correlation between the Sr contents and IR values of I/S indicates that the variation in Sr contents by illitization may be insignificant (Figure 3.7E). Therefore, the Rb/Sr fractionation of clay samples is mainly controlled by the addition of Rb during the illitization of I/S. Subsample-scale Rb/Sr fractionation is also observed and the variation in  $^{87}\text{Rb}/^{86}\text{Sr}$  ratio is generally below 1.5 (Figures 3.5A to 3.5E). Such a small degree of Rb/Sr fractionation may be a response to the microscale chemical variation in the precipitation environment, and each analyzed subsample may contain I/S particles of slightly variable degrees of

illitization.

Illitization has the potential to homogenize the initial Sr isotopic composition of clays and the  $^{87}\text{Rb}/^{86}\text{Sr}$  and  $^{87}\text{Sr}/^{86}\text{Sr}$  values for subsamples generally define a linear relation (Figures 3.5A to 3.5E). Regressions of the data of three samples, H6 (Figure 3.5B), KQ1 (Figure 3.5C) and TZ67 (Figure 3.5E), yield isochron ages similar to the corresponding K-Ar ages and reflect the timing of illitization (Table 3.1). The consistency between Rb-Sr and K-Ar ages suggest that Sr isotopic homogeneity was attained during the illitization. Furthermore, the Rb-Sr age for TZ67 ( $235 \pm 8$  Ma; Figure 3.5E), which contains 100% I/S (Table 3.1), has a better precision than H6 ( $148 \pm 68$  Ma; Figure 3.5B) and KQ1 ( $351 \pm 97$  Ma; Figure 3.5C), and this suggests that Sr isotopic homogenization may be easier attained within I/S particles than among different Sr-bearing phases (Table 3.1).

Closed-system behavior is another critical issue for Rb-Sr geochronology (Clauer et al., 2014). The isotope chronometer documents the time elapsed since the latest closure of the  $^{87}\text{Rb}$ - $^{87}\text{Sr}$  isotope system (Clauer et al., 2014). The acceptable Rb-Sr ages yielded by samples H6, KQ1 and TZ67 suggest that the Rb-Sr system in these samples did not undergo later disturbance. The Rb-Sr isotope system can show an open-system behavior during the illitization (Altaner and Ylagan, 1997), since it depends on the temperature and availability of reactants (Bethke et al., 1986). Thus, processes that change one of the conditions may terminate illitization

and hence maintain a closed-system.

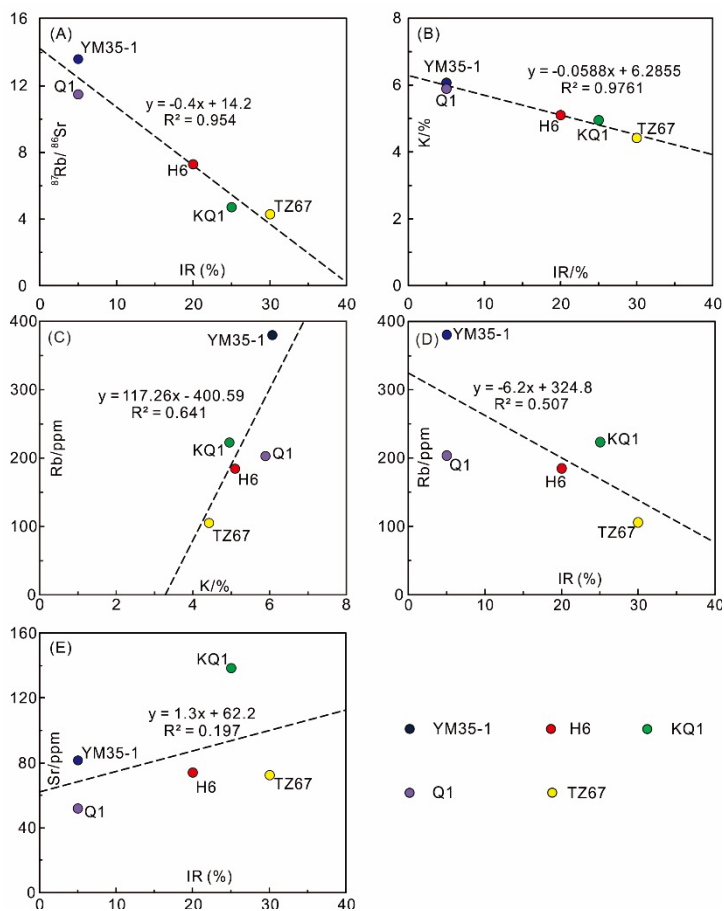


**Figure 3.7:** The average Rb-Sr contents and  $^{87}\text{Rb}/^{86}\text{Sr}$  ratios of each sample are compared with the XRD data. A:  $^{87}\text{Rb}/^{86}\text{Sr}$  vs interstratified ratio (IR) of I/S. IR is the percentage of smectite layers in I/S; B: potassium (K) content vs IR of I/S; C: Rb content vs K content; D: Rb content vs IR of I/S; E: Sr content vs IR of I/S.

### 3.5.2 Geological significance of the Rb-Sr isochron ages

Geological factors such as burial, hydrothermal activity, and hydrocarbon charge can influence illitization and reset the Rb-Sr isotope system in clays (Ehrenberg and Nadeau, 1989; Uysal et al., 2001; Zhang et al., 2011).

Burial-induced temperature increments may increase the degree of illitization of clays, as temperatures increase with depth, facilitating illitization of I/S (Ehrenberg and Nadeau, 1989; Franks and Zwingmann, 2010; Środoń et al., 2009). Burial history analyses show that the maximum temperatures for the Silurian strata in H6, KQ1 and TZ67 were ~138 °C, ~180 °C and ~150 °C, respectively (Figs. 8A-8C; Zhang et al., 2011; Zhu et al., 2012b), and not relevant to the respective IR of I/S (Table 3.1). Therefore, illitization of I/S in these samples may be more dependent on the availability of reactants.

Potassium, the dominant interlayer cation in illite, is a significant reactant for illitization and is more depleted in hydrocarbons compared to formation water in the reservoir. The hydrocarbon charge may, therefore, inhibit the illitization process and reset the Rb-Sr isotope chronometer (Hamilton et al., 1989; Zhang et al., 2011). The Rb-Sr ages for H6, KQ1 and TZ67 are consistent with their K-Ar ages and the timing of hydrocarbon charge is constrained by basin modelling (Figures 3.8A to 3.8C; Zhang et al., 2016). Therefore, the Rb-Sr ages likely represent the timing of hydrocarbon charge in respective regions.

The new Rb-Sr age data therefore support the hypothesis of Zhang et al. (2016) that the timing of hydrocarbon charge in the Silurian reservoir varies locally (Zhang et al., 2016). The hydrocarbon charge occurred earlier in the east of the Manjiaer depression (late Caledonian-Hercynian) compared to the southwest (Indosinian) and northwest of the depression (Yanshanian) (Figure 3.8D). The Manjiaer depression is a major tectonic unit accommodating mature source rocks in the Tarim Basin and hydrocarbons discovered in the SBS around the depression have been demonstrated to be generated by source rocks within the depression (Zhao et al., 2008). Modelling implies that source rocks in the east side of the Majiaer Depression reached the maturity window earlier than in the west side of the depression (Zhao et al., 2008), resulting in the earlier timing of hydrocarbon accumulation in KQ1 than H6 and TZ67 (Figure 3.8D). The earlier timing of hydrocarbon charge in TZ67 than in H6 may be due to the shorter distance between drillhole TZ67 and the source kitchen, which was located near the Tazhong uplift during the late Hercynian (Zhang et al., 2011).

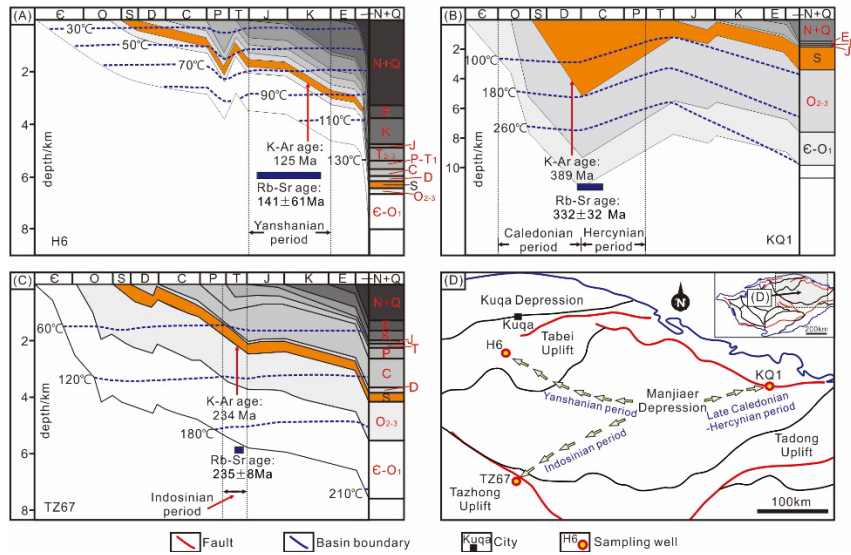


**Figure 3.8:** Based on the Rb-Sr and K-Ar age data and basin modelling results, the timing of hydrocarbon charge in the SBS of is constrained: A: H6, Yanshanian period; B: KQ1, Late Caledonian to Hercynian period and C: TZ67, Indosinian period. D: Generalized map showing the timing of hydrocarbon charge. The burial history diagrams are modified after Zhu et al. (2012b) for H6 and Zhang et al. (2011) for KQ1 and TZ67.

### 3.5.3 Implications for Rb-Sr clay hydrocarbon charge geochronology

This study presents new Rb-Sr isotope data for five SBS illitic clay samples from the Tarim Basin and shows that a sufficient spread in  $^{87}\text{Rb}/^{86}\text{Sr}$  occurs at the subsample scale to allow construction of an isochron. Regressions of Rb-Sr data for samples H6, KQ1, and TZ67 yield three ages:  $148 \pm 68 \text{ Ma}$  ( $2\sigma$ , Figure 3.5B),  $351 \pm 97 \text{ Ma}$  ( $2\sigma$ , Figure 3.5C) and  $235 \pm 8 \text{ Ma}$  ( $2\sigma$ , Figure 3.5E), respectively. These

Rb-Sr isochron ages are consistent with the timing of hydrocarbon charge as determined by K-Ar geochronology (125 Ma, 390 Ma and 234 Ma, respectively; Table 3.1) and basin modelling results (Zhang et al., 2016). Therefore, the dating method used in this study has the potential to broadly constrain the timing of hydrocarbon charge.

The Rb-Sr isotope data of samples YM35-1 and Q1 did not yield acceptable isochron ages (Figures 3.5A and 3.5D). For the mixed-layer illite/smectite, the K and Ar atoms reside in the interlayer space. The closure of K-Ar isotope system is mainly influenced by heat-induced Ar-exchange (Kralik, 1983) and the closure temperature is estimated to be  $260 \pm 30$  °C (Evans, 1996). The burial history of the studied area show that the temperature of Silurian strata is below this temperature (Zhang et al., 2011). Therefore, the K-Ar isotope system is unlikely to be disturbed by the post-dating reset events. For the Rb-Sr isotope system, besides hosted in the interlayer sites, parts of Rb-Sr atoms are absorbed by the external surface of I/S particles (Chaudhuri and Brookins, 1979, Gorokhov et al., 1994). The Rb-Sr atoms hosted by the interlayer sites should be inert to the external influence, whereas those absorbed by the external surface are readily removed by hydrothermal fluids (Kralik, 1983). Therefore, the Rb-Sr isotope system in I/S is more sensitive to hydrothermal fluids.

There was widespread hydrothermal flow in the Tarim Basin during the early Permian, associated with the 300–275 Ma Tarim Large Igneous Province (LIP; e.g. Xu et al., 2014; Zhou et al., 2009). The hydrothermal events extensively influenced the western and Central

Tarim Basin (Figure 3.1B; e.g. Cai et al., 2008; Jin et al., 2006; Li et al., 2011). Sample KQ1 was collected from the eastern Tarim Basin, where the influence of the Tarim LIP is insignificant (Figure 3.1B), whereas samples YM35-1, H6, Q1 and TZ67 were collected from the area affected by the Tarim LIP (Figure 3.1B). The hydrocarbon charge in samples H6 and TZ67 occurred subsequent to the Tarim LIP (Figure 3.9; Zhang et al., 2016), thus, the Rb-Sr isotope system in these samples can record the timing of hydrocarbon charge, which is the latest event in the region. In contrast, the timing of hydrocarbon charge in samples YM35-1 and Q1 is older than the Tarim LIP (Figure 3.9). Therefore, the Rb-Sr isotope chronometer that originally recorded the timing of hydrocarbon charge was most likely disturbed by hydrothermal activity (e.g. hydrothermal leaching of Rb/Sr atoms at easily-exchangeable sites of clays) associated with the LIP. Hydrothermal alteration may result in extensive subsample-scale redistribution of Rb-Sr atoms (e.g. sample YM35-1), or Sr isotopic heterogeneity, which further results in an apparent age for Q1 (484 Ma, an early Ordovician age) that is older than the formation age of the host (early Silurian).

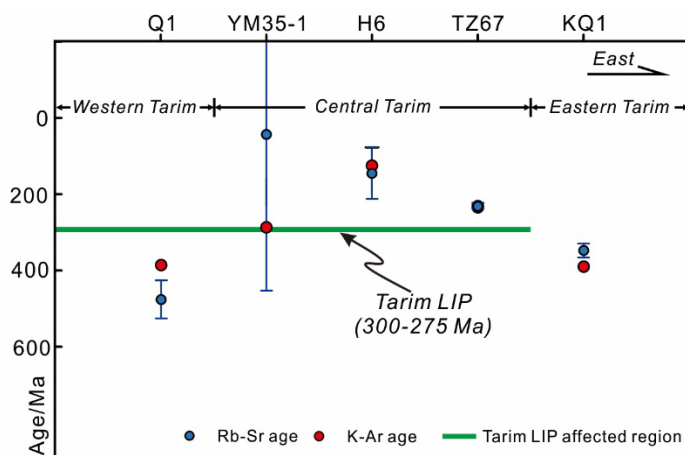


**Figure 3.9:** Schematic diagram showing the temporal and spatial relation between the hydrocarbon charge and early Permian Tarim LIP in the Tarim Basin.

### 3.6 Conclusions

This study involved subsample scale (3 – 4 mg) Rb-Sr isotopic analysis of illitic clays utilizing samples from the Silurian bituminous sandstone (SBS) in the Tarim Basin, NW China. The results show that the Rb-Sr dating method has potential for dating hydrocarbon systems.

(1) The Rb-Sr analyses for samples H6, KQ1 and TZ67 yield isochron ages of  $141 \pm 61$  Ma,  $332 \pm 32$  Ma and  $235 \pm 8$  Ma (errors quoted at  $2\sigma$ ), respectively. These ages are similar to the corresponding K-Ar ages (125 Ma, 389 Ma and 234 Ma, respectively), previously determined on the same samples (Zhang et

al., 2016).

(2) Mixed-layer illite/smectite (I/S) is the dominant clay species (>50%) in all the samples. The illitization of smectite layers in I/S introduces Rb to clays, thus fractionating the  $^{87}\text{Rb}/^{86}\text{Sr}$  ratios. Minor Rb/Sr fractionation is observed at the subsample scale and suggests that each subsample may contain I/S particles of slightly variable degree of illitization. Smectite illitization also has the potential to homogenize the initial Sr isotopic composition of clays as evidenced by the Rb-Sr isochrons yielded in this study. Hydrocarbon charge may cease the illitization process and result in closed-system behavior of the Rb-Sr isotope system in clays. Therefore, the Rb-Sr isochron ages for samples H6, KQ1 and TZ67 are interpreted as recording the timing of hydrocarbon charge: they are consistent with basin modelling results.

(4) Rb-Sr isotope analysis for samples YM35-1 and Q1 did not yield acceptable isochrons for constraining the timing of hydrocarbon charge. This may be caused by post-charge hydrothermal activity associated with the early Permian Tarim LIP. Hydrothermal alteration may result in extensive subsample-scale redistribution of Rb-Sr atoms (e.g. sample YM35-1), or generate Sr isotopic heterogeneity, which results in an apparent age that is older than the formation age of the host (e.g. Q1).

## **Acknowledgments**

This work was supported by the “Hundred Talents Program” of Shanxi Province, China, the Science Foundation of Chang’an University (grant number 310827163412), and Strategic Priority Research Program of the Chinese Academy of Sciences (Grant No. XDA14010401).

## References

ALTANER, S. P. & YLAGAN, R. F. 1997. Comparison of structural models of mixed-layer illite/smectite and reaction mechanisms of smectite illitization. *Clays and Clay Minerals*, 45, 517-533.

BETHKE, C. M., VERGO, N. & ALTANER, S. P. 1986. Pathways of smectite illitization. *Clays and Clay Minerals*, 34, 125-135.

BOFINGER, V., COMPSTON, W. & VERNON, M. 1968. The application of acid leaching to the Rb-Sr dating of a Middle Ordovician shale. *Geochimica et Cosmochimica Acta*, 32, 823-833.

BUSCH, B., HILGERS, C., LANDER, R. H., BONNELL, L. M. & ADELMANN, D. 2018. Reservoir quality and burial model evaluation by kinetic quartz and illite cementation modeling: Case study of Rotliegendes, north Germany. *AAPG Bulletin*, 102, 293-307.

CAI, C., LI, K., LI, H. & ZHANG, B. 2008. Evidence for cross formational hot brine flow from integrated  $^{87}\text{Sr}/^{86}\text{Sr}$ , REE and fluid inclusions of the Ordovician veins in Central Tarim, China. *Applied Geochemistry*, 23, 2226-2235.

CHAUDHURI, S. & BROOKINS D. G. 1979. The Rb-Sr systematics in acid-leached clay minerals. *Chemical Geology* 24, 231-242.

CLAUER, N. 2013. The K-Ar and  $^{40}\text{Ar}/^{39}\text{Ar}$  methods revisited for dating fine-grained K-bearing clay minerals. *Chemical Geology*, 354, 163-185.

CLAUER, N., CHAUDHURI, S., KRALIK, M. & BONNOT-COURTOIS, C. 1993. Effects of experimental leaching on Rb-Sr and K-Ar isotopic systems and REE contents of diagenetic illite. *Chemical Geology*, 103, 1-16.

CLAUER, N., GIBLIN, P. & LUCAS, J. 1984. Sr and Ar isotope studies of detrital smectites from the Atlantic Ocean (DSDP, Legs 43, 48 and 50). *Chemical geology*, 46, 141-151.

CLAUER, N., JOURDAN, F. & ZWINGMANN, H. 2011. Dating petroleum emplacement by illite  $^{40}\text{Ar}/^{39}\text{Ar}$  laser stepwise heating: Discussion. *AAPG Bulletin*, 95, 2107-2111.

CLAUER, N., ŠRODOŇ, J., FRANCU, J. & ŠUCHA, V. 1997. K-Ar dating of illite fundamental particles separated from illite-smectite. *Clay Minerals*, 32, 181-196.

CLAUER, N., WILLIAMS, L. B. & FALLICK, A. E. 2014. Genesis of nanometric illite crystals elucidated by light-element (hydrogen, lithium, boron and oxygen) isotope tracing, and K-Ar and Rb-Sr dating. *Chemical Geology*, 383, 26-50.

EHRENBERG, S. & NADEAU, P. 1989. Formation of diagenetic illite in sandstones of the Garn Formation, Haltenbanken area, Mid-Norwegian continental shelf. *Clay Minerals*, 24, 233-253.

EVANS, J. 1996. Dating the transition of smectite to illite in Palaeozoic mudrocks using the Rb–Sr whole-rock technique. *Journal of the Geological Society* 153, 101-108.

FRANKS, S. G. & ZWINGMANN, H. 2010. Origin and timing of late diagenetic illite in the Permian–Carboniferous Unayzah sandstone reservoirs of Saudi Arabia. *AAPG Bulletin*, 94, 1133-1159.

GOROKHOV, I., CLAUER, N., TURCHENKO, T., MELNIKOV, N., KUTYAVIN, E., PIRRUS, E. AND BASKAKOV, A. 1994. Rb–Sr systematics of Vendian-Cambrian claystones from the east European Platform: implications for a multi-stage illite evolution. *Chemical Geology* 112, 71-89.

GOROKHOV, I., SIEDLECKA, A., ROBERTS, D., MELNIKOV, N. & TURCHENKO, T. 2001. Rb–Sr dating of diagenetic illite in Neoproterozoic shales, Varanger Peninsula, northern Norway. *Geological Magazine*, 138, 541-562.

GUO, X., LIU, K., JIA, C., SONG, Y., ZHAO, M., ZHUO, Q. & LU, X. 2016. Hydrocarbon accumulation processes in the Dabei tight-gas reservoirs, Kuqa Subbasin, Tarim Basin, northwest China. *AAPG Bulletin*, 100, 1501-1521.

HAMILTON, P., KELLEY, S. & FALLICK, A. E. 1989. K-Ar dating of illite in hydrocarbon reservoirs. *Clay Minerals*, 24, 215-231.

HANSON, A., ZHANG, S., MOLDOWAN, J., LIANG, D. & ZHANG, B. 2000. Molecular organic geochemistry of the Tarim Basin, northwest China. *AAPG Bulletin*, 84, 1109-1128.

HU, S., WILKES, H., HORSFIELD, B., CHEN, H. & LI, S. 2016. On the origin, mixing and alteration of crude oils in the Tarim Basin. *Organic Geochemistry*, 97, 17-34.

HUANG, H., ZHANG, S. & SU, J. 2016. Palaeozoic oil–source correlation in the Tarim Basin, NW China: A review. *Organic Geochemistry*, 94, 32-46.

JIA, C. & WEI, G. 2002. Structural characteristics and petroliferous features of Tarim Basin. *Chinese Science Bulletin*, 47, 1-11.

JIN, Z., ZHU, D., ZHANG, X., HU, W. & SONG, Y. 2006. Hydrothermally fluoritized Ordovician carbonates as reservoir rocks in the Tazhong area, central Tarim Basin, NW China. *Journal of Petroleum Geology*, 29, 27-40.

KANG, Y. & KANG, Z. 1996. Tectonic evolution and oil and gas of Tarim Basin. *Journal of Southeast Asian Earth Sciences*, 13, 317-325.

KRALIK, M. 1983. Interpretation of K–Ar and Rb–Sr data from fine fractions of weakly metamorphosed shales and carbonate rocks at the base of the northern calcareous Alps (Salzburg, Austria). *Tschermaks Mineralogische und Petrographische Mitteilungen* 32, 49-67.

LI, C.-F., CHU, Z.-Y., GUO, J.-H., LI, Y.-L., YANG, Y.-H. & LI, X.-H. 2015a. A rapid single column separation scheme for high-precision Sr–Nd–Pb isotopic analysis in geological samples using thermal ionization mass spectrometry. *Analytical Methods*, 7, 4793-4802.

LI, C.-F., GUO, J.-H., CHU, Z.-Y., FENG, L.-J. & WANG, X.-C. 2015b. Direct High-Precision Measurements of the  $^{87}\text{Sr}/^{86}\text{Sr}$  Isotope Ratio in Natural Water without Chemical Separation Using Thermal Ionization Mass Spectrometry Equipped with 1012  $\Omega$  Resistors. *Analytical Chemistry*, 87, 7426-7432.

LI, K., CAI, C., HE, H., JIANG, L., CAI, L., XIANG, L., HUANG, S. & ZHANG, C. 2011. Origin of palaeo-waters in the Ordovician carbonates in Tahe oilfield, Tarim Basin: constraints from fluid inclusions and Sr, C and O isotopes. *Geofluids*, 11, 71-86.

LI, S., AMRANI, A., PANG, X., YANG, H., SAID-AHMAD, W., ZHANG, B. & PANG, Q. 2015c. Origin and quantitative source assessment of deep oils in the Tazhong Uplift, Tarim Basin. *Organic Geochemistry*, 78, 1-22.

LUDWIG, K. 2003. User's manual for Isoplot 3.00: a geochronological toolkit for Microsoft Excel. Berkeley Geochronology Center. Special publication, 4, 1-71.

LUO, X., ZHAO, Z. & MENG, Y. 2015. Application of an odd/even predominance of n-alkanes in oil–source rock correlation: taking the lower Paleozoic strata of the Tarim Basin as an example. *Toxicological & Environmental Chemistry*, 97, 409-416.

MIDDLETON, A. W., UYSAL, I. T., BRYAN, S. E., HALL, C. M. & GOLDING, S. D. 2014. Integrating  $^{40}\text{Ar}$ – $^{39}\text{Ar}$ ,  $^{87}\text{Rb}$ – $^{87}\text{Sr}$  and  $^{147}\text{Sm}$ – $^{143}\text{Nd}$  geochronology of authigenic illite to evaluate tectonic reactivation in an intraplate setting, central Australia. *Geochimica et Cosmochimica Acta*, 134, 155-174.

MORTON, J. P. 1985a. Rb-Sr dating of diagenesis and source age of clays in Upper Devonian black shales of Texas. *Geological Society of America Bulletin*, 96, 1043-1049.

MORTON, J. P. 1985b. Rb-Sr evidence for punctuated illite/smectite diagenesis in the Oligocene Frio Formation, Texas Gulf Coast. *Geological Society of America Bulletin*, 96, 114-122.

MUTLU, H., TONGUÇ UYSAL, I., ALTUNEL, E., KARABACAK, V., FENG, Y., ZHAO, J.-X. & ATALAY, O. 2010. Rb–Sr systematics of fault gouges from the North Anatolian Fault Zone (Turkey). *Journal of Structural Geology*, 32, 216-221.

POLLASTRO, R. M. 1993. Considerations and applications of the illite/smectite geothermometer in hydrocarbon-bearing rocks of Miocene to Mississippian age. *Clays and Clay Minerals*, 41, 119-119.

ROTENBERG, E., DAVIS, D. W., AMELIN, Y., GHOSH, S. & BERGQUIST, B. A. 2012. Determination of the decay-constant of  $^{87}\text{Rb}$  by laboratory accumulation of  $^{87}\text{Sr}$ . *Geochimica et Cosmochimica Acta*, 85, 41-57.

ŚRODOŃ, J., CLAUER, N., HUFF, W., DUDEK, T. & BANAS, M. 2009. K-Ar dating of the Lower Palaeozoic K-bentonites from the Baltic Basin and the Baltic Shield: implications for the role of temperature and time in the illitization of smectite. *Clay Minerals*, 44, 361-387.

TIAN, H., XIAO, X., WILKINS, R. W., GAN, H., XIAO, Z., LIU, D. & GUO, L. 2008. Formation and evolution of Silurian paleo-oil pools in the Tarim Basin, NW China. *Organic Geochemistry*, 39, 1281-1293.

UYSAL, I. T., GOLDING, S. D. & THIEDE, D. S. 2001. K-Ar and Rb-Sr dating of authigenic illite-smectite in Late Permian coal measures, Queensland, Australia: implication for thermal history. *Chemical Geology*, 171, 195-211.

UYSAL, I. T., MORY, A. J., GOLDING, S. D., BOLHAR, R. & COLLERSON, K. D. 2005. Clay mineralogical, geochemical and

isotopic tracing of the evolution of the Woodleigh impact structure, Southern Carnarvon Basin, Western Australia. *Contributions to Mineralogy and Petrology*, 149, 576-590.

WASSERBURG, G., HAYDEN, R. & JENSEN, K. J. 1956. A40-K40 dating of igneous rocks and sediments. *Geochimica et Cosmochimica Acta*, 10, 153-165.

XIAO, Z., LI, M., HUANG, S., WANG, T., ZHANG, B., FANG, R., ZHANG, K., NI, Z., ZHAO, Q. & WANG, D. 2016. Source, oil charging history and filling pathways of the Ordovician carbonate reservoir in the Halahatang Oilfield, Tarim Basin, NW China. *Marine and Petroleum Geology*, 73, 59-71.

XU, Y.-G., WEI, X., LUO, Z.-Y., LIU, H.-Q. & CAO, J. 2014. The Early Permian Tarim Large Igneous Province: main characteristics and a plume incubation model. *Lithos*, 204, 20-35.

YUN, J.-B., SHI, H.-S., ZHU, J.-Z., ZHAO, L.-H. & QIU, H.-N. 2010. Dating petroleum emplacement by illite  $^{40}\text{Ar}/^{39}\text{Ar}$  laser stepwise heating. *AAPG Bulletin*, 94, 759-771.

ZHANG, Y., LIU, K. & LUO, X. 2016. Evaluation of  $^{40}\text{Ar}/^{39}\text{Ar}$  Geochronology of Authigenic Illites in Determining Hydrocarbon Charge Timing: A Case Study from the Silurian Bituminous Sandstone Reservoirs, Tarim Basin, China. *Acta Geologica Sinica (English Edition)*, 90, 684-703.

ZHANG, Y., ZWINGMANN, H., LIU, K., TODD, A. & LUO, X. 2011. Hydrocarbon charge history of the Silurian bituminous sandstone reservoirs in the Tazhong uplift, Tarim Basin, China. AAPG Bulletin, 95, 395-412.

ZHAO, M.-J., WANG, Z.-M., PAN, W.-Q., LIU, S.-B., QIN, S.-F. & HAN, J.-F. 2008. Lower palaeozoic source rocks in Manjiaer sag, Tarim Basin. Petroleum Exploration and Development, 35, 417-423.

ZHOU, M.-F., ZHAO, J.-H., JIANG, C.-Y., GAO, J.-F., WANG, W. & YANG, S.-H. 2009. OIB-like, heterogeneous mantle sources of Permian basaltic magmatism in the western Tarim Basin, NW China: implications for a possible Permian large igneous province. Lithos, 113, 583-594.

ZHU, G., CUI, J., SU, J., YANG, H., ZHANG, B., HU, J. & ZHU, Y. 2012a. Accumulation and reformation of Silurian reservoir in the northern Tarim Basin. Acta Geologica Sinica (English edition), 86, 209-225.

ZHU, G., ZHANG, S., LIU, K., YANG, H., ZHANG, B., SU, J. & ZHANG, Y. 2013a. A well-preserved 250 million-year-old oil accumulation in the Tarim Basin, western China: Implications for hydrocarbon exploration in old and deep basins. Marine and Petroleum Geology, 43, 478-488.

ZHU, G., ZHANG, S., SU, J., HUANG, H., YANG, H., GU, L., ZHANG, B. & ZHU, Y. 2012b. The occurrence of ultra-deep heavy

oils in the Tabei Uplift of the Tarim Basin, NW China. *Organic Geochemistry*, 52, 88-102.

ZHU, G., ZHANG, S., SU, J., ZHANG, B., YANG, H., ZHU, Y. & GU, L. 2013b. Alteration and multi-stage accumulation of oil and gas in the Ordovician of the Tabei Uplift, Tarim Basin, NW China: Implications for genetic origin of the diverse hydrocarbons. *Marine and Petroleum Geology*, 46, 234-250.

ZWINGMANN, H., CLAUER, N. & GAUPP, R. 1999. Structure-related geochemical (REE) and isotopic (K-Ar, Rb-Sr,  $\delta^{18}\text{O}$ ) characteristics of clay minerals from Rotliegend sandstone reservoirs (Permian, northern Germany). *Geochimica et Cosmochimica Acta*, 63, 2805-2823.

## **Chapter 4**

# **Direct Dating of Alteration of Paleo-Oil Pools Using Rubidium-Strontium Pyrite Geochronology**

**Shaojie Li, Xuan-Ce Wang, Chao-Feng Li, Keyu Liu, Simon A. Wilde, Si-Yu Hu**

*Marine and Petroleum Geology, To be submitted*

## Abstract

Direct dating of petroleum systems by hydrocarbons or associated authigenic minerals is crucial for petroleum system analysis and hydrocarbon exploration. The precipitation of authigenic pyrite in petroliferous basins is commonly genetically associated with hydrocarbon generation, migration, accumulation, or destruction. Pyrite rubidium-strontium (Rb-Sr) isotope dilution thermal ionization mass spectrometry (ID-TIMS) is a well-developed technique and its successful application for high-temperature ore systems suggests that this dating method has the potential to directly date key processes in low-temperature petroleum systems. Rb-Sr data for pyrites in two Ordovician carbonate rock specimens collected from a depth of ~4952m in the YD2 well in the Yudong region, northern Tarim Basin (NW China), yield identical isochron ages, within analytical uncertainties:  $206 \pm 13$  ( $2\sigma$ ) and  $224 \pm 28$  Ma ( $2\sigma$ ). SEM investigations demonstrate that Rb and Sr atoms mainly reside in the crystal lattice of the pyrites because neither fluid nor mineral inclusions are found in the pyrites, utilizing high-resolution SEM mapping. The Rb-Sr isochron relations documented in the two samples indicate that sufficient Rb/Sr fractionation and initial Sr isotopic homogenization can occur for geochronology. In addition, the closure temperature (227–320 °C) for the Rb-Sr isotope system in pyrite is higher than the precipitation temperature for pyrite in petroleum-related systems (below 200°C), suggesting that the Rb-Sr age for pyrite is not overprinted by post-precipitation alteration.

Integrating the lead-strontium-sulfur isotopes of the pyrites with burial history analysis, the ages are interpreted as the timing of alteration of the paleo-oil pool by a hydrothermally-triggered thermochemical sulfate reduction process. This study demonstrates that Rb-Sr pyrite geochronology, combined with radiogenic and stable isotope analyses, can be used to evaluate the temporal evolution of oil pools. This approach has the potential for dating of petroleum systems worldwide.

**Key words:** Rb-Sr pyrite geochronology, pyrite Pb-Sr-S isotope, Ordovician paleo-oil pool, Kuqa Depression, Tarim Basin

## 4.1 Introduction

Establishing the absolute timing of key events in petroleum systems (e.g., hydrocarbon generation, charge and alteration) is crucial for petroleum system analysis and hydrocarbon exploration, yet it is still highly challenging to obtain reliable and precise isotopic ages. Recent studies have applied radiometric isotope techniques to directly date hydrocarbons (e.g. rhenium-osmium (Re-Os); Georgiev et al., 2016) or associated authigenic illite (e.g. potassium-argon (K-Ar); Zhang et al., 2011) to constrain the absolute age of these events.

Hydrocarbon-associated authigenic minerals can provide important constraints on hydrocarbon generation and subsequent processes, and may be datable targets. Authigenic pyrite is ubiquitous in petroliferous basins and is commonly associated with source rock deposition (Berner, 1984), hydrocarbon generation/expulsion (Rasmussen, 2005), secondary migration/charge (Ellis, 2007), and post-accumulation alteration (Machel et al., 1995). Trace element composition of pyrite is directly related to the paleo-environment (water body, hydrothermal system, and organic-inorganic fluid interaction) in which it was precipitated (Large et al., 2009, 2014; Reich et al., 2013). Pyrite usually contains Rb and Sr at ug/g level (Li et al., 2008; Yang and Zhou, 2001). The sensitive isotope-dilution thermal ionization mass spectrometry (ID-TIMS) technique and low blank chemistry chromatography developed in our laboratory permit high-precision Rb-Sr isotopic analysis of pyrite of a very small

sample size (2 – 6 mg; Li et al., 2015a, b). This technique improved the ability to reflect the potential chemical heterogeneity among crystal grains, which has been masked by the convectonal method using a large-size aliquot. Therefore, the Rb-Sr technique may be a favorable dating method for hydrocarbon-associated pyrite. The aim of this study is to investigate whether this is the case and evaluate the geological implication of pyrite Rb-Sr geochronology as applied to petroleum systems.

## **4.2 Geological background**

The Kuqa Depression is situated in the northern part of the Tarim Basin, northwest (NW) China and consists of seven structural units (Northern Monoclinical Belt, Kelasu Thrust Belt, Yiqikelike Thrust Belt, Baicheng Sag, Qiulitage Thrust Belt, Yangxia Sag and Southern Slope Belt; Figure 4.1). The Yudong region lies in the Southern Slope Belt (Figure 4.1) and consists of Paleozoic-Cenozoic sediments (Liu et al., 2016). Three major tectonic events have affected the Kuqa Depression: (1) a peripheral foreland basin stage (late Permian to Middle Triassic); (2) a rift basin stage (Late Triassic to Middle Jurassic), and (3) a rejuvenated foreland basin stage (early Neogene to the present-day) (Liu et al., 2016). In well YD-2, Lower Ordovician strata are uncomfortably overlain by Jurassic sediments (Figure 4.2A), indicating the Middle Ordovician to Triassic rocks have been eroded during multi-stage tectonic movements that affected this region (Jia and Wei, 2002).

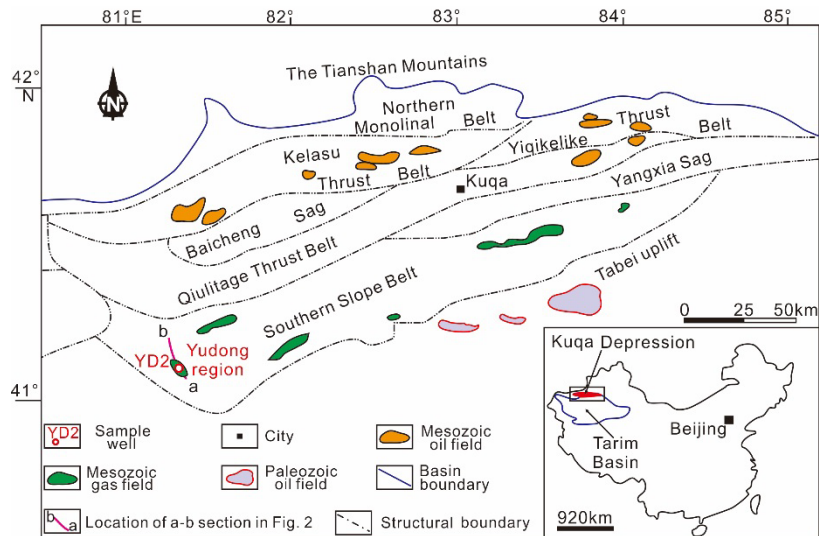


**Figure 4.1:** Major structural units within the Kuqa Depression of the Tarim Basin, NW China, showing the location of drillhole YD-2 within the Southern Slope Belt. The inset shows the locations of the Kuqa Depression and Tarim Basin in China (modified after Liu et al. (2016)).

Pyrite is widely distributed in Ordovician hydrocarbon-bearing carbonate rocks within the Tarim Basin and formed either as a by-product of thermochemical sulfate reduction (TSR) or bacterial sulfate reduction (BSR) (Cai et al., 2001, 2002, 2009a; Li et al., 2012; Lü et al., 2007; Jia et al., 2015; Zhu and Meng, 2010). Sulfate minerals can be reduced to hydrogen sulfide (H<sub>2</sub>S) by hydrocarbons either through bacterial metabolism (i.e. BSR) or thermochemical activity (i.e. TSR), and H<sub>2</sub>S can be further transformed into pyrite provided there is sufficient iron (Machel et al., 1995). BSR-derived pyrites mainly occur in karst breccias and are characterized by depleted  $\delta^{34}\text{S}$  values ranging from -25.7‰ to -4.7‰ in the Tarim Basin (Cai et al., 2002; Jia et al., 2015; Li et al., 2012; Lü et al., 2007;

Zhu and Meng, 2010). Such pyrites were precipitated in a low-temperature environment (60 – 80 °C) when hydrocarbon-charged reservoirs were uplifted to the surface/ subsurface and karstified (Jia et al., 2015; Zhu and Meng, 2010). TSR-derived pyrites mainly occur in fractures or coexist with other hydrothermal minerals (e.g. calcite; Li et al., 2011; Jia et al., 2015; Zhu and Meng, 2010). Pyrites of TSR origin have more enriched  $\delta^{34}\text{S}$  values that are distributed between 11.2‰ and 31.3‰ in the Tarim Basin (Cai et al., 2001, 2009a; Jia et al., 2015; Zhu and Meng, 2010). TSR requires a higher temperature environment (100–180 °C) compared to BSR (Machel et al., 1995), and the TSR process in the Tarim Basin is profoundly influenced by magmatism and associated hydrothermal activities that created a high-temperature environment and facilitated TSR (Li et al., 2011; Jia et al., 2015; Zhu and Meng, 2010).

The Yudong region is a significant petroleum exploration province in the Kuqa Depression of the northern Tarim Basin (Figure 4.1). Here, the Ordovician carbonate rocks are reservoirs for hydrocarbons generated from Cambro-Ordovician marine source rocks (Huang et al., 2016). YD-2 is the only well so far drilled into Ordovician-hosted hydrocarbons in the Yudong region, where limited heavy oil of uncommercial value ( $\sim 0.2\text{m}^3/\text{day}$ ) has been recovered from the interval between 4945 m and 4983.5 m during formation testing (Figure 4.2A; Zhou et al., 2015). Disseminated pyrite is commonly present in the oil-bearing interval and this provides a valuable opportunity to test the applicability of Rb-Sr

pyrite geochronology to petroleum systems.

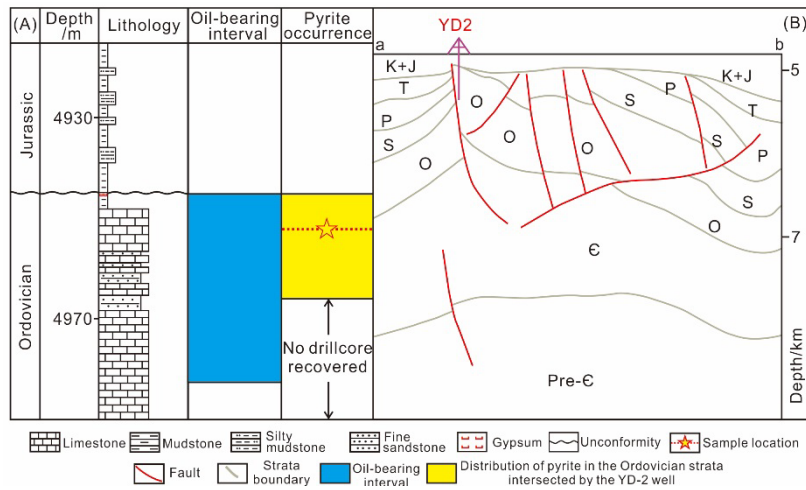


**Figure 4.2:** A: Main features of drillhole YD-2. Limited amounts of heavy oil have been obtained from Ordovician strata (4945 m and 4983.5 m). B: A cross-section shows the structure and strata nearby drillhole YD2. The location of the cross-section is shown in Figure 4.1. Є–Cambrian; O–Ordovician; S–Silurian; P–Permian; T–Triassic; J–Jurassic; K–Cretaceous.

### 4.3 Samples and analytical method

Pyrite samples analyzed in this study were separated from two pyrite-rich drillcore specimens (A and B) taken from a depth of ~4952 m in the YD-2 well (Figure 4.2A). Thin sections were also made of the host rock. Stereo binocular microscopy and scanning electron microscope-energy-dispersive X-ray spectroscopy (SEM-EDS, 200kV, Zeiss Ultra plus Field Emission SEM at CSIRO, Perth, Western Australia) were employed to investigate the petrographic

features of the samples.

Pyrite was separated by crushing the specimens in a porcelain mortar, followed by gravity sorting, electromagnetic separation and hand-picking under a binocular microscope. The pyrite separates were cleaned with Milli-Q water and analytical-grade ethanol to further improve their purity and remove any possible contamination introduced by the mineral separation process. The two separate pyrite samples were prepared and dried completely on a hotplate prior to undertaking chemical analysis.

Pyrite sub-samples were randomly picked from each sample. Each sub-sample was weighed (2 – 6 mg) using an AG104 Mettler Toledo analytical balance and dissolved, along with  $^{87}\text{Rb}$ - $^{84}\text{Sr}$  isotopic tracers, in 14N  $\text{HNO}_3$  (~0.1 mL) in screw-top PFA Savillex vials. Rubidium, strontium, and lead fractions of each sub-sample were separated and purified using a mini-column containing ~30  $\mu\text{L}$  of Sr Spec resin (Li et al., 2015a). Isotope ratios and elemental concentrations of Rb and Sr were determined using ID-TIMS on a multi-collector Triton plus instrument at the State Key Laboratory of Lithospheric Evolution, Institute of Geology and Geophysics, Chinese Academy of Sciences (IGGCAS) in Beijing, following the technique of Li et al. (2015a, b). Lead isotope ratios were also measured by TIMS using the same instrument.  $^{87}\text{Sr}/^{86}\text{Sr}$  ratios were normalized to  $^{88}\text{Sr}/^{86}\text{Sr} = 8.375209$  (Li et al., 2015a, b) using the exponential law. Duplicate analyses of Sr standard NBS987 during this study yielded a mean  $^{87}\text{Sr}/^{86}\text{Sr}$  value of  $0.710244 \pm 0.000012$

( $2\sigma$ ,  $n=4$ ), in good agreement with the reported value of  $0.710251 \pm 0.000016$  (Li et al., 2015a). Analytical uncertainties in  $^{87}\text{Rb}/^{86}\text{Sr}$  ratios were less than 1%. The blank during the analytical session was less than 3 pg for Rb, 6 pg for Sr and 100 pg for Pb. Therefore, the contribution of total blank on the Rb-Sr and Pb isotopes can be ignored. Rb-Sr isochron ages of pyrites were calculated using the ISOPLLOT 3.0 software (Ludwig, 2003), applying a decay constant ( $\lambda^{87}\text{Rb}$ ) of  $1.396 \times 10^{-11} \text{ yr}^{-1}$  (Rotenberg et al., 2012). For Pb isotopes, in-run precision of individual analyses was better than 0.02 % (2 RSE). Isotope fractionation effect during Pb isotopic analysis was corrected by external correction with a NIST 981 standard. Acids used during the Rb-Sr-Pb chemistry were all analytical reagent (AR) grade and were purified utilizing a Savillex<sup>TM</sup> DST-1000 sub-boiling distillation system. Ultrapure water with resistivity of  $18.2 \text{ M}\Omega\cdot\text{cm}^{-1}$  obtained from a Milli-Q Element system was used throughout this work.

Sulfur isotopes of pyrites (25 – 50 mg for each) were determined using a Finnigan MAT 252 mass spectrometer using the dual inlet method at IGGCAS. The sulfur isotope data are expressed in  $\delta$  notion relative to Vienna Canyon Diablo Troilite (VCDT), and two duplicate analyses were conducted for each sample (reproducibility of  $\delta^{34}\text{S}$  value is  $\pm 0.1 - 0.3\text{‰}$ ). Analytical precision for  $\delta^{34}\text{S}$  values of the duplicate analyses of IAEA standards (IAEA-S1, IAEA-S2 and IAEA-S3) was better than  $\pm 0.1\text{‰}$  ( $1\sigma$ , SD).

## 4.4 Results

### 4.4.1 Petrographic observations

Pyrite crystals were characterized by using both stereo binocular microscope photomicrographs (Figures 4.3A and 4.3B) and scanning electron microscope-energy-dispersive X-ray spectroscopy (SEM-EDS) images (Figures 4.4A to 4.4I). SEM images illustrate that pyrite, calcite and quartz are intergrown and show embayment structures (Figure 4.4A), suggesting that these minerals were precipitated contemporaneously from hydrothermal fluids which may have migrated along faults near the YD-2 well (Figure 4.2B). The coexistence of pyrite and bitumen was also observed in this study (Figure 4.3B), which indicates that the formation of pyrite in the sampled reservoir rock may be the result of the interaction between hydrocarbon and hydrothermal fluid.

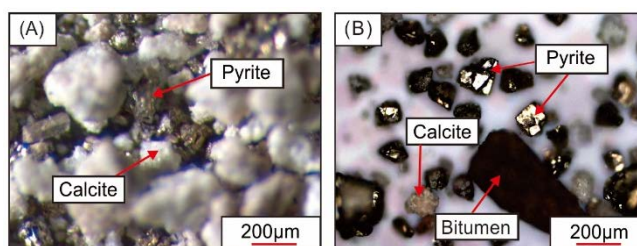


**Figure 4.3:** Stereo binocular microscope photomicrographs (reflective light) showing that (A) pyrites are disseminated in the samples and coexist with calcite in specimen A, and (B) that bitumen coexists with pyrite and calcite in specimen B.

The high-resolution SEM images show that the pyrite contains no mineral or fluid inclusions (Figures 4.4B to 4.4I). Furthermore, potassium elemental mapping of pyrite indicates the K content is below the detection limit of the instrument (Figures 4.5A to 4.5H). The lack of K also established the absence of K-bearing inclusions that might accommodate Rb.

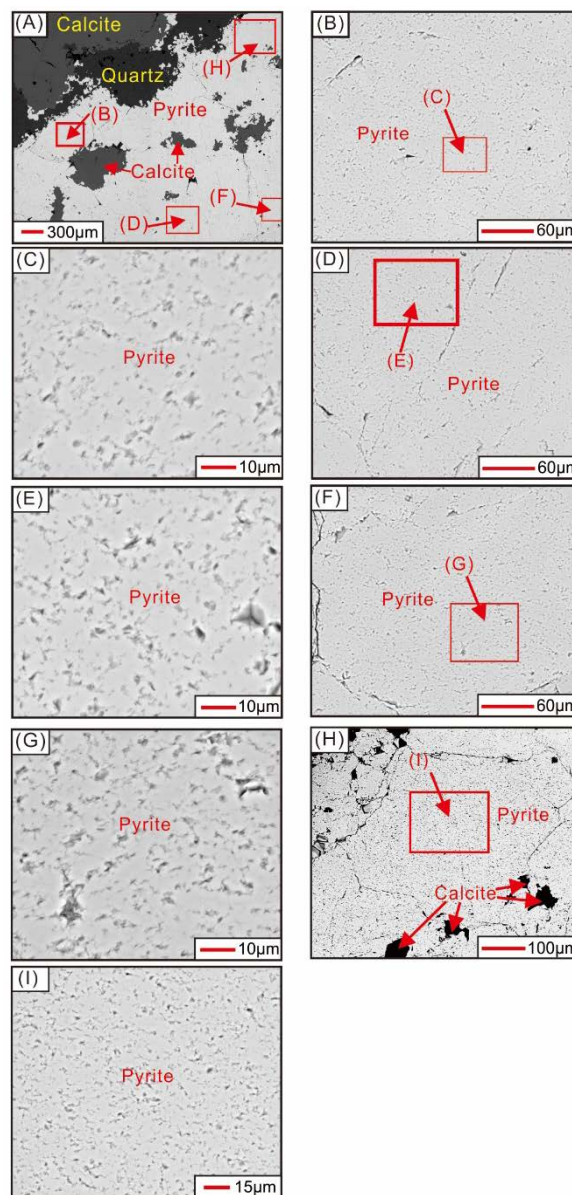


**Figure 4.4:** A: typical SEM image of thin section showing embayment structures between pyrite, calcite and quartz, suggesting coeval precipitation from hydrothermal fluid. B-I: high resolution SEM images showing pyrites are clean and lack mineral or fluid inclusions. The red rectangles show the sites of selected images, identified by the appropriate letters.

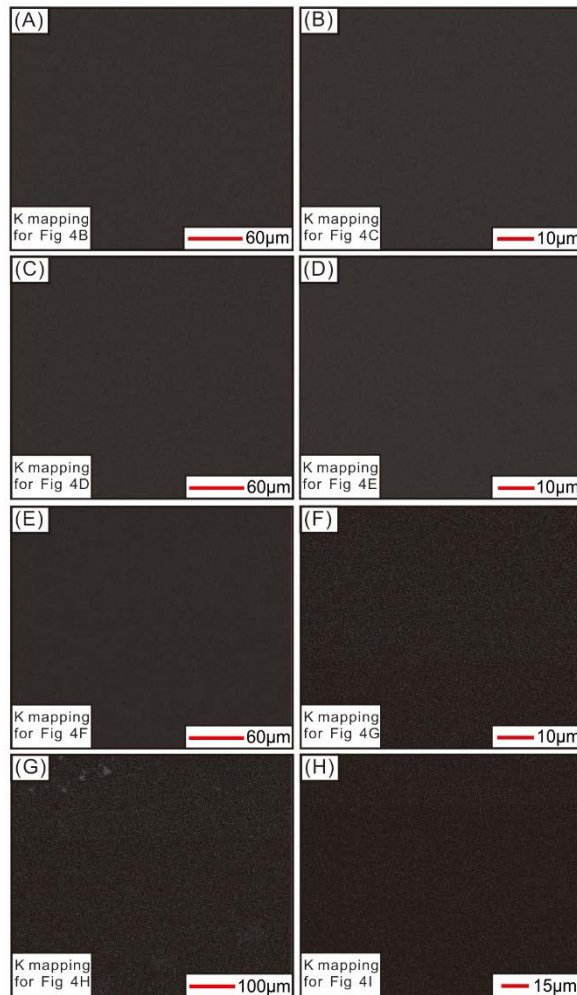


**Figure 4.5:** SEM-EDS elemental mapping of potassium (K) in pyrite shown in Figures 4.4B (A), 4.4C (B), 4.4D (C), 4.4E (D), 4.4F (E), 4.4G (F), 4.4H(G) and 4.4I (H). The results show that the K content of the pyrites

is below the detection limit for of the instrument, supporting the absence of K-rich inclusion.

#### **4.4.2 Rb-Sr-Pb-S isotope data and isochron ages**

Pyrite sub-samples from specimen A contain 0.1353 – 0.1655 ppm Rb and 0.1358 – 0.1958 ppm Sr and have  $^{87}\text{Rb}/^{86}\text{Sr}$  and  $^{87}\text{Sr}/^{86}\text{Sr}$  ratios of 2.355 – 3.379 and 0.718340 – 0.721307, respectively (Table 4.1), yielding an isochron age of  $206 \pm 13$  Ma ( $2\sigma$ ), with an initial  $^{87}\text{Sr}/^{86}\text{Sr}$  ratio ( $\text{Sr}_i$ ) of  $0.71138 \pm 0.00048$  ( $2\sigma$ ) (Figure 4.6A). Pyrite sub-samples from specimen B contain 0.1891 – 0.2611 ppm Rb and 0.2154 – 0.2511 ppm Sr (Table 4.1). An isochron age of  $224 \pm 28$  Ma ( $2\sigma$ ) with a  $\text{Sr}_i$  of  $0.7100 \pm 0.0011$  ( $2\sigma$ ) (Figure 4.6B) is regressed from their  $^{87}\text{Rb}/^{86}\text{Sr}$  and  $^{87}\text{Sr}/^{86}\text{Sr}$  ratios, which are 2.543 – 3.124 and 0.718049 – 0.719882, respectively (Table 4.1). The two Rb-Sr isochrons produce identical ages and  $\text{Sr}_i$ , within analytical uncertainties, indicating that they are not mixing isochron ages and that the analyzed pyrites were precipitated coevally.

Pyrite sub-samples from both specimens have similar Pb isotope ratios. The ratios of  $^{206}\text{Pb}/^{204}\text{Pb}$ ,  $^{207}\text{Pb}/^{204}\text{Pb}$  and  $^{208}\text{Pb}/^{204}\text{Pb}$  are 18.275 – 18.972, 15.546 – 15.712 and 38.245 – 38.797, respectively (Table 4.1).  $\delta^{34}\text{S}$  values of the pyrites range from 31.032‰ to 31.799‰ (Table 4.1).

**Table 4.1:** Rubidium-strontium-lead-sulfur isotope data for pyrite sub-samples from specimens A and B in this study

Sample	Rb [ppm]	Sr [ppm]	$^{87}\text{Rb}/^{86}\text{Sr}$	$^{87}\text{Sr}/^{86}\text{Sr}$	$\pm 2\sigma$	$^*\text{Sr}_i$	$^{206}\text{Pb}/^{204}\text{Pb}$	$\pm 2\sigma$	$^{207}\text{Pb}/^{204}\text{Pb}$	$\pm 2\sigma$	$^{208}\text{Pb}/^{204}\text{Pb}$	$\pm 2\sigma$	Analysis No.	$\delta^{34}\text{S}(\text{‰})$
A-1	0.1644	0.1420	3.379	0.721307	0.000031	0.711409	18.355	0.006	15.546	0.005	38.245	0.013		
A-2	0.1353	0.1373	2.856	0.719757	0.000033	0.711392	18.482	0.002	15.672	0.002	38.797	0.005	A	31.624
A-3	0.1459	0.1358	3.133	0.720542	0.000036	0.711365	18.361	0.002	15.603	0.001	38.398	0.004		
A-4	0.1637	0.1890	2.511	0.718813	0.000019	0.711456	18.484	0.003	15.646	0.002	38.493	0.006		
A-5	0.1655	0.1938	2.480	0.718702	0.000029	0.711436	18.334	0.004	15.616	0.004	38.390	0.008	**A_D	31.799
A-6	0.1580	0.1947	2.355	0.718340	0.000030	0.711442	18.363	0.003	15.643	0.003	38.465	0.007		
A-7	0.1647	0.1958	2.438	0.718401	0.000039	0.711261	18.451	0.003	15.607	0.003	38.418	0.007		
B-1	0.2251	0.2214	2.946	0.719290	0.000026	0.709903	18.374	0.003	15.621	0.002	38.413	0.006	B	31.310
B-2	0.2611	0.2511	3.014	0.719580	0.000026	0.709978	18.343	0.004	15.618	0.003	38.427	0.008		
B-3	0.1891	0.2154	2.543	0.718049	0.000024	0.709946	18.275	0.004	15.588	0.003	38.306	0.008	B_D	31.032
B-4	0.2383	0.2211	3.124	0.719882	0.000024	0.709931	18.972	0.004	15.712	0.003	38.711	0.007		

$^*\text{Sr}_i$  values were calculated at  $t=206$  Ma and  $224$  Ma for specimens A and B, respectively. **\*\*D** denotes duplicate analysis.

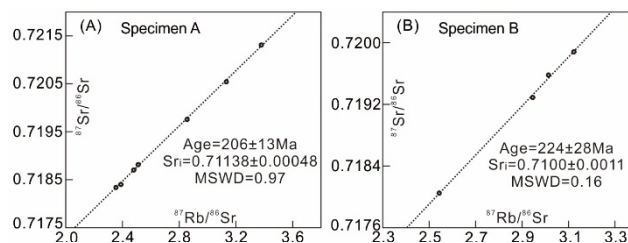


**Figure 4.6:** A-B: Rubidium-Strontium isochrons of pyrite separates from carbonate rock specimens A and B, respectively. ( $\text{Sr}_i$  represents the initial  $^{87}\text{Sr}/^{86}\text{Sr}$  ratio. MSWD is the mean square of weighted deviates.)

## 4.5 Discussion

### 4.5.1 Pyrite Rb-Sr geochronology: a robust dating technique for petroleum systems

In contrast to ore-associated pyrite where the Rb-Sr budget is mainly attributed to K-rich inclusions (Li et al., 2008; Yang and Zhou, 2000), Rb and Sr atoms mainly reside in the crystal lattice, since inclusions are absent in the pyrite utilized in this study (Figure 4.4). The Rb-Sr data also support the absence of K-rich inclusions because: 1) a compiled Rb-Sr dataset (Figure 4.7) suggests that most (~87.1%) ore-related pyrites have either Rb or Sr contents higher than the pyrite samples (~0.3 ppm) in this study; 2) randomly-selected sub-samples of each specimen have similar Rb-Sr concentrations (Table 4.1). This also implies that Rb and Sr in this case cannot be mainly attributed to randomly distributed K-rich inclusions.

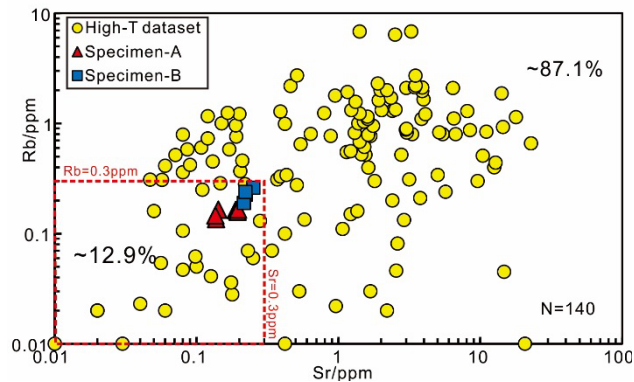


**Figure 4.7:** Comparison of Rb-Sr concentration data for pyrite in this study (specimens A and B) and pyrite samples obtained from high-temperature ore systems (log-log scale). Ore-related pyrite samples in the red rectangle have Rb and Sr concentration lower than pyrite in this study, and these samples occupy ~12.9% of the entire dataset. Rb-Sr data sources: Cao et al., 2015; Dong et al., 2016; Han et al., 2007; Hu et al., 2015; Li et al., 2008; Ni et al., 2012; Ravikant and Golani, 2011; Sun et al., 2014; Wang et al., 2015; Wang et al., 2014; Yang and Zhou, 2001; Yao et al., 2006; Zhang et al., 2003; Zhao et al., 2013; Zhou et al., 2013.

The absence of K-rich inclusions in the pyrite suggests that initial Sr isotopic homogenization can be attained during the precipitation of pyrite. The Rb-Sr age of the pyrite should therefore be a true isochron age rather than a mixing isochron age. In addition, closure temperature for the Rb-Sr isotope system in pyrite is estimated between 227°C and 320 °C (Yang and Zhou, 2000), which is higher than the temperature attained in petroleum systems, e.g. 60 – 100 °C for oil generation (Machel et al., 1995), below 100 °C for hydrocarbon charge (Ellis, 2007), and 100 – 180 °C for hydrocarbon

destruction (Machel et al., 1995). This implies that the Rb-Sr geochronometer in pyrite is insensitive to post-precipitation events and unlikely to be overprinted in petroleum systems. Therefore, the Rb-Sr isotope system in pyrite documents the timing of its precipitation. The age data can be further used to constrain petroleum system events by integrating radiogenic (e.g. Pb, Sr) and stable isotope (e.g. S) analysis for the dated pyrite.

#### **4.5.2 Source of metals in hydrothermal fluid**

Ordovician carbonate rocks intersected by YD-2 were deposited in a marine environment that is characterized by the general lack of terrigenous input (Zhang and Huang, 2005). Therefore, pyrite in the Ordovician reservoir is unlikely to be of detrital origin, but most likely formed through in-situ precipitation (Riciputi et al., 1996). Hydrothermal fluid is an important carrier of ore metals (e.g. Fe, Pb; Hedenquist and Lowenstern, 1994), and can provide a potential source of iron for the formation of pyrite in carbonate rocks. The coexistence of pyrite with other hydrothermal minerals (e.g. calcite, quartz) and the embayment structures between these minerals shown in photomicrographs (Figure 4.4A) demonstrate a hydrothermal origin for the pyrites. This is also supported by their coeval precipitation ages. The Rb-Sr isochron ages of the pyrites of ca. 224–206 Ma are younger than the depositional age of their host rock (i.e. Ordovician), but approach the onset time of rifting in the Kuqa Depression (Late Triassic), when hydrothermal activity was

widespread (Liu et al., 2016).

Metals contained in hydrothermal fluids from which the pyrites precipitated could have originated from three main repositories: the mantle, crust, and/or the metamorphic basement of the sedimentary basin. Here, lead-strontium isotope compositions of the pyrites can provide important constraints on the sources of metal in fluid systems (e.g. Yang and Zhou, 2001), and a compiled Pb-Sr isotope dataset for these three repositories within or adjacent to the Tarim Basin was employed to constrain the possible metal sources for the hydrothermal fluid (Figure 4.8). The origin of trace metals in the pyrite, which were inherited from the hydrothermal fluid therefore can be determined.

As shown in Figures 4.9A to 4.9C, lead-strontium isotope ratios of the studied pyrites plot in a field that overlaps the fields defined by mafic (e.g. basalt)-ultramafic (e.g. ultramafic intrusion), felsic (e.g. granite), and metamorphic rocks (e.g. schist), but are more closely associated with the felsic rocks. Lead isotope plots also show a mixed source for the pyrites, as the sub-sample analyses are distributed in a field that overlaps the three potential sources in the plots of  $^{207}\text{Pb}/^{204}\text{Pb}$ - $^{206}\text{Pb}/^{204}\text{Pb}$  (Figure 4.10A) and  $^{208}\text{Pb}/^{204}\text{Pb}$ - $^{206}\text{Pb}/^{204}\text{Pb}$  (Figure 4.10B). We note that one pyrite sub-sample (B-4) plots outside the main trend on the Pb-Pb isotope plots (Figure 4.10), reflecting some Pb isotope heterogeneity.

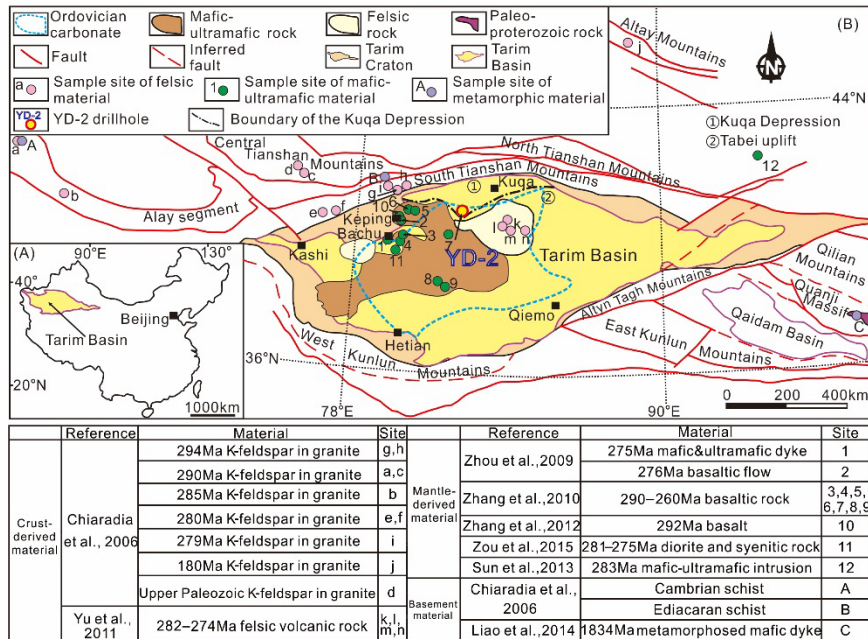


**Figure 4.8:** A: Location of the Tarim Basin in China; B: Map showing sample sites for Pb and Sr isotope data from published studies. a–n—Sample sites of felsic material (e.g. granite); 1–12—Sample sites of mafic (e.g. basalt) and ultramafic material (e.g. ultramafic intrusion); A–C—Sample sites of metamorphic material (e.g. schist).

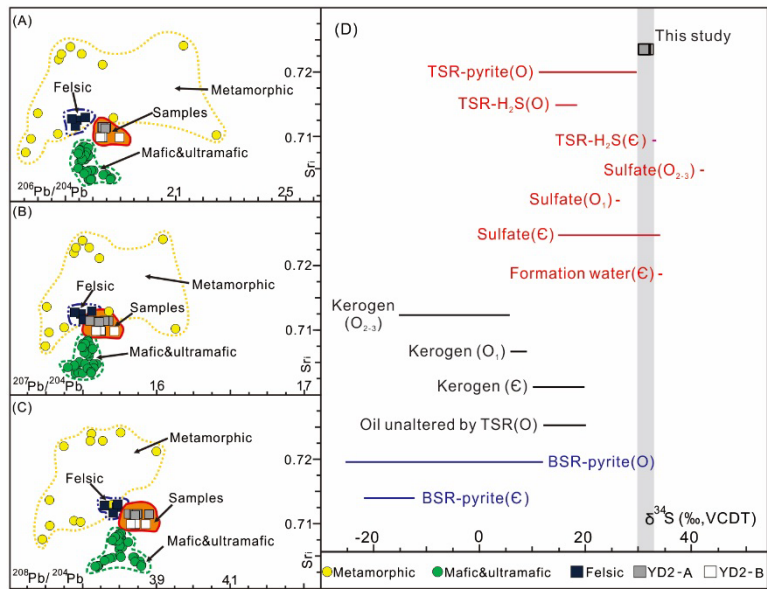


**Figure 4.9:** A:  $Sr_i$ - $^{206}Pb/^{204}Pb$ , B:  $Sr_i$ - $^{207}Pb/^{204}Pb$ , C:  $Sr_i$ - $^{208}Pb/^{204}Pb$  and D: S isotope ratios of the pyrites in this study compared with spatially and temporally associated materials from the literature. Whole-rock Pb isotope ratios were corrected to their initial ratios. C–Cambrian; O–Ordovician; TSR–thermochemical sulfate reduction; BSR–bacterial sulfate reduction;  $Sr_i$ –initial  $^{87}Sr/^{86}Sr$  value; VCDT–Vienna Canyon Diablo Troilite. Lead and strontium isotope data sources: (1) felsic rocks: Chiaradia et al. (2006) and Yu et al., (2011); (2) mafic and ultramafic rocks: Zhou et al. (2009), Zhang et al. (2010), Zhang et al. (2012), Zou et al. (2015), Sun et al. (2013); (3) metamorphic rocks: Chiaradia et al. (2006) and Liao et al. (2014). Sulfur isotope data sources: (1) Ordovician BSR-derived pyrites: Cai et al. (2002), Jia et al. (2015), Lü et al. (2007) and Zhu and Meng (2010); (2) Ordovician TSR-derived pyrites: Cai et al. (2001), Cai et al. (2009a), Jia et al. (2015), and Zhu and Meng (2010); (3) Middle-Upper Ordovician sulfates: Lü et al. (2007); (4) Ordovician TSR-derived  $H_2S$ : Zhu et al.

(2014); (5) Lower Ordovician sulfates: Cai et al. (2002); (6) Lower Ordovician kerogen: Cai et al. (2009b); (7) Middle-Upper Ordovician kerogen: Cai et al. (2009b); (8) Middle-Upper Ordovician non-degraded oil: Cai et al. (2009b); (9) Cambrian BSR-derived pyrites: Jia et al. (2015) and Li et al. (2012); (10) Cambrian sulfates: Cai et al. (2001), Cai et al. (2002), Jia et al. (2015) and Li et al. (2012); (11) Cambrian formation water: Jia et al. (2015); (12) Cambrian TSR-derived H<sub>2</sub>S: Jia et al. (2015); (13) Cambrian kerogen: Cai et al. (2009b).

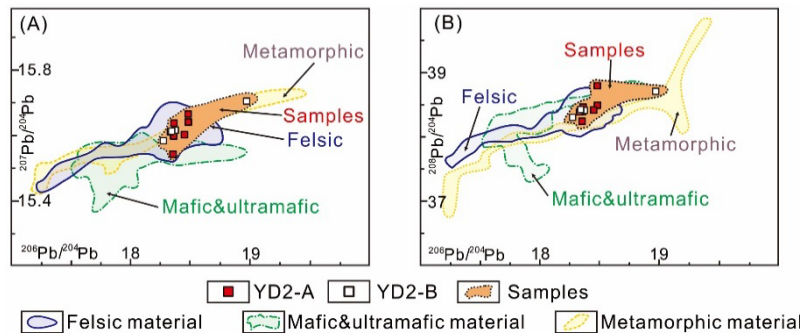


**Figure 4.10:** Lead isotope ratios of pyrite sub-samples compared with spatially and temporally associated materials. A:  $^{207}\text{Pb}/^{204}\text{Pb}$ - $^{206}\text{Pb}/^{204}\text{Pb}$ ; B:  $^{208}\text{Pb}/^{204}\text{Pb}$ - $^{206}\text{Pb}/^{204}\text{Pb}$ . Lead isotope ratios in (A) and (B) are corrected to their initial ratios. The fields of metamorphic, felsic and mafic-ultramafic rocks are drawn according to lead isotope data of material from the literature. Lead isotope data sources: (1) felsic rocks: Chiaradia et al. (2006) and Yu et al., (2011); (2) mafic and ultramafic rocks: Zhou et al. (2009), Zhang et al. (2010), Zhang et al. (2012), Zou et al. (2015), Sun et al. (2013); (3) metamorphic rocks: Chiaradia et al. (2006) and Liao et al. (2014).

### 4.5.3 Source of sulfur

Sulfur in pyrites from carbonate reservoirs can be directly inherited from the thermal degradation of organosulfur compounds in crude oil or obtained from H<sub>2</sub>S, which can be generated either through TSR or BSR (Worden and Smalley, 1996).

Sulfur isotope composition of pyrites can provide an important constraint on the origin of their sulfur. As shown in Figure 4.9D,  $\delta^{34}\text{S}$  values of the pyrites are compared with sulfur isotope ratios of potential sulfur providers (e.g. kerogen, oil, sulfate, formation water) and products of TSR and BSR (e.g. pyrites, H<sub>2</sub>S). The large discrepancy between  $\delta^{34}\text{S}$  values of pyrites in this study (31.032‰ to 31.799‰) and kerogen or oil unaltered by TSR (-15.3‰ to 19.4‰ and 11.9‰ to 20.5‰, respectively) precludes the possibility of direct inheritance of sulfur from hydrocarbon precursors (Figure 4.9D). The pyrites are also unlikely to have been precipitated via BSR processes because their  $\delta^{34}\text{S}$  values are more enriched than BSR-derived pyrites, which have  $\delta^{34}\text{S}$  values ranging from -25.7‰ to -11.6‰ (Figure 4.9D). Instead, the similarity in  $\delta^{34}\text{S}$  values between the studied pyrites and pyrites (11.200‰ to 29.700‰) and H<sub>2</sub>S (14.210‰ to 33.000‰) that are produced by TSR processes in the Tarim Basin indicates that the pyrites from YD-2 most likely are by-products of TSR processes. Furthermore, a TSR origin is also supported by the insignificant sulfur isotope fractionation between pyrites and sulfates ( $\delta^{34}\text{S} = 14.840\text{‰} - 42.100\text{‰}$ ), especially those in Ordovician strata ( $\delta^{34}\text{S} = 24.460\text{‰} - 42.100\text{‰}$ ) (Figure 4.9D), because TSR processes result in less sulfur isotope fractionation

between sulfates and pyrites when compared with those in BSR processes (Machel et al., 1995).

TSR requires the presence of both sulfates (either as minerals or dissolved in formation water) and hydrocarbons, as well as a relative high temperature (100 – 180° C) (Machel et al., 1995). Several lines of evidence support that TSR might have taken place in the Ordovician reservoir intersected by the YD-2 well: (1) both the industrial discovery of heavy oil flows and evidence from photomicrographs of solid bitumen (Figure 4.3B) imply that there should have been sufficient reactive hydrocarbons for sulfate reduction processes to occur; (2) gypsum was identified in the Ordovician strata at a depth of ~4950.1 m in the YD-2 well (i.e. ~1.9 m above the sampling depth) (Figure 4.2A; Zhou et al., 2015), which may have been the  $\text{SO}_4^{2-}$  source for the TSR; and (3) a case study of fluid inclusions hosted by hydrothermal minerals (e.g. calcite) from the Ordovician carbonate reservoir in the northern Tarim Basin suggests that the temperature of hydrothermal fluids in this region was higher than 154° C, which can readily facilitate TSR processes (Li et al., 2011).

#### **4.5.4 Timing of alteration of the paleo-oil pool**

The wide distribution of hydrothermal minerals in Ordovician hydrocarbon reservoirs indicates the common occurrence of hydrothermal activity in the Tarim Basin (e.g. Cai et al., 2008). The hydrothermal mineral assemblage of pyrite + calcite + quartz is also

present in samples in this study (Figure 4.4A). Previous studies have indicated that migrated hydrocarbons can be altered by hydrothermal fluid in three ways: (1) modifying the molecular composition of hydrocarbons, e.g. generating typical biomarkers of combustion; (2) the preferential loss of components with depleted carbon isotope compositions; and (3) facilitating the TSR process by providing a high temperature environment (Huang et al., 2016).

Although hydrothermal activities and their influence on hydrocarbons have been well documented, their absolute timing is poorly constrained. The Rb-Sr isochron ages of ca. 224–206 Ma obtained in this study indicate that the pyrites precipitated from hydrothermal fluid associated with Late Triassic rifting in the Kuqa Depression, and not early Permian magmatism, as previously proposed (e.g. Li et al., 2011). The pyrite Rb-Sr geochronologic evidence is consistent with the lack of early Permian magmatic records in the region, since few Permian magmatic rocks have been identified in the Yudong area, suggesting that any thermal influence of early Permian magmatism was insignificant (e.g. Xu et al., 2014).

As discussed in the preceding sections, the studied pyrites are also indicators of the TSR process. Therefore, Rb-Sr isochron ages of pyrite may also record the timing of TSR alteration of paleo-oil pools if hydrothermal activity and TSR occur contemporaneously. Burial history analysis indicates that there was regional uplift during the late Permian to Middle Triassic in the Kuqa Depression (Liu et al., 2016). Hydrogen sulfide generated prior to the uplifting event could

have potentially leaked from the Ordovician reservoir due to erosion of the caprocks. Therefore, hydrogen sulfide precursors of the pyrites may have been generated after the Middle Triassic. Considering the Late Triassic precipitation age of the pyrites, it is reasonable to deduce that both the hydrothermal activity and TSR occurred at ca. 224 – 206 Ma. Hydrothermal fluid flow can result in a high-temperature environment, which is essential for TSR. Thus, we propose that hydrothermal activity was a key factor in triggering TSR processes in the Ordovician reservoirs of the Yudong region of the Tarim Basin.

## **4.6 Conclusions**

This study integrates low-blank, high-sensitive Rb-Sr ID-TIMS dating with Pb-S isotope analysis, with the aim of directly dating and characterizing key events in petroleum system evolution using small pyrite samples (2 – 6 mg). Through applying this method to samples taken from an Ordovician carbonate reservoir in the Yudong region of the Kuqa Depression, northern Tarim Basin, the timing of hydrothermally-triggered TSR alteration of a paleo-oil pool is established at ca. 224 – 206 Ma. SEM investigations demonstrate that Rb and Sr atoms mainly reside in the crystal lattice of the pyrites, because neither fluid nor mineral inclusions are found in the pyrites. The Rb-Sr isochrons indicate that the sufficient Rb/Sr fractionation and initial Sr isotopic homogenization can occur at sub-sample scale to enable the samples to be dated by this method. In addition, the

closure temperature (227 – 320 °C) for the Rb-Sr isotope system in pyrite is estimated to be higher than the precipitation temperature for pyrite in petroleum-related environments (below 200°C), suggesting that the Rb-Sr age of pyrite was not overprinted by post-precipitation alteration. This study therefore confirms that Rb-Sr pyrite geochronology is potentially an important tool for constraining events in petroleum systems. Besides obtaining reliable isotopic ages, the determination of stable (e.g. S) and radiogenic (e.g. Sr and Pb) isotopes of pyrites can lead to a greater understanding of petroleum systems.

## **Acknowledgments**

We thank Professor Lian-Jun Feng (Institute of Geology and Geophysics, CAS, Beijing) for sulfur isotope analyses. This work was supported by the Australian Research Council (ARC) Future Fellowship (FT140100826), the SINOPEC Key Laboratory on Hydrocarbon Accumulation (No. 33550007-17-ZC0613-0031), the National Major Petroleum Project of China (No. 2011ZX05006), and Strategic Priority Research Program of the Chinese Academy of Sciences (Grant No. XDA14010401). We also thank A/Prof. Fred Jourdan (Curtin University) for constructive suggestions on the constraints placed on dating methods for pyrites.

## References

BERNER, R. A. 1984. Sedimentary pyrite formation: an update. *Geochimica et cosmochimica Acta*, 48, 605-615.

CAI, C., HU, W. & WORDEN, R. H. 2001. Thermochemical sulphate reduction in Cambro–Ordovician carbonates in Central Tarim. *Marine and Petroleum Geology*, 18, 729-741.

CAI, C., LI, K., ANLAI, M., ZHANG, C., XU, Z., WORDEN, R. H., WU, G., ZHANG, B. & CHEN, L. 2009a. Distinguishing Cambrian from Upper Ordovician source rocks: Evidence from sulfur isotopes and biomarkers in the Tarim Basin. *Organic Geochemistry*, 40, 755-768.

CAI, C., LI, K., LI, H. & ZHANG, B. 2008. Evidence for cross formational hot brine flow from integrated  $^{87}\text{Sr}/^{86}\text{Sr}$ , REE and fluid inclusions of the Ordovician veins in Central Tarim, China. *Applied Geochemistry*, 23, 2226-2235.

CAI, C., WORDEN, R. H., WANG, Q., XIANG, T., ZHU, J. & CHU, X. 2002. Chemical and isotopic evidence for secondary alteration of natural gases in the Hetianhe Field, Bachu Uplift of the Tarim Basin. *Organic Geochemistry*, 33, 1415-1427.

CAI, C., ZHANG, C., CAI, L., WU, G., JIANG, L., XU, Z., LI, K., MA, A. & CHEN, L. 2009b. Origins of Palaeozoic oils in the Tarim Basin: evidence from sulfur isotopes and biomarkers. *Chemical*

Geology, 268, 197-210.

CAO, H.-W., ZHANG, S.-T., SANTOSH, M., ZHENG, L., TANG, L., LI, D., ZHANG, X.-H. & ZHANG, Y.-H. 2015. The Luanchuan Mo–W–Pb–Zn–Ag magmatic–hydrothermal system in the East Qinling metallogenic belt, China: Constrains on metallogenesis from C–H–O–S–Pb isotope compositions and Rb–Sr isochron ages. *Journal of Asian Earth Sciences*, 111, 751-780.

CHIARADIA, M., KONOPELKO, D., SELTMANN, R. & CLIFF, R. A. 2006. Lead isotope variations across terrane boundaries of the Tien Shan and Chinese Altay. *Mineralium Deposita*, 41, 411-428.

DONG, L., WAN, B., YANG, W., DENG, C., CHEN, Z., YANG, L., CAI, K. & XIAO, W. 2016. Rb-Sr geochronology of single gold-bearing pyrite grains from the Katbasu gold deposit in the South Tianshan, China and its geological significance. *Ore Geology Reviews*, 100, 99-110.

ELLIS, G. 2007. Hydrocarbon entrapment in Triassic to late Jurassic reservoirs in the Timor Sea, Australia-new insights. *APPEA Journal*, 47, 39-53.

GEORGIEV, S. V., STEIN, H. J., HANNAH, J. L., GALIMBERTI, R., NALI, M., YANG, G. & ZIMMERMAN, A. 2016. Re–Os dating of maltenes and asphaltenes within single samples of crude oil. *Geochimica et Cosmochimica Acta*, 179, 53-75.

HAN, Y., LI, X., ZHANG, S., ZHANG, Y. & CHEN, F. 2007. Single grain Rb-Sr dating of euhedral and cataclastic pyrite from the Qiyugou gold deposit in western Henan, central China. *Chinese Science Bulletin*, 52, 1820-1826.

HEDENQUIST, J. W. & LOWENSTERN, J. B. 1994. The role of magmas in the formation of hydrothermal ore deposits. *Nature*, 370, 519-527.

HU, Q., WANG, Y., MAO, J., WEI, R., LIU, S., YE, D., YUAN, Q. & DOU, P. 2015. Timing of the formation of the Changba-Lijiagou Pb-Zn ore deposit, Gansu Province, China: Evidence from Rb-Sr isotopic dating of sulfides. *Journal of Asian Earth Sciences*, 103, 350-359.

HUANG, H., ZHANG, S. & SU, J. 2016. Palaeozoic oil-source correlation in the Tarim Basin, NW China: A review. *Organic Geochemistry*, 94, 32-46.

JIA, C. & WEI, G. 2002. Structural characteristics and petroliferous features of Tarim Basin. *Chinese Science Bulletin*, 47, 1-11.

JIA, L., CAI, C., YANG, H., LI, H., WANG, T., ZHANG, B., JIANG, L. & TAO, X. 2015. Thermochemical and bacterial sulfate reduction in the Cambrian and Lower Ordovician carbonates in the Tazhong Area, Tarim Basin, NW China: evidence from fluid inclusions, C, S, and Sr isotopic data. *Geofluids*, 15, 421-437.

LARGE, R. R., DANYUSHEVSKY, L., HOLLIT, C., MASLENNIKOV, V., MEFFRE, S., GILBERT, S., BULL, S., SCOTT, R., EMSBO, P. & THOMAS, H. 2009. Gold and trace element zonation in pyrite using a laser imaging technique: Implications for the timing of gold in orogenic and Carlin-style sediment-hosted deposits. *Economic Geology*, 104, 635-668.

LARGE, R. R., HALPIN, J. A., DANYUSHEVSKY, L. V., MASLENNIKOV, V. V., BULL, S. W., LONG, J. A., GREGORY, D. D., LOUNEJEVA, E., LYONS, T. W. & SACK, P. J. 2014. Trace element content of sedimentary pyrite as a new proxy for deep-time ocean–atmosphere evolution. *Earth and Planetary Science Letters*, 389, 209-220.

LI, C.-F., CHU, Z.-Y., GUO, J.-H., LI, Y.-L., YANG, Y.-H. & LI, X.-H. 2015a. A rapid single column separation scheme for high-precision Sr–Nd–Pb isotopic analysis in geological samples using thermal ionization mass spectrometry. *Analytical Methods*, 7, 4793-4802.

LI, C.-F., GUO, J.-H., CHU, Z.-Y., FENG, L.-J. & WANG, X.-C. 2015b. Direct High-Precision Measurements of the  $^{87}\text{Sr}/^{86}\text{Sr}$  Isotope Ratio in Natural Water without Chemical Separation Using Thermal Ionization Mass Spectrometry Equipped with 1012  $\Omega$  Resistors. *Analytical Chemistry*, 87, 7426-7432.

LI, K., CAI, C., HE, H., JIANG, L., CAI, L., XIANG, L., HUANG, S. & ZHANG, C. 2011. Origin of palaeo - waters in the Ordovician

carbonates in Tahe oilfield, Tarim Basin: constraints from fluid inclusions and Sr, C and O isotopes. *Geofluids*, 11, 71-86.

LI, Q.-L., CHEN, F., YANG, J.-H. & FAN, H.-R. 2008. Single grain pyrite Rb–Sr dating of the Linglong gold deposit, eastern China. *Ore Geology Reviews*, 34, 263-270.

LI, S., SHI, Q., PANG, X., ZHANG, B. & ZHANG, H. 2012. Origin of the unusually high dibenzothiophene oils in Tazhong-4 Oilfield of Tarim Basin and its implication in deep petroleum exploration. *Organic geochemistry*, 48, 56-80.

LIAO, F., ZHANG, L., CHEN, N., SUN, M., SANTOSH, M., WANG, Q. & MUSTAFA, H. A. 2014. Geochronology and geochemistry of meta-mafic dykes in the Quanji Massif, NW China: Paleoproterozoic evolution of the Tarim Craton and implications for the assembly of the Columbia supercontinent. *Precambrian Research*, 249, 33-56.

LIU, J., JIANG, Z., LIU, K., GUI, L. & XING, J. 2016. Hydrocarbon sources and charge history in the Southern Slope Region, Kuqa Foreland Basin, northwestern China. *Marine and Petroleum Geology*, 74, 26-46.

LÜ, X., XIE, Q., YANG, N. & LI, J. 2007. Hydrocarbon accumulation in deep fluid modified carbonate rock in the Tarim Basin. *Chinese Science Bulletin*, 52, 184-192.

LUDWIG, K. 2003. User's manual for Isoplot 3.00: a geochronological toolkit for Microsoft Excel, Berkeley Geochronology Center, California, Special Publication 4, 1-71.

MACHEL, H. G., KROUSE, H. R. & SASSEN, R. 1995. Products and distinguishing criteria of bacterial and thermochemical sulfate reduction. *Applied Geochemistry*, 10, 373-389.

NI, Z.-Y., CHEN, Y.-J., LI, N. & ZHANG, H. 2012. Pb–Sr–Nd isotope constraints on the fluid source of the Dahu Au–Mo deposit in Qinling Orogen, central China, and implication for Triassic tectonic setting. *Ore Geology Reviews*, 46, 60-67.

RASMUSSEN, B. 2005. Evidence for pervasive petroleum generation and migration in 3.2 and 2.63 Ga shales. *Geology*, 33, 497-500.

RAVIKANT, V. & GOLANI, P., 2011. Rb-Sr direct dating of pyrite from the Pipela VMS Zn-Cu prospect, Rajasthan, NW India. *Journal of the Geological Society of India*. 77, 149-159.

REICH, M., DEDITIUS, A., CHRYSSOULIS, S., LI, J.-W., MA, C.-Q., PARADA, M. A., BARRA, F. & MITTERMAYR, F. 2013. Pyrite as a record of hydrothermal fluid evolution in a porphyry copper system: A SIMS/EMPA trace element study. *Geochimica et Cosmochimica Acta*, 104, 42-62.

RICIPUTI, L. R., COLE, D. R. & MACHEL, H. G. 1996. Sulfide

formation in reservoir carbonates of the Devonian Nisku Formation, Alberta, Canada: An ion microprobe study. *Geochimica et Cosmochimica Acta*, 60, 325-336.

ROTENBERG, E., DAVIS, D. W., AMELIN, Y., GHOSH, S. & BERGQUIST, B. A. 2012. Determination of the decay-constant of  $^{87}\text{Rb}$  by laboratory accumulation of  $^{87}\text{Sr}$ . *Geochimica et Cosmochimica Acta*, 85, 41-57.

SUN, T., QIAN, Z.-Z., LI, C., XIA, M.-Z. & YANG, S.-H. 2013. Petrogenesis and economic potential of the Erhongwa mafic-ultramafic intrusion in the Central Asian Orogenic Belt, NW China: constraints from olivine chemistry, U–Pb age and Hf isotopes of zircons, and whole-rock Sr–Nd–Pb isotopes. *Lithos*, 182, 185-199.

SUN, W.-Y., LI, S.-R., SANTOSH, M., WANG, X. & ZHANG, L.-J., 2014. Isotope geochemistry and geochronology of the Qiubudong silver deposit, central North China Craton: implications for ore genesis and lithospheric dynamics. *Ore Geology Reviews*, 57, 229-242.

WANG, C., DENG, J., SANTOSH, M., CARRANZA, E.J.M., GONG, Q., GUO, C., XIA, R. & LAI, X., 2015. Timing, tectonic implications and genesis of gold mineralization in the Xincheng gold deposit, China: C–H–O isotopes, pyrite Rb–Sr and zircon fission track thermochronometry. *Ore Geology Reviews*, 65, 659-673.

WANG, Y., ZENG, Q. & LIU, J., 2014. Rb – Sr Dating of Gold -

bearing Pyrites from Wulaga Gold Deposit and its Geological Significance. *Resource Geology*, 64, 262-270.

WORDEN, R. & SMALLEY, P. 1996. H<sub>2</sub>S-producing reactions in deep carbonate gas reservoirs: Khuff Formation, Abu Dhabi. *Chemical Geology*, 133, 157-171.

XU, Y.-G., WEI, X., LUO, Z.-Y., LIU, H.-Q. & CAO, J. 2014. The Early Permian Tarim Large Igneous Province: main characteristics and a plume incubation model. *Lithos*, 204, 20-35.

YANG, J.-H. & ZHOU, X.-H. 2001. Rb-Sr, Sm-Nd, and Pb isotope systematics of pyrite: Implications for the age and genesis of lode gold deposits. *Geology*, 29, 711-714.

YANG, J. & ZHOU, X. 2000. The Rb-Sr isochron of ore and pyrite sub-samples from Linglong gold deposit, Jiaodong Peninsula, eastern China and their geological significance. *Chinese Science Bulletin*, 45, 2272-2277.

YAO, J., HUA, R. & LIN, J. 2006. REE, Pb-S isotope geochemistry, and Rb-Sr isochron age of pyrites in the Baoshan deposit, south Hunan province, China. *Acta Geologica Sinica*, 80, 1045-1054.

YU, J., MO, X., DONG, G., YU, X., XING, F., LI, Y. & HUANG, X. 2011. Felsic volcanic rocks from northern Tarim, NW China: Zircon U-Pb dating and geochemical characteristics. *Acta Petrologica Sinica*, 27, 2184-2194.

ZHANG, D., ZHOU, T., YUAN, F., JOWITT, S. M., FAN, Y. & LIU, S. 2012. Source, evolution and emplacement of Permian Tarim Basalts: evidence from U–Pb dating, Sr–Nd–Pb–Hf isotope systematics and whole rock geochemistry of basalts from the Keping area, Xinjiang Uygur Autonomous region, northwest China. *Journal of Asian Earth Sciences*, 49, 175-190.

ZHANG, L., SHEN, Y., LIU, T., ZENG, Q., LI, G. & LI, H. 2003.  $^{40}\text{Ar}/^{39}\text{Ar}$  and Rb–Sr isochron dating of the gold deposits on northern margin of the Jiaolai Basin, Shandong, China. *Science in China Series D: Earth Sciences*, 46, 708-718.

ZHANG, S. & HUANG, H. 2005. Geochemistry of Palaeozoic marine petroleum from the Tarim Basin, NW China: Part 1. Oil family classification. *Organic Geochemistry*, 36, 1204-1214.

ZHANG, Y., LIU, J. & GUO, Z. 2010. Permian basaltic rocks in the Tarim basin, NW China: implications for plume–lithosphere interaction. *Gondwana Research*, 18, 596-610.

ZHANG, Y., ZWINGMANN, H., LIU, K., TODD, A. & LUO, X. 2011. Hydrocarbon charge history of the Silurian bituminous sandstone reservoirs in the Tazhong uplift, Tarim Basin, China. *AAPG Bulletin*, 95, 395-412.

ZHAO, X.-F., ZHOU, M.-F., LI, J.-W., SELBY, D., LI, X.-H. & QI, L. 2013. Sulfide Re–Os and Rb–Sr isotope dating of the Kangdian IOCG metallogenic province, southwest China: Implications for

regional metallogenesis. *Economic Geology*, 108, 1489-1498.

ZHOU, J.-F., ZHANG, H.-Q., YU, J.-P., ZHU, Y.-F., YAO, Q.-Z. & YU-CHUN, Y. 2015. Analysis of the Hydrocarbon Accumulation Conditions and Exploration Potential in the Ordovician in Yudong Area of West Tabei Uplift. *Natural Gas Geoscience*, 26, 121-129.

ZHOU, M.-F., ZHAO, J.-H., JIANG, C.-Y., GAO, J.-F., WANG, W. & YANG, S.-H. 2009. OIB-like, heterogeneous mantle sources of Permian basaltic magmatism in the western Tarim Basin, NW China: implications for a possible Permian large igneous province. *Lithos*, 113, 583-594.

ZHOU, J., HUANG, Z., ZHOU, M., LI, X. & JIN, Z. 2013. Constraints of C–O–S–Pb isotope compositions and Rb–Sr isotopic age on the origin of the Tianqiao carbonate-hosted Pb–Zn deposit, SW China. *Ore Geology Reviews*, 53, 77-92.

ZHU, D.-Y. & MENG, Q.-Q. 2010. Genesis of pyrite in Ordovician carbonate of the Tarim Basin. *Acta Petrologica et Mineralogica*, 29, 516-524.

ZHU, G., ZHANG, B., YANG, H., SU, J. & HAN, J. 2014. Origin of deep strata gas of Tazhong in Tarim Basin, China. *Organic Geochemistry*, 74, 85-97.

ZOU, S.-Y., LI, Z.-L., SONG, B., ERNST, R. E., LI, Y.-Q., REN, Z.-Y., YANG, S.-F., CHEN, H.-L., XU, Y.-G. & SONG, X.-Y. 2015.

Zircon U–Pb dating, geochemistry and Sr–Nd–Pb–Hf isotopes of the Wajilitag alkali mafic dikes, and associated diorite and syenitic rocks: implications for magmatic evolution of the Tarim Large Igneous Province. *Lithos*, 212, 428-442.

## **Chapter 5**

### **Organic and Re-Os isotope geochemistry of bituminous dolomite in Anyue gasfield, Sichuan Basin, southwest China**

**Shaojie Li, Xuan-Ce Wang, Zhu-Yin Chu, Simon A. Wilde, Alex  
I. Holman, Kliti Grice, Keyu Liu**

*Organic Geochemistry, To be submitted*

## Abstract

Neoproterozoic-Cambrian marine bituminous dolomite is the natural gas reservoir for the giant Anyue gasfield in the central Sichuan Basin, southwest China. This study investigated the molecular composition of extractable organic matter and rhenium-osmium (Re-Os) isotope systematics of the bituminous dolomite using drillcores from the Anyue gasfield. Biodegradation-sensitive organic parameters classified samples into two groups: group 1 is characterized by an insignificant hump in saturated total ion chromatograms (TICs) and lower  $C_{28}$  norhopane/ $C_{29}$  hopane ( $NH_{28}/H_{29}$ ) values (0.38 – 0.52); whereas group 2 is characterized by an obvious hump in saturated TICs and higher  $NH_{28}/H_{29}$  values (0.85 – 1.05). This indicates that there are two components, biodegraded and fresh, in these samples, and that samples of group 2 contain higher proportions of the biodegraded component. Both components are over-mature (MPI-1 equivalent vitrinite reflectance values are 2.34% – 2.74%), and marine shale is their dominant source rock as suggested by diagnostic scatter plots ( $Ph/nC_{18}$ - $Pr/nC_{17}$  vs  $Pr/Ph$ ,  $Ph/nC_{18}$  vs  $Pr/nC_{17}$ ,  $C_{24}/C_{23}$  vs  $C_{22}/C_{21}$  tricyclic terpanes and  $C_{26}/C_{25}$  tricyclic terpane vs  $C_{31}R/C_{30}$  hopane ratios). Compared to the fresh component, the biodegraded component is characterized by (1) a higher proportion of carbonate-derived hydrocarbons (higher  $C_{31}R/C_{30}$  hopane ratio) and (2) a higher content of bacterial-derived organic matter (higher  $C_{27}/C_{29}$   $\alpha\alpha\alpha$  20R sterane ratio). The coexistence of biodegraded and fresh components suggests that two

episodes of paleo-oil charge may have occurred in the reservoir and that the earlier-charged hydrocarbons were biodegraded before the charge of the fresh component. Organic source and biodegradation influenced the Re-Os distribution in bituminous dolomite. Samples with higher Re-Os contents are characterized by higher C<sub>31</sub>R/C<sub>30</sub> hopane and NH<sub>28</sub>/H<sub>29</sub> ratios, indicating that carbonate-derived hydrocarbons may contain higher Re-Os contents and biodegradation could also result in higher contents of both elements. The positive trend between <sup>187</sup>Re/<sup>188</sup>Os and C<sub>31</sub>R/C<sub>30</sub> hopane ratios further indicates that the mixing of carbonate-/shale-derived hydrocarbons may influence the Re/Os fractionation. Duplicate analysis of a single bituminous dolomite reveals significant subsample-scale variation in Re-Os isotopic composition, and the Re-Os isotopic heterogeneity results in apparent isochron ages which are older than the depositional age of the host rock. A ternary mixing scenario is presented in the 1/<sup>192</sup>Os vs <sup>187</sup>Os/<sup>188</sup>Os plot of the samples, comprising components I (high Os concentration and <sup>187</sup>Os/<sup>188</sup>Os ratio), II (high Os concentration and low <sup>187</sup>Os/<sup>188</sup>Os ratio) and III (low Os concentration and <sup>187</sup>Os/<sup>188</sup>Os ratio). According to the correlations between biomarkers and Re-Os systematics, higher Os concentration of components I and II could have resulted from biodegradation and higher proportions of carbonate source contributions, thus, they may represent the signatures of the earlier-charged/biodegraded hydrocarbons, whereas component III corresponds to the later-charged fresh hydrocarbons. The mixing of carbonate- and shale-derived hydrocarbons in the earlier-charged

components may fractionate their Re/Os ratios, which further resulted in the variable  $^{187}\text{Os}/^{188}\text{Os}$  ratios between components I and II. Therefore, Os isotopic composition may be a potential indicator for characterizing hydrocarbon source in complex petroleum systems and provide additional evidence for cross-checking results obtained from other disciplines (e.g. biomarker geochemistry).

**Key words:** Organic geochemistry, Re-Os geochemistry, Neoproterozoic-Cambrian natural gas reservoir, bituminous dolomite, Sichuan Basin, southwest China.

## 5.1 Introduction

Industrial discoveries in recent years have extended the petroleum exploration frontier to ancient strata (e.g. Precambrian: Craig et al., 2013; Zou et al., 2015). The Neoproterozoic-Cambrian Anyue gasfield, hosted in marine bituminous dolomite, is a giant hydrocarbon reservoirs in the central Sichuan Basin, southwest China, containing  $\sim 10,000 \times 10^8 \text{ m}^3$  natural gas (Figure 5.1. Du et al., 2014; Zou et al., 2015). Petroleum system analysis has identified two main episodes of oil accumulation, during the Ordovician-Silurian and Triassic-middle Jurassic, after which natural gas was generated by thermal cracking of oils (Figure 5.2. Zou et al., 2015). A regional uplift occurred during the Devonian-Permian, between the two oil accumulation events (Zou et al., 2015). Paleotemperature of the Neoproterozoic-Cambrian dolomite reservoir was below 60 °C in the later stage of uplift (Carboniferous-Permian), which could result in biodegradation of oils (Figure 5.2. Zou et al., 2015). Indeed, the influence of biodegradation on the molecular composition of reservoir bitumen has been observed, e.g. the presence of demethylated hopanes (Shi et al., 2017). Early-charged oil may be more significantly influenced by biodegradation compared to the later-charged oils. Therefore, biodegradation-sensitive indicators have the potential to differentiate and characterize hydrocarbon sources of two oil accumulation events. The primary objective of this study was to fill this knowledge gap through investigating the molecular composition of extractable

organic matter and rhenium-osmium (Re-Os) isotopic geochemistry of the bituminous reservoir rocks intersected by petroleum drillholes in the Anyue gasfield (Figure 5.1A).

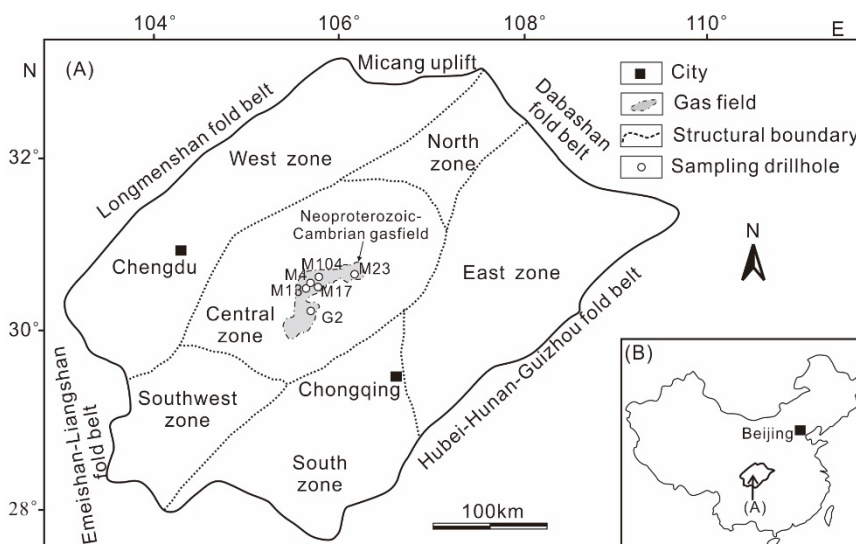


**Figure 5.1:** A: Simplified geological map of the Sichuan Basin, showing the location of the Anyue gasfield and studied petroleum drillholes. B: Location of Sichuan Basin in southwest China.

The molecular composition of extractable organic matter is sensitive to organic source, formation environment, maturation and biodegradation of hydrocarbons, thus it could provide significant information for characterizing hydrocarbon source rocks (Peters et al., 2005). Re and Os are two organophilic trace metallic elements (Ravizza and Turekian, 1989; Selby et al., 2007a) and  $^{187}\text{Os}$  is the radiogenic product of  $^{187}\text{Re}$  (Naldrett and Libby, 1948). Recent studies have revealed the potential of the  $^{187}\text{Re}$ - $^{187}\text{Os}$  isotope system for fingerprinting hydrocarbons (Cumming et al., 2014; Finlay et al.,

2011; Finlay et al., 2012; Ge et al., 2016; Ge et al., 2018; Georgiev et al., 2016; Lillis and Selby, 2013; Liu et al., 2018; Rooney et al., 2012). Therefore, Re-Os isotopic measurements may provide independent evidence for cross-checking conclusions drawn from organic parameters. In addition, knowledge about behaviour of the Re-Os isotopic system in bituminous dolomite is scant, and integration of organic geochemistry with Re-Os isotopes may improve understanding of this knowledge gap.

## **5.2 Geological background**

The Sichuan Basin is a large petroliferous basin located in southwest China, covering an area of  $\sim 1.8 \times 10^5$  km<sup>2</sup> (Figures 5.1A and 5.1B. Cheng et al., 2018; Zou et al., 2015). The basin was formed on the Precambrian Yangtze Craton basement, and surrounded by the Micang uplift-Dabashan, Hubei-Hunan-Guizhou, Emeishan-Liangshan and Longmenshan fold belts (Figure 5.1A. Du et al., 2014; Korsch et al., 1991; Zou et al., 2015). The Sichuan Basin can be divided into six zones, referred to as the north, east, south, southwest, west and central zones (Figures 5.1A. Du et al., 2014; Korsch et al., 1991; Zou et al., 2015). The Anyue gasfield is located in the central zone of the Sichuan Basin (Figure 5.1A).

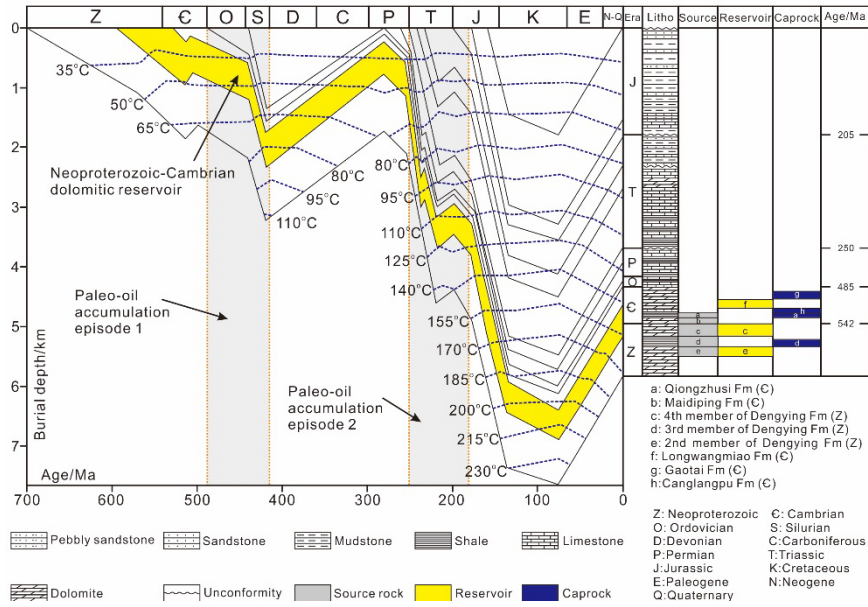


**Figure 5.2:** Burial history, petroleum system elements (source rock, reservoir and cap rocks) and petroleum accumulation events diagrams for the Neoproterozoic-Cambrian Anyue gas system in central Sichuan Basin Modified after Zou et al. (2015).

The basin accommodates sediments that were deposited from the Neoproterozoic to Cenozoic (Korsch et al., 1991). Five potential marine organic-rich hydrocarbon source beds have been identified for the Anyue gasfield, consisting of the second (dolomite), third (shale) and fourth (dolomite) members of the Neoproterozoic Dengying Formation, the lower Cambrian Maidiping (dolomite) and Qiongzhusi (shale) formations (Figure 5.2. Zou et al., 2015). Marine dolomitic rocks in the Neoproterozoic Dengying Formation and lower Cambrian Longwangmiao Formation are reservoirs of the Anyue gasfield (Figure 5.2. Cheng et al., 2018; Shi et al., 2017; Zou et al., 2015). The Lower Cambrian Gaotai, Canglangpu-Qiongzhusi

formations. and the third member of the Neoproterozoic Dengying Formation, are seals for the gas reservoirs (Figure 5.2. Shi et al., 2017; Zou et al., 2015).

Hydrocarbon gas in the reservoir is dominated by methane (CH<sub>4</sub>), but also contains some ethane (C<sub>2</sub>H<sub>6</sub>) (99.72% – 99.97% and 0.03% – 0.28%, respectively), with trace amount of propane (C<sub>3</sub>H<sub>8</sub>) (Shi et al., 2017; Wei et al., 2015). Natural gas has carbon isotopic ratios similar to kerogen in the potential source rocks, suggesting their genetic correlation (Shi et al., 2017; Wei et al., 2015).  $\delta^{13}\text{C}_1$  and  $\delta^{13}\text{C}_2$  values of natural gas are -33.9‰ to -32.1‰ and -35.3‰ to -26.8‰, respectively, overlapping  $\delta^{13}\text{C}$  values of the kerogen in the source rocks (Cambrian shales: -36.4‰ to -29.9‰, Neoproterozoic mudstone: -34.5‰ to -28.8‰, Neoproterozoic carbonate rock: -33.7‰ to -23.8‰. Shi et al., 2017; Wei et al., 2015). Biomarker and carbon isotopic studies of reservoir bitumen suggest that shales in the Neoproterozoic-early Cambrian strata may be the dominant source rocks, with a partial contribution from carbonate source rocks, e.g. low C<sub>22</sub>/C<sub>21</sub> tricyclic terpane, C<sub>24</sub>/C<sub>23</sub> tricyclic terpane, C<sub>31</sub> R/C<sub>30</sub> hopane, C<sub>35</sub>S/C<sub>34</sub>S hopane and C<sub>29</sub>/C<sub>30</sub> hopane ratios (Cheng et al., 2018), and depleted  $\delta^{13}\text{C}$  values (-28.8‰ – -25.6‰. Shi et al., 2017). Aromatic hydrocarbon maturation parameters suggest that reservoir bitumen is highly mature, with high methylphenanthrene ratios, a high methylphenanthrene distribution factor and high equivalent vitrinite reflectance values (1.3% – 2.9%. Cheng et al., 2018).

## **5.3 Samples and methods**

Eight bituminous dolomite reservoir drillcores were investigated from the Anyue gasfield in this study (Figure 5.1A and Table 5.1). Five samples were collected from the Cambrian Longwangmiao Formation, including two samples from depths of 4627 m and 4642 m in drillhole M17, two samples from depths of 4611m and 4622 m in drillhole M13 and one sample from a depth of 5442 m in drillhole M23 (Table 5.1). Three samples also were collected from the 4<sup>th</sup> member of the Neoproterozoic Dengying Formation, including one sample from a depth of 5715 m in drillhole M4, one sample from a depth of 5735 m in drillhole M104 and one sample from a depth of 5479 m in drillhole G2 (Table 5.1).

Each rock sample was divided into two parts for organic and inorganic analytical work: (1) microwave-assisted extraction of organic matter and gas chromatography-mass spectrometry (GC-MS), and (2) Re-Os chemistry and mass spectrometry.

### **5.3.1 Microwave-assisted extraction and silica gel chromatography of organic matter**

Approximately 20 grams of each rock sample was ground into powder for microwave-assisted extraction. The extraction was performed on a Milestone Start E microwave extraction unit at the Western Australian Organic & Isotope Geochemistry Centre (WA-OIGC), Curtin University, Australia. Powders of each sample were

placed in an extraction vessel with 50 mL of dichloromethane (DCM) + methanol solvent mixture (9:1). The extraction used a temperature program of 80° C for 15 minutes after a ramp of 8° C/min. After extraction, the sample was centrifuged and the solvent was transferred to a clean bottle containing activated copper for removing any elemental sulphur present in the sample. After sulphur-removal, the extract was further filtered using an activated MgSO<sub>4</sub> column (5.5cm × 0.5cm). The extract was then dried and re-dissolved in a clean beaker containing DCM and activated silica gel. The silica gel/extract powder mixture was loaded into an activated silica gel column (5.5cm×0.5cm) for compositional fractionation after evaporating the DCM. The saturated, aromatic and polar fractions were eluted with *n*-hexane (2ml), DCM in *n*-hexane (2ml, 30%) and a mixture of DCM and methanol (2ml, 1:1), respectively (Holman et al., 2012). The saturated and aromatic fractions were analysed by GC-MS after evaporation and re-dissolution in *n*-hexane.

### **5.3.2 Gas chromatography-mass spectrometry**

GC-MS analysis of saturated and aromatic fractions was conducted on a HP5973 MSD connected to a HP6890 gas chromatograph. The GC was equipped with a DB-1 capillary column (J&W Scientific, 60 m×0.25 mm i.d., 0.25 µm phase thickness). The GC oven was programmed from 40° C to 300° C (3° C/min) with initial and final hold times of 1 and 30 min, respectively. Samples were injected by a HP6890 auto-sampler and the carrier gas was helium at a linear

velocity of 28 cm/s. The MS was operating under the conditions of source temperature of 180° C, ionisation energy of 70 eV and electron multiplier voltage of 1800V. Aromatic fractions were scanned in full scan mode (mass range: 50 – 550 amu). Saturated fractions were scanned in both full scan mode (mass range: 50–550 amu) and selective ion monitoring (SIM) mode (m/z 83, 97, 123, 149, 163, 177, 183, 191, 205, 217, 218, 231, 259, 258, 372, 386, 400, 414.). Saturated and aromatic hydrocarbons were identified through comparisons with the mass spectra and retention times of reference compounds given in several publications (Asif et al., 2011; Chakhmakhchev et al., 1997; George et al., 2008; Grice et al., 2007; Hall et al., 2014; Huang and Li, 2016; Kruge, 2000; Wang et al., 1994). Molecular ratios were calculated based on the integration area of the corresponding compound peaks utilizing the HP ChemStation Data Analysis software.

### **5.3.3 Re-Os chemistry, negative thermal ionization mass spectrometry (N-TIMS) and multicollector-inductively coupled plasma mass spectrometry (MC-ICP-MS)**

Re-Os chemistry/mass spectrometry was carried out at the State Key Laboratory of Lithospheric Evolution, Institute of Geology and Geophysics, Chinese Academy of Sciences (IGGCAS), Beijing. Portions of fresh rock samples were cleaned with distilled water and dried completely prior to being broken into chips by a clean cloth-wrapped hammer. Rock chips were ground into powders (~200 mesh)

using an agate mill. Approximately 200 milligram powders of each sample were mixed with  $^{185}\text{Re}$ - $^{190}\text{Os}$  isotopic tracers and digested in 8 ml aqua regia (12N HCl: 16N HNO<sub>3</sub> = 1:3) in a Carius tube at 220° C for 48 hrs. Rhenium and osmium fractions were separated by solvent extraction (tetrachloromethane, CCl<sub>4</sub>). The rhenium fraction was purified through anion exchange chromatography, and the osmium fraction was purified using micro-distillation.

The rhenium fraction was dissolved in dilute nitric acid and measured by MC-ICP-MS (Thermo Fisher Scientific Neptune) in static mode using Faraday Cups. The osmium fraction was loaded onto high-purity platinum filaments and measured by N-TIMS (GV, Isoprobe-T) in peak-jumping mode using secondary electron multipliers. Acids used during the Re-Os chemistry were all analytical reagent (AR) grade and were purified utilizing a Savillex<sup>TM</sup> DST-1000 sub-boiling distillation system. Ultrapure water with resistivity of 18.2 MΩ·cm<sup>-1</sup> obtained from a Milli-Q Element system was used throughout this work.

Total procedural blanks of the chemistry were less than 1.0 pg for Os with  $^{187}\text{Os}/^{188}\text{Os}$  ratio of 0.170, and less than 3.4 pg for Re. Throughout the period of this study, the UMCP Os standard yielded  $^{187}\text{Os}/^{188}\text{Os}$  ratio of  $0.11384 \pm 0.00068$  (n = 4, 2σ). The in-house Re standard solution gave  $^{187}\text{Re}/^{185}\text{Re} = 1.69831 \pm 0.00050$  (n = 4, 2σ). The Re and Os contents, and  $^{187}\text{Os}/^{188}\text{Os}$  ratios were blank-corrected.  $^{187}\text{Os}/^{188}\text{Os}$  ratios were normalized to  $^{192}\text{Os}/^{188}\text{Os} = 3.08271$ . Re-Os isochron ages were calculated using the Isoplot T3.0 software

(Ludwig, 2003), applying a decay constant ( $\lambda^{187}\text{Re}$ ) of  $1.666 \times 10^{-11} \text{ yr}^{-1}$  (Selby et al., 2007b; Smoliar et al., 1996).

## 5.4 Results

### 5.4.1 Molecular composition of extractable organic matter

#### 5.4.1.1 Paraffin

The studied samples contain detectable saturated hydrocarbons (Figures 5.3 and A5.1). Both unimodal and bimodal distribution patterns are exhibited in *n*-alkanes (Figure A5.2). Samples M17-4627, M17-4642, M13-4611 and M13-4622 contain *n*-alkanes of a general unimodal pattern with a dominant peak in middle-chain (e.g.  $n\text{C}_{20}$ ,  $n\text{C}_{21}$ ,  $n\text{C}_{22}$  and  $n\text{C}_{23}$ ) and a minor peak in long-chain *n*-alkanes (e.g.  $n\text{C}_{29}$ , Figures A5.2A-5.2D). Samples M23-5442, M4-5715 and M104-5735 have more obvious bimodal patterns in *n*-alkanes with a large peak in  $n\text{C}_{17}$  or  $n\text{C}_{18}$  and a small peak in middle-chain *n*-alkanes (e.g.  $n\text{C}_{22}$ ,  $n\text{C}_{23}$  and  $n\text{C}_{24}$ , Figures A5.2E-A5.2G). Sample G2-5479 has two comparable peaks in *n*-alkanes,  $n\text{C}_{17}$  and  $n\text{C}_{26}$  (Figure A5.2H). In contrast to samples M17-4627, M17-4642, M13-4611 and M13-4622, saturated fractions in samples M23-5442, M4-5715, M104-5735 and G2-5479 have humps coexisting with middle-chain *n*-alkanes and higher contents of isoprenoid paraffins (e.g. pristane and phytane) (Figures 3 and A5.1). The studied samples do not have an odd/even preference, with carbon preference index (CPI)

and odd-even preference (OEP) values approximate 1 (Table 5.2). Pristane/phytane ratios (Pr/Ph) of the samples range between 0.27 and 1.10 (Table 5.2).

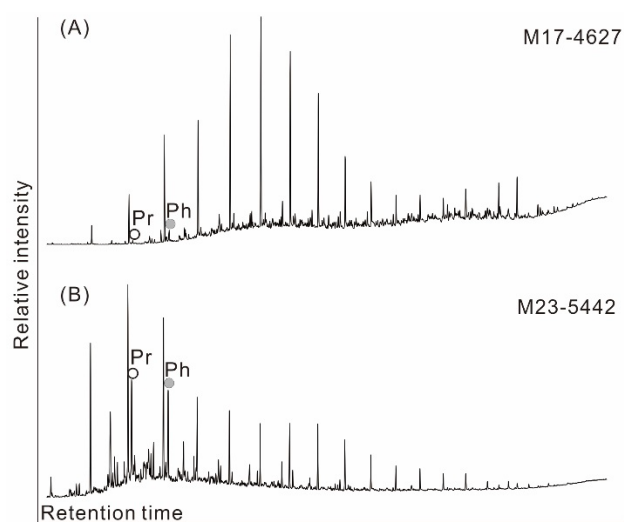


**Figure 5.3:** Representative total ion chromatograms (TICs) of saturated fractions of the studied samples.

**Table 5.1:** Basic information for bituminous dolomite samples from the Anyue gasfield used in this study

No	Drillhole	Depth/meter	Strata	Lithology
1	M17	4627	Cambrian Longwangmiao Formation	Bituminous dolomite
2	M17	4642	Cambrian Longwangmiao Formation	Bituminous dolomite
3	M13	4611	Cambrian Longwangmiao Formation	Bituminous dolomite
4	M13	4622	Cambrian Longwangmiao Formation	Bituminous dolomite
5	M23	5442	Cambrian Longwangmiao Formation	Bituminous dolomite
6	M4	5715	Neoproterozoic 4 <sup>th</sup> member of Dengying Formation	Bituminous dolomite
7	M104	5735	Neoproterozoic 4 <sup>th</sup> member of Dengying Formation	Bituminous dolomite
8	G2	5479	Neoproterozoic 4 <sup>th</sup> member of Dengying Formation	Bituminous dolomite

**Table 5.2:** Molecular ratios of n-alkanes and isoprenoid paraffin extracted from bituminous dolomite samples from the Anyue gasfield

ID	A	B	C	D	E	F	G	H	I
M17-4627	0.27	0.05	0.09	0.04	1.00	1.12	15.29	1.61	21
M17-4642	0.30	0.05	0.11	0.05	1.06	1.15	9.84	1.40	20
M13-4611	0.51	0.30	0.31	0.01	0.99	1.16	4.33	0.25	23
M13-4622	0.24	0.24	0.35	0.12	0.96	1.03	6.43	0.45	22
M23-5442	1.10	0.57	0.73	0.16	0.98	1.04	4.08	2.58	17
M4-5715	0.66	0.59	0.65	0.06	0.93	0.98	1.88	1.72	18
M104-5735	0.68	0.53	0.67	0.14	0.90	0.99	2.00	1.84	18
G2-5479	1.05	0.48	0.55	0.07	0.92	0.98	0.53	1.00	17

\*A:Pr/Ph; B: Pr/nC<sub>17</sub>; C: Ph/nC<sub>18</sub>; D: Ph/nC<sub>18</sub>-Pr/nC<sub>17</sub>; E: OEP =  $(nC_{19} + 6*nC_{21} + nC_{23}) / (4*nC_{20} + 4*nC_{22})$ ; F: CPI =  $0.5 * [(nC_{13} + nC_{15} + nC_{17} + nC_{19}) / (nC_{12} + nC_{14} + nC_{16} + nC_{18}) + (nC_{13} + nC_{15} + nC_{17} + nC_{19}) / (nC_{14} + nC_{16} + nC_{18} + nC_{20})]$ ; G:  $nC_{21} + nC_{22} / nC_{28} + nC_{29}$ ; H:  $\Sigma nC_{21} / \Sigma nC_{22+}$ ; I: Carbon number maximum of n-alkanes.

### 5.4.1.2 Terpane and sterane

Samples M23-5442, M4-5715, M104-5735 and G2-5479 have higher tricyclic terpanes/hopane ratios (TT/H) compared to samples M17-4627, M17-4642, M13-4611 and M13-4622 (Table 5.3 and Figure A5.3). The studied samples have similar terpane indicators sensitive to maturation (e.g. Ts/(Ts+Tm), Ts/C<sub>30</sub> hopane, C<sub>29</sub>Ts/(C<sub>29</sub> hopane+C<sub>29</sub> Ts), Table 5.3), depositional environment (e.g. gammacerane index, Table 5.3) and organic source (e.g. C<sub>21</sub>/C<sub>23</sub> TT, C<sub>22</sub>/C<sub>21</sub> TT, C<sub>24</sub>/C<sub>24</sub>+C<sub>26</sub> TT, C<sub>26</sub>/C<sub>25</sub> TT, C<sub>31</sub> R/C<sub>30</sub> H, Table 5.3). Demethylated hopanes were also identified in these samples with C<sub>28</sub> norhopane/C<sub>29</sub> hopane distributed between 0.38 and 1.05 (Table 5.3 and Figure A5.4).

In terms of steranes, the samples have similar C<sub>27</sub> diasteranes/(diasteranes + regular steranes) ratios (0.24–0.28). Samples M23-5442, M4-5715, M104-5735 and G2-5479 have higher pregnane/regular sterane but lower C<sub>27</sub>/C<sub>29</sub> regular sterane ratios compared to samples M17-4627, M17-4642, M13-4611 and M13-4622 (Table 5.4 and Figure A5.5). Sterane thermal maturity indicators of the samples, such as C<sub>29</sub> ααα20S/(20S+20R) regular sterane and C<sub>29</sub> αββ/(αββ+ααα) regular sterane, are distributed in similar ranges (Table 5.4).

**Table 5.3:** Molecular ratios of terpane extracted from bituminous dolomite samples from the Anyue gasfield

ID	A	B	C	D	E	F	G	H	I	J	K	L	M	N	O
M17-4627	0.72	0.50	0.31	0.51	0.63	0.06	0.37	0.48	0.16	0.19	0.54	10.54	0.19	0.61	0.41
M17-4642	0.46	0.65	0.32	0.34	0.87	0.05	0.21	0.50	0.20	0.20	0.58	11.21	0.14	0.65	0.38
M13-4611	0.50	0.53	0.35	0.40	0.69	0.05	0.22	0.45	0.15	0.22	0.56	10.14	0.18	0.61	0.46
M13-4622	0.47	0.64	0.33	0.47	0.70	0.05	0.23	0.45	0.15	0.21	0.54	9.53	0.19	0.56	0.52
M23-5442	1.22	0.47	0.22	0.60	0.52	0.09	0.84	0.49	0.18	0.25	0.54	8.21	0.18	0.55	0.85
M4-5715	1.35	0.46	0.20	0.60	0.63	0.08	0.86	0.50	0.16	0.24	0.53	9.31	0.20	0.65	1.04
M104-5735	1.28	0.47	0.19	0.68	0.48	0.10	1.09	0.50	0.19	0.23	0.53	7.94	0.20	0.59	1.05
G2-5479	1.35	0.46	0.20	0.64	0.47	0.11	1.19	0.53	0.22	0.26	0.54	7.02	0.16	0.58	1.03

\*A:  $C_{21}/C_{23}$  tricyclic terpane; B:  $C_{24}/C_{23}$  tricyclic terpane; C:  $C_{22}/C_{21}$  tricyclic terpane; D:  $C_{24}/C_{24}+C_{26}$  tricyclic terpane; E:  $C_{26}/C_{25}$  tricyclic terpane; F:  $C_{24}$  tetracyclic terpane/ $C_{30}$  hopane; G: tricyclic terpane/hopane; H: Ts/Ts+Tm; I: Ts/ $C_{30}$  hopane; J:  $C_{29}Ts/(C_{29}hopane+C_{29}Ts)$ ; K:  $C_{29}/C_{30}$  hopane; L: Gammacerane index=  $100 * \text{gammacerane}/(\text{gammacerane}+C_{30} \text{ hopane})$ ; M:  $C_{31} R/C_{30}$  hopane; N:  $C_{32}22S/C_{32} (22S+22R)$  hopane; O:  $C_{28}$  norhopane/ $C_{29}$  hopane.

**Table 5.4:** Molecular ratios of sterane and aromatic hydrocarbons extracted from bituminous dolomite samples from the Anyue gasfield

ID	A	B	C	D	E	F	G	H	I	J	K	L	M	N
M17-4627	0.04	30.26	28.26	41.48	0.76	0.68	0.42	0.40	0.24	-	-	-	-	-
M17-4642	0.03	28.79	32.55	38.66	0.77	0.84	0.47	0.37	0.24	-	2.27	0.65	-	-
M13-4611	0.05	28.22	29.74	42.04	0.62	0.71	0.44	0.37	0.26	-	3.82	0.73	-	-
M13-4622	0.04	30.12	28.73	41.14	0.72	0.70	0.44	0.38	0.24	-	2.13	0.63	-	-
M23-5442	0.24	34.47	28.22	37.31	1.03	0.76	0.54	0.39	0.28	0	1.65	0.58	1.20	2.34
M4-5715	0.30	35.18	29.58	35.24	1.02	0.84	0.49	0.39	0.27	0	1.47	0.52	0.98	2.46
M104-5735	0.34	33.24	28.74	38.02	0.97	0.76	0.47	0.44	0.28	0.04	1.65	0.59	0.47	2.74
G2-5479	0.30	36.09	28.48	35.42	1.04	0.80	0.50	0.40	0.28	0.06	2.15	0.60	0.53	2.71

\*A: ( $C_{21-22}$ ) pregnane /( $C_{27-29}$ ) regular sterane; B: Percentage of  $C_{27}$  regular sterane in all regular steranes (%); C: Percentage of  $C_{28}$  regular sterane in all regular steranes (%); D: Percentage of  $C_{29}$  regular sterane in all regular steranes (%); E:  $C_{27}/C_{29}$   $\alpha\alpha\alpha$  20R sterane; F:  $C_{28}/C_{29}$  sterane; G:  $C_{29}$   $\alpha\alpha\alpha$ 20S/(20S+20R) regular sterane; H:  $C_{29}$   $\alpha\beta\beta/(\alpha\beta\beta+\alpha\alpha\alpha)$  regular sterane; I:  $C_{27}$  diasteranes/(diasteranes+ regular steranes); J: Dibenzothiophene/phenanthrene (DBT/P); K: Methylphenanthrene ratio (MPR) = 2-/1-MP; L: Methylphenanthrene distribution fraction (MPDF) = (3-+2-)/ $\Sigma$ MP; M: Methylphenanthrene index (MPI-1) =  $1.5 \times (3-MP+2-MP)/(P+9-MP+1-MP)$ ; N: vitrinite reflectance ( $R_c$ ) calculated based on MPI-1, and  $R_c = -0.55 \times MPI-1 + 3$ . \*\* - denotes compound was not detected.

### 5.4.1.3 Aromatic hydrocarbons

Some aromatic hydrocarbons were also detected in the samples (Figure A5.6). Compared to samples M17-4627, M17-4642, M13-4611 and M13-4622, more aromatic hydrocarbon species were found in samples M23-5442, M4-5715, M104-5735 and G2-5479, including dibenzothiophene (DBT), phenanthrene (P), methylphenanthrene (MP), dimethylphenanthrene (DMP), trimethylphenanthrene (TMP) and methyl-dibenzothiophene (MDBT) (Figure A5.6). Aromatic hydrocarbon maturation indicators show that these samples are over-mature with equivalent vitrinite reflectance values ( $R_o$ , %) calculated based on the methylphenanthrene index (MPI-1) are 2.34% – 2.74% (Table 5.4).

### 5.4.2 Re-Os systematics

The Re-Os data are listed in Table 5.5. The studied samples have higher Re contents (0.3333 – 8.592 part per billion, ppb) compared to Os contents (0.0280 – 0.1940 ppb; Table 5.5). The  $^{187}\text{Re}/^{188}\text{Os}$  and  $^{187}\text{Os}/^{188}\text{Os}$  ratios are 26.428–726.77 and 0.41993–6.8022, respectively (Table 5.5).

**Table 5.5:** Re-Os elemental and isotopic data for bituminous dolomite samples from the Anyue gasfield

ID	Re (ppb)	Os (ppb)	<sup>187</sup> Re/ <sup>188</sup> Os	2s	<sup>187</sup> Os/ <sup>188</sup> Os	2s	1/ <sup>192</sup> Os (ppb <sup>-1</sup> )
M17-4627	0.9241	0.0237	235.03	0.42	2.9984	0.0084	140.9
M17-4627_rpt1	0.8950	0.0283	186.01	0.52	2.3512	0.0136	111.8
M17-4627_rpt2	0.9710	0.0268	219.14	0.38	2.7920	0.0084	123.4
M17-4627_rpt3	0.9711	0.0269	219.28	0.35	2.8333	0.0075	123.4
M17-4642	0.3388	0.0279	66.135	0.126	1.4246	0.0057	102.7
M17-4642_rpt1	0.3373	0.0263	70.595	0.126	1.5339	0.0057	110.5
M17-4642_rpt2	0.3333	0.0194	98.022	0.238	2.1676	0.0104	160.2
M13-4611	1.189	0.0216	329.89	0.55	2.7705	0.0083	152.7
M13-4622	2.260	0.1389	83.887	0.075	0.69491	0.00111	18.93
M23-5442	1.026	0.1940	26.428	0.273	0.41993	0.00747	13.09
M23-5442_rpt1	0.9239	0.1046	46.366	0.939	0.86126	0.02508	25.63
M23-5442_rpt2	0.9069	0.0663	77.155	0.056	1.5753	0.0194	43.99
M4-5715	8.483	0.1726	319.08	1.78	2.9211	0.0154	19.41
M4-5715_rtp1	8.231	0.0971	726.77	3.14	6.8022	0.0486	47.46
M4-5715_rpt2	8.592	0.1668	338.75	2.47	3.0614	0.0220	20.36
M104-5735	3.466	0.1939	93.855	3.043	0.83915	0.03474	13.80
M104-5735_rpt1	3.498	0.0860	239.52	0.48	1.9884	0.0064	35.45
G2-5479	1.308	0.0403	188.33	3.61	1.9824	0.0745	75.51
G2-5479_rpt1	1.343	0.0805	87.544	0.747	0.86017	0.00843	33.33
G2-5479_rpt2	1.334	0.0280	296.34	1.41	3.0773	0.0270	121.4
G2-5479_rpt3	1.406	0.1214	58.255	0.744	0.48270	0.01757	21.08

\*rpt denotes replicate analysis. Re and Os contents, and <sup>187</sup>Os/<sup>188</sup>Os ratios were blank-corrected. <sup>187</sup>Os/<sup>188</sup>Os ratios were normalized to <sup>192</sup>Os/<sup>188</sup>Os = 3.08271.

## 5.5 Discussion

### 5.5.1 Binary mixing of biodegraded and fresh hydrocarbon components

Biodegradation-sensitive organic indicators, such as  $C_{28}$  norhopane/ $C_{29}$  hopane ( $NH_{28}/H_{29}$ ) and a hump in total ion chromatography (TIC) of saturated fractions, can be used to evaluate the extent of biodegradation (Huang and Li, 2016; Peters et al., 2005). The studied samples are classified into two groups based on biodegradation-sensitive parameters: (1) Group 1. Samples M17-4627, M17-4642, M13-4622 and M13-4622 have lower  $NH_{28}/H_{29}$  values (0.38 – 0.52), and a smaller hump over TICs of saturated fractions. This indicates that they contain more of the fresh component compared to the biodegraded component (Peters et al., 2005); (2) Group 2. Samples M23-5442, M4-5715, M104-5735 and G2-5479 have higher  $NH_{28}/H_{29}$  values (0.85 – 1.05, Group 2), and larger humps in TICs of the saturated fractions, suggesting that they have higher contents of the biodegraded component compared to the fresh component (Table 5.3. Peters et al., 2005). In this context, the biodegraded component may have been contributed by the first charge event, which occurred prior to the Carboniferous-Permian biodegradation event, whereas the fresh component was charged after biodegradation (Zou et al., 2015).

Molecular characteristics of the biodegraded and fresh components can be determined by plotting  $NH_{28}/H_{29}$  against organic parameters (Figures 5.4 and A5.7). Compared to the later-charged fresh component, the earlier-charged biodegraded component is characterized by higher pregnane/regular sterane, TT/H, Pr/nC<sub>17</sub>, Ph/nC<sub>18</sub>, C<sub>27</sub>/C<sub>29</sub>  $\alpha\alpha\alpha$  20R regular sterane, C<sub>29</sub> Ts/(C<sub>29</sub> Ts+C<sub>29</sub> hopane), Pr/Ph, Ts/Ts+Tm, C<sub>29</sub>  $\alpha\alpha\alpha$  20S/20S+20R sterane, C<sub>29</sub>  $\alpha\beta\beta$ /( $\alpha\alpha\alpha$ + $\alpha\beta\beta$ ) sterane, and C<sub>31</sub>R/C<sub>30</sub> hopane ratios, but lower C<sub>22</sub>/C<sub>21</sub>TT, gammacerane index, C<sub>26</sub>/C<sub>25</sub> TT and C<sub>24</sub>/C<sub>23</sub>TT (Figures 5.4 and A5.7). Similar to  $NH_{28}/H_{29}$ , organic parameters such as pregnane/regular sterane, TT/H, Pr/nC<sub>17</sub> and Ph/nC<sub>18</sub> ratios, are also increased with an increase in the biodegradation level, thus the earlier-charged biodegraded component is also characterized by higher values of these ratios (Figure 5.4. Peters et al., 2005). The other organic parameters, such as C<sub>27</sub>/C<sub>29</sub>  $\alpha\alpha\alpha$  20R regular sterane, Pr/Ph and Ts/Ts+Tm ratios, are affected by source, depositional environment or thermal maturation level of the organic matter, and these characteristics of the two components will be discussed in the following sections.

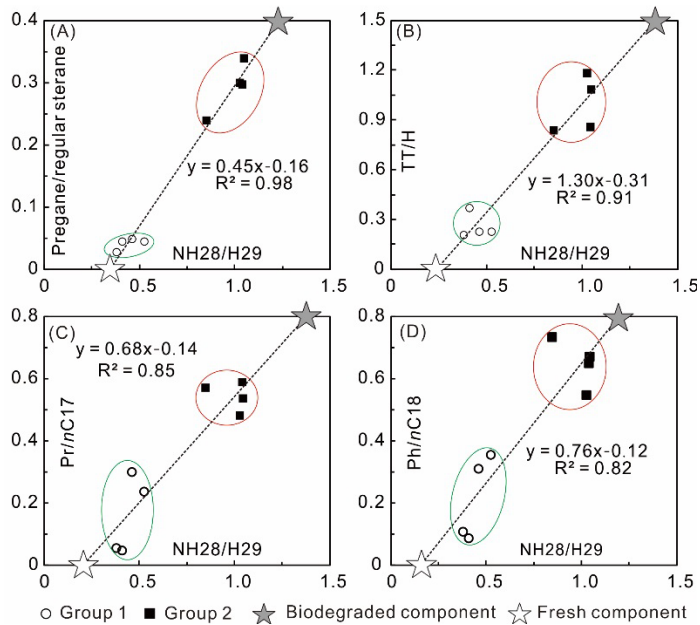


**Figure 5.4:** The ratio of C<sub>28</sub> norhopane/C<sub>29</sub> hopane (NH<sub>28</sub>/H<sub>29</sub>) is correlated positively with organic indicators including pregnane/regular sterane (A), tricyclic terpane (TT)/hopane (H) (B), Pr/nC<sub>17</sub> (C) and Ph/nC<sub>18</sub> (D).

### 5.5.2 Source of organic matter

The molecular composition of extracts preserves source information about the organic matter (Peters et al., 2005). The Pr/Ph vs (Ph/nC<sub>18</sub>-Pr/nC<sub>17</sub>) plot shows that organic matter of both groups of samples originated from a marine environment (Figure 5.5A. Hu et al., 2016). The Ph/nC<sub>18</sub> vs Pr/nC<sub>17</sub> plot also indicates a marine source for organic matter in both groups of samples, and that the difference between the two groups exhibited in the plot may be attributed to the influence of biodegradation and/or maturation effect (Figure 5.5B. Li et al., 2015). The relative abundance of C<sub>27</sub>, C<sub>28</sub> and C<sub>29</sub> regular steranes suggests a mixed organic source for the samples (Table 5.3

and Figure 5.5C). C<sub>27</sub> sterane is mainly derived from lower organisms (e.g. phytoplankton and red algae), whereas C<sub>29</sub> sterane may have originated from higher plants or bacteria (e.g. cyanobacteria and green algae) (Fowler and Douglas, 1987; Ourisson et al., 1987; Summons et al., 1988). Potential source rocks for hydrocarbons in the Anyue gasfield were deposited during the Neoproterozoic-Cambrian when higher plants were scarce, thus C<sub>29</sub> sterane may have been mainly contributed by bacterial sources (Peters et al., 2005). Samples of group 2 have higher C<sub>27</sub>/C<sub>29</sub>  $\alpha\alpha\alpha$  20R sterane ratios compared to samples of group 1 (0.97 – 1.04 and 0.62 – 0.77, respectively. Table 5.4), indicating a higher proportion of bacterial contribution to samples of group 2.

Both groups of samples are mixtures of the earlier-charged and later-charged components, but with different mixing proportions, thus, the source of organic matter in both components can be evaluated: (1) marine organic matter is the dominant input for source rocks of both components; (2) compared to the later-charged component, the earlier-charged component may have a higher contribution from bacterial organisms (e.g. cyanobacteria and also green algae).

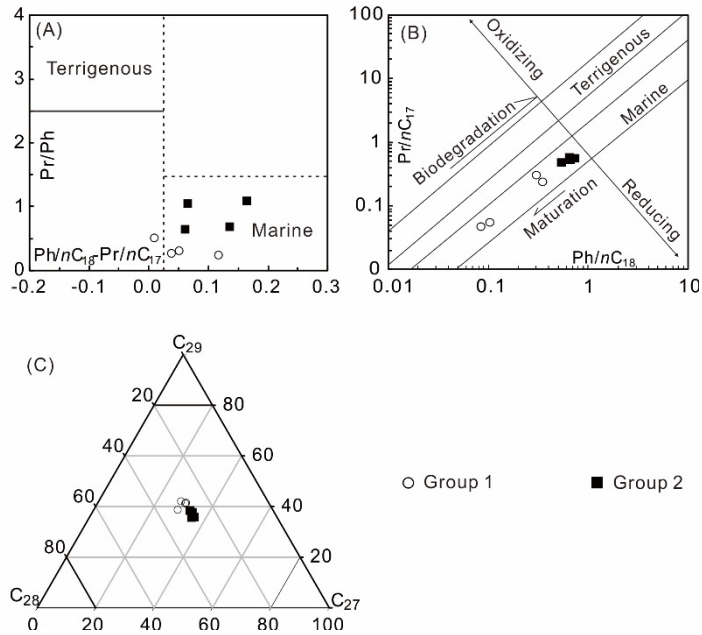


**Figure 5.5:** Scatter plots for characterizing the source of organic matter and depositional environment of the hydrocarbon source rocks. A: Pr/Ph vs Ph/nC<sub>18</sub>-Pr/nC<sub>17</sub>; B: Pr/nC<sub>17</sub> vs Ph/nC<sub>18</sub>; and C: ternary plot of C<sub>27</sub>-C<sub>28</sub>-C<sub>29</sub> regular steranes.

### 5.5.3 Lithology and formation environment of source rocks

There are two lithological types of potential hydrocarbon source rocks in the Anyue gasfield; shale and carbonate rocks (Figure 5.2. Cheng et al., 2018; Shi et al., 2017; Zou et al., 2015). Plots of C<sub>22</sub>/C<sub>21</sub> TTs vs C<sub>24</sub>/C<sub>23</sub> TTs and C<sub>26</sub>/C<sub>25</sub> TTs vs C<sub>31</sub> R/C<sub>30</sub> H ratios show that both groups of samples were mainly derived from marine shale source rock, but with a partial contribution from carbonate rocks (Figures 5.6A and 5.6B. Al-Ameri and Zumberge, 2012; Cheng et al.,

2018; Dutta et al., 2013; Peters et al., 2005; Shi et al., 2017). Low DBT/P ratios ( $< 0.1$ ) and  $C_{27}$  diteranes/(diasteranes + regular steranes) ratios (0.24 – 0.28) also support a shale-dominated source (Table 5.4). Samples of group 2 may have higher contributions derived from carbonate source rock according to Figures 5.6A-5.6B and their higher  $C_{27}$  diteranes/(diasteranes + regular steranes) ratios (0.27 – 0.28, Table 5.4). Therefore, both earlier- and later-charged components were mainly generated from shales, with the earlier-charged component containing higher proportions of carbonate-derived hydrocarbons.

The Pr/Ph ratios of the studied samples are 0.24 – 1.10, indicating that source rocks were deposited in an anoxic environment (Table 5.2, Peters et al., 2005). The anoxia is potentially attributed to the stratified water column in a hypersaline environment as suggested by the high gammacerane index ( $100 \times G/C_{30} H$ : 7.02 – 11.21, Table 5.3) and the negative correlation between Pr/Ph and gammacerane indices (Figure 5.6C, Peters et al., 2005). Higher salinity is typically accompanied by density stratification and decreased oxygen concentration in bottom water, which would result in low Pr/Ph values (Peters et al., 2005). Samples of group 1 have higher gammacerane indices and lower Pr/Ph ratios compared to samples of group 2 (Figure 5.6C). This indicates that source rocks for the later-charged component were deposited in an environment of higher salinity and degree of anoxia compared to source rocks of the earlier-charged component (Figure 5.6C).

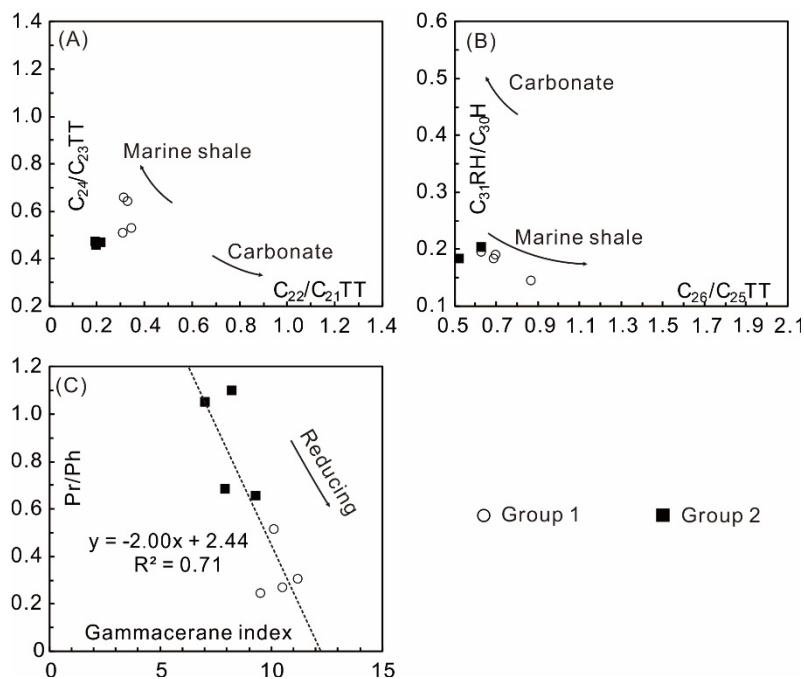


**Figure 5.6:** Scatter plots for characterizing lithological types and depositional environment of hydrocarbon source rock. A:  $C_{24}/C_{23}$  tricyclic terpane (TT) vs  $C_{22}/C_{21}$  TT; B:  $C_{31}R/C_{30}H$  vs  $C_{26}/C_{25}$  TT; C: Pr/Ph vs gammacerane index.

#### 5.5.4 Thermal maturity assessment

The samples in this study have homogeneous terpane and sterane maturation indicators, including  $C_{29}$  sterane  $\alpha\alpha\alpha 20S/(20S+20R)$  (0.42 – 0.54),  $C_{29}$  sterane  $\alpha\beta\beta/(\alpha\beta\beta+\alpha\alpha\alpha)$  (0.37 – 0.44),  $C_{32}$  H 22S/(22S+22R) (0.55 – 0.65) and Ts/(Ts+Tm) (0.45 – 0.53. Tables 5.3 and 5.4). Transformation from  $C_{29}$   $\alpha\alpha\alpha$  20R to  $C_{29}$   $\alpha\beta\beta$  20S regular sterane occurs with increasing thermal maturity, thus resulting in an increase in ratios of  $C_{29}$  sterane  $\alpha\alpha\alpha 20S/(20S+20R)$

and C<sub>29</sub> sterane  $\alpha\beta\beta/(\alpha\beta\beta+\alpha\alpha\alpha)$  (Peters et al., 2005). These two ratios reach endpoints of 0.4 – 0.5 and ~0.4 at early ( $R_o = \sim 0.8\%$ ) and late stages of oil maturity ( $R_o = \sim 1.2\%$ ), respectively (Peters et al., 2005). C<sub>32</sub> H 22S/(22S+22R) and Ts/Ts+Tm ratios are maturity-related terpane biomarker indices and the ratios end at ~0.6 and ~1.0 in the stages of early ( $R_o = \sim 0.7\%$ ) and late oil maturity ( $R_o = \sim 1.4$ ), respectively (Moldowan et al., 1985; Peters et al., 2005; Seifert and Moldowan, 1979). Therefore, terpane and sterane biomarker maturity-related ratios have arrived at endpoints, and the studied samples have reached a maturation level higher than peak oil maturity. Ts/Ts+Tm ratios of the samples are lower than the endpoint, which suggests that Ts/Ts+Tm may decrease with an increase in the maturation level after late-oil maturity (Peters et al., 2005).

Maturation level can also be evaluated by aromatic parameters such as the methylphenanthrene ratio (MPR), the methylphenanthrene distribution fraction (MPDF) and the methylphenanthrene index (MPI-1) (George and Ahmed, 2002; Kruge, 2000; Peters et al., 2005; Radke, 1988; Sivan et al., 2008). The studied samples have high MPR and MPDF values that range between 1.47 – 3.82 and 0.52 – 0.73, respectively (Table 5.4), suggesting high maturation levels (Cheng et al., 2018). MPI-1 correlates positively with maturity level within the oil window ( $R_o = 0.65 - 1.35\%$ ), but correlates negatively with further maturation after the oil window ( $R_o > 1.35\%$ ) (Radke, 1988). Based on biomarker maturation indicators, these samples have reached maturation levels higher than peak oil maturity,

thus the small MPI-1 values of these samples (0.47 – 1.20) represent maturation levels higher than the oil window (Table 5.4). Equivalent vitrinite reflectance values, calculated based on MPI-1, are 2.34% – 2.74% (Table 5.4), indicating that the samples are over-mature (Radke, 1988). The over-mature nature revealed by geochemical parameters is consistent with the cracking genesis of the reservoir bitumen (Cheng et al., 2018; Wei et al., 2015; Zou et al., 2015).

### **5.5.5 Re-Os geochemistry of bituminous dolomite**

#### **5.5.5.1 Re-Os elemental behaviour in bituminous dolomite**

Rhenium and osmium are two organophilic metallic elements (Finlay et al., 2011; Georgiev et al., 2016; Rooney et al., 2012; Selby and Creaser, 2005; Selby et al., 2007a). The present samples have Re contents (0.333 – 8.592 ppb) higher than the upper crust average (0.198 ppb. Figure 5.7A. Rudnick and Gao, 2003). Os contents of the samples are not consistently higher than the average value for the upper crust (0.031 ppb. Rudnick and Gao, 2003) and samples with Os contents below 0.031 ppb are dominantly from group 1, as classified in the preceding section (Figure 5.7A).

Concentrations of Re and Os correlate with organic geochemical indicators that are sensitive to organic source and biodegradation (Figure 5.8), indicating that both factors may influence the distribution of Re and Os in the bituminous dolomitic reservoir. Re and Os contents correlate positively with C<sub>31</sub> R/C<sub>30</sub> hopane and

NH<sub>28</sub>/H<sub>29</sub> ratios (Figures 5.8A-5.8D). Hydrocarbons generated from carbonate source rocks are characterized by higher C<sub>31</sub>R/C<sub>30</sub> hopane ratios compared to shale-derived hydrocarbons (Al-Ameri and Zumberge, 2012; Cheng et al., 2018; Peters et al., 2005; Shi et al., 2017). Thus, the carbonate-derived hydrocarbons may be characterized by higher Re-Os concentrations. The redistribution of Re and Os during biodegradation may be caused by the preferential removal of lower-molecular-weight compounds from the hydrocarbons. Heavy fractions (e.g. asphaltene) dominate the Re-Os budget in hydrocarbons (Selby et al., 2007a). Removal of light fractions, which are more susceptible to biodegradation (Peters et al., 2005), may not significantly affect the metal budget in the reservoir but provide more spaces for accommodating later-charged metal-bearing hydrocarbons. Therefore, the biodegradation was able to increase the Re-Os concentration of dolomite. The positive correlation between <sup>187</sup>Re/<sup>188</sup>Os and C<sub>31</sub>R/C<sub>30</sub> hopane ratios further suggests that carbonate-derived hydrocarbons may be characterized by higher <sup>187</sup>Re/<sup>188</sup>Os ratios and the mixing of carbonate- and shale-derived hydrocarbons may influence the Re/Os fractionation (Figure 5.8E).

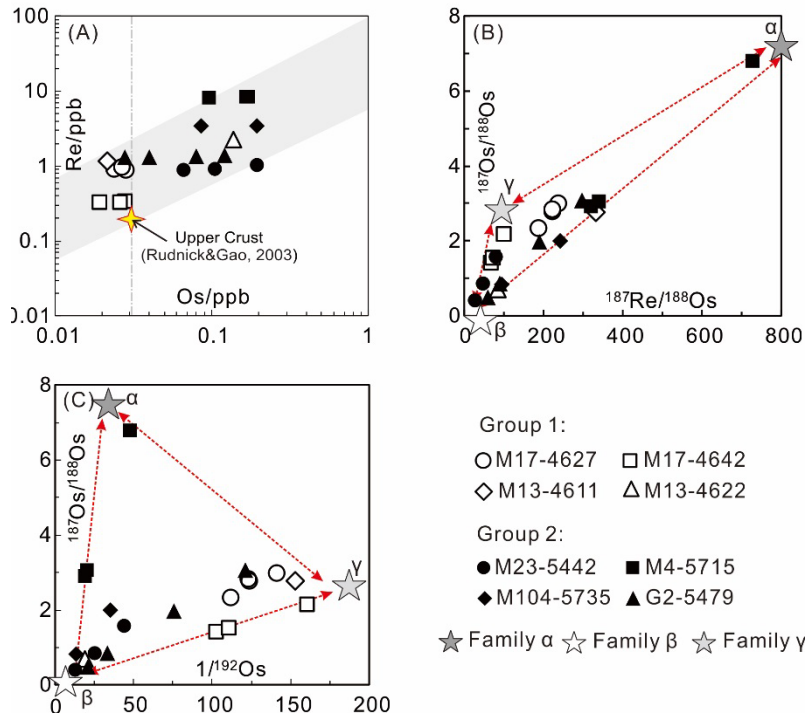


**Figure 5.7:** Re-Os data of the studied samples. A: Re vs Os contents. Data of the Upper Crust average are from Rudnick and Gao (2003); B:  $^{187}\text{Os}/^{188}\text{Os}$  vs  $^{187}\text{Re}/^{188}\text{Os}$  ratios; and C:  $^{187}\text{Os}/^{188}\text{Os}$  vs  $1/^{192}\text{Os}$  ratios.

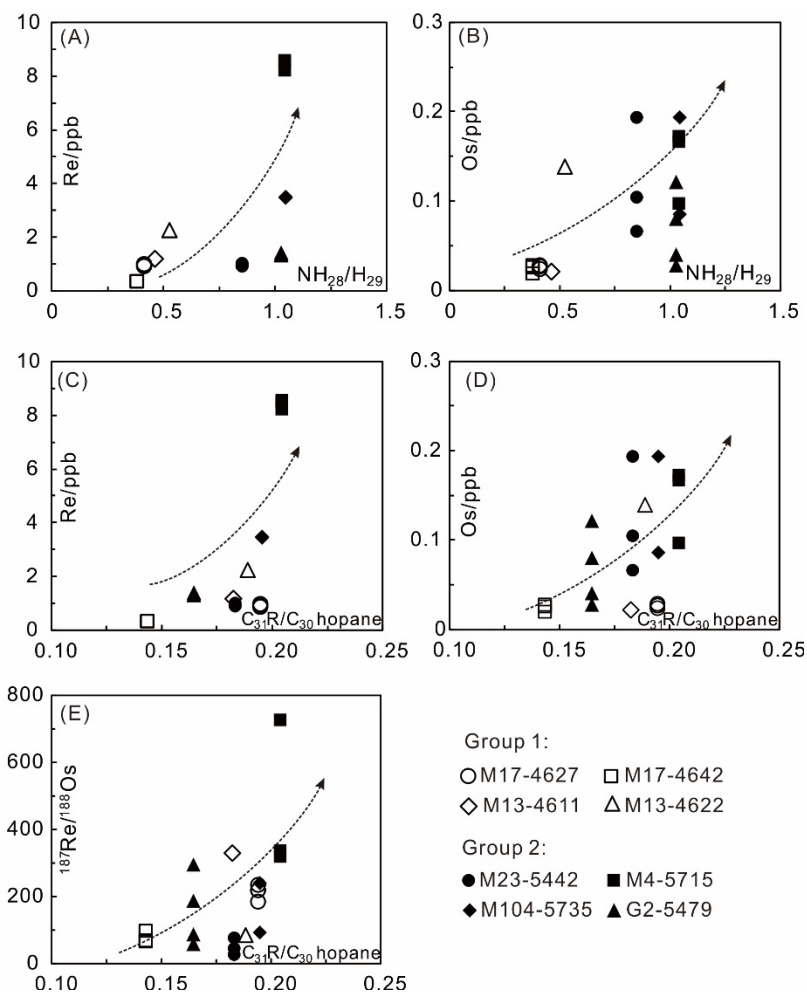


**Figure 5.8:** Correlations between Re-Os data and organic indicators. A: Re content vs  $\text{C}_{28}$  norhopane/ $\text{C}_{29}$  hopane ( $\text{NH}_{28}/\text{H}_{29}$ ); B: Os content vs  $\text{NH}_{28}/\text{H}_{29}$ ; C: Re content vs  $\text{C}_{31}\text{R}/\text{C}_{30}$  hopane; D: Os content vs  $\text{C}_{31}\text{R}/\text{C}_{30}$  hopane; and E:  $^{187}\text{Re}/^{188}\text{Os}$  vs  $\text{C}_{31}\text{R}/\text{C}_{30}$  hopane.

### 5.5.5.2 Re-Os isotopic heterogeneity in bituminous dolomite

Duplicate analysis of a single bituminous dolomite sample reveals significant variation in Re-Os isotopic composition, and subsample-scale spread in  $^{187}\text{Re}/^{188}\text{Os}$  and  $^{187}\text{Os}/^{188}\text{Os}$  ratios of 31.89 – 407.69

and 0.6472 – 3.881, respectively, which are comparable to differences between different samples (Table 5.5). This suggests that Re-Os isotopes are heterogeneously distributed in the samples and pulverizing (~200 mesh) did not physically homogenize the Re-Os isotopic composition of sample powders (Li et al., 2015).

A rigorous positive linear relation is established for  $^{187}\text{Re}/^{188}\text{Os}$  and  $^{187}\text{Os}/^{188}\text{Os}$  ratios of each of the duplicated samples (Figures 5.9A and 5.9C). Regressions of these linear relations yield dates which are older than the depositional age of the reservoir (Figures 5.9A and 5.9C). This suggests that the apparent isochrons defined by duplicate analysis of each sample are mixing isochrons which may result from initial Os isotopic heterogeneity, as indicated by positive linear relations between  $1/^{192}\text{Os}$  and  $^{187}\text{Os}/^{188}\text{Os}$  ratios (Figures 5.9B and 5.9D. Li et al., 2015). Therefore, Os isotopic equilibrium may not be completely achieved in the bituminous dolomite gas reservoir.

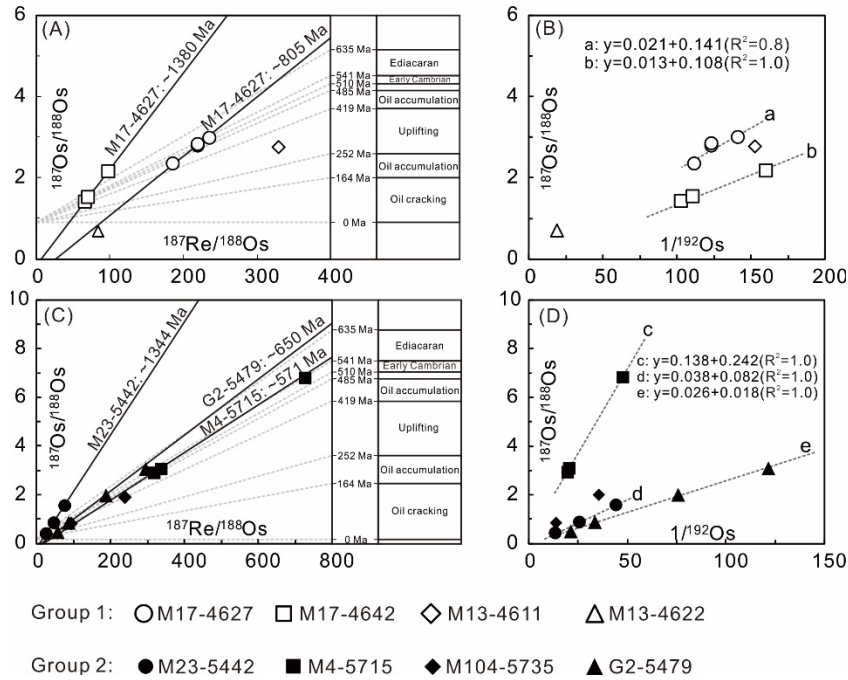


**Figure 5.9:** A:  $^{187}\text{Os}/^{188}\text{Os}$  vs  $^{187}\text{Re}/^{188}\text{Os}$  ratios of group 1 samples; B:  $^{187}\text{Os}/^{188}\text{Os}$  vs  $1/^{192}\text{Os}$  ratios of group 1 samples; C:  $^{187}\text{Os}/^{188}\text{Os}$  vs  $^{187}\text{Re}/^{188}\text{Os}$  ratios of group 2 samples; and D:  $^{187}\text{Os}/^{188}\text{Os}$  vs  $1/^{192}\text{Os}$  ratios of group 2 samples.

### 5.5.5.3 Implication for hydrocarbon fingerprinting

A ternary mixing of families  $\alpha$  (high Os concentration and  $^{187}\text{Os}/^{188}\text{Os}$  ratio),  $\beta$  (high Os concentration and low  $^{187}\text{Os}/^{188}\text{Os}$  ratio) and  $\gamma$  (low Os concentration and  $^{187}\text{Os}/^{188}\text{Os}$  ratio) is observed in the  $1/^{192}\text{Os}$ - $^{187}\text{Os}/^{188}\text{Os}$  plot (Figure 5.7C). The family  $\gamma$  is characterized by lower Os contents compared to families  $\alpha$  and  $\beta$ , and this may be caused by the lower biodegradation degree of  $\gamma$  according to the Os elemental behaviour in bituminous dolomite (Figure 5.8B). Mixing of carbonate-derived hydrocarbons with shale-derived hydrocarbons

may also increase concentrations of Re and Os in dolomite (Figures 5.8C and 5.8D), thus, family  $\gamma$  may also contain a lower proportion of carbonate-derived hydrocarbons compared to families  $\alpha$  and  $\beta$ . Present-day  $^{187}\text{Os}/^{188}\text{Os}$  ratios of the samples are the result of radiogenic decay of  $^{187}\text{Re}$ . Thus, Re/Os fractionation could influence the Os isotopic composition of the samples, and samples with higher  $^{187}\text{Re}/^{188}\text{Os}$  ratios would have more radiogenic  $^{187}\text{Os}/^{188}\text{Os}$  ratios. The mixing of carbonate-/shale-sourced hydrocarbons has the potential to fractionate Re/Os, therefore, this process may also be a factor differentiating family  $\alpha$  (high  $^{187}\text{Os}/^{188}\text{Os}$ ) from  $\beta$  and  $\gamma$  (low  $^{187}\text{Os}/^{188}\text{Os}$ , Figure 5.7C).

Based on Re-Os elemental behaviour, three Os isotopic components are considered to have existed in the dolomitic reservoir: earlier-charged carbonate-derived (I, high Os concentration and  $^{187}\text{Os}/^{188}\text{Os}$  ratio) and earlier-charged shale-derived hydrocarbons (II, high Os concentration and low  $^{187}\text{Os}/^{188}\text{Os}$  ratio), together with later-charged shale-derived hydrocarbons (III, low Os concentration and  $^{187}\text{Os}/^{188}\text{Os}$  ratio) (Figure 5.10). Different mixing scenarios are presented for two groups of samples: II-III binary mixing and I-II-III ternary mixing, respectively (Figure 5.10). Samples of group 1 are dominated by component III with partial contributions from components I and II, suggesting that these samples mainly contain the later-charged hydrocarbons (Figure 5.10). The ternary mixing shown for group 2 samples indicates that the samples recorded both episodes of oil accumulation (Figure 5.10). The conclusions drawn

from Os isotopic systematics are consistent with the organic geochemical indicators as discussed in the preceding sections. Therefore, Os isotopic composition may be a potential indicator for characterizing hydrocarbon source and provide independent evidence for cross-checking results obtained from other disciplines (e.g. biomarker geochemistry).

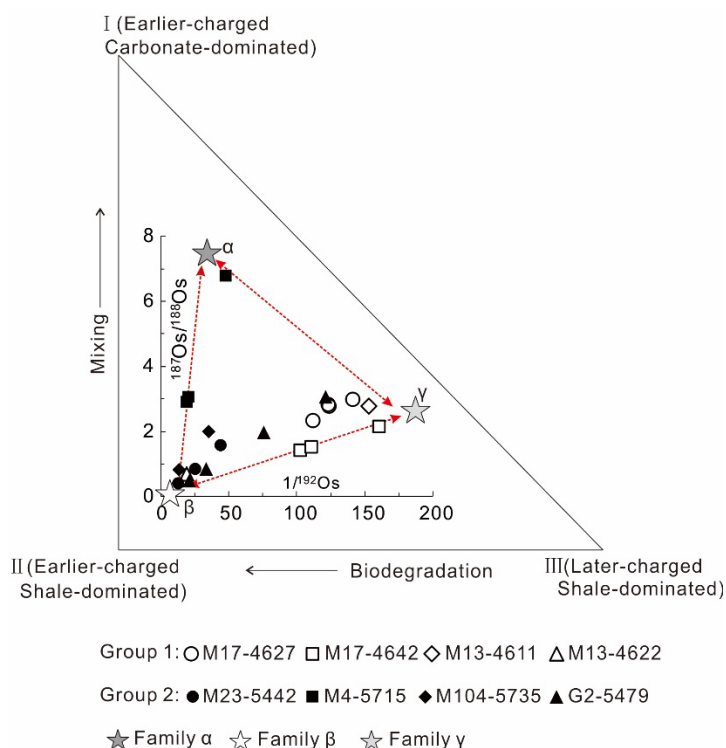


**Figure 5.10:** The  $^{187}\text{Os}/^{188}\text{Os}$  vs  $^{187}\text{Re}/^{188}\text{Os}$  plot shows that three Os isotopic components are identified in the bituminous dolomite reservoir of the Anyue gasfield. Components I, II and III represents the earlier-charged/carbonate-dominated, earlier-charged/shale-dominated and later-charged/shale-dominated hydrocarbons.

## 5.6 Conclusions

Neoproterozoic-Cambrian marine bituminous dolomite is the natural gas reservoir for the giant Anyue gasfield in central Sichuan Basin, southwest China. This study investigated the molecular composition of organic extracts and Re-Os systematics of the dolomitic reservoir using samples obtained from drillcores. Biodegradation-sensitive organic parameters classified samples into two groups: group 1 is characterized an insignificant hump in saturated TICs and low  $\text{NH}_{28}/\text{H}_{29}$  values (0.38 – 0.52); whereas group 2 is characterized by an obvious hump in saturated TICs and higher  $\text{NH}_{28}/\text{H}_{29}$  values (0.85 – 1.05). This indicates that there are two components, biodegraded and fresh, in these samples and that samples of group 2 contain higher proportions of the biodegraded component. Reservoir burial history shows that regional uplifting occurred between the two major episodes of oil accumulation, which created a low-temperature environment suitable for biodegradation. Therefore, the biodegraded and fresh components most likely represent earlier- and later-charged hydrocarbons, respectively. The scatter plots of  $\text{Ph}/n\text{C}_{18}$ - $\text{Pr}/n\text{C}_{17}$  vs  $\text{Pr}/\text{Ph}$ ,  $\text{Ph}/n\text{C}_{18}$  vs  $\text{Pr}/n\text{C}_{17}$ ,  $\text{C}_{24}/\text{C}_{23}$  vs  $\text{C}_{22}/\text{C}_{21}$  tricyclic terpanes and  $\text{C}_{26}/\text{C}_{25}$  tricyclic terpane vs  $\text{C}_{31}\text{R}/\text{C}_{30}$  hopane ratios show that the source rocks for both episodes of oil accumulation were dominated by marine shales. However, carbonate source rock also contributed to the paleo-oil accumulation, especially the earlier-charged hydrocarbons, as suggested by their higher  $\text{C}_{31}\text{R}/\text{C}_{30}$  hopane ratios. The higher  $\text{C}_{27}/\text{C}_{29}$   $\alpha\alpha\alpha$  20R sterane ratios indicate that the

earlier-charged hydrocarbons may contain higher proportions of bacterial-derived materials than later-charged hydrocarbons. Source rocks for the earlier-charged hydrocarbons were deposited under a more reducing environment than source rocks for the later-charged hydrocarbons, as suggested by their lower Pr/Ph ratios. Both earlier- and later-charged hydrocarbons reached the over-mature stage. Equivalent virtrinite reflectance values, calculated on MPI-1 indices, are 2.34% – 2.74% and saturated hydrocarbon maturation indicators have reached the end-points.

Distribution of Re and Os in the samples is influenced by organic source and the biodegradation level of the hydrocarbons. Rhenium- and osmium- enriched end-members are characterized by higher  $C_{31}R/C_{30}$  hopane and  $NH_{28}/H_{29}$  ratios. These correlations indicate that carbonate-derived hydrocarbons likely contain higher Re-Os concentrations and that biodegradation may increase the Re-Os concentration in dolomite. The positive correlation between  $^{187}Re/^{188}Os$  and  $C_{31}R/C_{30}$  hopane ratios suggests that mixing of carbonate-/shale-derived hydrocarbons likely influenced Re/Os fractionation. Duplicate analysis of a single sample reveals significant subsample-scale variation in Re-Os isotopic composition, suggesting that the Re-Os isotopes are heterogeneously distributed in the bituminous dolomites. A rigorous positive linear relation was established for  $^{187}Re/^{188}Os$  and  $^{187}Os/^{188}Os$  ratios of each duplicate sample and regressions of the linear relations yield dates older than the reservoir depositional ages. Positive linear relations between

$1/^{192}\text{Os}$  and  $^{187}\text{Os}/^{188}\text{Os}$  ratios of duplicate analyses suggest that isochronous trends may be mixing lines caused by initial Os isotopic heterogeneity.

A ternary mixing scenario is presented in the plot of  $1/^{192}\text{Os}$  vs  $^{187}\text{Os}/^{188}\text{Os}$ , including I (high Os concentration and  $^{187}\text{Os}/^{188}\text{Os}$  ratio), II (high Os concentration and low  $^{187}\text{Os}/^{188}\text{Os}$  ratio) and III (low Os concentration and  $^{187}\text{Os}/^{188}\text{Os}$  ratio). Based on the behaviour of Re and Os in bituminous dolomite, Os isotopic ternary mixing may be attributed to the influence of biodegradation and mixing of the hydrocarbon source. Higher Os concentration in components I and II could have resulted from paleo-biodegradation, thus, they may represent the earlier-charged hydrocarbons, whereas component III would correspond to the later-charged fresh hydrocarbons. Mixing of carbonate- and shale-derived hydrocarbons in the earlier-charged components fractionated Re/Os, which further resulted in variable  $^{187}\text{Os}/^{188}\text{Os}$  ratios between components I and II. Therefore, Os isotopic composition may be a potential indicator for characterizing hydrocarbon source in complex petroleum systems and provide independent evidence for cross-checking results obtained by other methods (e.g. biomarker geochemistry).

## **Acknowledgments**

This work was supported by the Strategic Priority Research Program of the Chinese Academy of Sciences (grant No. XDA20070304), “Hundred Talents Program” of Shaanxi Province, China (grant

number 310827163412).

## References

AL-AMERI, T. K. & ZUMBERGE, J. 2012. Middle and upper Jurassic hydrocarbon potential of the Zagross fold Belt, North Iraq. *Marine and Petroleum Geology*, 36, 13-34.

ASIF, M., FAZEELAT, T. & GRICE, K. 2011. Petroleum geochemistry of the Potwar Basin, Pakistan: 1. Oil–oil correlation using biomarkers,  $\delta^{13}\text{C}$  and  $\delta\text{D}$ . *Organic Geochemistry*, 42, 1226-1240.

CHAKHMAKHCHEV, A., SUZUKI, M. & TAKAYAMA, K. 1997. Distribution of alkylated dibenzothiophenes in petroleum as a tool for maturity assessments. *Organic Geochemistry*, 26, 483-489.

CHENG, B., CHEN, Z., CHEN, T., YANG, C. & WANG, T.-G. 2018. Biomarker signatures of the Ediacaran–Early Cambrian origin petroleum from the central Sichuan Basin, South China: Implications for source rock characteristics. *Marine and Petroleum Geology*, 96, 577-590.

CRAIG, J., BIFFI, U., GALIMBERTI, R., GHORI, K., GORTER, J., HAKHOO, N., LE HERON, D., THUROW, J. & VECOLI, M. 2013. The palaeobiology and geochemistry of Precambrian hydrocarbon

source rocks. *Marine and Petroleum Geology*, 40, 1-47.

CUMMING, V. M., SELBY, D., LILLIS, P. G. & LEWAN, M. D. 2014. Re–Os geochronology and Os isotope fingerprinting of petroleum sourced from a Type I lacustrine kerogen: Insights from the natural Green River petroleum system in the Uinta Basin and hydrous pyrolysis experiments. *Geochimica et Cosmochimica Acta*, 138, 32-56.

DU, J., ZOU, C., XU, C., HE, H., SHEN, P., YANG, Y., LI, Y., WEI, G., WANG, Z. & YANG, Y. 2014. Theoretical and technical innovations in strategic discovery of a giant gas field in Cambrian Longwangmiao Formation of central Sichuan paleo-uplift, Sichuan Basin. *Petroleum Exploration and Development*, 41, 294-305.

DUTTA, S., BHATTACHARYA, S. & RAJU, S. V. 2013. Biomarker signatures from Neoproterozoic–early Cambrian oil, western India. *Organic Geochemistry*, 56, 68-80.

FINLAY, A. J., SELBY, D. & OSBORNE, M. J. 2011. Re-Os geochronology and fingerprinting of United Kingdom Atlantic margin oil: Temporal implications for regional petroleum systems. *Geology*, 39, 475-478.

FINLAY, A. J., SELBY, D. & OSBORNE, M. J. 2012. Petroleum source rock identification of United Kingdom Atlantic Margin oil fields and the Western Canadian Oil Sands using Platinum, Palladium, Osmium and Rhenium: Implications for global petroleum

systems. *Earth and Planetary Science Letters*, 313, 95-104.

FOWLER, M. & DOUGLAS, A. G. 1987. Saturated hydrocarbon biomarkers in oils of Late Precambrian age from Eastern Siberia. *Organic Geochemistry*, 11, 201-213.

GE, X., SHEN, C., SELBY, D., DENG, D. & MEI, L. 2016. Apatite fission-track and Re-Os geochronology of the Xuefeng uplift, China: Temporal implications for dry gas associated hydrocarbon systems. *Geology*, 44, 491-494.

GE, X., SHEN, C., SELBY, D., WANG, J., MA, L., RUAN, X., HU, S. & MEI, L. 2018. Petroleum-generation timing and source in the northern Longmen Shan thrust belt, Southwest China: Implications for multiple oil-generation episodes and sources. *AAPG Bulletin*, 102, 913-938.

GEORGE, S. & AHMED, M. 2002. Use of aromatic compound distributions to evaluate organic maturity of the Proterozoic middle Velkerri Formation, McArthur Basin, Australia. In KEEP, M. & MOSS, S.J. (Eds), 2002. *The Sedimentary Basins of Western Australia 3: Proceedings of the Petroleum Exploration Society of Australia Symposium*, Perth, WA, 2002. 253-270.

GEORGE, S. C., VOLK, H., DUTKIEWICZ, A., RIDLEY, J. & BUICK, R. 2008. Preservation of hydrocarbons and biomarkers in oil trapped inside fluid inclusions for > 2 billion years. *Geochimica et Cosmochimica Acta*, 72, 844-870.

GEORGIEV, S. V., STEIN, H. J., HANNAH, J. L., GALIMBERTI, R., NALI, M., YANG, G. & ZIMMERMAN, A. 2016. Re–Os dating of maltenes and asphaltenes within single samples of crude oil. *Geochimica et Cosmochimica Acta*, 179, 53-75.

GRICE, K., NABBefeld, B. & MASLEN, E. 2007. Source and significance of selected polycyclic aromatic hydrocarbons in sediments (Hovea-3 well, Perth Basin, Western Australia) spanning the Permian–Triassic boundary. *Organic Geochemistry*, 38, 1795-1803.

HALL, P. A., MCKIRDY, D. M., GRICE, K. & EDWARDS, D. S. 2014. Australasian asphaltite strandings: Their origin reviewed in light of the effects of weathering and biodegradation on their biomarker and isotopic profiles. *Marine and Petroleum Geology*, 57, 572-593.

HOLMAN, A. I., GRICE, K., JARAULA, C. M., SCHIMMELMANN, A. & BROCKS, J. J. 2012. Efficiency of extraction of polycyclic aromatic hydrocarbons from the Paleoproterozoic Here's Your Chance Pb/Zn/Ag ore deposit and implications for a study of Bitumen II. *Organic Geochemistry*, 52, 81-87.

HU, S., WILKES, H., HORSFIELD, B., CHEN, H. & LI, S. 2016. On the origin, mixing and alteration of crude oils in the Tarim Basin. *Organic Geochemistry*, 97, 17-34.

HUANG, H. & LI, J. 2016. Molecular composition assessment of biodegradation influence at extreme levels—A case study from oilsand bitumen in the Junggar Basin, NW China. *Organic Geochemistry*, 103, 31-42.

KORSCH, R., HUAZHAO, M., ZHAOCAI, S. & GORTER, J. 1991. The Sichuan basin, southwest China: a late Proterozoic (Sinian) petroleum province. *Precambrian Research*, 54, 45-63.

KRUGE, M. A. 2000. Determination of thermal maturity and organic matter type by principal components analysis of the distributions of polycyclic aromatic compounds. *International Journal of Coal Geology*, 43, 27-51.

LI, J., WANG, X.-C., XU, J.-F., XU, Y.-G., TANG, G.-J. & WANG, Q. 2015. Disequilibrium-induced initial Os isotopic heterogeneity in gram aliquots of single basaltic rock powders: Implications for dating and source tracing. *Chemical Geology*, 406, 10-17.

LI, S., AMRANI, A., PANG, X., YANG, H., SAID-AHMAD, W., ZHANG, B. & PANG, Q. 2015b. Origin and quantitative source assessment of deep oils in the Tazhong Uplift, Tarim Basin. *Organic Geochemistry*, 78, 1-22.

LILLIS, P. G. & SELBY, D. 2013. Evaluation of the rhenium–osmium geochronometer in the Phosphoria petroleum system, Bighorn Basin of Wyoming and Montana, USA. *Geochimica et Cosmochimica Acta*, 118, 312-330.

LIU, J., SELBY, D., OBERMAJER, M. & MORT, A. 2018. Rhenium–osmium geochronology and oil–source correlation of the Duvernay petroleum system, Western Canada sedimentary basin: Implications for the application of the rhenium–osmium geochronometer to petroleum systems. *AAPG Bulletin*, 102, 1627-1657.

LUDWIG, K. 2003. User's manual for Isoplot 3.00: a geochronological toolkit for Microsoft Excel. Berkeley Geochronology Center. Special publication, 4, 1-71.

MOLDOWAN, J. M., SEIFERT, W. K. & GALLEGOS, E. J. 1985. Relationship between petroleum composition and depositional environment of petroleum source rocks. *AAPG Bulletin*, 69, 1255-1268.

NALDRETT, S. & LIBBY, W. 1948. Natural radioactivity of rhenium. *Physical Review*, 73, 487.

OURISSON, G., ROHMER, M. & PORALLA, K. 1987. Prokaryotic hopanoids and other polyterpenoid sterol surrogates. *Annual Reviews in Microbiology*, 41, 301-333.

PETERS, K., WALTERS, C. & MOLDOWAN, J. 2005. The Biomarker Guide, vol. 2. Biomarkers in petroleum systems and Earth history, 483-705p.

RADKE, M. 1988. Application of aromatic compounds as maturity

indicators in source rocks and crude oils. *Marine and Petroleum Geology*, 5, 224-236.

RAVIZZA, G. & TUREKIAN, K. K. 1989. Application of the  $^{187}\text{Re}$ - $^{187}\text{Os}$  system to black shale geochronometry. *Geochimica et Cosmochimica Acta*, 53, 3257-3262.

ROONEY, A. D., SELBY, D., LEWAN, M. D., LILLIS, P. G. & HOUZAY, J.-P. 2012. Evaluating Re–Os systematics in organic-rich sedimentary rocks in response to petroleum generation using hydrous pyrolysis experiments. *Geochimica et Cosmochimica Acta*, 77, 275-291.

RUDNICK, R. L. & GAO, S. 2003. Composition of the continental crust. *Treatise on geochemistry*, 3, 1-64p.

SEIFERT, W. K. & MOLDOWAN, J. M. 1979. The effect of biodegradation on steranes and terpanes in crude oils. *Geochimica et Cosmochimica Acta*, 43, 111-126.

SELBY, D. & CREASER, R. A. 2005. Direct Radiometric Dating of Hydrocarbon Deposits Using Rhenium-Osmium Isotopes. *Science*, 308, 1293-1295.

SELBY, D., CREASER, R. A. & FOWLER, M. G. 2007a. Re–Os elemental and isotopic systematics in crude oils. *Geochimica et Cosmochimica Acta*, 71, 378-386.

SELBY, D., CREASER, R. A., STEIN, H. J., MARKEY, R. J. &

HANNAH, J. L. 2007b. Assessment of the  $^{187}\text{Re}$  decay constant by cross calibration of Re–Os molybdenite and U–Pb zircon chronometers in magmatic ore systems. *Geochimica et Cosmochimica Acta*, 71, 1999-2013.

SHI, C., CAO, J., TAN, X., LUO, B., ZENG, W. & HU, W. 2017. Discovery of oil bitumen co-existing with solid bitumen in the Lower Cambrian Longwangmiao giant gas reservoir, Sichuan Basin, southwestern China: Implications for hydrocarbon accumulation process. *Organic Geochemistry*, 108, 61-81.

SIVAN, P., DATTA, G. C. & SINGH, R. R. 2008. Aromatic biomarkers as indicators of source, depositional environment, maturity and secondary migration in the oils of Cambay Basin, India. *Organic Geochemistry*, 39, 1620-1630.

SMOLIAR, M. I., WALKER, R. J. & MORGAN, J. W. 1996. Re-Os ages of group IIA, IIIA, IVA, and IVB iron meteorites. *Science*, 271, 1099.

SUMMONS, R. E., POWELL, T. G. & BOREHAM, C. J. 1988. Petroleum geology and geochemistry of the Middle Proterozoic McArthur Basin, Northern Australia: III. Composition of extractable hydrocarbons. *Geochimica et Cosmochimica Acta*, 52, 1747-1763.

WANG, Z., FINGAS, M. & LI, K. 1994. Fractionation of a light crude oil and identification and quantitation of aliphatic, aromatic, and biomarker compounds by GC-FID and GC-MS, part II. *Journal*

of Chromatographic Science, 32, 367-382.

WEI, G., XIE, Z., SONG, J., YANG, W., WANG, Z., LI, J., WANG, D., LI, Z. & XIE, W. 2015. Features and origin of natural gas in the Sinian–Cambrian of central Sichuan paleo-uplift, Sichuan Basin, SW China. *Petroleum Exploration and Development*, 42, 768-777.

ZOU, C., YANG, Z., DAI, J., DONG, D., ZHANG, B., WANG, Y., DENG, S., HUANG, J., LIU, K., YANG, C., WEI, G. & PAN, S. 2015. The characteristics and significance of conventional and unconventional Sinian–Silurian gas systems in the Sichuan Basin, central China. *Marine and Petroleum Geology*, 64, 386-402.

## Appendix 5

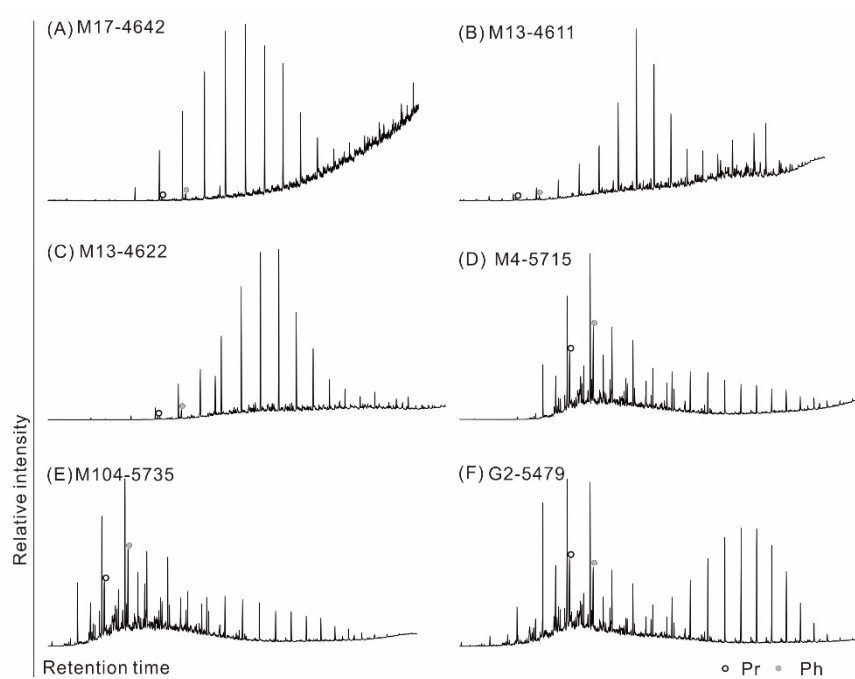


**Figure A5.1:** Total ion chromatograms (TICs) of saturated fractions of the studied samples.

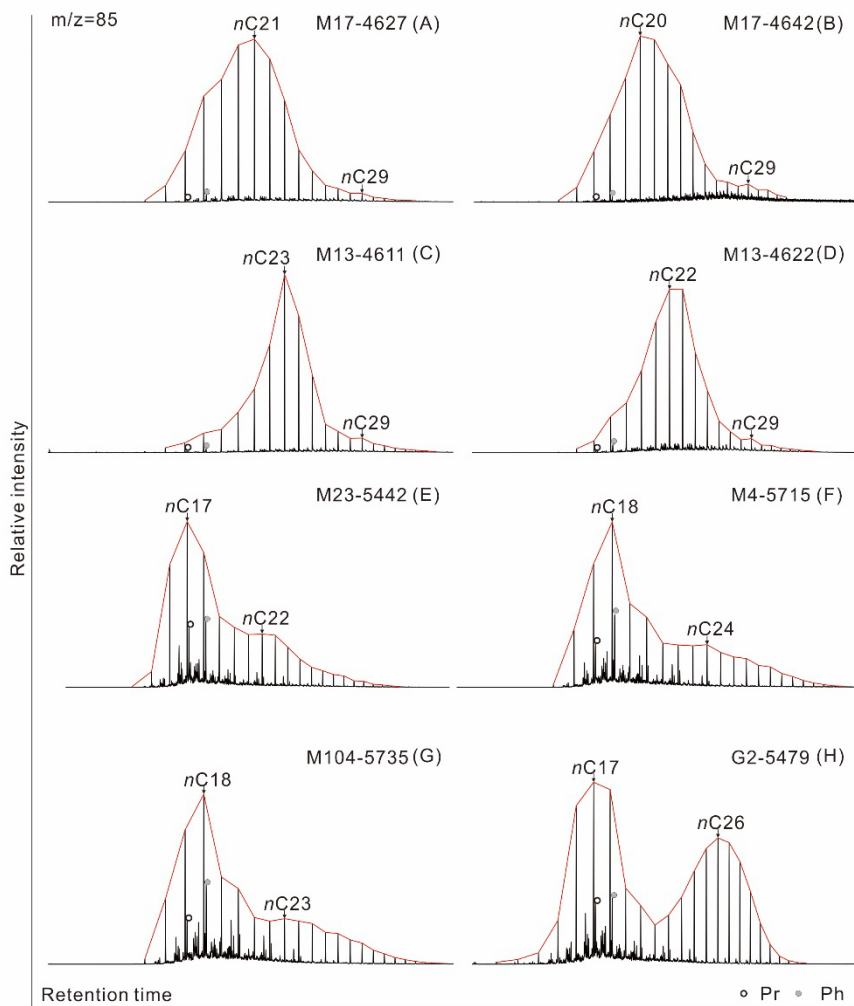


**Figure A5.2:** M/Z 85 mass chromatograms showing distribution patterns of *n*-alkanes of the studied samples.

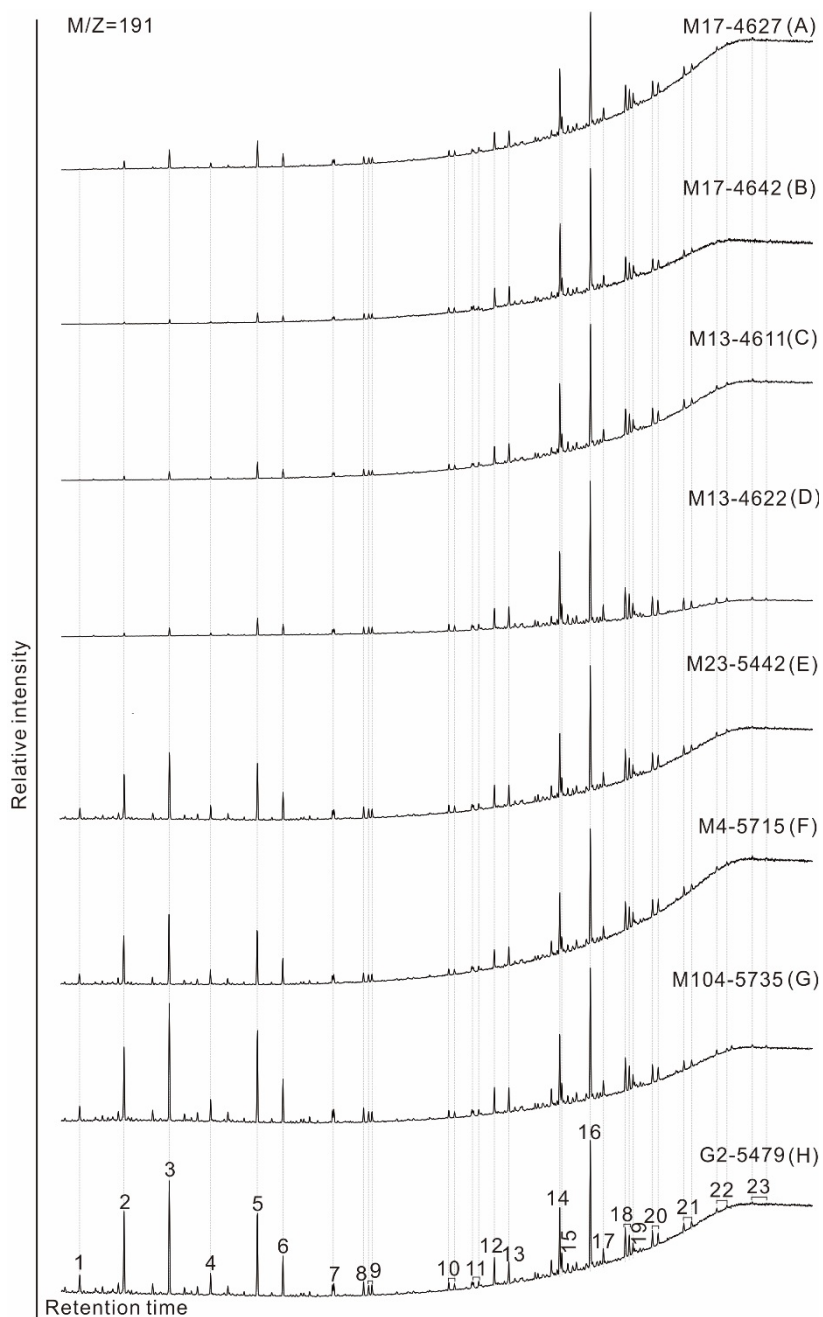


**Figure A5.3:** M/Z 191 mass chromatograms showing distribution patterns of terpanes of the studied samples. Hydrocarbon compounds are identified as labelled: 1: C<sub>19</sub> tricyclic terpene (TT); 2: C<sub>20</sub> TT; 3: C<sub>21</sub> TT; 4: C<sub>22</sub> TT; 5: C<sub>23</sub> TT; 6: C<sub>24</sub> TT; 7: C<sub>25</sub> TT; 8: C<sub>24</sub> tetracyclic terpene; 9: C<sub>26</sub> TT; 10: C<sub>28</sub> TT; 11: C<sub>29</sub> TT; 12: C<sub>27</sub> 18 $\alpha$  hopane (Ts); 13: C<sub>27</sub> 17 $\alpha$  hopane (Tm); 14: C<sub>29</sub>

hopane; 15: C<sub>29</sub> Ts; 16: C<sub>30</sub> hopane; 17: C<sub>29</sub> moretane; 18: C<sub>31</sub> hopanes; 19: Gammacerane; 20: C<sub>32</sub> hopanes; 21: C<sub>33</sub> hopanes; 22: C<sub>34</sub> hopanes; 23: C<sub>35</sub> hopanes.

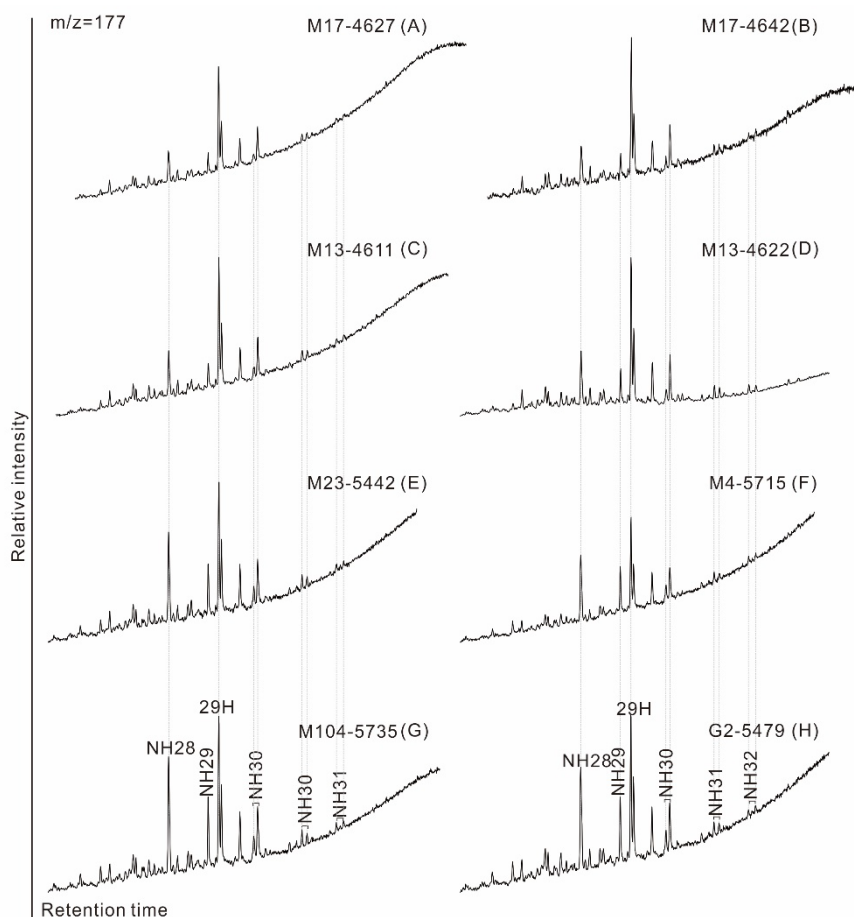


**Figure A5.4:** M/Z 177 mass chromatograms showing distribution patterns of demethylated hopanes of the studied samples.

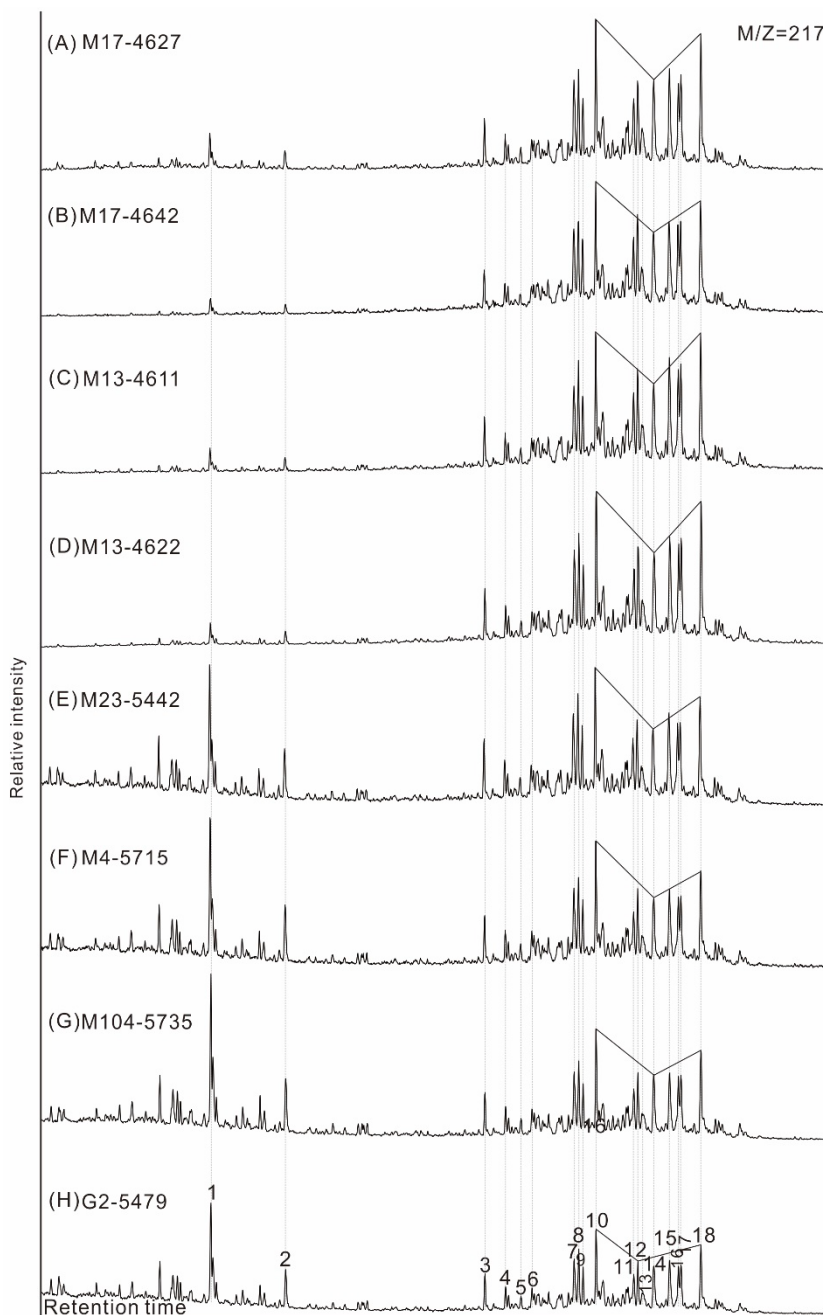


**Figure A5.5:** M/Z 217 mass chromatograms showing distribution patterns of steranes of the studied samples. Hydrocarbon compounds are identified as labelled: 1: C<sub>21</sub> pregnane; 2: C<sub>22</sub> pregnane; 3: C<sub>27</sub> β $\alpha$  20S diasterane; 4: C<sub>27</sub> β $\alpha$  20R diasterane; 5: C<sub>27</sub> αβ 20S diasterane; 6: C<sub>27</sub> αβ 20R diasterane; 7: C<sub>27</sub> ααα 20S regular sterane; 8: C<sub>27</sub> αββ 20R regular sterane; 9: C<sub>27</sub>

regular  $\alpha\beta\beta$  20S sterane; 10: C<sub>27</sub> regular  $\alpha\alpha\alpha$  20R sterane; 11: C<sub>28</sub>  $\alpha\alpha\alpha$  20S regular sterane; 12: C<sub>28</sub>  $\alpha\beta\beta$  20R regular sterane; 13 C<sub>28</sub>  $\alpha\beta\beta$  20S regular sterane; 14: C<sub>28</sub>  $\alpha\alpha\alpha$  20R regular sterane; 15: C<sub>29</sub>  $\alpha\alpha\alpha$  20S regular sterane; 16: C<sub>29</sub>  $\alpha\beta\beta$  20R regular sterane; 17: C<sub>29</sub>  $\alpha\beta\beta$  20S regular sterane; 18: C<sub>29</sub>  $\alpha\alpha\alpha$  20R regular sterane.

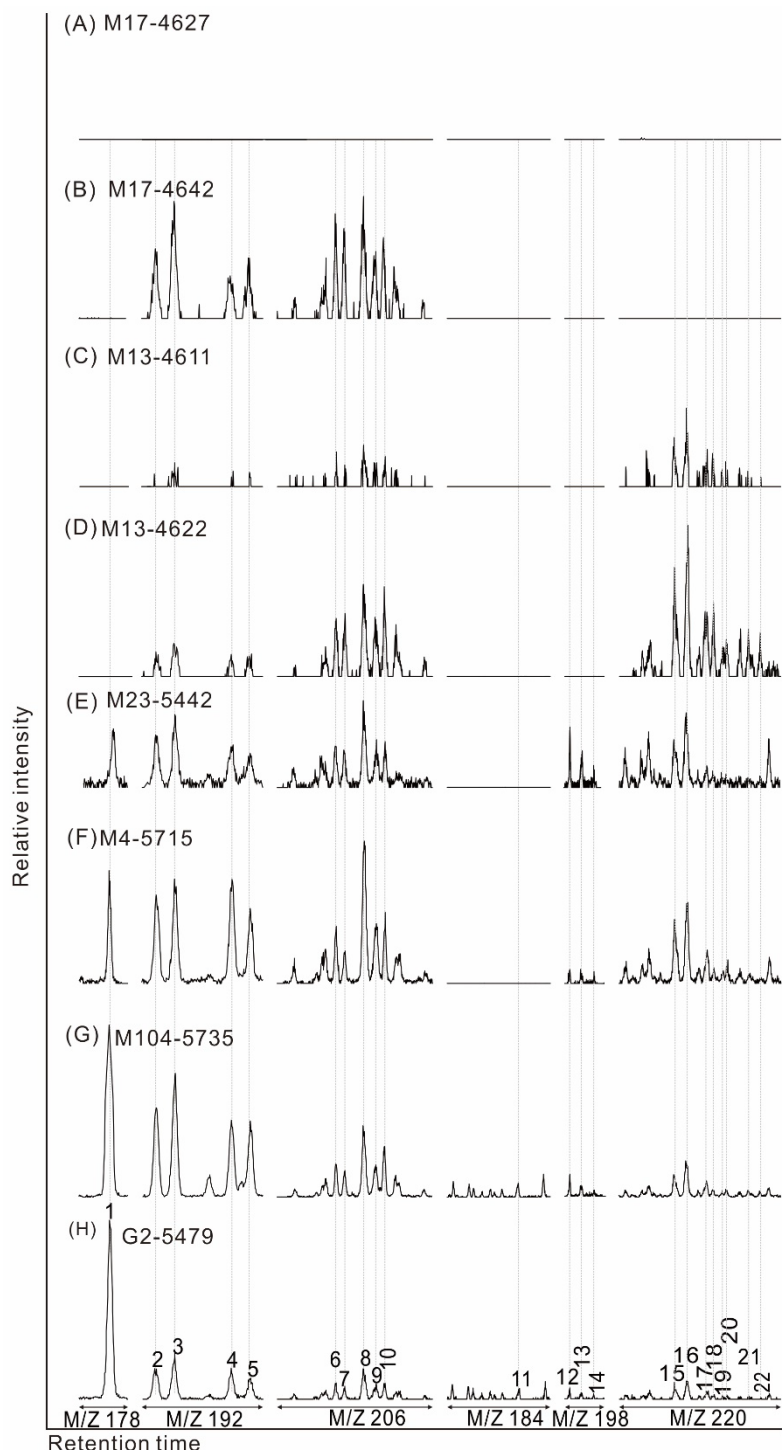


**Figure A5.6:** Mass chromatograms showing distribution patterns of aromatic hydrocarbons. Hydrocarbon compounds are identified as labelled.

1: Phenanthrene; 2: 3-methylphenanthrene (MP); 3: 2-MP; 4: 9-MP; 5: 1-MP; 6: 3,5- dimethylphenanthrene (DMP) + 2,6-DMP; 7:2,7-DMP; 8: 1,3-DMP + 2,10-DMP + 3,9-DMP + 3,10-DMP; 9: 1,6-DMP + 2,9-DMP + 2,5-DMP; 10: 1,7-DMP; 11: Dibenzothiophene (DBT); 12: 4-methyldibenzothiophene (MDBT); 13: 2-MDBT + 3-MDBT; 14: 1-MDBT; 15: 1,3,6- trimethylphenanthrene (TMP) + 1,3,10-TMP + 2,6,10-TMP + 2-ethyl, 5-MP; 16: 1,3,7-TMP + 2,6,9-TMP + 2,7,9-TMP + 7-ethyl, 1-MP; 17: 1,3,9-TMP + 2,3,6-TMP; 18: 1,6,9-TMP + 1,7,9-TMP + 2,3,7-TMP; 19: 1,3,8-TMP; 20: 2,3,10-TMP; 21: 1,6,7-TMP; 22: 1,2,6-TMP.

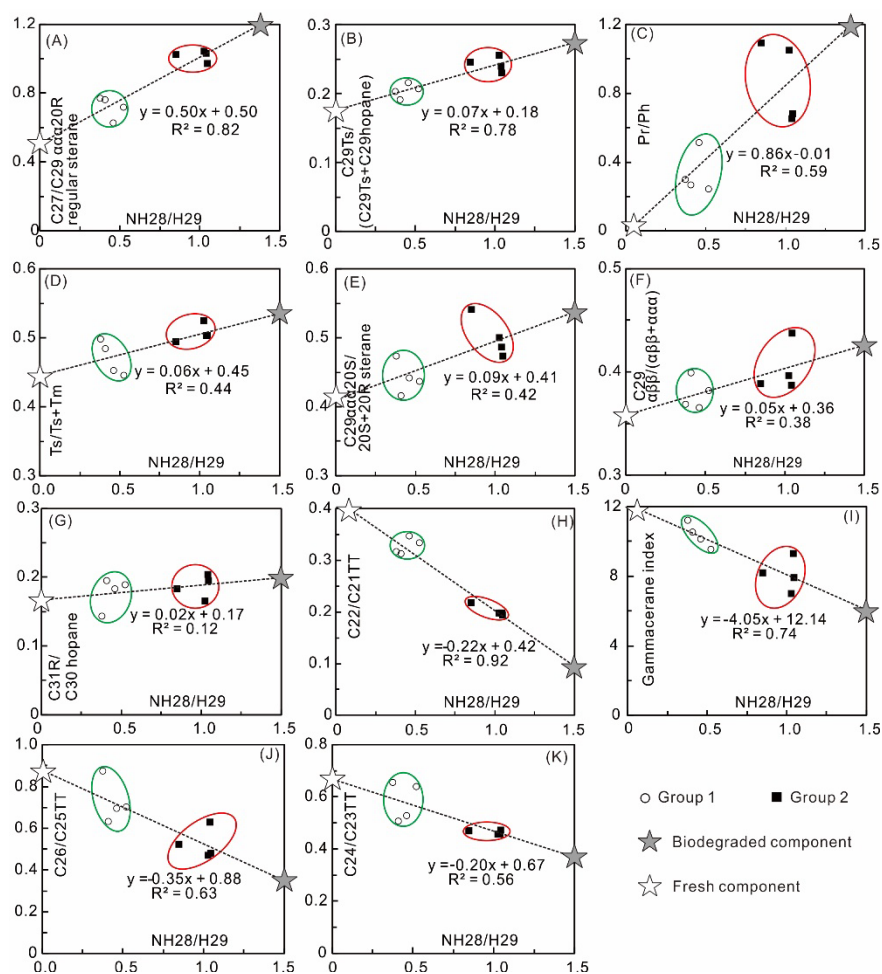


**Figure A5.7:** The ratio of C<sub>28</sub> norhopane/C<sub>29</sub> hopane (NH<sub>28</sub>/H<sub>29</sub>) is plotted against different organic indicators, including C<sub>27</sub>/C<sub>29</sub> ααα 20R regular sterane (A), C<sub>29</sub>Ts/(C<sub>29</sub>Ts+C<sub>29</sub> hopane) (B), Pr/Ph (C), Ts/Ts+Tm (D), C<sub>29</sub> ααα20S/20S+20R sterane (E), C<sub>29</sub> αββ/(αββ + ααα) (F), C<sub>31</sub>R/C<sub>30</sub> hopane (G), C<sub>22</sub>/C<sub>21</sub>TT (H), gammacerane index (I), C<sub>26</sub>/C<sub>25</sub>TT(J) and C<sub>24</sub>/C<sub>23</sub>TT (K).

## **Chapter 6**

### **Conclusions**

This study investigated the rubidium-strontium (Rb-Sr) and rhenium-osmium (Re-Os) isotopic systematics in petroleum systems and examined the potential of these robust geochronometers for dating and characterizing petroleum system events, integrated with organic and inorganic geochemistry. Petroleum system isotopic geochronology is an emerging aspect of geochemical studies of petroleum systems, and provides quantitative constraints on the temporal evolution of petroleum systems. This new branch of study has been hampered primarily by a limited understanding of the behaviour of the radiometric isotopes in petroleum system events, and appropriate selection of dating methods and targets. The aims of this project were to characterize the radiometric isotopic signatures (Re-Os and Rb-Sr) of naturally occurring hydrocarbon-associated substances (authigenic minerals, source rock and reservoir), to relate these signatures with petroleum system events, and further to unravel the potential application of these novel geochemical tools for

petroleum system analysis.

## **Dating hydrothermally facilitated hydrocarbon generation by Re-Os isotope geochemistry**

The Re-Os isotopic systematics of the Barney Creek Formation (BCF) hydrocarbon source rock in the McArthur Basin, northern Australia are investigated, using samples from drillholes GRNT-79-5 and Lamont Pass 3. A positive isochronous trend is defined by nine samples (Group 1) in the plot of  $^{187}\text{Re}/^{188}\text{Os}$ - $^{187}\text{Os}/^{188}\text{Os}$  ratios, and six samples deviate from the trend in the plot (Group 2). Regression of the isochronous trend yields an isotopic age of  $1624 \pm 62$  Ma (Model 3,  $2\sigma$ , MSWD=23) with an initial  $^{187}\text{Os}/^{188}\text{Os}$  ratio of  $0.34 \pm 0.20$  ( $2\sigma$ ). The age may not represent the timing of deposition because samples come from a vertical interval spanning over a large distance (96.6 – 511.7 meters in GRNT-79-5 and 781.1 – 803.4 meters in Lamont Pass 3) which may have resulted in heterogeneous initial Os isotopic composition. Instead, the Re-Os isotope system in these samples may have been reset by a post-depositional event, which homogenized the Os isotopic composition. Hydrothermally facilitated lamalginite-to-hydrocarbon conversion (i.e. hydrocarbon generation) is a factor resetting the Re-Os isotope system in Group 1 samples. Organic petrographic observation identified two types of organic matter in the studied samples including lamalginite (kerogen) and solid bitumen (hydrocarbon product), and lamalginite-enriched samples have lower Re-Os contents and  $^{187}\text{Re}/^{188}\text{Os}$  ratios compared

to lamalginite-depleted samples. These features suggest that lamalginite-to-hydrocarbon conversion may have remobilised two elements and fractionated  $^{187}\text{Re}/^{188}\text{Os}$  ratios in these samples.  $T_{\text{max}}$  values of the samples also support that hydrocarbon generation resulted in Re-Os re-distribution and Re/Os fractionation as there are positive trends in the plots of  $T_{\text{max}}$ -Re contents,  $T_{\text{max}}$ -Os contents and  $T_{\text{max}}$ - $^{187}\text{Re}/^{188}\text{Os}$  ratios. Hydrocarbon generation may have been facilitated by the contemporaneous hydrothermal activity which was responsible for the formation of the BCF-hosted McArthur River Pb-Zn-Ag deposit because it increased the temperature of BCF to above the oil window temperature. Hydrothermal fluids may have also brought additional Re-Os metal budget to the samples. Re and Os can be extracted from hydrothermal fluids and fixed in organic matter during hydrocarbon generation because of their organophilic properties. Therefore, the Re-Os isochronous trend obtained in this study may be resulted from the hydrothermally facilitated hydrocarbon generation event. In contrast to the closed-system  $^{187}\text{Os}$  isotopic behaviour retained in the Group 1 samples, decoupling of  $^{187}\text{Re}$  and  $^{187}\text{Os}$  in the Group 2 samples indicates an open-system behaviour (i.e.  $^{187}\text{Os}$  loss). Higher degree of  $^{187}\text{Os}$  loss occurred in samples with higher extent of deviation from the isochronous trend in the  $^{187}\text{Re}/^{188}\text{Os}$ - $^{187}\text{Os}/^{188}\text{Os}$  plot and the loss event ceased earlier in these samples compared to samples with lower extent of deviation from the trend.

## **Dating hydrocarbon charge by Rb-Sr illitic clay subsample geochronology**

The Rb-Sr isotopic composition was determined for small aliquots (3–4 mg) of five individual illitic clay samples from a Silurian bituminous sandstone in the Tarim Basin, northwest China, yielding three isochron ages:  $141 \pm 61$  Ma,  $332 \pm 32$  Ma and  $235 \pm 8$  Ma ( $2\sigma$ ) (**Chapter 3**). The studied samples are mainly composed of mixed-layer illite/smectite (I/S). The positive correlation between illitization degree (the percentage of illite in I/S) and  $^{87}\text{Rb}/^{86}\text{Sr}$  ratio suggests that illitization of I/S fractionated Rb/Sr. Rb-Sr ages represent the timing of hydrocarbon charge which inhibited the incorporation of Rb and Sr in I/S particles because hydrocarbons are more depleted in metals compared to the formation water, and this resulted in a closed-system behaviour for the Rb-Sr isotope system in I/S. The Rb-Sr ages are also consistent with previously-determined K-Ar ages of the samples (125 Ma, 389 Ma and 234 Ma). Rb-Sr isotope analyses of two samples did not yield isochron ages. This suggests that the conditions for producing isochrons were not satisfied, which may be caused by disturbance of the isotope system by post-charge hydrothermal events. The outcomes of this study show the robust potential of Rb-Sr clay subsample geochronology for cross-checking isotopic ages yielded by other systems (e.g. K-Ar system) and constraining the timing of hydrocarbon charge.

## **Dating hydrocarbon alteration by Rb-Sr pyrite**

## **subsample geochronology**

The Rb-Sr data for pyrites in two Ordovician carbonate reservoir specimens from the Tarim Basin, northwest China, yielded identical isochron ages within analytical uncertainties:  $206 \pm 13$  ( $2\sigma$ ) and  $224 \pm 28$  Ma ( $2\sigma$ ) (**Chapter 4**). Pyrite coexists with solid bitumen in the reservoir, suggesting the potential link between precipitation of pyrite and hydrocarbons. The heavy sulphur isotopic composition of the pyrite (31.032 – 31.799‰) suggests they were formed by thermochemical sulphate reduction (TSR) alteration of paleo-oil pools. Lead isotopes of pyrite indicate that fluids in which the crystals were precipitated mainly originated from crustal repositories. Burial history shows that reservoir temperature at 206 – 224 Ma was lower than the temperature necessary for TSR (100 – 180° C), thus the precipitation of TSR-pyrite was likely triggered by regional hydrothermal activity that resulted in a high-temperature environment. This study demonstrates that Rb-Sr pyrite subsample geochronology, combined with radiogenic and stable isotope analyses, can be used to determine the timing of hydrocarbon alteration.

## **Characterizing hydrocarbon source by organic and Re-Os isotopic geochemistry**

Molecular composition of organic extracts and Re-Os isotopic systematics were investigated for the Neoproterozoic-Cambrian

bituminous dolomitic natural gas reservoir in the Sichuan Basin, southwest China (**Chapter 5**). Biodegradation-sensitive organic parameters classified samples into two groups: group 1 is characterized by an insignificant hump in saturated total ion chromatograms (TICs) and low  $\text{NH}_{28}/\text{H}_{29}$  values (0.38 – 0.52); whereas group 2 is characterized by an obvious hump in saturated TICs and higher  $\text{NH}_{28}/\text{H}_{29}$  values (0.85 – 1.05). This indicates that there are two components, biodegraded and fresh, in these samples, and that samples of group 2 have higher proportions of the biodegraded component. Both components are over-mature (MPI-1 equivalent vitrinite reflectance values are 2.34% – 2.74%), and marine shale is their dominant source rock as indicated by diagnostic scatter plots ( $\text{Ph}/n\text{C}_{18}\text{-Pr}/n\text{C}_{17}$  vs  $\text{Pr}/\text{Ph}$ ,  $\text{Ph}/n\text{C}_{18}$  vs  $\text{Pr}/n\text{C}_{17}$ ,  $\text{C}_{24}/\text{C}_{23}$  vs  $\text{C}_{22}/\text{C}_{21}$  tricyclic terpanes and  $\text{C}_{26}/\text{C}_{25}$  tricyclic terpane vs  $\text{C}_{31}\text{R}/\text{C}_{30}$  hopane ratios). Compared to the fresh component, the biodegraded component is characterized by (1) a higher proportion of carbonate-derived hydrocarbons (higher  $\text{C}_{31}\text{R}/\text{C}_{30}$  hopane ratio) and (2) a higher content of bacterial-derived organic matter (higher  $\text{C}_{27}/\text{C}_{29}$   $\alpha\alpha\alpha$  20R sterane ratio). The coexistence of biodegraded and fresh components suggests that two episodes of paleo-oil charge occurred in the reservoir and that the earlier-charged hydrocarbons were biodegraded before the charge of the fresh component. Organic source and biodegradation influenced the Re-Os distribution in the bituminous dolomite. Samples with higher Re-Os contents are characterized by higher  $\text{C}_{31}\text{R}/\text{C}_{30}$  hopane and  $\text{NH}_{28}/\text{H}_{29}$  ratios, indicating that carbonate-derived hydrocarbons likely contained

higher Re-Os contents and that biodegradation can also result in higher contents of both elements. The positive trend between  $^{187}\text{Re}/^{188}\text{Os}$  and  $\text{C}_{31}\text{R}/\text{C}_{30}$  hopane ratios further indicates that the mixing of carbonate-/shale-derived hydrocarbons can influence the Re/Os fractionation. Duplicate analysis of a single bituminous dolomite reveals significant subsample-scale variation in Re-Os isotopic composition, and this Re-Os isotopic heterogeneity resulted in apparent isochron ages that are older than the depositional age of the host rock. A ternary mixing scenario is presented in the  $1/^{192}\text{Os}$  vs  $^{187}\text{Os}/^{188}\text{Os}$  plot of the samples, including I (high Os concentration and  $^{187}\text{Os}/^{188}\text{Os}$  ratio), II (high Os concentration and low  $^{187}\text{Os}/^{188}\text{Os}$  ratio) and III (low Os concentration and  $^{187}\text{Os}/^{188}\text{Os}$  ratio). According to the correlations between biomarkers and Re-Os systematics, the higher Os concentration in components I and II may have resulted from biodegradation and a greater proportion of carbonate source contribution, thus, they may represent the signatures of the earlier-charged/biodegraded hydrocarbons, whereas component III corresponds to the later-charged fresh hydrocarbons. The mixing of carbonate- and shale-derived hydrocarbons in the earlier-charged components may have fractionated their Re/Os ratios, which further resulted in the variable  $^{187}\text{Os}/^{188}\text{Os}$  ratios between components I and II. Therefore, Os isotopic composition may be a potential indicator for characterizing the hydrocarbon source in complex petroleum systems and provide additional evidence for cross-checking results obtained by other techniques (e.g. biomarker geochemistry).

## Limitations and future work

This PhD project is a preliminary attempt to investigate the Re-Os and Rb-Sr isotopic systematics in petroleum systems and the applicability of these two robust geochronometers for dating and characterizing ancient petroleum system events. More work is necessary to fully realise the potential of isotope geochronology in petroleum system analysis.

Efficiency of obtaining Re-Os isotopic data could be enhanced by improving analytical aspects of the Re-Os geochronological technique. Carius tube digestion was adopted during the course of this study mainly due to the low blank that is characteristic of the method (**Chapters 2 and 5**). However, when digesting organic-rich samples, such methodology may result in explosion of the tubes because the digestion medium (concentrated acid) can oxidize organic compounds to gaseous carbon dioxide. This is not only dangerous, but also it increases the amount of time to undertake the laboratory work. This scenario is especially common for samples with low Re-Os contents. To recover sufficient materials for measuring by mass spectrometer, a large amount of powder (e.g. >500 milligrams) is required for samples depleted in Re and Os, and this increases the risk of explosion during sample digestion. High pressure asher (HPA) may be an alternative digestion method because it can prevent explosion even with large amounts of organic-rich material. However, leaking may occur during digestion by the

HPA method, and thus optimizing HPA vessels may also be required in the future. Unlike Re isotopic ratios which were measured by multi-collector inductively plasma mass spectrometer (MC-ICP-MS), Os isotopic ratios were measured using a thermal ionization mass spectrometer (TIMS). It generally takes more than 30 minutes to measure Os isotopic ratios for a sample by TIMS in the Faraday cup static mode, and the amount of time will be doubled or even tripled if the sample has low signals and needs to be measured in secondary electron multiplier peak-jumping mode. Although measurement of isotopic ratios on MC-ICP-MS is commonly finished within 5 minutes per sample, this instrument might not be suitable for Os measurement due to the significant memory effect of Os on the sample injection system. Thus, developing an improved sample induction or cleaning system for the MC-ICP-MS will significantly facilitate Os measurements in the future.

Besides constraining the timing of hydrocarbon generation by Re-Os source rock geochronology and fingerprinting hydrocarbons using the Os isotopic composition, there could be more potential applications of Re-Os isotope pairs for determining petroleum system events, and this requires more knowledge of Re-Os isotopic behaviour. Partitioning of Re and Os between kerogen (i.e. hydrocarbon precursor), retained hydrocarbon and migrated hydrocarbon is not completely understood. Although our results (**Chapter 2**) indicate that Re-Os redistribution occurs between kerogen and hydrocarbons, and partial Re-Os budgets have been

expelled away from the source rock as carried by migrating hydrocarbons, it is still unclear whether the Re-Os isotope system in hydrocarbons maintains a closed-system during secondary migration (i.e. migration from source rock to hydrocarbon trap). This is fundamental to determining whether the Re-Os geochronometer in migrated hydrocarbons can be used for dating hydrocarbon generation. One potential method is to monitor the Re-Os isotopic composition of oils sampled from traps that are distributed along the migration path, from distal to proximal. This study does show the robust potential of Re-Os isotopic systematics for differentiating hydrocarbon sources in petroleum systems containing more than one source rock (**Chapter 5**). Other organophilic metals (e.g. vanadium, nickel) or radiogenic isotopic ratios (e.g. lead and neodymium) may also be able to serve as indicators for quantitatively estimating contributions of different source rocks in complex petroleum systems. Therefore, understanding behaviour of these inorganic metals in petroleum system events (e.g. metal source and redistribution during hydrocarbon generation/migration) will also be necessary.

Rubidium-strontium subsample geochronology is another robust method for petroleum system geochronological studies, as it unravels the Rb/Sr heterogeneity at subsample level and enables establishment of an isochron for a single sample (**Chapters 3 and 4**). Chapters 3 and 4 explored the application of this dating method to authigenic pyrite and illitic clay. Rb-Sr isotopic ages of pyrite

were interpreted as dating the timing of hydrocarbon alteration, because pyrite was precipitated by thermochemical sulphate reduction during hydrothermal alteration of the paleo-oil pool (**Chapter 4**). Besides this scenario, pyrite can also be formed during source rock deposition, hydrocarbon generation and charge, thus, coupled with geochemical and microscopy investigation of pyrite genesis, pyrite Rb-Sr subsample analysis should have robust potential for petroleum system geochronology. Rb-Sr isotope systems in illitic clay record the end-time of smectite illitization, and the Rb-Sr ages were interpreted as determining the timing of hydrocarbon charge, because emplacement of hydrocarbon inhibits illitization and maintains a closed-system (**Chapter 3**). Likewise, there is also multiple genesis of illitic clays, e.g. diagenesis and hydrothermal precipitation, thus Rb-Sr illitic clay subsample geochronology may also have the potential to constrain the timing of these events in petroleum systems.

This doctoral study has only realised a small portion of the potential of applying geochronological tools for petroleum system analysis. More functions of this inorganic geochemical toolkit will definitely be unlocked in the future by case studies of young and ancient, marine and terrigenous petroleum systems across the world.

## **Bibliography**

Every reasonable effort has been made to acknowledge the owners of copyright material. I would be pleased to hear from any copyright owner who has been omitted or incorrectly acknowledged.

### **A**

ALESSANDRELLO, A., BEEMAN, J., BROFFERIO, C., CREMONESI, O., FIORINI, E., GIULIANI, A., HALLER, E., MARGESIN, B., MONFARDINI, A. & NUCCIOTTI, A. 1999. Bolometric measurements of beta decay spectra of  $^{187}\text{Re}$  with crystals of silver perrhenate. *Physics Letters B*, 457, 253-260.

ABBASSI, S., KENNEDY, M. & SCHAEFER, B. 2017. Dating Deposition and Petroleum Migration from the Same Samples Using the Re/Os Geochronometer. *Goldschmidt Abstracts*, 2.

AL-AMERI, T. K. & ZUMBERGE, J. 2012. Middle and upper Jurassic hydrocarbon potential of the Zagross fold Belt, North Iraq. *Marine and Petroleum Geology*, 36, 13-34.

ALTANER, S. P. & YLAGAN, R. F. 1997. Comparison of structural models of mixed-layer illite/smectite and reaction mechanisms of

smectite illitization. *Clays and Clay Minerals*, 45, 517-533.

ARNABOLDI, C., BROFFERIO, C., CREMONESI, O., FIORINI, E., BIANCO, C. L., MARTENSSON, L., NUCCIOTTI, A., PAVAN, M., PESSINA, G. & PIRRO, S. 2003. Bolometric bounds on the antineutrino mass. *Physical Review Letters*, 91, 161802.

ASHKTORAB, K., JÄNECKE, J. & BECCHETTI, F. 1993. Beta decay of Re 187 and cosmochronology. *Physical Review C*, 47, 2954.

ASIF, M., FAZEELAT, T. & GRICE, K. 2011. Petroleum geochemistry of the Potwar Basin, Pakistan: 1. Oil–oil correlation using biomarkers,  $\delta^{13}\text{C}$  and  $\delta\text{D}$ . *Organic Geochemistry*, 42, 1226-1240.

ASTM D7708. 2015. Standard Test Method for Microscopical Determination of the Reflectance of Vitrinite Dispersed in Sedimentary Rocks. Annual book of ASTM Standards: Petroleum Products, Lubricants, and Fossil Fuels; Gaseous Fuels; Coal and Coke 5, 5.06: ASTM International, West Conshohocken, PA.

## **B**

BARUCH, E. T., KENNEDY, M. J., LÖHR, S. C. & DEWHURST, D. N. 2015. Feldspar dissolution-enhanced porosity in Paleoproterozoic shale reservoir facies from the Barney Creek Formation (McArthur Basin, Australia) Feldspar Dissolution-Enhanced Porosity in Paleoproterozoic Shale Reservoir Facies from

the Barney Creek Formation. AAPG Bulletin, 99, 1745-1770.

BERNER, R. A. 1984. Sedimentary pyrite formation: an update. *Geochimica et cosmochimica Acta*, 48, 605-615.

BETHKE, C. M., VERGO, N. & ALTANER, S. P. 1986. Pathways of smectite illitization. *Clays and Clay Minerals*, 34, 125-135.

BOFINGER, V., COMPSTON, W. & VERNON, M. 1968. The application of acid leaching to the Rb-Sr dating of a Middle Ordovician shale. *Geochimica et Cosmochimica Acta*, 32, 823-833.

BOREHAM, C., CRICK, I. & POWELL, T. 1988. Alternative calibration of the Methylphenanthrene Index against vitrinite reflectance: Application to maturity measurements on oils and sediments. *Organic Geochemistry*, 12, 289-294.

BULL, S. 1998. Sedimentology of the Palaeoproterozoic Barney Creek formation in DDH BMR McArthur 2, southern McArthur basin, northern territory. *Australian Journal of Earth Sciences*, 45, 21-31.

BUSCH, B., HILGERS, C., LANDER, R. H., BONNELL, L. M. & ADELMANN, D. 2018. Reservoir quality and burial model evaluation by kinetic quartz and illite cementation modeling: Case study of Rotliegendes, north Germany. *AAPG Bulletin*, 102, 293-307.

## C

CAI, C., AMRANI, A., WORDEN, R. H., XIAO, Q., WANG, T., GVIRTZMAN, Z., LI, H., SAID-AHMAD, W. & JIA, L. 2016. Sulfur isotopic compositions of individual organosulfur compounds and their genetic links in the Lower Paleozoic petroleum pools of the Tarim Basin, NW China. *Geochimica et Cosmochimica Acta*, 182, 88-108.

CAI, C., HU, W. & WORDEN, R. H. 2001. Thermochemical sulphate reduction in Cambro–Ordovician carbonates in Central Tarim. *Marine and Petroleum Geology*, 18, 729-741.

CAI, C., LI, K., ANLAI, M., ZHANG, C., XU, Z., WORDEN, R. H., WU, G., ZHANG, B. & CHEN, L. 2009a. Distinguishing Cambrian from Upper Ordovician source rocks: Evidence from sulfur isotopes and biomarkers in the Tarim Basin. *Organic Geochemistry*, 40, 755-768.

CAI, C., LI, K., LI, H. & ZHANG, B. 2008. Evidence for cross formational hot brine flow from integrated  $^{87}\text{Sr}/^{86}\text{Sr}$ , REE and fluid inclusions of the Ordovician veins in Central Tarim, China. *Applied Geochemistry*, 23, 2226-2235.

CAI, C., WORDEN, R. H., WANG, Q., XIANG, T., ZHU, J. & CHU, X. 2002. Chemical and isotopic evidence for secondary alteration of natural gases in the Hetianhe Field, Bachu Uplift of the Tarim Basin. *Organic Geochemistry*, 33, 1415-1427.

CAI, C., ZHANG, C., CAI, L., WU, G., JIANG, L., XU, Z., LI, K.,

MA, A. & CHEN, L. 2009b. Origins of Palaeozoic oils in the Tarim Basin: evidence from sulfur isotopes and biomarkers. *Chemical Geology*, 268, 197-210.

CAMPBELL-MILLER, M. D. & SIMARD, B. 1996. First ionization potentials of tungsten and rhenium by mass-selected double-resonance ionization spectroscopy. *JOSA B*, 13, 2115-2120.

CAO, H.-W., ZHANG, S.-T., SANTOSH, M., ZHENG, L., TANG, L., LI, D., ZHANG, X.-H. & ZHANG, Y.-H. 2015. The Luanchuan Mo–W–Pb–Zn–Ag magmatic–hydrothermal system in the East Qinling metallogenic belt, China: Constrains on metallogenesis from C–H–O–S–Pb isotope compositions and Rb–Sr isochron ages. *Journal of Asian Earth Sciences*, 111, 751-780.

CHAFFEE, A. L. & JOHNS, R. 1983. Polycyclic aromatic hydrocarbons in Australian coals. I. Angularly fused pentacyclic tri- and tetraaromatic components of Victorian brown coal. *Geochimica et Cosmochimica Acta*, 47, 2141-2155.

CHAKHMAKHCHEV, A., SUZUKI, M. & TAKAYAMA, K. 1997. Distribution of alkylated dibenzothiophenes in petroleum as a tool for maturity assessments. *Organic Geochemistry*, 26, 483-489.

CHAUDHURI, S. & BROOKINS D. G. 1979. The Rb-Sr systematics in acid-leached clay minerals. *Chemical Geology* 24, 231-242.

CHEN, J., WALTER, M. R., LOGAN, G. A., HINMAN, M. C. & SUMMONS, R. E. 2003. The Paleoproterozoic McArthur River (HYC) Pb/Zn/Ag deposit of northern Australia: organic geochemistry and ore genesis. *Earth and Planetary Science Letters*, 210, 467-479.

CHENG, B., CHEN, Z., CHEN, T., YANG, C. & WANG, T.-G. 2018. Biomarker signatures of the Ediacaran–Early Cambrian origin petroleum from the central Sichuan Basin, South China: Implications for source rock characteristics. *Marine and Petroleum Geology*, 96, 577-590.

CHIARADIA, M., KONOPELKO, D., SELTMANN, R. & CLIFF, R. A. 2006. Lead isotope variations across terrane boundaries of the Tien Shan and Chinese Altay. *Mineralium Deposita*, 41, 411-428.

CHUNG, H. M. & SACKETT, W. M. 1979. Use of stable carbon isotope compositions of pyrolytically derived methane as maturity indices for carbonaceous materials. *Geochimica et Cosmochimica Acta*, 43, 1979-1988.

CLAUER, N. 2013. The K-Ar and  $^{40}\text{Ar}/^{39}\text{Ar}$  methods revisited for dating fine-grained K-bearing clay minerals. *Chemical Geology*, 354, 163-185.

CLAUER, N., CHAUDHURI, S., KRALIK, M. & BONNOT-COURTOIS, C. 1993. Effects of experimental leaching on Rb–Sr and K–Ar isotopic systems and REE contents of diagenetic illite.

Chemical Geology, 103, 1-16.

CLAUER, N., GIBLIN, P. & LUCAS, J. 1984. Sr and Ar isotope studies of detrital smectites from the Atlantic Ocean (DSDP, Legs 43, 48 and 50). Chemical geology, 46, 141-151.

CLAUER, N., JOURDAN, F. & ZWINGMANN, H. 2011. Dating petroleum emplacement by illite  $^{40}\text{Ar}/^{39}\text{Ar}$  laser stepwise heating: Discussion. AAPG Bulletin, 95, 2107-2111.

CLAUER, N., ŚRODOŃ, J., FRANCU, J. & ŠUCHA, V. 1997. K-Ar dating of illite fundamental particles separated from illite-smectite. Clay Minerals, 32, 181-196.

CLAUER, N., WILLIAMS, L. B. & FALLICK, A. E. 2014. Genesis of nanometric illite crystals elucidated by light-element (hydrogen, lithium, boron and oxygen) isotope tracing, and K-Ar and Rb-Sr dating. Chemical Geology, 383, 26-50.

CLAYTON, C. 1991. Carbon isotope fractionation during natural gas generation from kerogen. Marine and Petroleum Geology, 8, 232-240.

COHEN, A. S., COE, A. L., BARTLETT, J. M. & HAWKESWORTH, C. J. 1999. Precise Re-Os ages of organic-rich mudrocks and the Os isotope composition of Jurassic seawater. Earth and Planetary Science Letters, 167, 159-173.

CRAIG, J., BIFFI, U., GALIMBERTI, R., GHORI, K., GORTER, J.,

HAKHOO, N., LE HERON, D., THUROW, J. & VECOLI, M. 2013. The palaeobiology and geochemistry of Precambrian hydrocarbon source rocks. *Marine and Petroleum Geology*, 40, 1-47.

CREASER, R. A., SANNIGRAHI, P., CHACKO, T. & SELBY, D. 2002. Further evaluation of the Re-Os geochronometer in organic-rich sedimentary rocks: A test of hydrocarbon maturation effects in the Exshaw Formation, Western Canada Sedimentary Basin. *Geochimica et Cosmochimica Acta*, 66, 3441-3452.

CREASER, R., PAPANASTASSIOU, D. & WASSERBURG, G. 1991. Negative thermal ion mass spectrometry of osmium, rhenium and iridium. *Geochimica et Cosmochimica Acta*, 55, 397-401.

CRICK, I. H. 1992. Petrological and maturation characteristics of organic matter from the Middle Proterozoic McArthur Basin, Australia. *Australian Journal of Earth Sciences*, 39, 501-519.

CRICK, I. H., BOREHAM, C. J., COOK, A. C. & POWELL, T. G. 1988. Petroleum geology and geochemistry of Middle Proterozoic McArthur Basin, northern Australia II: assessment of source rock potential. *AAPG Bulletin*, 72, 1495-1514.

CUMMING, V. M., SELBY, D. & LILLIS, P. G. 2012. Re-Os geochronology of the lacustrine Green River Formation: insights into direct depositional dating of lacustrine successions, Re-Os systematics and paleocontinental weathering. *Earth and Planetary Science Letters*, 359, 194-205.

CUMMING, V. M., SELBY, D., LILLIS, P. G. & LEWAN, M. D. 2014. Re–Os geochronology and Os isotope fingerprinting of petroleum sourced from a Type I lacustrine kerogen: Insights from the natural Green River petroleum system in the Uinta Basin and hydrous pyrolysis experiments. *Geochimica et Cosmochimica Acta*, 138, 32-56.

## **D**

DAI, J., ZOU, C., LIAO, S., DONG, D., NI, Y., HUANG, J., WU, W., GONG, D., HUANG, S. & HU, G. 2014. Geochemistry of the extremely high thermal maturity Longmaxi shale gas, southern Sichuan Basin. *Organic Geochemistry*, 74, 3-12.

DAVIDSON, G. & DASHLOOTY, S. 1993. The Glyde Sub-basin: A volcanoclastic-bearing pull-apart basin coeval with the McArthur River base-metal deposit, Northern Territory. *Australian Journal of Earth Sciences*, 40, 527-543.

DEMAISON, G. 1984. The generative basin concept. *AAPG Memoir, Petroleum Geochemistry and Basin Evaluation*, 1-14.

DONG, L., WAN, B., YANG, W., DENG, C., CHEN, Z., YANG, L., CAI, K. & XIAO, W. 2016. Rb-Sr geochronology of single gold-bearing pyrite grains from the Katbasu gold deposit in the South Tianshan, China and its geological significance. *Ore Geology Reviews*, 100, 99-110.

DOW, W. G. 1974. Application of oil-correlation and source-rock data to exploration in Williston Basin. AAPG bulletin, 58, 1253-1262.

DU, J., ZOU, C., XU, C., HE, H., SHEN, P., YANG, Y., LI, Y., WEI, G., WANG, Z. & YANG, Y. 2014. Theoretical and technical innovations in strategic discovery of a giant gas field in Cambrian Longwangmiao Formation of central Sichuan paleo-uplift, Sichuan Basin. Petroleum Exploration and Development, 41, 294-305.

DUNSTER, J. 2007. Gas shows in Glyde sub-basin, accessed June 9, 2014. Minerals Exploration Reports, Northern Territory Geological Survey. <http://www.geoscience.nt.gov.au/gemis/ntgsjspui/handle/1/74198>.

DUTTA, S., BHATTACHARYA, S. & RAJU, S. V. 2013. Biomarker signatures from Neoproterozoic–early Cambrian oil, western India. Organic Geochemistry, 56, 68-80.

## **E**

EHRENBERG, S. & NADEAU, P. 1989. Formation of diagenetic illite in sandstones of the Garn Formation, Haltenbanken area, Mid-Norwegian continental shelf. Clay Minerals, 24, 233-253.

ELLIS, G. 2007. Hydrocarbon entrapment in Triassic to late Jurassic reservoirs in the Timor Sea, Australia-new insights. APPEA Journal, 47, 39-53.

EVANS, J. 1996. Dating the transition of smectite to illite in Palaeozoic mudrocks using the Rb–Sr whole-rock technique. *Journal of the Geological Society* 153, 101-108.

## **F**

FAURE, G. & MENSING, T. M. 2005. *Isotopes: principles and applications*, John Wiley & Sons Inc. 928p.

FINLAY, A. J., SELBY, D. & OSBORNE, M. J. 2011. Re-Os geochronology and fingerprinting of United Kingdom Atlantic margin oil: Temporal implications for regional petroleum systems. *Geology*, 39, 475-478.

FINLAY, A. J., SELBY, D. & OSBORNE, M. J. 2012. Petroleum source rock identification of United Kingdom Atlantic Margin oil fields and the Western Canadian Oil Sands using Platinum, Palladium, Osmium and Rhenium: Implications for global petroleum systems. *Earth and Planetary Science Letters*, 313, 95-104.

FLANNERY, E. N. & GEORGE, S. C. 2014. Assessing the syngeneity and indigeneity of hydrocarbons in the ~1.4 Ga Velkerri Formation, McArthur Basin, using slice experiments. *Organic Geochemistry*, 77, 115-125.

FOWLER, M. & DOUGLAS, A. G. 1987. Saturated hydrocarbon biomarkers in oils of Late Precambrian age from Eastern Siberia. *Organic Geochemistry*, 11, 201-213.

FRANKS, S. G. & ZWINGMANN, H. 2010. Origin and timing of late diagenetic illite in the Permian–Carboniferous Unayzah sandstone reservoirs of Saudi Arabia. *AAPG Bulletin*, 94, 1133-1159.

FUEX, A. 1977. The use of stable carbon isotopes in hydrocarbon exploration. *Journal of Geochemical Exploration*, 7, 155-188.

## **G**

GALEAZZI, M., FONTANELLI, F., GATTI, F. & VITALE, S. 2000. End-point energy and half-life of the  $^{187}\text{Re}$   $\beta$  decay. *Physical Review C*, 63, 014302.

GE, X., SHEN, C., SELBY, D., DENG, D. & MEI, L. 2016. Apatite fission-track and Re-Os geochronology of the Xuefeng uplift, China: Temporal implications for dry gas associated hydrocarbon systems. *Geology*, 44, 491-494.

GE, X., SHEN, C., SELBY, D., WANG, G., YANG, Z., GONG, Y. & XIONG, S. 2017. Neoproterozoic-Cambrian petroleum system evolution of the Micang Shan uplift, Northern Sichuan Basin, China: Insights from pyrobitumen Re-Os geochronology and apatite fission track analysis. *AAPG Bulletin*, 102, 1429-1453

GE, X., SHEN, C., SELBY, D., WANG, J., MA, L., RUAN, X., HU, S. & MEI, L. 2018. Petroleum-generation timing and source in the northern Longmen Shan thrust belt, Southwest China: Implications for multiple oil-generation episodes and sources. *AAPG Bulletin*,

102, 913-938.

GEORGE, S. & AHMED, M. 2002. Use of aromatic compound distributions to evaluate organic maturity of the Proterozoic middle Velkerri Formation, McArthur Basin, Australia. In KEEP, M. & MOSS, S.J. (Eds), 2002. *The Sedimentary Basins of Western Australia 3: Proceedings of the Petroleum Exploration Society of Australia Symposium*, Perth, WA, 2002. 253-270.

GEORGE, S. C., VOLK, H., DUTKIEWICZ, A., RIDLEY, J. & BUICK, R. 2008. Preservation of hydrocarbons and biomarkers in oil trapped inside fluid inclusions for > 2 billion years. *Geochimica et Cosmochimica Acta*, 72, 844-870.

GEORGIEV, S. V., STEIN, H. J., HANNAH, J. L., GALIMBERTI, R., NALI, M., YANG, G. & ZIMMERMAN, A. 2016. Re–Os dating of maltenes and asphaltenes within single samples of crude oil. *Geochimica et Cosmochimica Acta*, 179, 53-75.

GLIKSON, M. 2001. The application of electron microscopy and microanalysis in conjunction with organic petrology to further the understanding of organic–mineral association: examples from Mount Isa and McArthur Basins, Australia. *International Journal of Coal Geology*, 47, 139-159.

GLIKSON, M., GOLDING, S. & SOUTHGATE, P. 2006. Thermal evolution of the ore-hosting Isa superbasin: Central and northern Lawn Hill platform. *Economic Geology*, 101, 1211-1229.

GLIKSON, M., TAYLOR, D. & MORRIS, D. 1992. Lower Palaeozoic and Precambrian petroleum source rocks and the coalification path of alginite. *Organic Geochemistry*, 18, 881-897.

GOROKHOV, I., CLAUER, N., TURCHENKO, T., MELNIKOV, N., KUTYAVIN, E., PIRRUS, E. AND BASKAKOV, A. 1994. Rb-Sr systematics of Vendian-Cambrian claystones from the east European Platform: implications for a multi-stage illite evolution. *Chemical Geology* 112, 71-89.

GOROKHOV, I., SIEDLECKA, A., ROBERTS, D., MELNIKOV, N. & TURCHENKO, T. 2001. Rb-Sr dating of diagenetic illite in Neoproterozoic shales, Varanger Peninsula, northern Norway. *Geological Magazine*, 138, 541-562.

GRICE, K., NABBefeld, B. & MASLEN, E. 2007. Source and significance of selected polycyclic aromatic hydrocarbons in sediments (Hovea-3 well, Perth Basin, Western Australia) spanning the Permian-Triassic boundary. *Organic Geochemistry*, 38, 1795-1803.

GUO, T. & ZHANG, H. 2014. Formation and enrichment mode of Jiaoshiha shale gas field, Sichuan Basin. *Petroleum Exploration and Development*, 41, 31-40.

GUO, X., LIU, K., JIA, C., SONG, Y., ZHAO, M., ZHUO, Q. & LU, X. 2016. Hydrocarbon accumulation processes in the Dabei tight-gas reservoirs, Kuqa Subbasin, Tarim Basin, northwest China. *AAPG*

Bulletin, 100, 1501-1521.

## H

HALL, P. A., MCKIRDY, D. M., GRICE, K. & EDWARDS, D. S. 2014. Australasian asphaltite strandings: Their origin reviewed in light of the effects of weathering and biodegradation on their biomarker and isotopic profiles. *Marine and Petroleum Geology*, 57, 572-593.

HAMILTON, P., KELLEY, S. & FALLICK, A. E. 1989. K-Ar dating of illite in hydrocarbon reservoirs. *Clay Minerals*, 24, 215-231.

HAN, Y., LI, X., ZHANG, S., ZHANG, Y. & CHEN, F. 2007. Single grain Rb-Sr dating of euhedral and cataclastic pyrite from the Qiyugou gold deposit in western Henan, central China. *Chinese Science Bulletin*, 52, 1820-1826.

HAN, Y., MAHLSTEDT, N. & HORSFIELD, B. 2015. The Barnett Shale: compositional fractionation associated with intraformational petroleum migration, retention and expulsion. *AAPG Bulletin*, 99, 2173-2202.

HANSON, A., ZHANG, S., MOLDOWAN, J., LIANG, D. & ZHANG, B. 2000. Molecular organic geochemistry of the Tarim Basin, northwest China. *AAPG Bulletin*, 84, 1109-1128.

HEDENQUIST, J. W. & LOWENSTERN, J. B. 1994. The role of

magmas in the formation of hydrothermal ore deposits. *Nature*, 370, 519-527.

HEMMENDINGER, A. & SMYTHE, W. 1937. The radioactive isotope of rubidium. *Physical Review*, 51, 1052.

HIRATA, T. 2000. Development of a flushing spray chamber for inductively coupled plasma-mass spectrometry. *Journal of Analytical Atomic Spectrometry*, 15, 1447-1450.

HITES, R. A., LAFLAMME, R. E. & FARRINGTON, J. W. 1977. Sedimentary polycyclic aromatic hydrocarbons: the historical record. *Science*, 198, 829-831.

HOFFMAN, E., NALDRETT, A., VAN LOON, J., HANCOCK, R. & MANSON, A. 1978. The determination of all the platinum group elements and gold in rocks and ore by neutron activation analysis after preconcentration by a nickel sulphide fire-assay technique on large samples. *Analytica Chimica Acta*, 102, 157-166.

HOLMAN, A. I., GRICE, K., JARAULA, C. M. & SCHIMMELMANN, A. 2014. Bitumen II from the Paleoproterozoic Here's Your Chance Pb/Zn/Ag deposit: Implications for the analysis of depositional environment and thermal maturity of hydrothermally-altered sediments. *Geochimica et Cosmochimica Acta*, 139, 98-109.

HOLMAN, A. I., GRICE, K., JARAULA, C. M.,

SCHIMMELMANN, A. & BROCKS, J. J. 2012. Efficiency of extraction of polycyclic aromatic hydrocarbons from the Paleoproterozoic Here's Your Chance Pb/Zn/Ag ore deposit and implications for a study of Bitumen II. *Organic Geochemistry*, 52, 81-87.

HU, Q., WANG, Y., MAO, J., WEI, R., LIU, S., YE, D., YUAN, Q. & DOU, P. 2015. Timing of the formation of the Changba–Lijiagou Pb–Zn ore deposit, Gansu Province, China: Evidence from Rb–Sr isotopic dating of sulfides. *Journal of Asian Earth Sciences*, 103, 350-359.

HU, S., WILKES, H., HORSFIELD, B., CHEN, H. & LI, S. 2016. On the origin, mixing and alteration of crude oils in the Tarim Basin. *Organic Geochemistry*, 97, 17-34.

HUANG, H. & LI, J. 2016. Molecular composition assessment of biodegradation influence at extreme levels—A case study from oilsand bitumen in the Junggar Basin, NW China. *Organic Geochemistry*, 103, 31-42.

HUANG, H., ZHANG, S. & SU, J. 2016. Palaeozoic oil–source correlation in the Tarim Basin, NW China: A review. *Organic Geochemistry*, 94, 32-46.

HUGHES, W. B. 1984. Use of thiophenic organosulfur compounds in characterizing crude oils derived from carbonate versus siliciclastic sources. *AAPG Studies in Geology*, 181-196.

HUNT, J.M. 1996. Petroleum Geochemistry and Geology. Second Edition. W.H. Freeman and Company, New York, 743p.

HURTIG, N., GEORGIEV, S., STEIN, H. & HANNAH, J. 2019. Re-Os systematics in petroleum during water-oil interaction: The effects of oil chemistry. *Geochimica et Cosmochimica Acta*, 247, 142-161.

## **J**

JACKSON, M. J., POWELL, T. G., SUMMONS, R. E. & SWEET, I. P. 1986. Hydrocarbon shows and petroleum source rocks in sediments as old as  $1.7 \times 10^9$  years. *Nature*, 322, 727-729.

JACKSON, M., SWEET, I. & POWELL, T. 1988. Studies on petroleum geology and geochemistry, Middle Proterozoic, McArthur Basin Northern Australia I: petroleum potential. *APEA Journal*, 28, 283-302.

JARRETT, A. J. M., COX, G. M., SOUTHBY, C., HONG, Z., PALATY, P., CARR, L. & HENSON, P. 2018. Source rock geochemistry of the McArthur Basin, northern Australia: Rock-Eval pyrolysis data release. Record 2018/24. Geoscience Australia, Canberra, 24, 1-25.

JARVIE, D. M., HILL, R. J., RUBLE, T. E. & POLLASTRO, R. M. 2007. Unconventional shale-gas systems: The Mississippian Barnett Shale of north-central Texas as one model for thermogenic shale-gas assessment. *AAPG bulletin*, 91, 475-499.

JIA, C. & WEI, G. 2002. Structural characteristics and petroliferous features of Tarim Basin. *Chinese Science Bulletin*, 47, 1-11.

JIA, L., CAI, C., YANG, H., LI, H., WANG, T., ZHANG, B., JIANG, L. & TAO, X. 2015. Thermochemical and bacterial sulfate reduction in the Cambrian and Lower Ordovician carbonates in the Tazhong Area, Tarim Basin, NW China: evidence from fluid inclusions, C, S, and Sr isotopic data. *Geofluids*, 15, 421-437.

JIA, W., PENG, P. & XIAO, Z. 2008. Carbon isotopic compositions of 1, 2, 3, 4-tetramethylbenzene in marine oil asphaltenes from the Tarim Basin: Evidence for the source formed in a strongly reducing environment. *Science in China Series D: Earth Sciences*, 51, 509-514.

JIA, W., XIAO, Z., YU, C. & PENG, P. A. 2010. Molecular and isotopic compositions of bitumens in Silurian tar sands from the Tarim Basin, NW China: Characterizing biodegradation and hydrocarbon charging in an old composite basin. *Marine and Petroleum Geology*, 27, 13-25.

JIN, Z., ZHU, D., ZHANG, X., HU, W. & SONG, Y. 2006. Hydrothermally fluoritized Ordovician carbonates as reservoir rocks in the Tazhong area, central Tarim Basin, NW China. *Journal of Petroleum Geology*, 29, 27-40.

## **K**

KANG, Y. & KANG, Z. 1996. Tectonic evolution and oil and gas of Tarim Basin. *Journal of Southeast Asian Earth Sciences*, 13, 317-325.

KAWKA, O. E. & SIMONEIT, B. R. 1990. Polycyclic aromatic hydrocarbons in hydrothermal petroleum from the Guaymas Basin spreading center. *Applied Geochemistry*, 5, 17-27.

KENDALL, B., CREASER, R. A., GORDON, G. W. & ANBAR, A. D. 2009a. Re–Os and Mo isotope systematics of black shales from the Middle Proterozoic Velkerri and Wollogorang Formations, McArthur Basin, northern Australia. *Geochimica et Cosmochimica Acta*, 73, 2534-2558.

KENDALL, B., CREASER, R. A. & SELBY, D. 2009b. <sup>187</sup>Re–<sup>187</sup>Os geochronology of Precambrian organic-rich sedimentary rocks. Geological Society, London, Special Publications, 326, 85-107.

KLEMME, H. & ULMISHEK, G. F. 1991. Effective petroleum source rocks of the world: stratigraphic distribution and controlling depositional factors (1). *AAPG Bulletin*, 75, 1809-1851.

KORSCH, R., HUAZHAO, M., ZHAOCAI, S. & GORTER, J. 1991. The Sichuan basin, southwest China: a late Proterozoic (Sinian) petroleum province. *Precambrian Research*, 54, 45-63.

KRALIK, M. 1982. Rb-Sr age determinations on Precambrian carbonate rocks of the Carpentarian McArthur basin, Northern

Territories, Australia. *Precambrian Research*, 18, 157-170.

KRALIK, M. 1983. Interpretation of K– Ar and Rb– Sr data from fine fractions of weakly metamorphosed shales and carbonate rocks at the base of the northern calcareous Alps (Salzburg, Austria). *Tschermaks Mineralogische und Petrographische Mitteilungen* 32, 49-67.

KRUGE, M. A. 2000. Determination of thermal maturity and organic matter type by principal components analysis of the distributions of polycyclic aromatic compounds. *International Journal of Coal Geology*, 43, 27-51.

## **L**

LAFLAMME, R. E. & HITES, R. A. 1978. The global distribution of polycyclic aromatic hydrocarbons in recent sediments. *Geochimica et Cosmochimica Acta*, 42, 289-303.

LANDIS, C.R. & Castaño, J.R. 1995. Maturation and bulk chemical properties of a suite of solid hydrocarbons. *Organic Geochemistry*, 22, 137-149.

LARGE, R. R., BULL, S. W., MCGOLDRICK, P. J. & WALTERS, S. 2005. Stratiform and strata-bound Zn-Pb-Ag deposits in Proterozoic sedimentary basins, northern Australia. *Economic Geology*, 100, 931-963.

LARGE, R. R., DANYUSHEVSKY, L., HOLLIT, C., MASLENNIKOV, V., MEFFRE, S., GILBERT, S., BULL, S., SCOTT, R., EMSBO, P. & THOMAS, H. 2009. Gold and trace element zonation in pyrite using a laser imaging technique: Implications for the timing of gold in orogenic and Carlin-style sediment-hosted deposits. *Economic Geology*, 104, 635-668.

LARGE, R. R., HALPIN, J. A., DANYUSHEVSKY, L. V., MASLENNIKOV, V. V., BULL, S. W., LONG, J. A., GREGORY, D. D., LOUNEJEVA, E., LYONS, T. W. & SACK, P. J. 2014. Trace element content of sedimentary pyrite as a new proxy for deep-time ocean–atmosphere evolution. *Earth and Planetary Science Letters*, 389, 209-220.

LAWLEY, C., SELBY, D. & IMBER, J. 2013. Re-Os molybdenite, pyrite, and chalcopyrite geochronology, lupa goldfield, southwestern Tanzania: tracing metallogenic time scales at midcrustal shear zones hosting orogenic Au deposits. *Economic Geology*, 108, 1591-1613.

LEWAN, M. & MAYNARD, J. 1982. Factors controlling enrichment of vanadium and nickel in the bitumen of organic sedimentary rocks. *Geochimica et Cosmochimica Acta*, 46, 2547-2560.

LI, C.-F., CHU, Z.-Y., GUO, J.-H., LI, Y.-L., YANG, Y.-H. & LI, X.-H. 2015a. A rapid single column separation scheme for high-precision Sr–Nd–Pb isotopic analysis in geological samples using thermal ionization mass spectrometry. *Analytical Methods*, 7, 4793-

4802.

LI, C.-F., CHU, Z.-Y., GUO, J.-H., LI, Y.-L., YANG, Y.-H. & LI, X.-H. 2015b. A rapid single column separation scheme for high-precision Sr–Nd–Pb isotopic analysis in geological samples using thermal ionization mass spectrometry. *Analytical Methods*, 7, 4793-4802.

LI, C.-F., GUO, J.-H., CHU, Z.-Y., FENG, L.-J. & WANG, X.-C. 2015c. Direct High-Precision Measurements of the  $^{87}\text{Sr}/^{86}\text{Sr}$  Isotope Ratio in Natural Water without Chemical Separation Using Thermal Ionization Mass Spectrometry Equipped with 1012  $\Omega$  Resistors. *Analytical Chemistry*, 87, 7426-7432.

LI, J., LIANG, X.-R., XU, J.-F., SUZUKI, K. & DONG, Y.-H. 2010. Simplified technique for the measurements of Re-Os isotope by multicollector inductively coupled plasma mass spectrometry (MC-ICP-MS). *Geochemical Journal*, 44, 73-80.

LI, J., WANG, X.-C., XU, J.-F., XU, Y.-G., TANG, G.-J. & WANG, Q. 2015. Disequilibrium-induced initial Os isotopic heterogeneity in gram aliquots of single basaltic rock powders: Implications for dating and source tracing. *Chemical Geology*, 406, 10-17.

LI, K., CAI, C., HE, H., JIANG, L., CAI, L., XIANG, L., HUANG, S. & ZHANG, C. 2011. Origin of palaeo-waters in the Ordovician carbonates in Tahe oilfield, Tarim Basin: constraints from fluid inclusions and Sr, C and O isotopes. *Geofluids*, 11, 71-86.

LI, Q.-L., CHEN, F., YANG, J.-H. & FAN, H.-R. 2008. Single grain pyrite Rb–Sr dating of the Linglong gold deposit, eastern China. *Ore Geology Reviews*, 34, 263-270.

LI, S., AMRANI, A., PANG, X., YANG, H., SAID-AHMAD, W., ZHANG, B. & PANG, Q. 2015c. Origin and quantitative source assessment of deep oils in the Tazhong Uplift, Tarim Basin. *Organic Geochemistry*, 78, 1-22.

LI, S., SHI, Q., PANG, X., ZHANG, B. & ZHANG, H. 2012. Origin of the unusually high dibenzothiophene oils in Tazhong-4 Oilfield of Tarim Basin and its implication in deep petroleum exploration. *Organic geochemistry*, 48, 56-80.

LIAO, F., ZHANG, L., CHEN, N., SUN, M., SANTOSH, M., WANG, Q. & MUSTAFA, H. A. 2014. Geochronology and geochemistry of meta-mafic dykes in the Quanji Massif, NW China: Paleoproterozoic evolution of the Tarim Craton and implications for the assembly of the Columbia supercontinent. *Precambrian Research*, 249, 33-56.

LILLIS, P. G. & SELBY, D. 2013. Evaluation of the rhenium–osmium geochronometer in the Phosphoria petroleum system, Bighorn Basin of Wyoming and Montana, USA. *Geochimica et Cosmochimica Acta*, 118, 312-330.

LINDNER, M., LEICH, D. A., RUSS, G. P., BAZAN, J. M. & BORG, R. J. 1989. Direct determination of the half-life of <sup>187</sup>Re.

*Geochimica et Cosmochimica Acta*, 53, 1597-1606.

LINDNER, M., LEICH, D., BORG, R., RUSS, G., BAZAN, J., SIMONS, D. & DATE, A. 1986. Direct laboratory determination of the <sup>187</sup>Re half-life. *Nature*, 320, 246-248.

LINDSAY, J. 2001. Basin dynamics and mineralisation, McArthur Basin, northern Australia. *Australian Journal of Earth Sciences*, 48, 703-720.

LIU, J., JIANG, Z., LIU, K., GUI, L. & XING, J. 2016. Hydrocarbon sources and charge history in the Southern Slope Region, Kuqa Foreland Basin, northwestern China. *Marine and Petroleum Geology*, 74, 26-46.

LIU, J., SELBY, D., OBERMAJER, M. & MORT, A. 2018. Rhenium–osmium geochronology and oil–source correlation of the Duvernay petroleum system, Western Canada sedimentary basin: Implications for the application of the rhenium–osmium geochronometer to petroleum systems. *AAPG Bulletin*, 102, 1627-1657.

LIU, K. & EADINGTON, P. 2005. Quantitative fluorescence techniques for detecting residual oils and reconstructing hydrocarbon charge history. *Organic Geochemistry*, 36, 1023-1036.

LOGAN, G. A., HINMAN, M. C., WALTER, M. R. & SUMMONS, R. E. 2001. Biogeochemistry of the 1640 Ma McArthur River (HYC)

lead-zinc ore and host sediments, Northern Territory, Australia. *Geochimica et Cosmochimica Acta*, 65, 2317-2336.

LÜ, X., XIE, Q., YANG, N. & LI, J. 2007. Hydrocarbon accumulation in deep fluid modified carbonate rock in the Tarim Basin. *Chinese Science Bulletin*, 52, 184-192.

LUCK, J.-M. & ALLÈGRE, C. J. 1983.  $^{187}\text{Re}$ – $^{187}\text{Os}$  systematics in meteorites and cosmochemical consequences. *Nature*, 302, 130-132.

LUCK, J.-M., BIRCK, J.-L. & ALLEGRE, C.-J. 1980.  $^{187}\text{Re}$ – $^{187}\text{Os}$  systematics in meteorites: early chronology of the Solar System and age of the Galaxy. *Nature*, 283, 256-259.

LUDWIG, K. 2003. User's manual for Isoplot 3.00: a geochronological toolkit for Microsoft Excel. Berkeley Geochronology Center. Special publication, 4, 1-71.

LUO, X., ZHAO, Z. & MENG, Y. 2015. Application of an odd/even predominance of n-alkanes in oil–source rock correlation: taking the lower Paleozoic strata of the Tarim Basin as an example. *Toxicological & Environmental Chemistry*, 97, 409-416.

## **M**

MA, Y., GUO, X., GUO, T., HUANG, R., CAI, X. & LI, G. 2007. The Puguang gas field: New giant discovery in the mature Sichuan

Basin, southwest China. AAPG Bulletin, 91, 627-643.

MA, Y., ZHANG, S., GUO, T., ZHU, G., CAI, X. & LI, M. 2008. Petroleum geology of the Puguang sour gas field in the Sichuan Basin, SW China. Marine and Petroleum Geology, 25, 357-370.

MACHEL, H. 2001. Bacterial and thermochemical sulfate reduction in diagenetic settings—old and new insights. Sedimentary Geology, 140, 143-175.

MACHEL, H. G., KROUSE, H. R. & SASSEN, R. 1995. Products and distinguishing criteria of bacterial and thermochemical sulfate reduction. Applied Geochemistry, 10, 373-389.

MAGOON, L. B. & DOW, W. G. 1994. The petroleum system, in L. B. Magoon and W. G. Dow, eds., The petroleum system—from source to trap. AAPG Memoir 60, 3-24.

MAHDAOUI, F., MICHELS, R., REISBERG, L., PUJOL, M. & POIRIER, Y. 2015. Behavior of Re and Os during contact between an aqueous solution and oil: Consequences for the application of the Re–Os geochronometer to petroleum. Geochimica et Cosmochimica Acta, 158, 1-21.

MAHDAOUI, F., REISBERG, L., MICHELS, R., HAUTEVELLE, Y., POIRIER, Y. & GIRARD, J.-P. 2013. Effect of the progressive precipitation of petroleum asphaltenes on the Re–Os radioisotope system. Chemical Geology, 358, 90-100.

MAKISHIMA, A. & NAKAMURA, E. 2006. Determination of Os and Re isotope ratios at subpicogram levels using MC-ICPMS with solution nebulization and multiple ion counting. *Analytical Chemistry*, 78, 3794-3799.

MAO, J., XIE, G., BIERLEIN, F., QÜ, W., DU, A., YE, H., PIRAJNO, F., LI, H. M., GUO, B. & LI, Y. 2008. Tectonic implications from Re–Os dating of Mesozoic molybdenum deposits in the East Qinling–Dabie orogenic belt. *Geochimica et Cosmochimica Acta*, 72, 4607-4626.

MASLEN, E., GRICE, K., MÉTAYER, P. L., DAWSON, D. & EDWARDS, D. 2011. Stable carbon isotopic compositions of individual aromatic hydrocarbons as source and age indicators in oils from western Australian basins. *Organic Geochemistry*, 42, 387-398.

MATTAUCH, J. 1937. Das Paar  $^{87}\text{Rb}$ — $^{87}\text{Sr}$  und die Isobarenregel. *Naturwissenschaften*, 25, 189-191.

MCLIMANS, R. K. 1987. The application of fluid inclusions to migration of oil and diagenesis in petroleum reservoirs. *Applied Geochemistry*, 2, 585-603.

MEIJA, J., COPLEN, T. B., BERGLUND, M., BRAND, W. A., DE BIÈVRE, P., GRÖNING, M., HOLDEN, N. E., IRRGEHER, J., LOSS, R. D. & WALCZYK, T. 2016. Isotopic compositions of the elements 2013 (IUPAC technical Report). *Pure and Applied Chemistry*, 88, 293-306.

MEISEL, T., MOSER, J., FELLNER, N., WEGSCHEIDER, W. & SCHOENBERG, R. 2001. Simplified method for the determination of Ru, Pd, Re, Os, Ir and Pt in chromitites and other geological materials by isotope dilution ICP-MS and acid digestion. *Analyst*, 126, 322-328.

MEISSNER, F. F., WOODWARD, J. & CLAYTON, J. L. 1984. Stratigraphic relationships and distribution of source rocks in the greater Rocky Mountain region, Rocky Mountain Association of Geologists.

MEYERHOFF, A. A. 1980. Geology and petroleum fields in Proterozoic and Lower Cambrian strata, Lena-Tunguska petroleum province, eastern Siberia, USSR. *AAPG Special Volumes: Giant Oil and Gas Fields of the Decade 1968-1978*, 225-252.

MIDDLETON, A. W., UYSAL, I. T., BRYAN, S. E., HALL, C. M. & GOLDING, S. D. 2014. Integrating  $^{40}\text{Ar}$ – $^{39}\text{Ar}$ ,  $^{87}\text{Rb}$ – $^{87}\text{Sr}$  and  $^{147}\text{Sm}$ – $^{143}\text{Nd}$  geochronology of authigenic illite to evaluate tectonic reactivation in an intraplate setting, central Australia. *Geochimica et Cosmochimica Acta*, 134, 155-174.

MOLDOWAN, J. M., SEIFERT, W. K. & GALLEGOS, E. J. 1985. Relationship between petroleum composition and depositional environment of petroleum source rocks. *AAPG Bulletin*, 69, 1255-1268.

MORGAN, J. W. & WALKER, R. J. 1989. Isotopic determinations

of rhenium and osmium in meteorites by using fusion, distillation and ion-exchange separations. *Analytica Chimica Acta*, 222, 291-300.

MORTON, J. P. 1985a. Rb-Sr dating of diagenesis and source age of clays in Upper Devonian black shales of Texas. *Geological Society of America Bulletin*, 96, 1043-1049.

MORTON, J. P. 1985b. Rb-Sr evidence for punctuated illite/smectite diagenesis in the Oligocene Frio Formation, Texas Gulf Coast. *Geological Society of America Bulletin*, 96, 114-122.

MUNSON, T. 2014. Petroleum geology and potential of the onshore Northern Territory, 2014, Northern Territory Geological Survey.

MUKHERJEE, I. & LARGE, R. 2017. Application of pyrite trace element chemistry to exploration for SEDEX style Zn-Pb deposits: McArthur Basin, Northern Territory, Australia. *Ore Geology Reviews*, 81, 1249-1270.

MURRAY, A. P., SUMMONS, R. E., BOREHAM, C. J. & DOWLING, L. M. 1994. Biomarker and n-alkane isotope profiles for Tertiary oils: relationship to source rock depositional setting. *Organic Geochemistry*, 22, 521IN5-542IN6.

MUTLU, H., TONGUÇ UYSAL, I., ALTUNEL, E., KARABACAK, V., FENG, Y., ZHAO, J.-X. & ATALAY, O. 2010. Rb–Sr systematics of fault gouges from the North Anatolian Fault Zone (Turkey).

Journal of Structural Geology, 32, 216-221.

## N

NALDRETT, S. & LIBBY, W. 1948. Natural radioactivity of rhenium. *Physical Review*, 73, 487.

NEBEL, O., SCHERER, E. E. & MEZGER, K. 2011. Evaluation of the  $^{87}\text{Rb}$  decay constant by age comparison against the U–Pb system. *Earth and Planetary Science Letters*, 301, 1-8.

NI, Z.-Y., CHEN, Y.-J., LI, N. & ZHANG, H. 2012. Pb–Sr–Nd isotope constraints on the fluid source of the Dahu Au–Mo deposit in Qinling Orogen, central China, and implication for Triassic tectonic setting. *Ore Geology Reviews*, 46, 60-67.

NORMAN, M., BENNETT, V., MCCULLOCH, M. & KINSLEY, L. 2002. Osmium isotopic compositions by vapor phase sample introduction using a multi-collector ICP-MS. *Journal of analytical atomic spectrometry*, 17, 1394-1397.

NOZAKI, T., SUZUKI, K., RAVIZZA, G., KIMURA, J. I. & CHANG, Q. 2012. A Method for Rapid Determination of Re and Os Isotope Compositions Using ID-MC-ICP-MS Combined with the Sparging Method. *Geostandards and Geoanalytical Research*, 36, 131-148.

## O

ODERMATT, J. R. & CURIALE, J. A. 1991. Organically bound metals and biomarkers in the Monterey Formation of the Santa Maria Basin, California. *Chemical geology*, 91, 99-113.

OURISSON, G., ROHMER, M. & PORALLA, K. 1987. Prokaryotic hopanoids and other polyterpenoid sterol surrogates. *Annual Reviews in Microbiology*, 41, 301-333.

OXBURGH, R. 2001. Residence time of osmium in the oceans. *Geochemistry, Geophysics, Geosystems*, 2.

## **P**

PAGE, R. & SWEET, I. 1998. Geochronology of basin phases in the western Mt Isa Inlier, and correlation with the McArthur Basin. *Australian Journal of Earth Sciences*, 45, 219-232.

PAGE, R., JACKSON, M. & KRASSAY, A. 2000. Constraining sequence stratigraphy in north Australian basins: SHRIMP U–Pb zircon geochronology between Mt Isa and McArthur River. *Australian Journal of Earth Sciences*, 47, 431-459.

PEGRAM, W., KRISHNASWAMI, S., RAVIZZA, G. & TUREKIAN, K. 1992. The record of sea water 187Os/186Os variation through the Cenozoic. *Earth and Planetary Science Letters*, 113, 569-576.

PERRODON, A. & MASSE, P. 1984. Subsidence, sedimentation

and petroleum systems. *Journal of Petroleum Geology*, 7, 5-25.

PETERS, K., WALTERS, C. & MOLDOWAN, J. 2005. The Biomarker Guide, vol. 2. Biomarkers in petroleum systems and Earth history, 483-705p.

PEUCKER-EHRENBRINK, B. & RAVIZZA, G. 2000. The marine osmium isotope record. *Terra Nova*, 12, 205-219.

POLLASTRO, R. M. 1993. Considerations and applications of the illite/smectite geothermometer in hydrocarbon-bearing rocks of Miocene to Mississippian age. *Clays and Clay Minerals*, 41, 119-119.

## **R**

RADKE, M. 1988. Application of aromatic compounds as maturity indicators in source rocks and crude oils. *Marine and Petroleum Geology*, 5, 224-236.

RADKE, M., WELTE, D. & WILLSCH, H. 1986. Maturity parameters based on aromatic hydrocarbons: Influence of the organic matter type. *Organic geochemistry*, 10, 51-63.

RASMUSSEN, B. 2005. Evidence for pervasive petroleum generation and migration in 3.2 and 2.63 Ga shales. *Geology*, 33, 497-500.

RAVIKANT, V. & GOLANI, P., 2011. Rb-Sr direct dating of pyrite from the Pipela VMS Zn-Cu prospect, Rajasthan, NW India. *Journal*

of the Geological Society of India. 77, 149-159.

RAVIZZA, G. & TUREKIAN, K. K. 1989. Application of the  $^{187}\text{Re}$ - $^{187}\text{Os}$  system to black shale geochronometry. *Geochimica et Cosmochimica Acta*, 53, 3257-3262.

RAWLINGS, D. 1999. Stratigraphic resolution of a multiphase intracratonic basin system: the McArthur Basin, northern Australia. *Australian Journal of Earth Sciences*, 46, 703-723.

REICH, M., DEDITIUS, A., CHRYSSOULIS, S., LI, J.-W., MA, C.-Q., PARADA, M. A., BARRA, F. & MITTERMAYR, F. 2013. Pyrite as a record of hydrothermal fluid evolution in a porphyry copper system: A SIMS/EMPA trace element study. *Geochimica et Cosmochimica Acta*, 104, 42-62.

REISBERG, L. & MEISEL, T. 2002. The Re-Os Isotopic System: A Review of Analytical Techniques. *Geostandards Newsletter*, 26, 249-267.

RICIPUTI, L. R., COLE, D. R. & MACHEL, H. G. 1996. Sulfide formation in reservoir carbonates of the Devonian Nisku Formation, Alberta, Canada: An ion microprobe study. *Geochimica et Cosmochimica Acta*, 60, 325-336.

RODRIGUES, S., BLUETT, J., FERGUSON, B. R., GOLDING, S. D. & TITUS, L. 2015. Maturation profile at the Glyde Gas Discovery in the Southern McArthur Basin, Australia. *Search and Discovery*

Article #10799, AAPG Datapages.

ROONEY, A. D., SELBY, D., LEWAN, M. D., LILLIS, P. G. & HOUZAY, J.-P., 2012. Evaluating Re–Os systematics in organic-rich sedimentary rocks in response to petroleum generation using hydrous pyrolysis experiments. *Geochimica et Cosmochimica Acta*, 77, 275-291.

ROSENFELD, W. D. & SILVERMAN, S. R. 1959. Carbon isotope fractionation in bacterial production of methane. *Science*, 130, 1658-1659.

ROSMAN, K. & TAYLOR, P. 1998. Isotopic compositions of the elements 1997 (Technical Report). *Pure and Applied Chemistry*, 70, 217-235.

ROTENBERG, E., DAVIS, D. W., AMELIN, Y., GHOSH, S. & BERGQUIST, B. A. 2012. Determination of the decay-constant of  $^{87}\text{Rb}$  by laboratory accumulation of  $^{87}\text{Sr}$ . *Geochimica et Cosmochimica Acta*, 85, 41-57.

RUDNICK, R. L. & GAO, S. 2003. Composition of the continental crust. *Treatise on geochemistry*, 3, 1-64p.

## **S**

SCHOENBERG, R., NÄGLER, T. F. & KRAMERS, J. D. 2000. Precise Os isotope ratio and Re–Os isotope dilution measurements

down to the picogram level using multicollector inductively coupled plasma mass spectrometry. *International Journal of Mass Spectrometry*, 197, 85-94.

SCHOWALTER, T. T. 1979. Mechanics of secondary hydrocarbon migration and entrapment. *AAPG bulletin*, 63, 723-760.

SEIFERT, W. K. & MOLDOWAN, J. M. 1979. The effect of biodegradation on steranes and terpanes in crude oils. *Geochimica et Cosmochimica Acta*, 43, 111-126.

SELBY, D. & CREASER, R. A. 2003. Re–Os geochronology of organic rich sediments: an evaluation of organic matter analysis methods. *Chemical Geology*, 200, 225-240.

SELBY, D. & CREASER, R. A. 2005. Direct Radiometric Dating of Hydrocarbon Deposits Using Rhenium-Osmium Isotopes. *Science*, 308, 1293-1295.

SELBY, D., CREASER, R. A. & FOWLER, M. G. 2007a. Re–Os elemental and isotopic systematics in crude oils. *Geochimica et Cosmochimica Acta*, 71, 378-386.

SELBY, D., CREASER, R. A., STEIN, H. J., MARKEY, R. J. & HANNAH, J. L. 2007b. Assessment of the  $^{187}\text{Re}$  decay constant by cross calibration of Re–Os molybdenite and U–Pb zircon chronometers in magmatic ore systems. *Geochimica et Cosmochimica Acta*, 71, 1999-2013.

SEN, I. S. & PEUCKER-EHRENBRINK, B. 2014. Determination of Osmium Concentrations and  $^{187}\text{Os}/^{188}\text{Os}$  of Crude Oils and Source Rocks by Coupling High-Pressure, High-Temperature Digestion with Sparging  $\text{OsO}_4$  into a Multicollector Inductively Coupled Plasma Mass Spectrometer. *Analytical chemistry*, 86, 2982-2988.

SHEN, J., PAPANASTASSIOU, D. & WASSERBURG, G. 1996. Precise Re-Os determinations and systematics of iron meteorites. *Geochimica et Cosmochimica Acta*, 60, 2887-2900.

SHI, C., CAO, J., BAO, J., ZHU, C., JIANG, X. & WU, M. 2015. Source characterization of highly mature pyrobitumens using trace and rare earth element geochemistry: Sinian–Paleozoic paleo-oil reservoirs in South China. *Organic Geochemistry*, 83, 77-93.

SHI, C., CAO, J., TAN, X., LUO, B., ZENG, W. & HU, W. 2017. Discovery of oil bitumen co-existing with solid bitumen in the Lower Cambrian Longwangmiao giant gas reservoir, Sichuan Basin, southwestern China: Implications for hydrocarbon accumulation process. *Organic Geochemistry*, 108, 61-81.

SHIREY, S. B. & WALKER, R. J. 1995. Carius tube digestion for low-blank rhenium-osmium analysis. *Analytical Chemistry*, 67, 2136-2141.

SHIREY, S. B. & WALKER, R. J. 1998. The Re-Os isotope system in cosmochemistry and high-temperature geochemistry. *Annual*

Review of Earth and Planetary Sciences, 26, 423-500.

SIVAN, P., DATTA, G. C. & SINGH, R. R. 2008. Aromatic biomarkers as indicators of source, depositional environment, maturity and secondary migration in the oils of Cambay Basin, India. *Organic Geochemistry*, 39, 1620-1630.

SMOLIAR, M. I., WALKER, R. J. & MORGAN, J. W. 1996. Re-Os ages of group IIA, IIIA, IVA, and IVB iron meteorites. *Science*, 271, 1099.

SOFER, Z. 1984. Stable carbon isotope compositions of crude oils: application to source depositional environments and petroleum alteration. *Aapg Bulletin*, 68, 31-49.

ŚRODOŃ, J., CLAUER, N., HUFF, W., DUDEK, T. & BANAS, M. 2009. K-Ar dating of the Lower Palaeozoic K-bentonites from the Baltic Basin and the Baltic Shield: implications for the role of temperature and time in the illitization of smectite. *Clay Minerals*, 44, 361-387.

STOUT, S. A. 1992. Aliphatic and aromatic triterpenoid hydrocarbons in a Tertiary angiospermous lignite. *Organic Geochemistry*, 18, 51-66.

SUMMONS, R. E., POWELL, T. G. & BOREHAM, C. J. 1988. Petroleum geology and geochemistry of the Middle Proterozoic McArthur Basin, Northern Australia: III. Composition of extractable

hydrocarbons. *Geochimica et Cosmochimica Acta*, 52, 1747-1763.

SUN, T., QIAN, Z.-Z., LI, C., XIA, M.-Z. & YANG, S.-H. 2013. Petrogenesis and economic potential of the Erhongwa mafic-ultramafic intrusion in the Central Asian Orogenic Belt, NW China: constraints from olivine chemistry, U-Pb age and Hf isotopes of zircons, and whole-rock Sr-Nd-Pb isotopes. *Lithos*, 182, 185-199.

SUN, W.-Y., LI, S.-R., SANTOSH, M., WANG, X. & ZHANG, L.-J., 2014. Isotope geochemistry and geochronology of the Qiubudong silver deposit, central North China Craton: implications for ore genesis and lithospheric dynamics. *Ore Geology Reviews*, 57, 229-242.

SUZUKI, K., MIYATA, Y. & KANAZAWA, N. 2004. Precise Re isotope ratio measurements by negative thermal ionization mass spectrometry (NTI-MS) using total evaporation technique. *International Journal of Mass Spectrometry*, 235, 97-101.

SYMONS, D. 2007. Paleomagnetism of the HYC Zn-Pb SEDEX Deposit, Australia: evidence of an epigenetic origin. *Economic Geology*, 102, 1295-1310.

## **T**

TAYLOR, G.H., TEICHMULLER, M., DAVIS, A., DIESSEL, C.F.K., LITCKE, R. & ROBERT, P. 1998. *Organic Petrology*. Gebrüder Borntraeger, Berlin. 704p.

TIAN, H., XIAO, X., WILKINS, R. W., GAN, H., XIAO, Z., LIU, D. & GUO, L. 2008. Formation and evolution of Silurian paleo-oil pools in the Tarim Basin, NW China. *Organic Geochemistry*, 39, 1281-1293.

TISSOT, B.P. & WELTE, D.H. 1984. *Petroleum formation and occurrence*. Second edition. Springer-Verlag, Heidelberg. 699p.

## U

ULMISHEK, G. 1986. Stratigraphic aspects of petroleum resource assessment. In *Oil and Gas Assessment: Methods and Applications* (eds. D.D. RICE). AAPG Studies in Geology. 21, 59-68.

UYSAL, I. T., GOLDING, S. D. & THIEDE, D. S. 2001. K–Ar and Rb–Sr dating of authigenic illite–smectite in Late Permian coal measures, Queensland, Australia: implication for thermal history. *Chemical Geology*, 171, 195-211.

UYSAL, I. T., MORY, A. J., GOLDING, S. D., BOLHAR, R. & COLLERSON, K. D. 2005. Clay mineralogical, geochemical and isotopic tracing of the evolution of the Woodleigh impact structure, Southern Carnarvon Basin, Western Australia. *Contributions to Mineralogy and Petrology*, 149, 576-590.

## V

VANDENBROUCKE, M. & LARGEAU, C. 2007. Kerogen origin,

evolution and structure. *Organic Geochemistry*, 38, 719-833.

VOLK, H., DUTKIEWICZ, A., GEORGE, S. & RIDLEY, J. 2003. Oil migration in the Middle Proterozoic Roper Superbasin, Australia: evidence from oil inclusions and their geochemistries. *Journal of Geochemical Exploration*, 78, 437-441.

## W

WAKEHAM, S. G., SCHAFFNER, C. & GIGER, W. 1980. Polycyclic aromatic hydrocarbons in Recent lake sediments—II. Compounds derived from biogenic precursors during early diagenesis. *Geochimica et Cosmochimica Acta*, 44, 415-429.

WANG, C., DENG, J., SANTOSH, M., CARRANZA, E.J.M., GONG, Q., GUO, C., XIA, R. & LAI, X., 2015. Timing, tectonic implications and genesis of gold mineralization in the Xincheng gold deposit, China: C–H–O isotopes, pyrite Rb–Sr and zircon fission track thermochronometry. *Ore Geology Reviews*, 65, 659-673.

WANG, Y., ZENG, Q. & LIU, J., 2014. Rb–Sr Dating of Gold-bearing Pyrites from Wulaga Gold Deposit and its Geological Significance. *Resource Geology*, 64, 262-270.

WANG, Z., FINGAS, M. & LI, K. 1994. Fractionation of a light crude oil and identification and quantitation of aliphatic, aromatic, and biomarker compounds by GC-FID and GC-MS, part II. *Journal of Chromatographic Science*, 32, 367-382.

WASSERBURG, G., HAYDEN, R. & JENSEN, K. J. 1956. A40-K40 dating of igneous rocks and sediments. *Geochimica et Cosmochimica Acta*, 10, 153-165.

WEI, G., CHEN, G., DU, S., ZHANG, L. & YANG, W. 2008. Petroleum systems of the oldest gas field in China: Neoproterozoic gas pools in the Weiyuan gas field, Sichuan Basin. *Marine and Petroleum Geology*, 25, 371-386.

WEI, G., XIE, Z., SONG, J., YANG, W., WANG, Z., LI, J., WANG, D., LI, Z. & XIE, W. 2015. Features and origin of natural gas in the Sinian–Cambrian of central Sichuan paleo-uplift, Sichuan Basin, SW China. *Petroleum Exploration and Development*, 42, 768-777.

WILLIFORD, K. H., GRICE, K., LOGAN, G. A., CHEN, J. & HUSTON, D. 2011. The molecular and isotopic effects of hydrothermal alteration of organic matter in the Paleoproterozoic McArthur River Pb/Zn/Ag ore deposit. *Earth and Planetary Science Letters*, 301, 382-392.

WORDEN, R. & SMALLEY, P. 1996. H<sub>2</sub>S-producing reactions in deep carbonate gas reservoirs: Khuff Formation, Abu Dhabi. *Chemical Geology*, 133, 157-171.

WORTMANN, U. G., BERNASCONI, S. M. & BÖTTCHER, M. E. 2001. Hypersulfidic deep biosphere indicates extreme sulfur isotope fractionation during single-step microbial sulfate reduction. *Geology*, 29, 647-650.

WU, J., LI, Z. & WANG, X.-C., 2016. Comment on “Behavior of Re and Os during contact between an aqueous solution and oil: Consequences for the application of the Re–Os geochronometer to petroleum”[*Geochim. Cosmochim. Acta* 158 (2015) 1–21]. *Geochimica et Cosmochimica Acta*, 186, 344-347.

## X

XIAO, X., LIU, D. & FU, J. 1996. Multiple phases of hydrocarbon generation and migration in the Tazhong petroleum system of the Tarim Basin, People's Republic of China. *Organic Geochemistry*, 25, 191-197.

XIAO, Z., LI, M., HUANG, S., WANG, T., ZHANG, B., FANG, R., ZHANG, K., NI, Z., ZHAO, Q. & WANG, D. 2016. Source, oil charging history and filling pathways of the Ordovician carbonate reservoir in the Halahatang Oilfield, Tarim Basin, NW China. *Marine and Petroleum Geology*, 73, 59-71.

XU, Y.-G., WEI, X., LUO, Z.-Y., LIU, H.-Q. & CAO, J. 2014. The Early Permian Tarim Large Igneous Province: main characteristics and a plume incubation model. *Lithos*, 204, 20-35.

## Y

YAMASHITA, Y., TAKAHASHI, Y., HABA, H., ENOMOTO, S. & SHIMIZU, H. 2007. Comparison of reductive accumulation of Re and Os in seawater–sediment systems. *Geochimica et*

Cosmochimica Acta, 71, 3458-3475.

YANG, J. & ZHOU, X. 2000. The Rb-Sr isochron of ore and pyrite sub-samples from Linglong gold deposit, Jiaodong Peninsula, eastern China and their geological significance. Chinese Science Bulletin, 45, 2272-2277.

YANG, J.-H. & ZHOU, X.-H. 2001. Rb-Sr, Sm-Nd, and Pb isotope systematics of pyrite: Implications for the age and genesis of lode gold deposits. Geology, 29, 711-714.

YAO, J., HUA, R. & LIN, J. 2006. REE, Pb-S isotope geochemistry, and Rb-Sr isochron age of pyrites in the Baoshan deposit, south Hunan province, China. Acta Geologica Sinica, 80, 1045-1054.

YU, J., MO, X., DONG, G., YU, X., XING, F., LI, Y. & HUANG, X. 2011. Felsic volcanic rocks from northern Tarim, NW China: Zircon U-Pb dating and geochemical characteristics. Acta Petrologica Sinica, 27, 2184-2194.

YUN, J.-B., SHI, H.-S., ZHU, J.-Z., ZHAO, L.-H. & QIU, H.-N. 2010. Dating petroleum emplacement by illite  $^{40}\text{Ar}/^{39}\text{Ar}$  laser stepwise heating. AAPG Bulletin, 94, 759-771.

## **Z**

ZHANG, D., ZHOU, T., YUAN, F., JOWITT, S. M., FAN, Y. & LIU, S. 2012. Source, evolution and emplacement of Permian Tarim

Basalts: evidence from U–Pb dating, Sr–Nd–Pb–Hf isotope systematics and whole rock geochemistry of basalts from the Keping area, Xinjiang Uygur Autonomous region, northwest China. *Journal of Asian Earth Sciences*, 49, 175-190.

ZHANG, L., SHEN, Y., LIU, T., ZENG, Q., LI, G. & LI, H. 2003.  $^{40}\text{Ar}/^{39}\text{Ar}$  and Rb-Sr isochron dating of the gold deposits on northern margin of the Jiaolai Basin, Shandong, China. *Science in China Series D: Earth Sciences*, 46, 708-718.

ZHANG, S. & HUANG, H. 2005. Geochemistry of Palaeozoic marine petroleum from the Tarim Basin, NW China: Part 1. Oil family classification. *Organic Geochemistry*, 36, 1204-1214.

ZHANG, S., HANSON, A., MOLDOWAN, J., GRAHAM, S., LIANG, D., CHANG, E. & FAGO, F. 2000. Paleozoic oil–source rock correlations in the Tarim basin, NW China. *Organic Geochemistry*, 31, 273-286.

ZHANG, S., LIANG, D., LI, M., XIAO, Z. & HE, Z. 2002. Molecular fossils and oil-source rock correlations in Tarim Basin, NW China. *Chinese Science Bulletin*, 47, 20-27.

ZHANG, Y., LIU, J. & GUO, Z. 2010. Permian basaltic rocks in the Tarim basin, NW China: implications for plume–lithosphere interaction. *Gondwana Research*, 18, 596-610.

ZHANG, Y., LIU, K. & LUO, X. 2016. Evaluation of  $^{40}\text{Ar}/^{39}\text{Ar}$

Geochronology of Authigenic Illites in Determining Hydrocarbon Charge Timing: A Case Study from the Silurian Bituminous Sandstone Reservoirs, Tarim Basin, China. *Acta Geologica Sinica (English Edition)*, 90, 684-703.

ZHANG, Y., ZWINGMANN, H., LIU, K., TODD, A. & LUO, X. 2011. Hydrocarbon charge history of the Silurian bituminous sandstone reservoirs in the Tazhong uplift, Tarim Basin, China. *AAPG Bulletin*, 95, 395-412.

ZHAO, M.-J., WANG, Z.-M., PAN, W.-Q., LIU, S.-B., QIN, S.-F. & HAN, J.-F. 2008. Lower palaeozoic source rocks in Manjiaer sag, Tarim Basin. *Petroleum Exploration and Development*, 35, 417-423.

ZHAO, X.-F., ZHOU, M.-F., LI, J.-W., SELBY, D., LI, X.-H. & QI, L. 2013. Sulfide Re-Os and Rb-Sr isotope dating of the Kangdian IOCG metallogenic province, southwest China: Implications for regional metallogenesis. *Economic Geology*, 108, 1489-1498.

ZHOU, J., HUANG, Z., ZHOU, M., LI, X. & JIN, Z. 2013. Constraints of C–O–S–Pb isotope compositions and Rb–Sr isotopic age on the origin of the Tianqiao carbonate-hosted Pb–Zn deposit, SW China. *Ore Geology Reviews*, 53, 77-92.

ZHOU, J.-F., ZHANG, H.-Q., YU, J.-P., ZHU, Y.-F., YAO, Q.-Z. & YU-CHUN, Y. 2015. Analysis of the Hydrocarbon Accumulation Conditions and Exploration Potential in the Ordovician in Yudong Area of West Tabei Uplift. *Natural Gas Geoscience*, 26, 121-129.

ZHOU, M.-F., ZHAO, J.-H., JIANG, C.-Y., GAO, J.-F., WANG, W. & YANG, S.-H. 2009. OIB-like, heterogeneous mantle sources of Permian basaltic magmatism in the western Tarim Basin, NW China: implications for a possible Permian large igneous province. *Lithos*, 113, 583-594.

ZHU, D.-Y. & MENG, Q.-Q. 2010. Genesis of pyrite in Ordovician carbonate of the Tarim Basin. *Acta Petrologica et Mineralogica*, 29, 516-524.

ZHU, G., CUI, J., SU, J., YANG, H., ZHANG, B., HU, J. & ZHU, Y. 2012a. Accumulation and reformation of Silurian reservoir in the northern Tarim Basin. *Acta Geologica Sinica (English edition)*, 86, 209-225.

ZHU, G., ZHANG, B., YANG, H., SU, J. & HAN, J. 2014. Origin of deep strata gas of Tazhong in Tarim Basin, China. *Organic Geochemistry*, 74, 85-97.

ZHU, G., ZHANG, S., LIU, K., YANG, H., ZHANG, B., SU, J. & ZHANG, Y. 2013a. A well-preserved 250 million-year-old oil accumulation in the Tarim Basin, western China: Implications for hydrocarbon exploration in old and deep basins. *Marine and Petroleum Geology*, 43, 478-488.

ZHU, G., ZHANG, S., SU, J., HUANG, H., YANG, H., GU, L., ZHANG, B. & ZHU, Y. 2012b. The occurrence of ultra-deep heavy oils in the Tabei Uplift of the Tarim Basin, NW China. *Organic*

Geochemistry, 52, 88-102.

ZHU, G., ZHANG, S., SU, J., ZHANG, B., YANG, H., ZHU, Y. & GU, L. 2013b. Alteration and multi-stage accumulation of oil and gas in the Ordovician of the Tabei Uplift, Tarim Basin, NW China: Implications for genetic origin of the diverse hydrocarbons. *Marine and Petroleum Geology*, 46, 234-250.

ZOU, C., YANG, Z., DAI, J., DONG, D., ZHANG, B., WANG, Y., DENG, S., HUANG, J., LIU, K., YANG, C., WEI, G. & PAN, S. 2015. The characteristics and significance of conventional and unconventional Sinian–Silurian gas systems in the Sichuan Basin, central China. *Marine and Petroleum Geology*, 64, 386-402.

ZOU, S.-Y., LI, Z.-L., SONG, B., ERNST, R. E., LI, Y.-Q., REN, Z.-Y., YANG, S.-F., CHEN, H.-L., XU, Y.-G. & SONG, X.-Y. 2015. Zircon U–Pb dating, geochemistry and Sr–Nd–Pb–Hf isotopes of the Wajilitag alkali mafic dikes, and associated diorite and syenitic rocks: implications for magmatic evolution of the Tarim Large Igneous Province. *Lithos*, 212, 428-442.

ZWINGMANN, H., CLAUER, N. & GAUPP, R. 1999. Structure-related geochemical (REE) and isotopic (K-Ar, Rb-Sr,  $\delta^{18}\text{O}$ ) characteristics of clay minerals from Rotliegend sandstone reservoirs (Permian, northern Germany). *Geochimica et Cosmochimica Acta*, 63, 2805-2823.